Development of methods to study bacterial cell signaling *in vivo*

by

Samuel Wilson Duvall

B.S., Bethany College, 2015

Submitted to the Graduate Faculty of the

Dietrich School of Arts and Sciences in partial fulfillment

of the requirements for the degree of

Doctor of Philosophy

University of Pittsburgh

2020

UNIVERSITY OF PITTSBURGH

DIETRICH SCHOOL OF ARTS AND SCIENCES

This dissertation was presented

by

Samuel Wilson Duvall

It was defended on

November 23, 2020

and approved by

Sunil Saxena, Professor and Department Chair, Department of Chemistry

Steve Weber, Professor, Department of Chemistry

Joseph McCormick, Professor and Department Chair, Bayer School of Natural and Environmental Sciences Biological Sciences, Duquesne University

Thesis Advisor/Dissertation Director: W. Seth Childers, Assistant Professor, Department of Chemistry

Development of methods to study bacterial cell signaling *in vivo*

Samuel Wilson Duvall, PhD

University of Pittsburgh, 2020

Our understanding of bacterial signaling systems is still in its early stages. As we learn more about how bacteria respond to environmental and intracellular cues, we will be able to tackle some of the most important problems related to bacteria. Drug-resistance, agriculture, environmental remediation, and more global problems will be better understood and potentially solved in some way by our understanding of bacterial signaling systems. Two-component systems are the foundation of bacterial signaling. Currently, we lack tools for studying two-component signaling systems *in vivo* and with greater depth than simply whether two proteins colocalize or not. In this dissertation, I will explore the development of tools to study members of two-component signaling systems and the proteins that scaffold them.

Chapter 2 will explore the first example of a histidine kinase FRET sensor which showcases the potential for this type of FRET sensor for any histidine kinase. I provide details on its design and controls for working with it on conventional epifluorescent microscopes. Chapter 3 expands on the use of the CckA-FRET biosensor and previously reported leucine zipper technology to understand the domain interactions of the pseudokinase DivL with the histidine kinase CckA. In Chapter 4, I apply knowledge of histidine kinases to the current antibiotic crisis.

Scaffolding proteins play a multitude of roles in bacteria. In Chapter 5 I will explore PodJ, the multirole scaffolding protein that can recruit PopZ in order to add depth to a signaling network. Chapter 6 will further look at an interesting phenotype of PodJ and how it relates to self-assembly

and curvature recognition. Chapter 6 will also cover new tool development for working in *C. crescentus*.

In each chapter, I will cover questions and future aims. This dissertation overall is aimed at the development of new ways of thinking about bacterial signaling systems and how to study them.

Table of contents

List of tables

List of figures

Abbreviations

6xHis	6xhistidine
A. tumefaciens	*Agrobacterium tumefaciens*
ADP	adenosine diphosphate
AMPPNP	adenyl-imidophosphate
AMPs	antimicrobial peptides
ATP	adenosine triphosphate
B. subtilis	*Bacillus subtilis*
BODIPY	boron dipyrromethene
BSA	bovine serum albumin
C. crescentus	*Caulobacter crescentus*
CA	catalytic assist
Cache	calcium channel and chemotaxis receptors
CC	coiled-coil
CCA	complimentary chromatic adaption
CCD	charged-coupled device
CDP	cytidine diphosphate
CHASE	cyclases/histidine kinases associated sensory extracellular
CTP	cytidine triphosphate
cyclic di-GMP	3'-5'-Cyclic diguanylic acid
DHp	dimerization and histidine phosphotransfer
DITE	aspartic acid, isoleucine, threonine, glutamic acid
DMSO	dimethyl sulfoxide
DNA	deoxyribonucleic acid
DSF	differential scanning fluorimetry
E. coli	*Escherichia coli*
ECFP	enhanced cyan fluorescent protein
EGFP	enhanced green fluorescent protein
EPR	electron paramagnetic resonance
EYFP	enhanced yellow fluorescent protein
FDAA	fluorescent D-amino acid
FN	fibronectin
FP	fluorescence polarization
FRET	fluorescence resonance energy transfer
GAF	cGMP-specific phosphodiesterases, adenyl cyclases, and FhlA
GFP	green fluorescent protein

GHKL	gyrases, Hsp90, histidine kinase, MutL
GT	glycosyl transferase
HAMP	histidine kinase, adenylate cyclase, methyl accepting, and phosphatases
HK	histidine kinase
Hsp90	heat shock protein 90
IPTG	isopropyl β-D-1-thiogalactopyranoside
LZ	leucine zipper
MS	mass spectroscopy
M2G	M2 plus glucose
MRSA	methicillin-resistant *Staphylococcus aureus*
NAD^+	nicotinamide adenine dinucleotide, oxidized form
NADH	nicotinamide adenine dinucleotide, reduced form
NMR	nuclear magnetic resonance
nNG	mNeonGreen
OD_{600}	optical density at 600 nm
P. aeruginosa	*Pseudomonas aeruginosa*
PAS	Per-Arnt-Sim
PBPs	penicillin-binding proteins
PBS	phosphate buffered solution
PD	pre-divisional
PEG	polyethylene glycol
PEP	phosphoenol pyruvate
PG	peptidoglycan binding
$PodJ_{AT}$	PodJ of *A. tumefaciens*
$PodJ_{CC}$	PodJ of *C. crescentus*
$PodJ_L$	PodJ long
$PodJ_S$	PodJ short
PVDF	polyvinylidene difluoride
PSE	proline, serine, glutamic acid
PYE	peptone yeast extract
pylT	pyrrolysyl tRNA
R_0	Förster radius
REC	receiver domain
RD	receiver domain
RF1	Release factor 1
RNA	ribonucleic acid
RR	response regulator
S. cerevisiae	*Saccharomyces cerevisiae*
SAR	structure activity relationship

SDS-PAGE	sodium dodecyl sulfate-polyacrylamide gel electrophoresis
SEC	size exclusion chromatography
sfGFP	superfolder green fluorescent protein
SH3	SRC homology 3 domain
SPOR	sporulation repeat
SPR	surface plasmon resonance
STKs	serine/threonine kinases
TBST	tris buffered saline plus Tween-20
tmRNA	transfer-messenger RNA
TNP-ATP	[2’(3’)-*O*-(2,4,6-trinitrophenyl)adenosine 5’-triphosphate]
tRNA	transfer ribonucleic acid
UAA	unnatural amino acid

Preface

Thank you to everyone who helped me get this far.

To my parents who have always believed I could do anything I put my mind to.

To my brother for pushing me harder.

To my best friend for all how far we've come since we left our little valley town.

To everyone I've met at Pitt who has helped open my world to new ideas.

To Kitty for making me a better teacher than I ever thought I could be.

To Taylor for putting up with me through it all.

To everyone who I have grown up with in the Childers lab as we all built a lab together.

Last but not least, to Seth for believing in my abilities as a scientist when I wouldn't and giving me the chance to walk this strange journey that is getting your doctorate.

1.0 Introduction

This chapter was written in collaboration with Kimberly Kowallis, Wei Zhao, and W. Seth Childers. Adapted by permission from Springer Nature: Springer eBook "Manipulation of Bacterial Signaling Using Engineered Histidine Kinases" by Kimberly A. Kowallis*, Samuel W. Duvall*, Wei Zhao, W. Seth Childers, * indicates co-first authors, Copyright (2020).

1.1 Potential for engineering histidine kinases

Two-component systems allow bacteria to respond to changes through signal recognition by the histidine kinase (HK) and transfer of the phosphate to its response regulator (RR).[1,2] The RR can then activate a response, which is often gene transcription.[3] HKs are typically homodimeric, embedded in the membrane, and have one or more sensory domains that regulate the kinase domain. The HK domain, while highly conserved, contains many customizable functions including optional phosphatase activity, alteration of phosphotransfer partner specificity, and regulation of kinase heterodimerization (Figure 1–1).

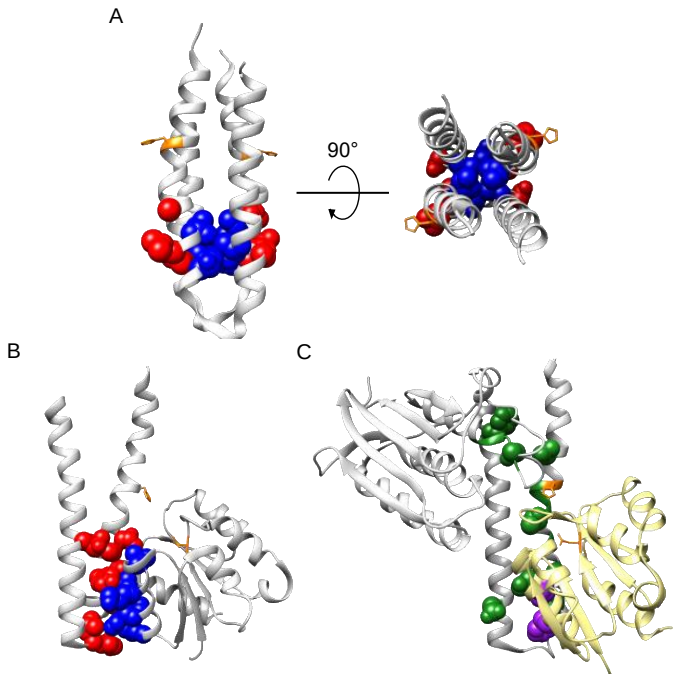

Figure 1–1 Customizable residues for the DHp bundle of a histidine kinase and the RD of a RR.
Phosphorylatable histidine and aspartic acid are colored orange. A) Residues involved in dimerization of the dimerization and histidine phosphorylation (DHp) domain are blue and buried in the bundle (PDB: 5B1N.[4] Residues in red are involved in RR specificity and are solvent exposed.[5] B) The HK853-RR468 crystal structure (PDB: 3DGE [6]) highlights residues involved in the HK/RR specificity. Residues in red are located on the HK and blue are located on the RR. C) HK853-RR468 crystal structure (PDB: 3DGE[6]) with residues in cyan denoting the DXXN phosphatase motif, residues in green denoting the GXGXG motif, with second X (T in HK853) shown as spherical [6], blue showing the T267 and Y272 residues located on the HK capable of reducing phosphatase activity[6], and purple for the I17 and F20 residues located on the RR that can be mutated to prevent phosphate back-transfer.[6] All crystal structures images generated using Chimera.[7]

The variation of these functions in the kinase domains generates an array of different phenotypic responses (Figure 1–2A).

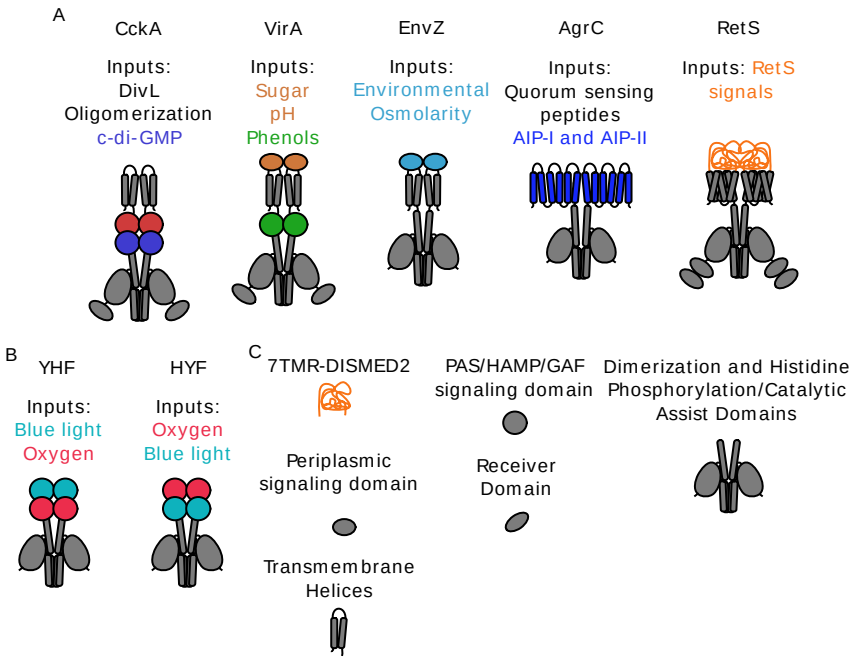

Figure 1–2 Signals and input domains of natural and synthetic HKs.
A) Domain architectures of 5 HKs with diverse sensing capabilities. Outputs include CckA activating transcription of cell-cycle regulated genes through the RR CtrA[8], VirA controlling virulence to plants and interkingdom gene transfer through the RR VirG[9], EnvZ controlling porin formation genes through the RR OmpR[10], AgrC activating virulence related genes[11], and RetS inhibiting GacS/GacA and PA1611 virulence pathways through heterodimer formation.[12] B) Depiction of the synthetic chimeras of FixL and YtvA YHF and HYF HKs. C) Legend of domain representations.

HKs exhibit the most remarkable diversity in the sensory domains with varied domain architectures and sensing capabilities.[1] As an example, *C. crescentus* cell-cycle kinase CckA homologs vary in the number and identity of PAS sensory domains across the alpha-proteobacteria (Figure 1–3).

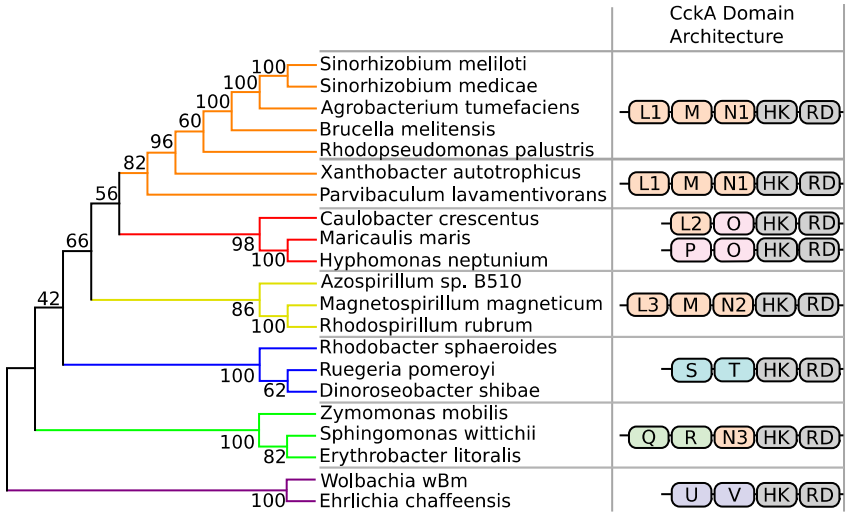

Figure 1–3 Analysis of CckA homologs in alphaproteobacteria species highlights diversity in signaling domains. Signaling domains are lettered and colored for predicted unique signaling domains (L1-V). Catalytic domains are conserved, colored gray, and labeled HK-RD.

This diversity highlights the potential evolution of new connections that can occur between input signals and output responses through domain shuffling of sensory domains. In contrast to many eukaryotic sensory proteins that contain flexible linkers between domains, the linker region that connects the sensor to the kinase domain often contains one or more helical folds that allosterically transmit signals between domains.[9,13-16]

Methods such as cysteine cross-linking[11,13,16] and mutagenesis have greatly contributed to the understanding of HK signal transmission mechanisms, but not without the unpredictable effects that point mutations can have on protein folding and activity. Crystallography[15,17-21] has also been a powerful technique to analyze the conformational states of HKs, but due to many HKs having one or more transmembrane domains, it is often difficult to isolate soluble full-length HKs. Furthermore, the transmembrane region is not dispensable for activity in some cases.[22,23] Additionally, the central dimerization and histidine phosphotransfer (DHp) domain must interact

with distinct domains to carryout kinase versus phosphotransfer functions, which leads to HK conformational diversity. To address these challenges, HK engineering strategies have provided a hypothesis-driven approach to test bacterial HK signal transmission mechanisms.

1.2 Chimeric histidine kinases

1.2.1 First generation chimeric HKs reveal the importance of the connecting helical linker in signal transmission

Early examples of engineered chimeric histidine kinases were generated by fusing the periplasmic and transmembrane domains of the *Escherichia coli* (*E. coli*) aspartate sensing Tar chemoreceptor protein to the cytoplasmic HK domains of the osmolarity sensing protein EnvZ of *E. coli*.[24,25] Construction and design of chimeric HKs has revealed that the linker region acts as a "structural joint" for transmitting signals between domains[26] and that linker compositional changes can place the kinase in the "on" or "off" state.[27]

It was further shown that the C-terminal region of many classes of sensory domains (e.g. HAMP (histidine kinase, adenylate cyclases, methyl accepting proteins, and phosphatases), PAS (Per-Arnt-Sim) and GAF (cGMP-specific phosphodiesterases, adenylyl cyclases, and FhlA) exploit a C-terminal helix that can allosterically transmit a signaling event from the sensor binding site to the histidine phosphorylation site.[28,29] The function of a chimeric HK is therefore dependent upon maintenance of the α-helix heptad periodicity. A second critical feature specific to PAS sensory domains is a structural motif that is positioned between the PAS domain and the C-terminal helix termed the DIT signal transmission motif.[16,30-33] The DITE motif is a PAS domain

signal transmission motif that is comprised **D**-(A/**I**/V)-(**T**/S)-**E** (DITE) at the N-terminal region of the last α-helix of the domain.[28] This motif forms hydrogen bonding and salt bridge interactions that couple the PAS fold to the C-terminal α-helix such that signal can alter the conformation of downstream domains.[28] Changing the conserved aspartic acid and threonine to aliphatic amino acids have been shown to abolish signal transduction through the α-helix.[15] The DIT motif mutations therefore present an approach to test if signals are transmitted from a given PAS domain to downstream effector domains through the helical linker.

1.2.2 Aromatic tuning to regulate HK interactions at the membrane-cytosolic interface

Transmission of a signal from the sensory domain in the periplasm to the cytoplasm is highly influenced by transmembrane helix interactions with the membrane. This can present a unique challenge when heterologously expressing a kinase from another organism, as changes in membrane composition can cause conformational changes and repositioning of the transmembrane helix and subsequently alter kinase activity.[18,34-36] The configuration of aromatic residues near the membrane interface has been shown to modulate HK activity *in vivo*.[35,37] The repositioning of aromatic residues at the membrane-cytosolic interface to change the interactions between the transmembrane helix and the membrane has been termed aromatic tuning.[38,39] As shown in Figure 1–4, the tryptophan is repositioned by one residue in both the N-terminal and C-terminal directions and this impacts the helix tilt angle or depth within the membrane. This aromatic tuning strategy can optimize the responsiveness of chimeric HKs by expanding the sensor's dynamic range, and in some cases, restoring kinase activity to an unresponsive chimera.[37]

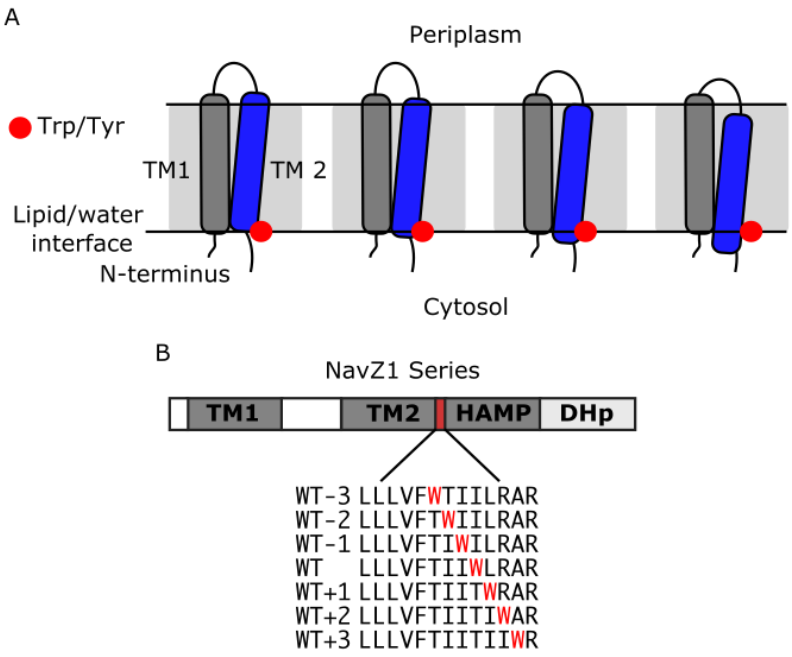

Figure 1–4 Aromatic tuning of transmembrane helices.
A) The impact of repositioning the aromatic tryptophan or tyrosine located at the lipid-water interface of the transmembrane and cytosol upon HK signaling. B) NavZ1 series highligts change in position of tryptophan.

1.2.3 Use of chimeric HKs to identify new signaling inputs

Due to the lack of conservation among sensory domains, it has been difficult to determine physiological signal inputs of the vast majority of HKs. One approach is engineering HK chimeras in which a sensory domain of unknown function is attached to well-characterized kinase domain. Combined with the cognate RR, a transcriptional gene reporter can be used to identify factors that activate or repress the signaling domain (Figure 1–5A).

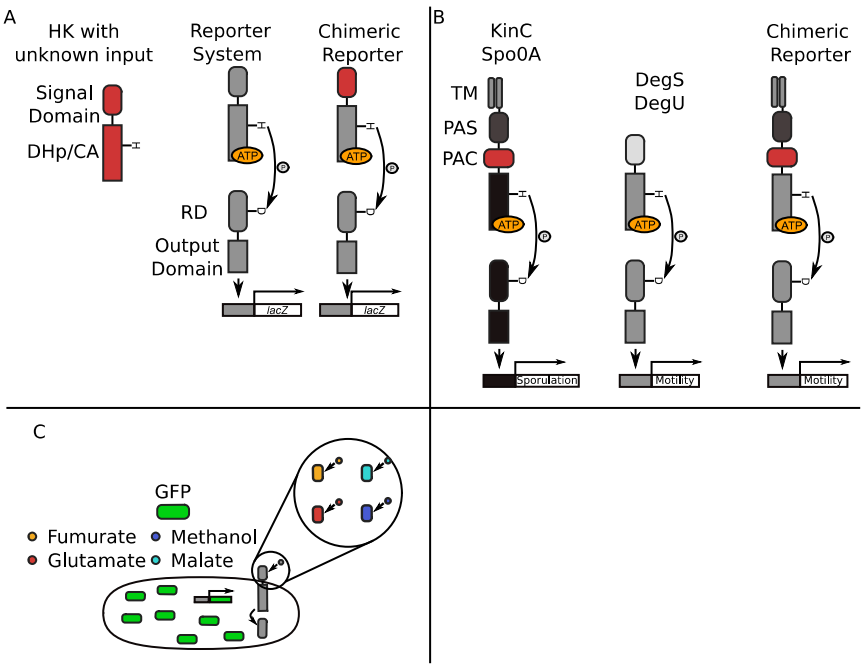

Figure 1–5 Design and application of chimeric histidine kinases to detect known and unknown signals.
A) General design of a HK chimera to report on the activity of an unknown signaling domain via β-galactosidase expression. B) A KinC/DegS reporter strain was generated such that membrane-damaging agent nyastatin could be sensed via KinC and trigger motility regulation through the DegS pathway. C) Small molecule reporters sensing fumurate, methanol, glutamate, and malate using the *E. coli* EnvZ/OmpR two-component system with GFP as a transcriptional readout.

This approach was used to characterize novel signals that regulate the sensory domain of the *Caulobacter crescentus* (*C. crescentus)* cell-cycle kinase CckA.[33] Prior to these studies, it was unclear what signals regulate CckA activity. In this study two design criteria were considered: first, selection of a well-understood kinase domain and downstream reporter and second, selection of the fusion site between the CckA sensor and the kinase. For this assay, the kinase should be orthogonal to the existing two-component systems encoded in the bacteria to insulate the chimeric HK from native two-component signaling networks. In this case Iniesta *et al.* selected a *C. crescentus* oxygen sensing FixL/FixJ β-galactosidase reporter used in strains with a knockout of the native FixL/FixJ signaling pathway.[40] To identify the best fusion sites a panel of CckA-FixL chimeras was constructed and screened. The most responsive CckA-FixL chimera was coupled together with data from a transposon screen to identify protein signals that regulate CckA's activity

and subcellular localization. This study revealed that a novel pseudokinase DivL promotes CckA activity through direct or indirect interaction with CckA's tandem sensory domain.[33] This example highlights the potential of coupling chimeric HKs together with fluorescent transcription reporter and high-throughput library approaches to identify signal inputs that modulate HKs that are critical for development or pathogenesis.

1.2.4 Re-wired developmental response and identification of potassium leakage sensor domain

Bacillus subtilis (*B. subtilis*) is a model organism for bacterial differentiation into diverse cell types. The membrane potential sensing kinase KinC in *B. subtilis* has been implicated in formation of biofilms in response to membrane damage due to exposure to surfactins and other antimicrobial agents.[41] Therefore it was proposed that KinC was a potassium leakage sensing kinase. To identify the domains of KinC involved in sensing the effects of potassium leakage, the sensor of KinC was attached to the well characterized *B. subtilis* HK DegS, which controls genes that regulate swarming behavior, in a DegS knockout strain. Using a swarm size assay with a strain containing the KinC-DegS chimera, it was demonstrated that the KinC sensory domain was a potassium leakage sensory directly or indirectly.[41] Wild-type cells typically respond to potassium leakage by upregulation of KinC biofilm genes, while the KinC-DegS chimera re-wires this response to potassium leakage to upregulate DegS-DegU motility genes (Figure 1–5B). This case illustrates the potential for synthetic developmental biology strategies to use HK chimeras to re-wire the behavioral logic of a bacterium.

1.2.5 Chimeric HKs as small molecule reporters

HKs can also be repurposed as sensors for metabolic engineering[42-45], optogenetic applications[46] or sensing disease related signals.[47] High-throughput screening methods using chimeric HKs have been designed to identify microorganisms that generate large quantities of chemicals for industrial processes.[48,49] These chimeras use the EnvZ/OmpR two-component system that regulates GFP expression under *ompC* output. Unique chimeras were constructed using the sensor domains that detect malate (MalK), methanol (FlhS), glutamate (DegS), and fumurate (DcuS) (Figure 1–5C).[42-45] These small molecule fluorescent biosensors will now enable future screens of bacterial libraries for isolation of unique chassis for production of feedstock and small molecules.

1.2.6 Tuning the dynamic range of HK reporters by varying the degree of phosphatase function

An inherent challenge to implementing HKs as cell based reporters is that each two component system has a defined signal detection range, and that range may not correspond to the application's required detection ranges[50]. Landry *et al.* utilized a computational model[51] that revealed decreasing phosphatase activity lowered the detection threshold without negatively affecting the dynamic range.[52]

The catalytic phosphatase residues are found in a conserved DxxxQ/H motif in the HisKA_3 family or E/DxxT/N motif in the HisKA family just downstream of the phosphorylatable histidine. The proposed mechanism for the HisKA_3 family asserts that the glutamine or histidine align a water molecule for the hydrolysis of the phosphate group and that the aspartic acid forms

a hydrogen bond with a conserved lysine of the response regulator.[53] Mutations to the glutamine/histidine or aspartic acid abolish or decrease phosphatase activity. The mechanism of the His_KA family appears to follow a similar mechanism as mutations to the threonine/asparagine result in loss of phosphatase activity.[53,54]

Other phosphatase activity mutants have been mapped to regions outside of the catalytic motif, and are thought to affect long-range conformational changes, interactions with the response regulator, the G2 box conformation, or nucleotide binding.[6,54,55] Landry *et al.* successfully applied the conserved G2 box motif mutation as a sensor tuning strategy by engineering the NarX kinase as a detector of nitrate from fertilizer.[52] The engineered system sensed a larger range of nitrate conditions in the native soil environment than the strain with wild-type NarX kinase. The authors suggest that this sensor can be coupled with nitrogen-fixing systems for agricultural and environmental safety applications.[56,57] Furthermore, this presents an attractive general strategy that can be used to fine tune detection thresholds for histidine kinase biosensors in synthetic biology.

1.3 The leucine zipper engineering strategy

1.3.1 The leucine zipper (LZ) fusion strategy to test the signal transmission mechanism of HKs

Studies of the long-range signal transmission from the sensory domain to the HK domain have led to a model of how these helical linkers propagate signal from the sensor to the HK domain. The model proposes that the helices form a coiled-coil interface that changes in response to signal binding. This conformational change is proposed to affect the position of the phosphorylatable

histidine in relation to the adenosine triphosphate (ATP) binding domain. This includes either taking on a kinase-active conformation or switching to a phosphotransfer or a phosphatase-active conformation (Figure 1–6).[15,18,20,58,59]

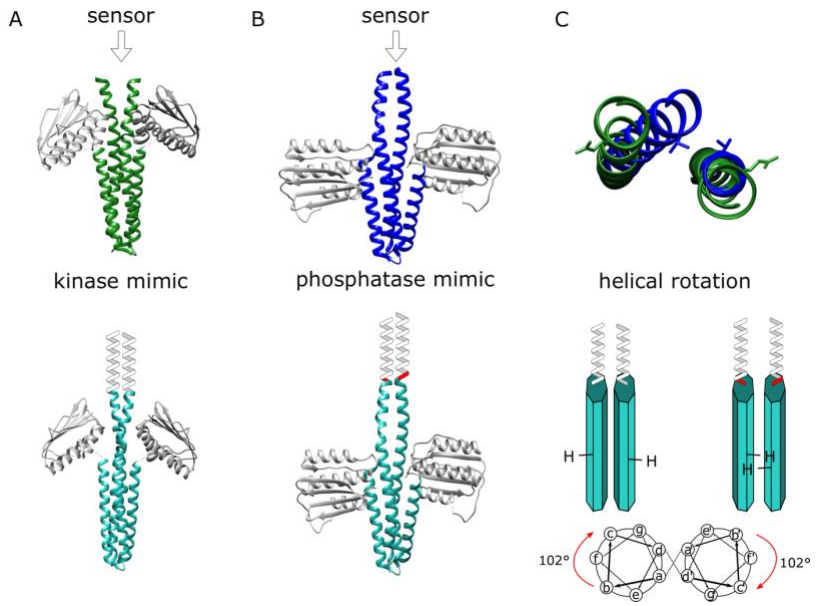

Figure 1–6 The leucine zipper (LZ) engineering strategy.
Crystal structures of the (A top) kinase mimic (H188E, PDB: 3GIE[18]) and (B top) phosphatase mimic (H188V, PDB: 3EHJ[18]) of DesK show bending and helical rotation, apparent in (C top) an overlay of the DHp domains from above. A, B, C bottom) The LZ fusion strategy is utilized to lock the kinase domain into distinct conformational states by addition or deletion of residues from the helical coil. All crystal structures images generated using Chimera.[7]

Other studies have suggested an electrostatic interaction between the signal transmission coiled-coil and the HK domain, which would similarly bias HK domain conformation.[9,13]

The ability to manipulate the conformation of the coiled-coil linkers has become a strategy for testing the HK signal transmission mechanism. The leucine zipper (LZ) of the *Saccharomyces cerevisiae* (*S. cerevisiae*) transcriptional activator GCN4 is a coiled-coil with a strong bias for one interface, with a K_d of dimerization in the 10 nM range.[60] Since the K_d of dimerization of the HK EnvZ is in the 0.4-10 µM range[5,61], it is proposed that covalent attachment of the LZ can stabilize the weaker HK coiled-coils in one conformation (Figure 1–6). This was first demonstrated to be an effective method to study signal transmission in a chemotaxis receptor[62] and later applied to the HKs VirA[9,63,64] and AgrC.[11,65] The LZ technique has been used to lock the catalytic domain of

VirA in predicted kinase-on, kinase-off, and partial-kinase states and contributed to a three-state ratchet model for activation. The LZ fusion strategy was applied to the AgrC kinase domain and coupled with cysteine cross-linking to demonstrate the periodicity of the activation of AgrC[11,65] in a mode similar to VirA kinase activation.

1.3.2 Leucine zipper fusions reveal a helical bundle ratchet model in VirA signal transmission

VirA is a transmembrane hybrid HK that is expressed from a tumor-inducing plasmid in the plant-associated pathogen *Agrobacterium tumefaciens* (*A. tumefaciens*). VirA responds to at least four signals, including pH, temperature, and plant-derived phenolics and monosaccharides, and integrates these signals to phosphorylate the RR VirG, which activates virulence factors.[66,67] The LZ approach was applied to investigate the mechanism by which VirA can integrate multiple signals with a goal of understanding plant host-bacterial communication (Figure 1–7).[9,63,64]

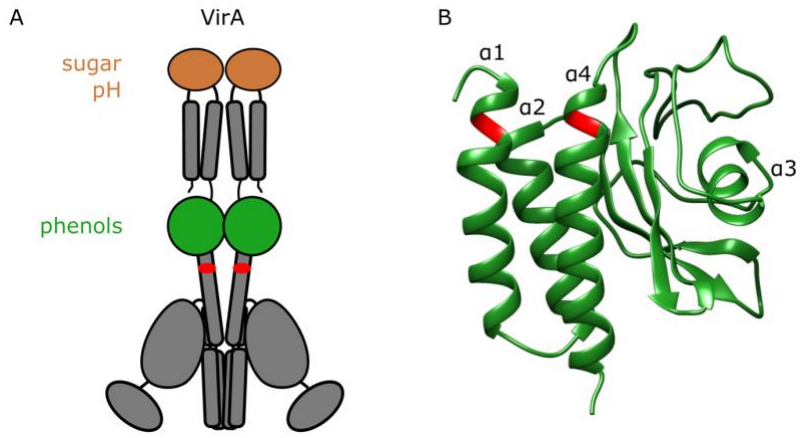

Figure 1–7 Application of leucine zipper strategy to VirA.
A) The domain architecture of VirA and B) the homology model of the cGMP phosphodiesterases, adenyl cyclases, and FhlA (GAF) domain of VirA compared to *Neisseria meningitdis* fRMsr.[9,68] LZ fusion sites are denoted in red. All crystal structures images generated using Chimera.[7]

The LZ was fused directly to the N-terminus of either α1 or α4 within the GAF sensory domain. At the fusion site an addition of 3 or 4 amino acids was incorporated to bias the coiled coil into a position corresponding to a 51° counterclockwise rotation or 51° clockwise rotation from the neutral position, respectively. It is important to note that the kinase domain in each LZ fusion contained the mutation G665E, which exhibits higher basal kinase activity but is still responsive to phenolic concentration.[9,63,64,69] This allowed for detection of a negative impact of the LZ fusion conformation upon kinase activity. The forced conformation of each fusion resulted in a distinct kinase activity measured by indirect RR control and an *in vivo* β-galactosidase activity assay. These data contributed to a ratchet model of activation in which phenolic signal binding causes rotation within the helical bundle which positions the kinase domain in an active conformation.[1,9,64]

It was further suggested that the rotation of the helical bundle places the phosphorylatable histidine into proximity with the ATP-binding domain, allowing phosphate transfer. To test this model, the LZ fusion strategy was applied just 24 amino acids N-terminal to the phosphorylatable histidine, and the position of the histidine in each fusion was predicted. The panel of chimeras was extended to include a full heptad rotation of 7 fusion sites and the variable kinase activity in a β-galactosidase activity assay matched the prediction of the ratchet model. By comparing VirA to a protein with a solved x-ray crystal structure HK0853[17], it was suggested that the active LZ fusions correspond to a conformation in which the histidine would indeed be brought into proximity with the ATP-binding domain.[9]

1.3.3 The leucine zipper fusion strategy was used to demonstrate the periodicity of AgrC

AgrC is a homodimeric transmembrane quorum sensing HK that regulates virulence upon sensing homologous or heterologous autoinducing peptides in *Staphylococcus aureus*. The linker between the sensor and kinase domain is predicted to have a helical fold.[11] A challenge in studying AgrC signal transmission *in vivo* is that the AgrC signaling cascade involves a positive feedback loop which can complicate transcriptional readouts.[70] Wang *et al.* used the LZ fusion strategy to manipulate the conformation of this linker to study the AgrC signal transmission mechanism *in vitro* using nanometer-scale lipid bilayer discs.[11,65]

A panel of 15 LZ fusions, corresponding to 2 heptad rotations, was constructed by fusing the GCN4 LZ to the N-terminus of the AgrC linker, truncating one amino acid from the AgrC linker at a time. Each truncation results in a predicted 102° rotation of the helical linker per residue. An *in vitro* protein phosphorylation assay revealed that the kinase activity could be fit to a sine wave function as a function of linker length with a periodicity of 3.6 amino acids, corresponding to one turn of the helix. The activities of each LZ fusion were compared to the basal, induced, and inhibited activities of full-length AgrC and equivalent activities were observed. These results indicated that AgrC transmits signals through conformational twisting of the sensor-kinase helical linker.

A cysteine cross-linking experiment of full-length AgrC resulted in characterization of the conformation of the linker in each signal-binding state. This data along with a study of AgrC homologs[65] allowed for defining the degree of rotation achieved by each state and led to a rheostat model in which each signal binding event results in a rotation in the linker and the attached kinase domain, dictating activity. This model is similar to the "ratchet model" of VirA, in that it revealed

a periodic trend in which insertion of residues modulates activity between kinase active, partial kinase activity and inactivity.

This fine-tuning of the dynamic range of kinase response may be an evolutionary tactic to regulate the amplitude of HK response. More broadly we envision that the LZ strategy could be used to test other modes of signal transmission such as reverse signaling[71,72], phosphatase activity, and phosphotransfer activity. This strategy could also be applied to kinases with diverse sensory domain architectures in which helical regions are proposed to be involved with signal transmission.[28] Furthermore, designed LZ fusions could be used to confer constitutive, intermediate, or null kinase activity to manipulate downstream responses.

1.4 The signal processing capabilities of tandem sensor kinases

Several unannotated HKs contain two or more distinct sensory domains, raising the intriguing possibility that these HKs use Boolean-like logic to interrogate multiple environmental signals. As an example, Figure 1–8 indicates that several HKs encoded within the genome of *C. crescentus* contain two or more sensory domains in tandem.

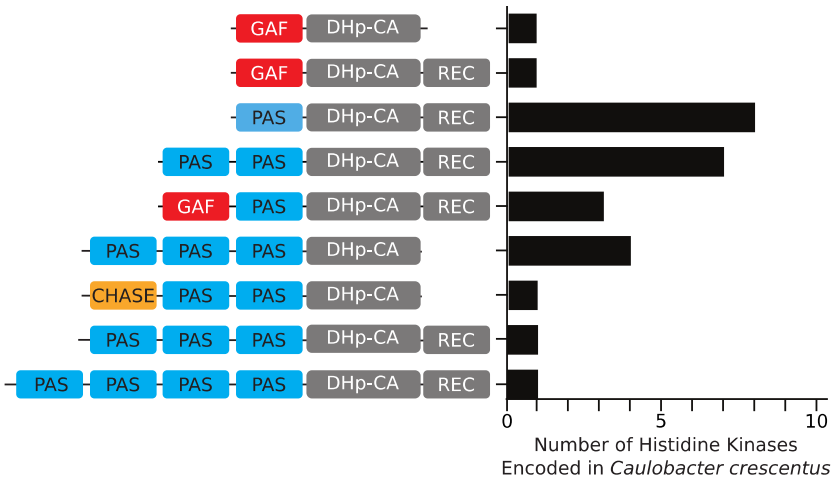

Figure 1–8 The domain architectures of all *Caulobacter crescentus* histidine kinases that contain a PAS or GAF sensory domain.
Signaling domains PAS, GAF, and cyclases/histidine kinases associated sensory extracellular (CHASE) domains are annotated and colored. Catalytic DHp/catalyic assist (CA) and receiver (REC) domains are in gray.

Indeed, the VirA HK processes phenolic signals and sugars in a AND gate manner that confirms the presence of two signals prior to triggering activation of the VirA-VirG virulence regulon (Figure 1–2A).[9,73] However, a significant challenge remains in that we have poor knowledge of the identity of most HK sensory domains. The lack of knowledge about input signals prevents studying how most multi-sensor kinases processes signals.

To understand the large family of multi-sensor HKs, engineered synthetic tandem-sensor kinases composed of the oxygen sensing PAS domain of FixL and the blue-light sensing LOV domain of YtvA were developed (Figure 1–2B).[74] Their designs indicated maintenance of α-helical secondary structure in their fusions was critical for kinase functions. This synthetic tandem-sensor kinase demonstrated that independent sensory domains could regulate kinase in an additive manner. Furthermore, their studies revealed that sensory domains more proximal to the HK domain had a larger impact than the distal sensory domain. The examples of VirA and the synthetic tandem sensors reveal the capability to program advanced signal processing within the HK sensory domain. This could be commonly used in nature to ensure stringency of signaling response as

highlighted in the VirA example[64], and also provides avenues to integrate and process signals for applications in synthetic biology.

1.4.1 Regulation of multi-sensor kinases through oligomerization

It has been proposed that a subset of multi-sensor domains control HK activity by toggling between dimer and tetramer states.[75,76] The *B. subtilis* HK KinA regulates the sporulation pathways and utilizes a 4-PAS sensory domain. The input signal of KinA was not well understood but signal transduction was predicted to be related to tetramerization.[75,77] To tackle this problem, the diguanylate cyclase protein YdaM N-terminal PAS domains were fused to KinA kinase domain to promote tetramerization to study how the sensory domain tetramerization regulates KinA signaling activity.[78] The authors observed through crosslinking assays that the YdaM fusion placed KinA into a tetramer conformation that was constitutively active.[76,78] This example illustrates that multiple sensor kinases may have the capacity to regulate oligomeric changes as a mechanism of HK activity control. Future work is needed to understand how broadly this oligomerization mechanism is used and if it is a common feature of multi-sensor HK as suggested by studies of KinA[78] and CckA[76] multi-sensor kinases.

1.4.2 Strategies to engineer HK heterodimerization

Compared to eukaryotic signaling pathways, bacteria appear to exhibit minimal cross-talk between signaling pathways in vivo and in vitro even though the DHp/CA domains of HKs are conserved across bacteria.79 Bacterial cell fitness is reliant on reducing unwanted cross-talk.79

However, heterodimerization of HKs can generate more complex regulatory modes as highlighted by studies of the P. aeruginosa GacS and RetS HK heterodimer complex (Figure 1–9).[80,81]

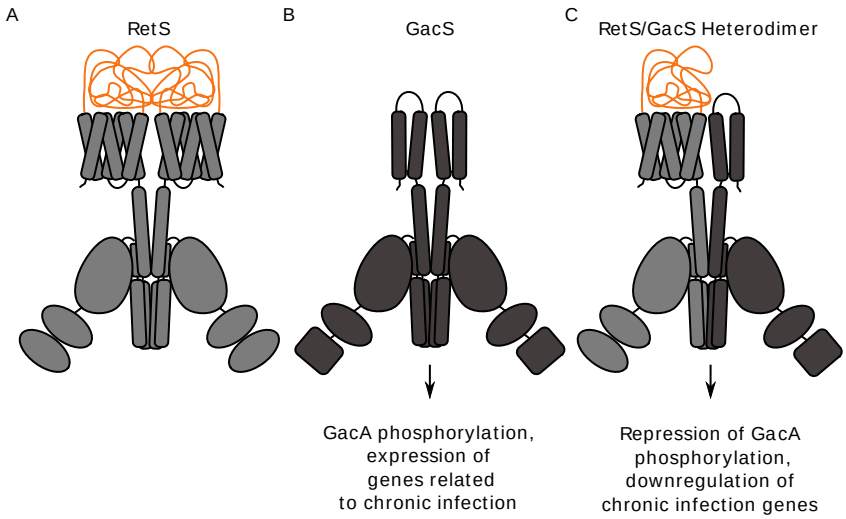

Figure 1–9 The RetS-GacS interactions dictate downstream regulation.
A) RetS homodimer, (B) GacS homodimer and a (C) RetS-GacS heterodimer. Orange lines represent the 7TMR-Dismed2 periplasmic domain of RetS. When GacS is a homodimer and receives input signals, GacA phosphorylation occurs and expression of genes related to chronic infection are transcribed. When RetS and GacS form a heterodimer, repression of GacA phosphorylation and downregulation of chronic infection genes occur.

These results highlight the importance of understanding how to engineer desired HK dimerization modes in order to wire HK heterodimerization to productively integrate information from two pathways. Comparison of EnvZ in *E. coli* and its closest HK homolog RstB, in *Pseudomonas aeruginosa* (*P. aeruginosa*), revealed residues that are required for these HKs to remain homodimers or function as heterodimers. Using covariation analysis, the base of the DHp bundle was identified as the region most likely contributing to homodimerization. To test this, residues from RstB were swapped into EnvZ. After two residue mutations, the engineered EnvZ variant was no longer able to heterodimerize with wild-type EnvZ as determined by a fluorescence resonance energy transfer (FRET) competition assay, but maintained homodimerization ability.[5] A set of residues buried at the base of four-helix bundle was identified which are sufficient for

regulating dimerization specificity, while leaving RR phosphotransfer specificity unperturbed (Figure 1–1A).[5]

The engineering of HK heterodimers may offer the potential to sense and integrate signals from each distinct sensory domain, however this remains to be explored. In addition, future work will determine the degree of HK heterodimerization specificity

1.4.3 Strategies to re-wire HK and RR phosphotransfer

HKs and RRs have co-evolved to exhibit specificity in phosphorylation activity in order to reduce HK-RR phosphotransfer cross-talk.[82] By rewiring HK-RR protein interaction interfaces, one can alter signaling flow from one HK to a different RR output, engineer a single HK to phosphorylate several RR outputs, or engineer the integration of many signals through many HKs that phosphotransfer to a single RR. The key interactions that modulate the phosphotransfer specificity are a suite of residues located on the solvent exposed surface of the DHp domain of the HK and the receiver domain (RD) of the cognate RR. The key residues that determine the specificity for the DHp tend to be solvent exposed and located at the base of the four-helix bundle, as well as in the loop region (Figure 1–1A,B).[5,83] Skerker *et al.* identified residues within EnvZ that could be mutated to other HK residues (RstB, CpxA, PhoR, AtoS, and PhoQ) to confer phosphotransfer specificity to their RRs.[83] This was accomplished by identifying residues that co-vary between HKs and RRs[84,85], and was consistent with the interaction interface observed with several HK-RR co-crystal structures.[6,86,87] The entire loop regions of each kinase were substituted into EnvZ, resulting in EnvZ variants that recognize and phosphorylate the corresponding RR targets.[83]

RR specificity residues have been identified through covariation analysis and can be applied to specific HKs through secondary structure alignment of DHp domains.[83] By applying these HK-RR interface mutations or switching the entire DHp loop region, multiple phosphorylation partners could be under the control of a single HK. This re-wiring could also generate new connectivity between signaling input and outputs. This also provides an alternative approach to the sensor-HK chimeras that would allow one to retain much of the native HK function and just alter the residues to direct phosphotransfer to a desired RR.

1.4.4 Engineering assembly and activation of HK signaling

Whitaker *et al.* took inspiration from eukaryotic signaling systems, which rely on scaffolds to colocalize and activate kinases, to design a modular prokaryotic system for synthetic biology.[88,89] The downstream signaling of a chimeric HK[90] was re-wired to activate non-cognate RRs[91] in a scaffold-dependent manner (Figure 1–10).

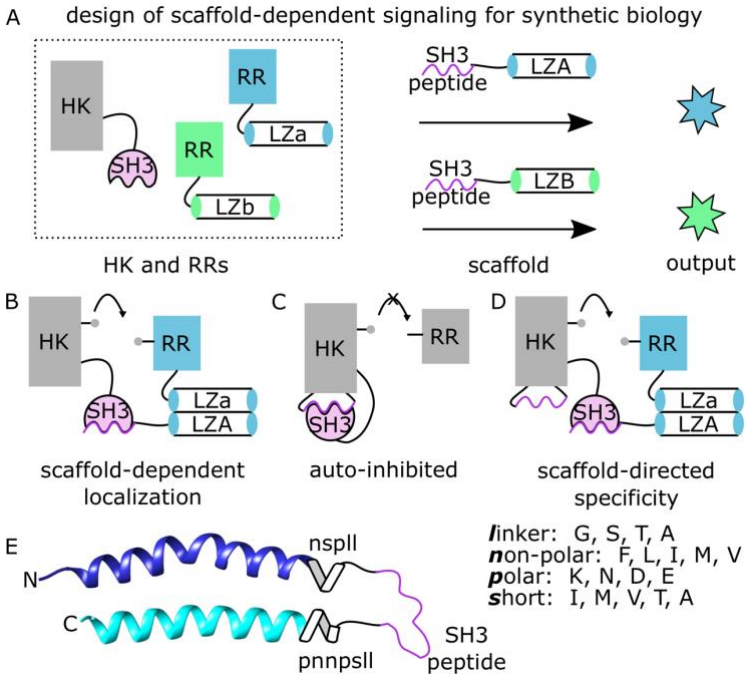

Figure 1–10 The design of scaffold-dependent signaling for HK synthetic biology.
A) The design of scaffold-dependent signaling for HK synthetic biology. The SH3-bound HK and LZ-bound RRs are expressed in the cell. Induction of scaffold dictates the downstream activity of the HK. B) Scaffold-dependent localization increases the effective concentration of the RR near the HK. C) The HK can be engineered with an autoinhibitory interaction. D) Induction of the scaffold co-localizes the components and relieves the autoinhibitory interaction to activate the signaling pathway. E) The design of the autoinhibitory interaction in the DHp of the chimeric HK TAZ1 (PDB: 5B1N[4]). All crystal structures images generated using Chimera.[7]

It has been demonstrated that HKs will transfer phosphate to non-cognate RRs with an increased effective concentration through direct tethering.[92,93] Whitaker *et al.* sought to increase the local concentration of the HK and its downstream RRs by designing scaffolds with two protein-protein interaction domains, the SRC homology 3 domain (SH3) peptide and LZ, which recruited the SH3-tagged HK and the LZ-tagged RR, respectively. The advantage of scaffold-dependent co-localization is that the RR specificity of the HK was successfully adjusted by induction levels of the scaffold as determined by a fluorescent gene expression reporter assay. However, the system was sensitive to the expression level of each component.

The system was further engineered so that the scaffold is necessary not only for colocalization of the HK and RR, but also for HK activation. The kinase domain was engineered

with an SH3 domain and an internal SH3 peptide such that the SH3 domain would block phosphotransfer to the RR until the scaffold SH3 peptide would compete for SH3 binding and activate the HK (Figure 1–10). Using the same fluorescent gene expression reporter, it was demonstrated that the scaffold was effective in colocalizing and activating two-component system signaling.

Insertion of the SH3 peptide into the kinase structure without affecting activity presented an interesting kinase engineering challenge. The turn between the helices in the DHp was chosen as the site for insertion because of its proximity to the RR binding site. However, direct insertion or the use of flexible linkers into this region did not yield an active kinase. A library of linkers, which mimicked the seven amino acids at the end of the DHp bundle, was created to extend the helical structure (Figure 1–10E). Additionally, two flexible amino acids were placed between the helical linker and the SH3 peptide at either end. Variants from the library were first screened for their ability to phosphorylate RR, and then for their conditional activation only in the presence of scaffold. The most promising library candidate was tested to confirm autoinhibition and scaffold-dependent activation. The modular signaling system designed here couples the roles of phosphotransfer and RR specificity and can therefore be extended to other two-component systems.

1.5 Conclusions and outlook

The engineering strategies discussed here have contributed to an understanding of how bacteria use two-component systems to respond to their environment. The ability to activate pathways orthogonally (LZs), change target specificity (rewiring HK/RR recognition), and change

signal inputs (sensory domain swaps) will allow researchers working on basic biology questions or synthetic biology tools to incorporate two-component system architectural elements. However, several challenges remain in our capability to predictably engineer HK function. Most notable is poor access to diverse well-characterized sensory domains and the incapability to predict sensory domain function based on primary sequence. Therefore further characterization of sensory domain structure and function is needed to understand the general design rules for how signals are perceived and distinguished. This includes investigation of how multi-sensor domains integrate multiple signals to regulate HK activity. A second major HK engineering opportunity is the engineering allosteric regulation through kinase-kinase interactions. Indeed, natural histidine kinase pairs suggest this as a mode of histidine kinase regulation, such as the *P. aeruginosa* RetS-GacS pair[81] and the *C. crescentus* DivL-CckA pair.[33,71,94] Another major drawback is that engineering principles used on one histidine kinase do not always translate to another. Two-component systems are diverse in function and structures so only well studied systems are amenable to engineering. Until more generalized rules are developed, two-component systems from major bacteria (*E. coli*, *B. subtilis*, etc) will comprise the majority of protein engineering of two-component systems. Further application of these HK engineering strategies and addressing these opportunities will enhance our understanding of bacterial impact upon human health and disease, agriculture, and environmental safety.

In this dissertation, I will expand the toolbox of HK engineering using the two-component system HK CckA from the alpha-proteobacterium *C. crescentus*. In Chapter 2 I will discuss the design, testing, and application of a histidine kinase FRET sensor that can report on subcellular populations in a living bacterium. Chapter 3 expands on the uses of the CckA-FRET biosensor and couples the FRET sensor technology with DivL engineered to lock it into different conformational

states using LZs. Chapter 4 comprises my work with a new class of antibiotics, HK inhibitors. Chapters 5 and 6 will show what has been learned about the scaffolding protein PodJ in the context of cell-cycle regulation and localization in *C. crescentus*.

2.0 CckA-FRET biosensor development

2.1 Introduction

Bacteria have evolved to survive in a wide range of environments such as fresh-water streams (*C. crescentus*)[95], the soil near plant roots (*A. Tumefacians*)[96] and the human lungs ˆ*P. aeruginosa*)[97]. With this environmental diversity, unique sets of signals to which each bacterium responds have occurred. These responses include quorum sensing[98], temperature change[99], chemotaxis[100], antibiotic exposure[101], and starvation[102]. Each can lead to different outputs such as biofilm formation[103], virulence[104], chemotaxis[105], motility[106], and replication (Figure 2–1).[107] Bacteria have evolved orthogonal, two-component signaling pathways to respond to these cues without unwanted cross-talk while transducing these signals[82]. However, many bacterial two-component systems have unknown functions. Thus, new methods are needed to spatially and temporally track their activity as a function of different stimuli (e.g. host derived signals).

2.1.1 Two-component signaling systems

The two-component system in its simplest form consists of an HK that upon detection of signals triggers an autophosphorylation reaction on a conserved histidine and phosphotransfer to a RR that performs its output activity in a phosphorylation-dependent manner (Figure 2–2).[1]

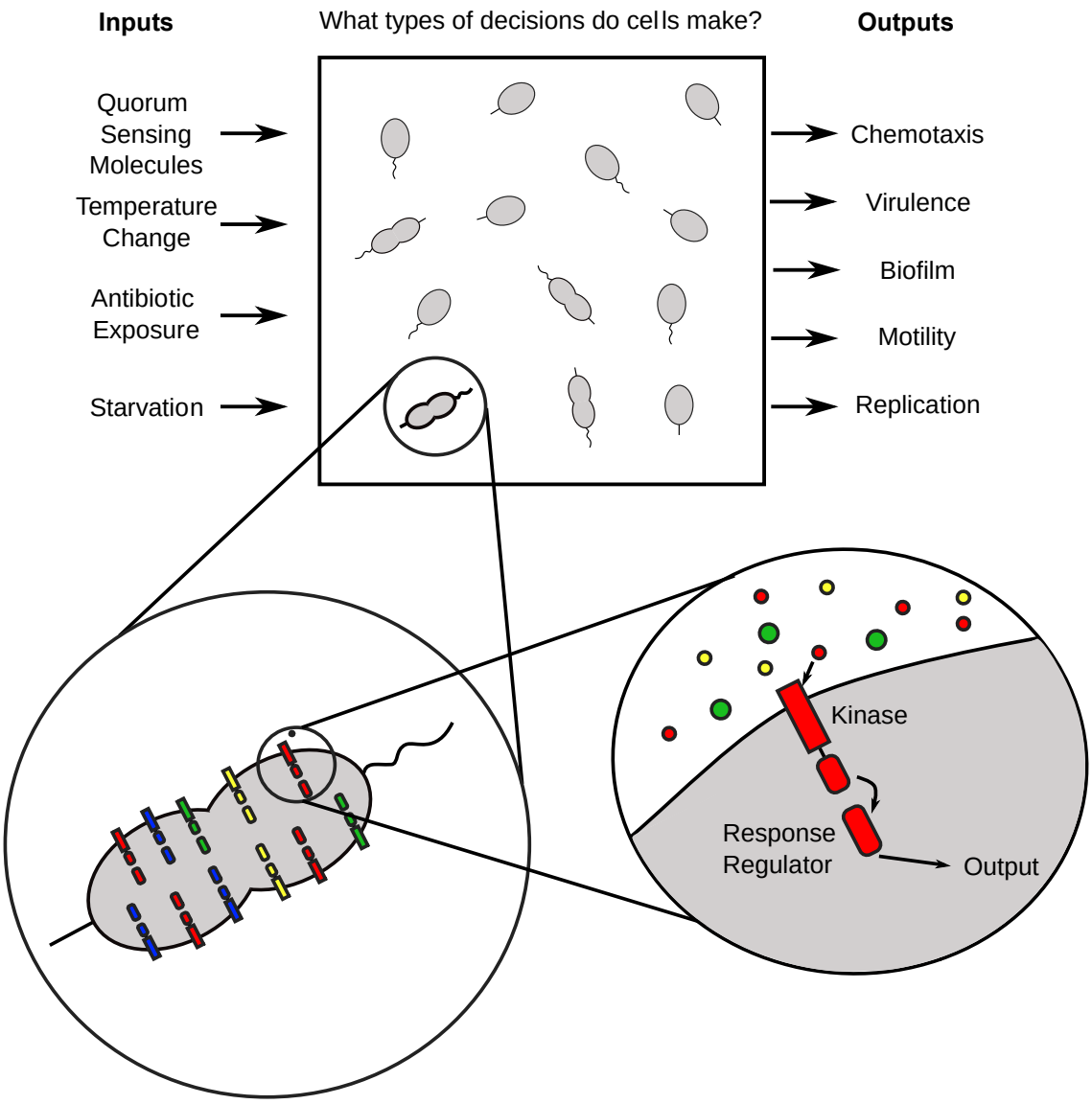

Figure 2–1 Bacteria make decisions based off their environment.
Bacteria have to make decisions on a wide array of inputs such as communicating with other bacteria (quorum sensing) and reacting to changes in the environment (temperature change, antibiotic exposure, starvation). Each of these inputs requires a signaling pathway that the bacteria can use to respond. Often, each input will have its own signaling pathway that leads to a downstream output such as chemotaxis, virulence, biofilm formation, motility, or replication. These orthogonal systems are used to tightly control the responses of bacteria.

HKs are multidomain proteins that consist of two general sections, a signal domain and a catalytic domain. The catalytic domain is made up of two sub-domains: a DHp domain, which contains the phosphorylatable histidine and a CA domain, which binds ATP (Figure 2–2).

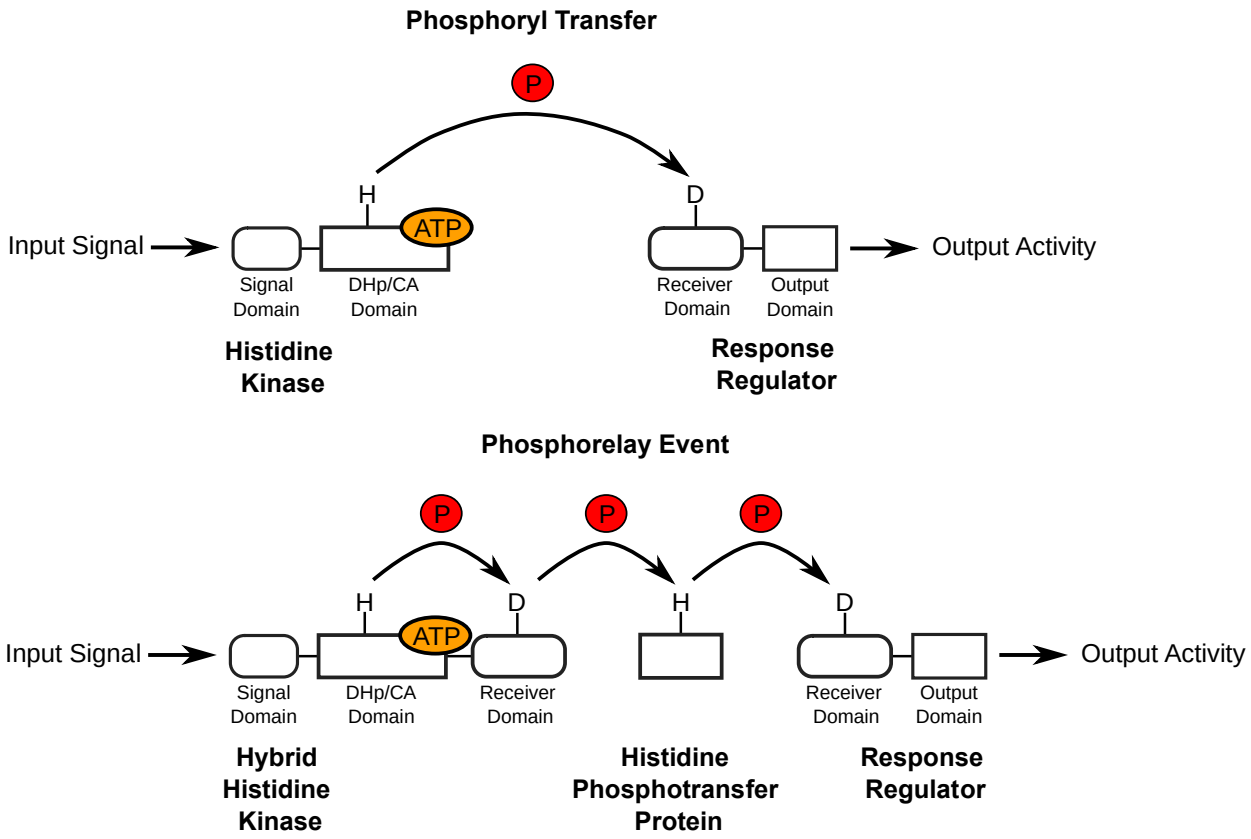

Figure 2–2 Two-component system architecture.
Bacteria use phosphoryl transfer and phosphorelay events to transmit signals. Phosphoryl transfer takes an input signal sensed by the signaling domain to cause an autophosphorylation of the conserved histidine in the DHp domain. This reaction is catalyzed by the CA domain. This phosphohistidine then transfers the phosphate to the conserved aspartate on the response regulators that leads to an output activity. The phosphorelay event follows the same events until the phosphohistidine transfer event. Instead of direct transfer to the response regulator aspartate, it is sent to the aspartate on the receiver domain of the hybrid-HK, then to the histidine of the histidine phosphotransfer protein, and finally to the aspartate on the receiver domain of the response regulator leading to the output activity. Figure adapted from Gao, *et al. Annu. Rev. Microbiol.* 2009, 63, 133-154.

The HK receives an input signal in the N-terminal signaling domain, which causes an autophosphorylation event to occur in the catalytic domain to phosphorylate the conserved histidine located on the DHp domain. Alignment of the γ-phosphate of ATP in the CA domain and the histidine within the DHp domain promotes histidine nucleophilic attack on ATP resulting in a phosphohistidine[108]. Once phosphorylated, the HK can then transfer this phosphate to its cognate RR (Figure 2–2).[109] The RR consists of an RD containing a conserved phosphorylatable aspartate residue. Phosphorylation of the receiver domain acts as a switch to regulate the activity of various output activities such as gene transcription (Figure 2–2).

The phosphorelay event (Figure 2–2) consists of a hybrid-HK that contains an RD on the C-terminus which receives the phosphate from the DHp domain. The phosphorylated RD then transfers the phosphate to a conserved histidine on a phosphotransfer protein, which then passes the phosphate to the aspartate on the RR, leading to the output activity. More than 50,000 two-component signaling proteins have been identified through genome analysis with ~75% utilizing a phosphoryl transfer system and the remaining 25% using a phosphorelay event.[1] Roughly 63% of response regulators contain deoxyribonucleic acid (DNA) DNA-binding output domains with the remaining output domains constituting enzymatic function, domain mediation, and RNA binding.[1]

Most HKs have also evolved to function as phosphatases; unlike in Eukaryotic systems where kinases and phosphatases are typically separate enzymes.[110] Once the phosphate is on the aspartate of the RD, the RD and DHp domain come into contact and form a stable, six-helix bundle that also maintains contacts with the catalytic domain and, if present, the sensory domains of the HK. The E/DXXN/T or DXXXQ motifs directly adjacent to the phosphorylatable histidine in the DHp domain contain the crucial residues to activate the hydrolysis of the phosphate group from the aspartate of the RD (Figure 2–3A).[53]

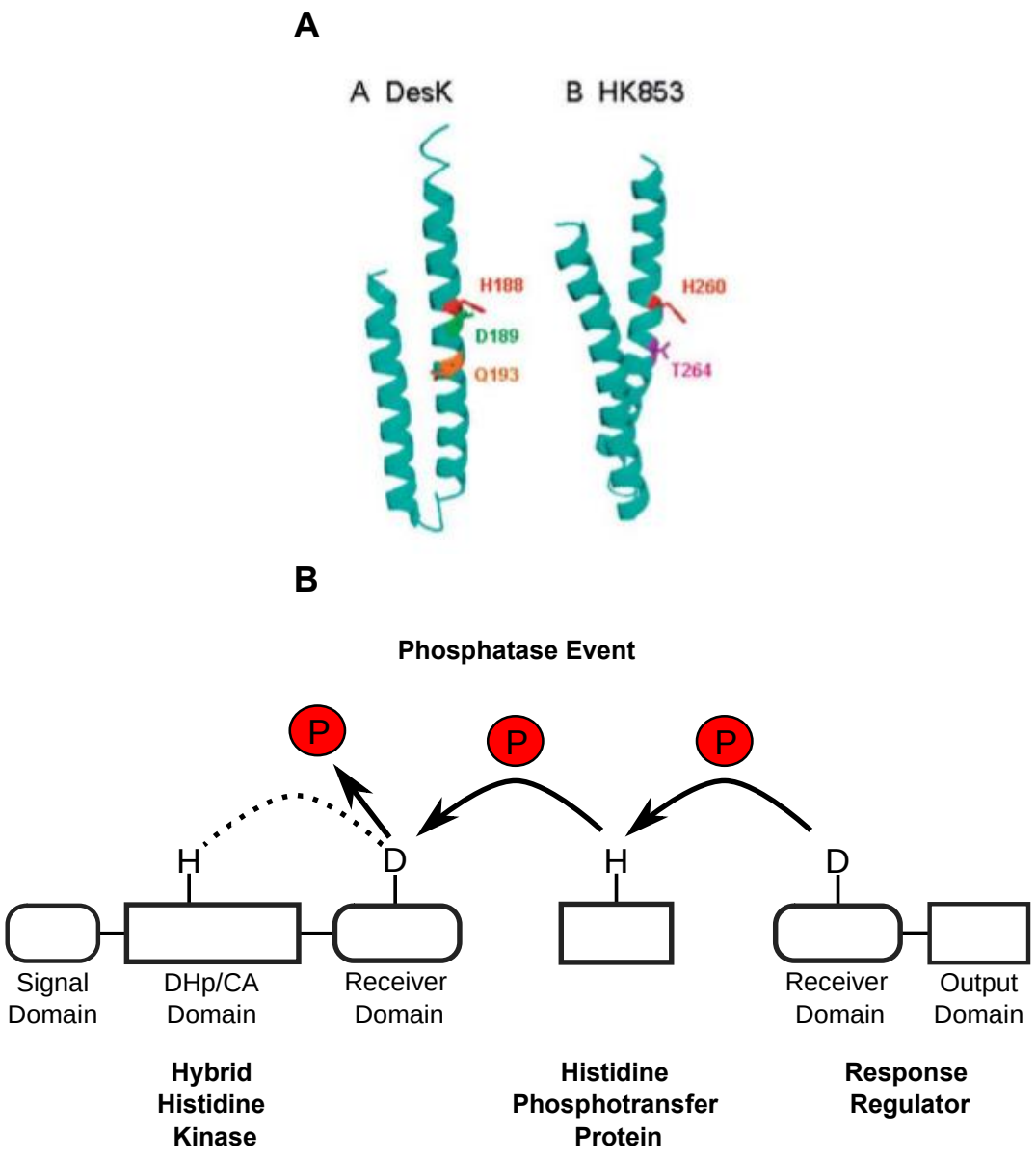

Figure 2–3 Histidine kinase phosphatase activity.
A) DesK is an example of an HK with the DXXXQ (D shown in green, Q shown in orange) motif for use in phosphatase activity. HK853 is an example of an HK with E/DXXN/T (T shown in fuschia) motif directly adjacent to the phosphorylatable histidine (shown in red). B) The phosphatase mechanism works like the phosphorelay, but in reverse. Once the phosphate has made it to the aspartate on the receiver domain of the HK, a DHp/CA/receiver domain interaction occurs in which the DXXXQ or E/DXXN/T motif stabilizes and activates water to act as nucleophile to cleave the phosphate bond. Figure adapted from Gao, *et al. Annu. Rev. Microbiol.* **2009**, *63*, 133-154.

DesK and HK853 are examples containing the histidine adjacent motifs (Figure 2–3A). This phosphatase event runs in reverse to the kinase mechanism (Figure 2–3B). This phosphatase

activity is important because it can speed up the autodephosphorylation of a response regulator, thus provide an active mechanism to rapidly switch off the activity of a response regulator.[53]

2.1.2 Sensory domain conformational changes regulate HK activity

HKs are multidomain proteins containing an N-terminal signaling domain attached to a catalytic domain. The signaling domains of HKs typically consist of HAMP, PAS, and GAF domains.[28] Each of these domains has a very distinct mode of signal transduction, but one common feature is the change in conformation of the signaling domain that leads to the activity change of the HK. An example of this is in the chimeric protein YF1 (Figure 2–4).

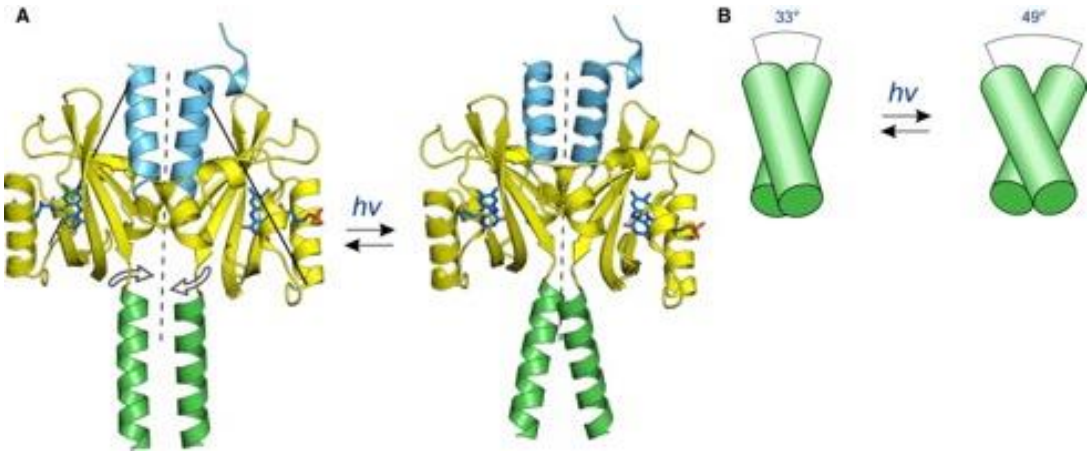

Figure 2–4 The chimeric HK YF1 twists in response to light.
A) The HK YF1 is a chimera of the light-oxygen-voltage (LOV) domain from *B. subtilis* YtvA and the DHP/CA of FixL in *Bradyrhizobium japonicum* is a good example of the conformational changes that a HK can undergo when incorporating a signal. In this case, 430 nm light causes the LOV domain to twist, resulting in twisting of the DHP/CA domain (not shown). B) Schematic of twisting that occurs when light is added to YF1. Figure used with permission from Diensthuber, *et al. Cell Struct. Funct.* **2013**, 21(7) 1127-1136.

This protein contains light-oxygen-voltage (LOV) domain that is in the PAS domain family of signal input domains.[15] The YF1 HK is an example of the conformational changes that occur in the signal domain upon signal integration. The LOV domain in YF1 binds a flavin cofactor that responds to 450-500nm light. Light causes a conformational change in the LOV domain that is

propagated to the kinase core through a conserved DITE motif located at the C-terminal region of the LOV domain (Figure 2–4A,B). The DITE motif forms five hydrogen bonds creating a rigid structure at the interface of sensory domain and kinase domain and is conserved among PAS domains (Figure 2–5).[30]

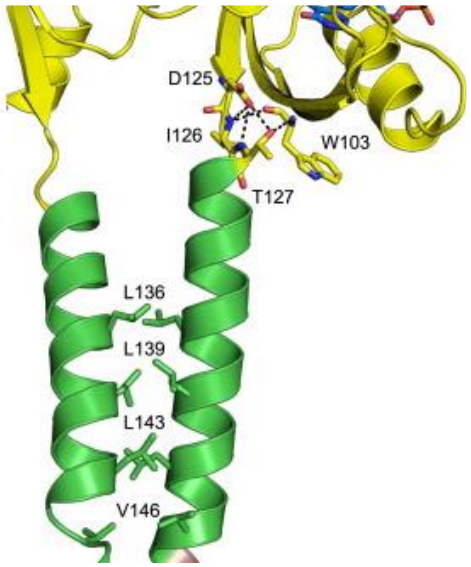

Figure 2–5 YF1 Jα helix crystal structure outlining the DIT motif and conserved leucines.
YF1 Jα helix interface outlines the DIT motif residue hydrogen bond interaction (yellow and green intersection). The hydrophobic residue interactions of the α-helix bundle are also outlined to show the 7n sequence. Figure used with permission from Diensthuber, *et al. Cell Struct. Funct.* **2013**, *21*(7) 1127-1136.

In this case, the LOV domain undergoes a twisting motion that propagates a signal through the coiled-coil C-terminus DITE region upon activation with light leading to a loss of kinase activity.[15] The work done on YF1 by the Möglich lab has added an important understanding of how a signal is transduced through conformational changes to regulate HK function.

2.1.3 CckA, the hybrid-HK of the master regulator CtrA

The cell-cycle kinase A (CckA) is the hybrid HK that phosphorylates and dephosphorylates the RR CtrA, which controls over 90 cell-cycle regulated genes and the inhibition of DNA

replication.[107,111,112] CckA is a 73 kDa, multisensory domain, hybrid HK consisting of an N-terminal transmembrane domain, two PAS domains, DHp, CA, and RD. CckA is bifunctional, containing both kinase and phosphatase enzymatic functions (Figure 2–6A,B).[113]

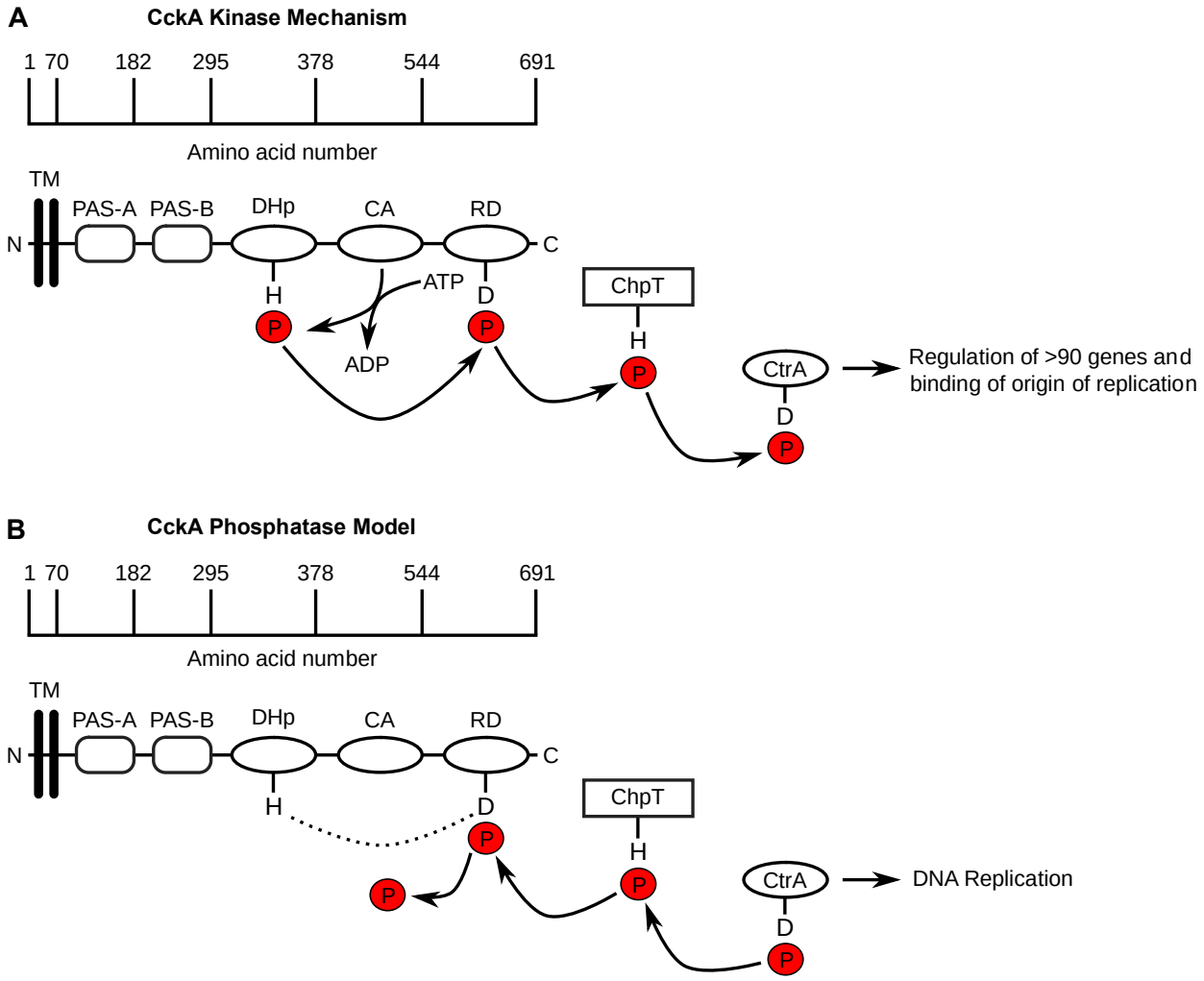

Figure 2–6 CckA kinase and phosphatase relays.
A) CckA is a hybrid-HK that autophosphorylates the histidine at residue 322 through a CA/ATP hydrolysis reaction. The phosphate is then passed to the receiver domain aspartate. The phosphate is then transferred to the phosphotransfer protein ChpT and finally to the response regulator CtrA. CtrA~P then activates over 90 cell-cycle related genes and blocks DNA replication. B) CckA can also act as a phosphatase through the reverse mechanism of accepting the phosphate from ChpT after it has been passed from CtrA. Unphosphorylated CtrA can no longer can block DNA replication in this form.

In the kinase mode, CckA autophosphorylates the conserved histidine (residue 322) residue located on the dimerization and histidine phosphorylation domain using ATP that is bound to the catalytic assist domain. Upon phosphorylation of the histidine, ADP is released. The phosphate is

then passed to the conserved aspartate on the receiver domain (residue 623). The phosphate is then passed to the histidine phosphotransfer protein ChpT (Figure 2–6A).[114] ChpT then passes the phosphate to the CtrA leading to dimerization and control of cell-cycle regulated genes (Figure 2–6A). In the phosphatase mode, a phosphate is passed from CtrA to ChpT. ChpT~P then passes the phosphate back to the aspartate of the RD of CckA where it is actively hydrolyzed by CckA's DHp domain (Figure 2–6B).[115]

The control of CckA activity is dependent on its localization, density, interaction with the pseudokinase DivL, and the levels of the secondary messenger molecule 3',5'-Cyclic diguanylic acid (cyclic di-GMP).[94,113,116-118] Work done by Mann *et al.* uncovered that CckA localization is dependent on both PAS domains; PAS A is necessary for clustering at the cell poles and PAS B is necessary for specific new cell pole localization. At low density CckA kinase activity is inactive, while at high density CckA kinase is active. Consistent, with PAS A's role in clustering, PAS A also regulates this density dependent autokinase activity.

PAS B is involved in cyclic di-GMP autokinase downregulation.[113] Upon binding cyclic di-GMP kinase activity is repressed and phosphatase functions are upregulated. Work done by Tsokos and co-workers provided genetic evidence that the single domain RR DivK inhibits CckA activity through an interaction with the pseudokinase DivL.[33,94] Additionally, it has been shown that DivL is necessary for both new cell pole localization of CckA and its activation as a kinase.[33,94] Clearly, these complexes (DivL/DivK~P and DivL) deactivate and activate CckA kinase activity, respectively.[33] Levels of cyclic di-GMP in *C. crescentus* fluctuate throughout the cell cycle and an asymmetric distribution had been confirmed through use of an *in vivo* FRET sensor that used the conformational change of YcgR, a cyclic di-GMP binding protein in *Salmonella enterica*, to report on cyclic di-GMP concentrations.[117,118] The FRET sensor showed an asymmetric distribution of

cyclic di-GMP along the medial axis following cell division with a higher concentration of cyclic di-GMP concentrated in the old cell compartment. Work done by Dubey led to how the asymmetric cyclic di-GMP distribution interacts with CckA structurally.[116] However, inspection of the CA crystal structure indicates that the N-terminal 6xhistidine (6xHis) tag may play a major artificial role in cyclic di-GMP's interaction with the CA domain (Figure 2–7A,B).

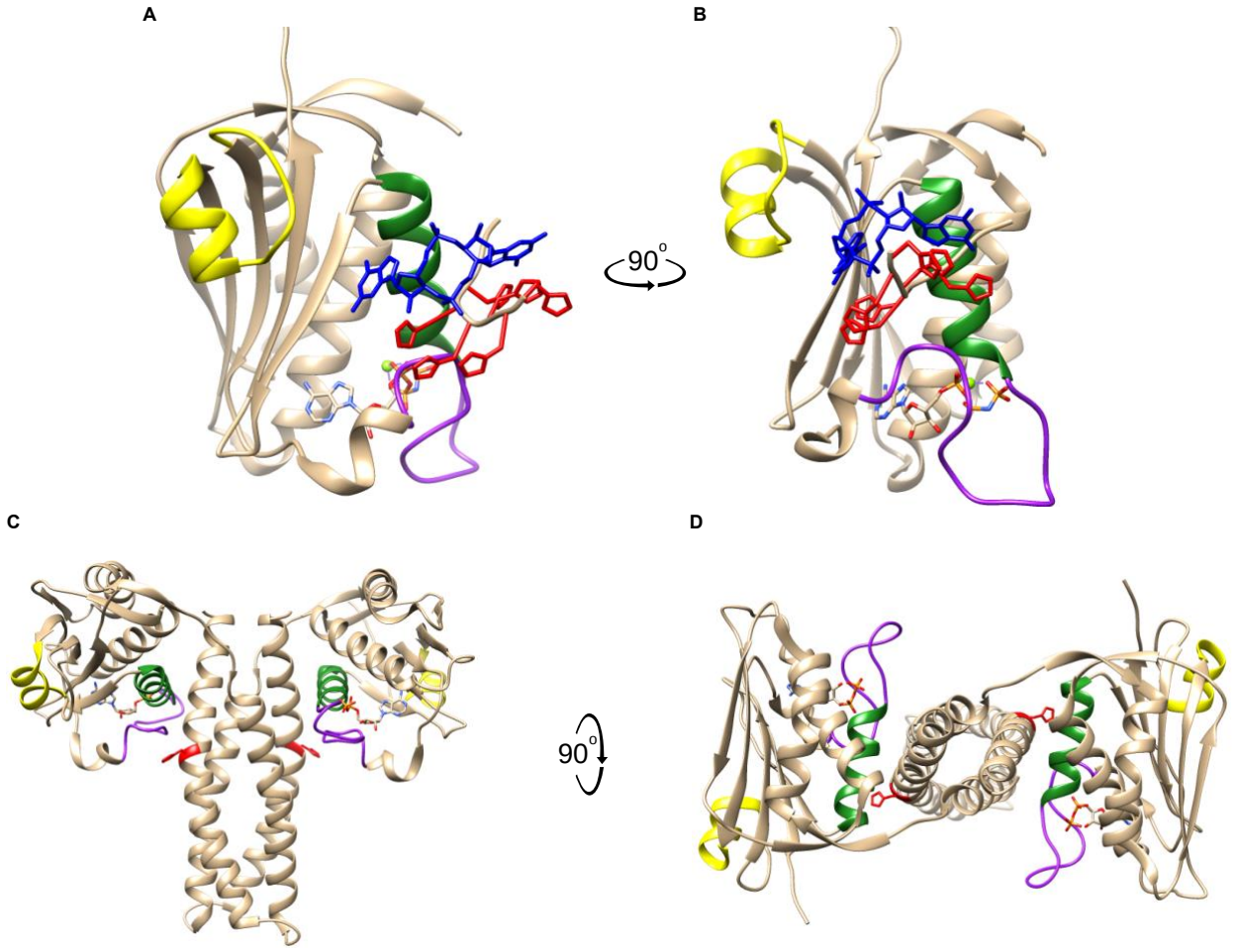

Figure 2–7 CckA DHp and CA crystal structures.
A and B are the CA domain of CckA, which was crystallized with Adneyl-imidophosphate (AMPPNP)/Mg^{2+} (multicolored molecule) and cyclic di-GMP (blue), viewed at different angles. A) cyclic di-GMP forms noncovalent contacts between the beta-sheet and gripper helix (green). AMPPNP/Mg^{2+} is covered by the ATP lid (purple) while the tower (yellow) shows no interactions. B) Turning the structure reveals an interaction of the cyclic di-GMP molecule with the 6xHis-tag motif (red) from another CA domain. C and D are the CckA DHp/CA domain crystal in symmetry with itself with a phosphorylatable H322 (red) and adenosine diphosphate (ADP)/Mg^{2+} shown as multicolor molecule viewed at different angles. C) Front view of DHp/CA shows where cyclic di-GMP would bind between the gripper helix (green) and would be sticking out near the phosphorylatable H322 red. D) Top-down view of four-helix bundle showing symmetry of the crystal. PDB codes 5IDJ and 5IDM.

The original crystal contained two CA domains, only one of which had a cyclic di-GMP molecule co-crystallized. Another telling result is the lack of cyclic di-GMP co-crystallization in the DHp crystal structure (Figure 2–7C,D). This result suggests that other domains may also interact to form a productive binding pocket for cyclic di-GMP. One candidate is PAS B, which has been previously shown to be required for cyclic di-GMP binding and cyclic di-GMP mediated inhibition of CckA.[113]

Understanding the conformation and activity that CckA has is important due to conflicting models currently proposed in the literature (Figure 2–8).

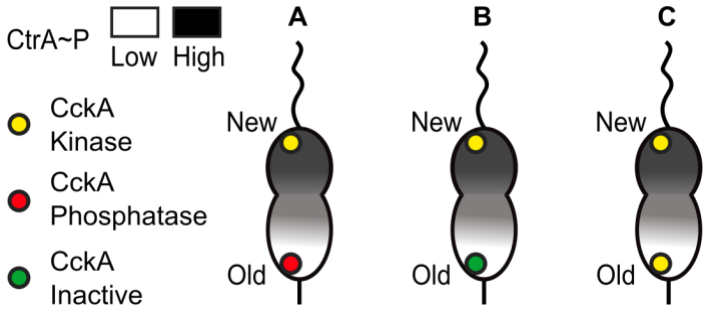

Figure 2–8 Three models have been proposed for what the activity of CckA at the stalk (old) pole during the predivisional step in the cell cycle.
CckA is a kinase at the new cell pole in all three models. In each model, CtrA~P levels are shaded from high (black) to low (white) with gray indicating levels between high and low to form a gradient from one cell pole to another. A) The Laub lab, using genetics and computational approach have proposed CckA acting as a phosphatase at the old pole.[119] B) The Jacobs-Wagner lab has proposed CckA as inactive or a depot at the old pole.[111] C) The Shapiro lab has proposed that CckA is active as a kinase at the old and new poles.[113] Methods need developed to resolve these three models *in vivo*.

All the models currently show that CckA is a kinase at the new cell pole, but differ in its state at the old cell pole. The Laub model predicts CckA as a phosphatase at the old cell pole (Figure 2–8A).[120] The Jacobs-Wagner model proposes that CckA is inactive and acts as a depot for excess CckA (Figure 2–8B).[33] The final model is the Shapiro model, which suggests CckA is a kinase at the old cell pole due to its higher density (Figure 2–8C).[113] To determine which model is correct, an *in vivo* reporter of CckA kinase activity needs to be developed that reports on activity state (inactive, phosphatase, kinase) with subcellular resolution.

2.1.4 RR phosphorylation gradient hypothesis underlies asymmetric cell division

RRs are the response activators in the bacterial phosphoryl transfer and phosphorelay systems. RRs consist of an N-terminal RD that is ~120 residues and contains a conserved, phosphorylatable aspartate. The C-terminal domain, known as the effector domain, is much less structurally conserved and depends on the output function.[1] CtrA is the last protein in the CckA/ChpT/CtrA pathway and when phosphorylated produces an output activity. CtrA is a response regulator containing the conserved N-terminal RD with a phosphorylatable aspartate residue at position 51. CtrA is a member of the OmpR family of RRs, meaning its DNA-binding effector domain falls in the winged-helix-turn-helix family (Figure 2–9A,B).[121]

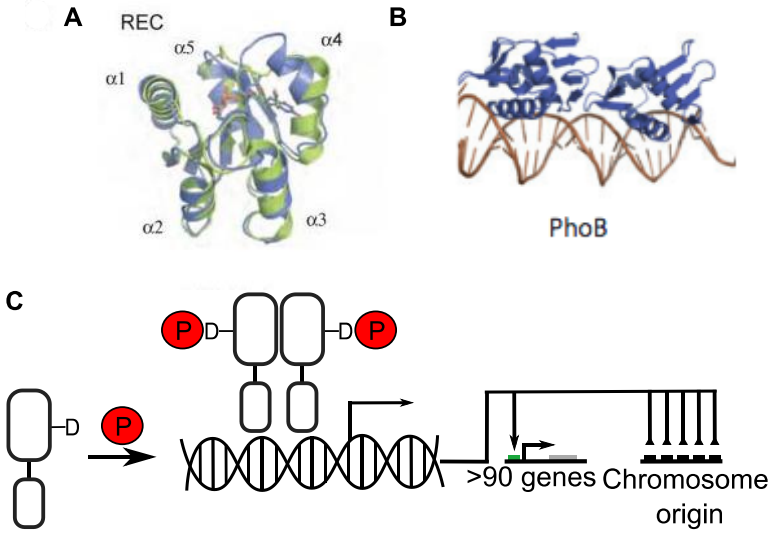

Figure 2–9 Receiver domain structure and DNA binding.
A) Phosphorylated (green) and unphosphorylated (blue) structures of the RD of PhoB are overlayed to show the conformational change of the RD upon phosphorylation. The beryllofluoride moiety to mimic phosphate is colored orange. B) The PhoB C-terminal effector domain is shown in blue bound to a "pho box" DNA sequence (brown double stranded helix). The PhoB effector domain is in the winged-helix-turn-helix family. C) CtrA dimerization scheme. CtrA is a monomer until phosphorylation of the conserved aspartate on the receiver domain. Once phosphorylation occurs, CtrA dimerizes and binds to DNA to promote gene transcription and binding to the origin of replication, blocking chromosome replication. Figure adapted from Gao, *et al. Annu. Rev. Microbiol.* **2009**, 63, 133-154.

The C-terminal effector domain of CtrA binds sites the origin of replication and binds to the promoters of the over 90 cell cycle-regulated genes upon phosphorylation of the RD (Figure 2–9C).[112,122] Work done by Laub *et al.* uncovered the cell cycle regulated genes controlled directly by CtrA and began to uncover the how *C. crescentus* timed the transcriptional events to cause asymmetric cell division.[112] Along with the timing of transcription, CtrA also plays a role in inhibiting replication of the chromosome. In order to inhibit replication, CtrA needs to be phosphorylated and be in a high enough abundance to constantly occupy the five binding sites at the origin of replication, including some sites that overlap DnaA-binding sites.[122] Phosphorylated CtrA has a K_d 35 to 100-times higher than unphosphorylated CtrA *in vitro* providing more evidence for CtrA phosphorylation blocking initiation of chromosome replication.[123] Upon compartmentalization of the daughter cells during the final stages of cell division, one compartment has a higher amount of phosphorylated CtrA to block chromosomal replication (new cell) while the other has low levels of CtrA~P to allow initiation of chromosome replication (old cell) (Figure 2–10).

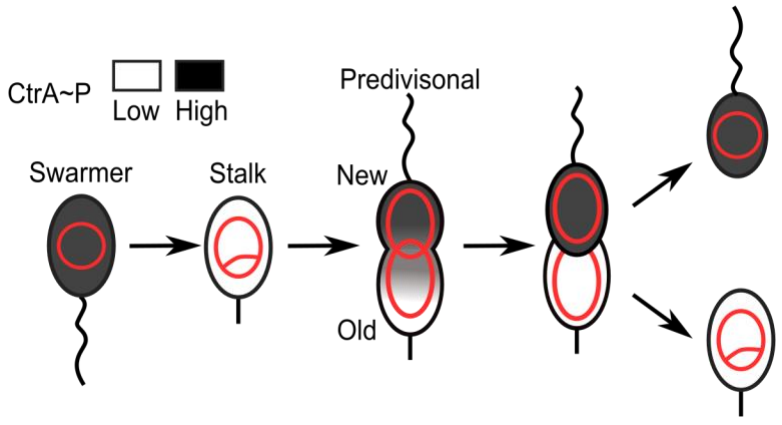

Figure 2–10 Asymmetric CtrA activity during and after cell division.
The red circle represents the chromosome. In the swarmer cell, the CtrA~P levels are high in order to block replication of the chromosome. Upon formation of the stalk, CtrA~P levels drop in order for chromosome replication to begin. As cell elongation and differentiation occurs, a gradient of CtrA~P forms along the length of the cell. Following cytokinesis, the swarmer progeny cell contains a high amount of CtrA~P to block chromosome replication while the stalk cell contains low CtrA~P to begin replication again.

Computational modeling has been used to identify that a gradient of phosphorylated CtrA could be possible in cells using CckA as a phosphatase (sink) at the old cell pole and a kinase (source) at the new cell pole, but *in vivo* evidence is lacking (Figure 2–10).[120]

2.1.5 Pseudokinase DivL plays a role in CckA activity

Pseudokinases are a class of enzymes that maintain a conserved kinase structure but have lost catalytic activity. Most pseudokinase studies so far have been done in Eukaryotic organisms. DivL is one of only a few well-studied pseudokinases in bacteria. DivL is a pseudokinase that has been implicated in the activation of CckA kinase activity.[71,94] Since DivL has lost kinase enzymatic activity, it has developed new signal integration mechanisms to switch the flow of signaling from sensor-to-kinase (Figure 2–11A) to kinase-to-sensor (Figure 2–11B).

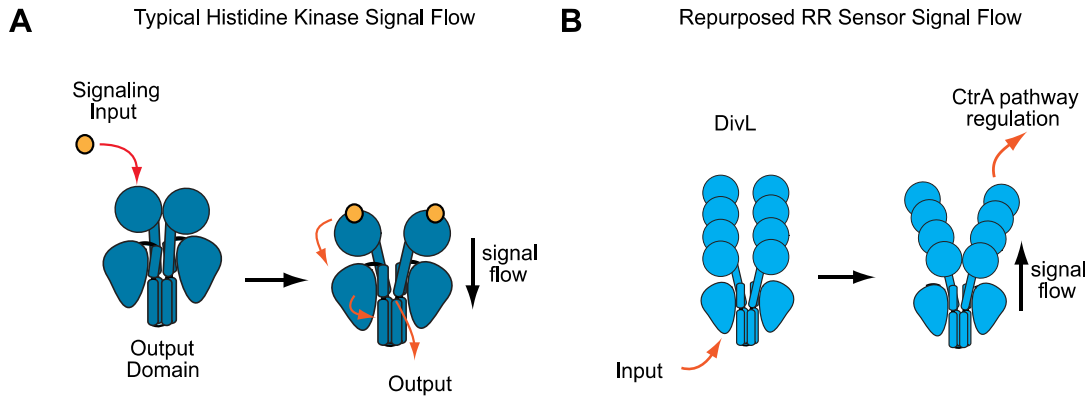

Figure 2–11 The signaling flow DivL is bottom-up, which is in reverse to a histidine kinase.
A) Typical HK signal flow starts with signaling input binding the sensory domains. Signal then flows down resulting in an output. B) DivL binds its input (DivK~P) selectively at the input domain site and in turn the allosteric change is propagated up the sensory domains. Figure provided by Kim Kowallis.

The most understood mechanism in how it accomplishes this is through its interaction with DivK/DivK~P. DivL selectively binds DivK~P over DivK.[71] DivL binds DivK~P (input) through an interaction with the response regulator docking module of DivL (Figure 2–11B). Structural characterization of the pseudokinase DivL captured the protein in two distinct conformations.

Differences between the two conformations revealed a pivoting motion around Tyr550 of the input helix of the dimerization and histidine phosphorylation four-helix bundle, which brings the catalytic assist domain closer to the DHp domain.[71] This information, along with signaling of sensory domains, can provide a basis for understanding a more complex set of conformational changes that regulate the activity of the cell-cycle kinase CckA in *C. crescentus*. Interestingly, DivK does not bind DivL in the same way as it does its HK DivJ. The affinity of DivK~P over DivK is affected by the sensor domain of DivL. Removal of the sensory domain removes specificity of DivK~P, implicating the sensory domain as an allosteric regulator of DivK~P binding.[71] Also it is known that DivL localizes to the new cell pole during predivisional phase where it plays a role in the modulation of CckA activity. DivK~P binding to DivL is implicated in CckA kinase activity modulation, but the way this modulation occurs remained unclear until work done by Childers' lab member Kim Kowallis uncovered that in DivL signaling works in a reverse manner (Figure 2–11B).[124] She was able to mimic DivL/DivK~P and DivL free states using leucine zippers to effectively lock DivL in different conformational states. This led to downstream effects through the CckA/CtrA pathway and provided direct evidence that DivL signal works in reverse through CckA.

2.1.6 FRET spectroscopy can be utilized to track protein conformation changes *in vivo*

A significant obstacle to studying bacterial signaling is a lack of approaches to monitor the spatial and temporal functional status of individual signaling proteins. Current strategies include monitoring final outputs of gene transcription and phosphate affinity (sodium dodecyl sulfate-polyacrylamide gel electrophoresis) SDS-PAGE to track pathway intermediate phosphorylation states in bulk measurements.[112,125] Protein conformations are directly related to protein function.

Different functions have effects on protein conformational changes. ATP binding, RR binding, and autophosphorylation by an HK are all examples of different conformational changes. Past analysis of HK crystal structures indicates that in the kinase active conformation, the DHp and CA domains come in close contact. While in other HK conformational states the CA and DHp domains are separated in space, which allows response regulator access to the DHp domain.[126] Homology models of CckA, based upon CpxA in different activity states[21], also suggests the change in domain spacing between different HK conformational states may be within a FRET range, which can report on distance change of less than 100 Å (Figure 2–12).[127]

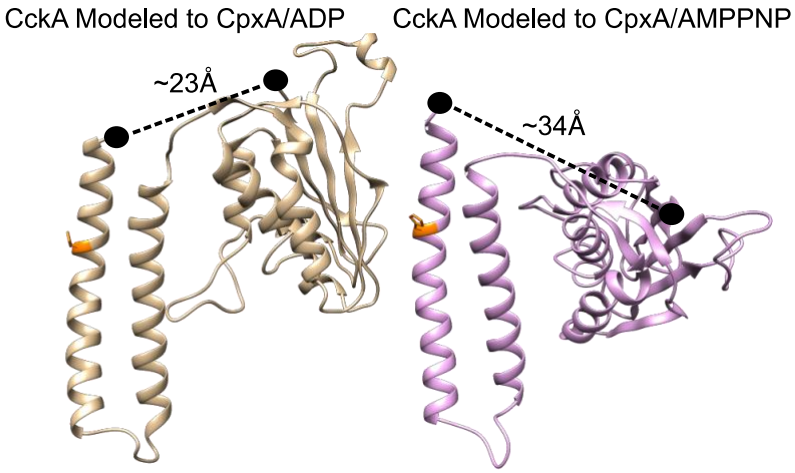

Figure 2–12 CckA modeling to CpxA to identify potential domain conformational changes.
CckA DHp/CA modeled to CpxA crystal structures bound to ADP (PDB: 4BIX) and AMPPNP (PDB: 4BIV) with residues at the top of the bundle and CA domain measured to signify the distance change that occurs between HK states.

Therefore, incorporation of a FRET pair into a single kinase monomer could capture a sum of intramolecular FRET from conformational changes and intermolecular FRET due to oligomeric changes. Success with this approach could be applied as new molecular imaging technology that reports on functional information of HKs with subcellular resolution. We have developed this approach to investigate how subcellular environments and input signals impact the *C. crescentus* cell-cycle kinase CckA. CckA is an essential HK that plays a role in enabling asymmetric cell

division in *C. crescentus*.[8,107,111] Past studies indicate that differences in the subcellular environments at the cell poles regulate CckA signaling activity to allow asymmetric cell division.[94,128-130] Localization of CckA at the cell poles is directed by the scaffolding protein PopZ.[131-134] Each cell pole is composed of distinct signaling proteins that exert opposite effects upon CckA. The old cell pole contains the kinase DivJ that promotes DivK phosphorylation and localized cyclic di-GMP production.[135,136] Both cyclic di-GMP and phosphorylated DivK (DivK~P) activate CckA phosphatase activity. Whereas the new cell pole contains the phosphatase PleC that dephosphorylates DivK and inactivates a critical diguanylate cyclase.[117,136,137] Therefore, CckA exhibits heterogeneity in function and conformation across the cell body that may be detectable by FRET.

FRET is the nonradiative energy transfer between donor and acceptor chromophores over a distance of 1-10 nm (10-100Å).[138] Upon excitation of a donor chromophore with light, a virtual photon from the donor will be transferred to the acceptor through non-radiative dipole-dipole coupling. Upon returning to the ground state, the acceptor chromophore can release a photon at the acceptor emission wavelength that can be detected (Figure 2–13A).

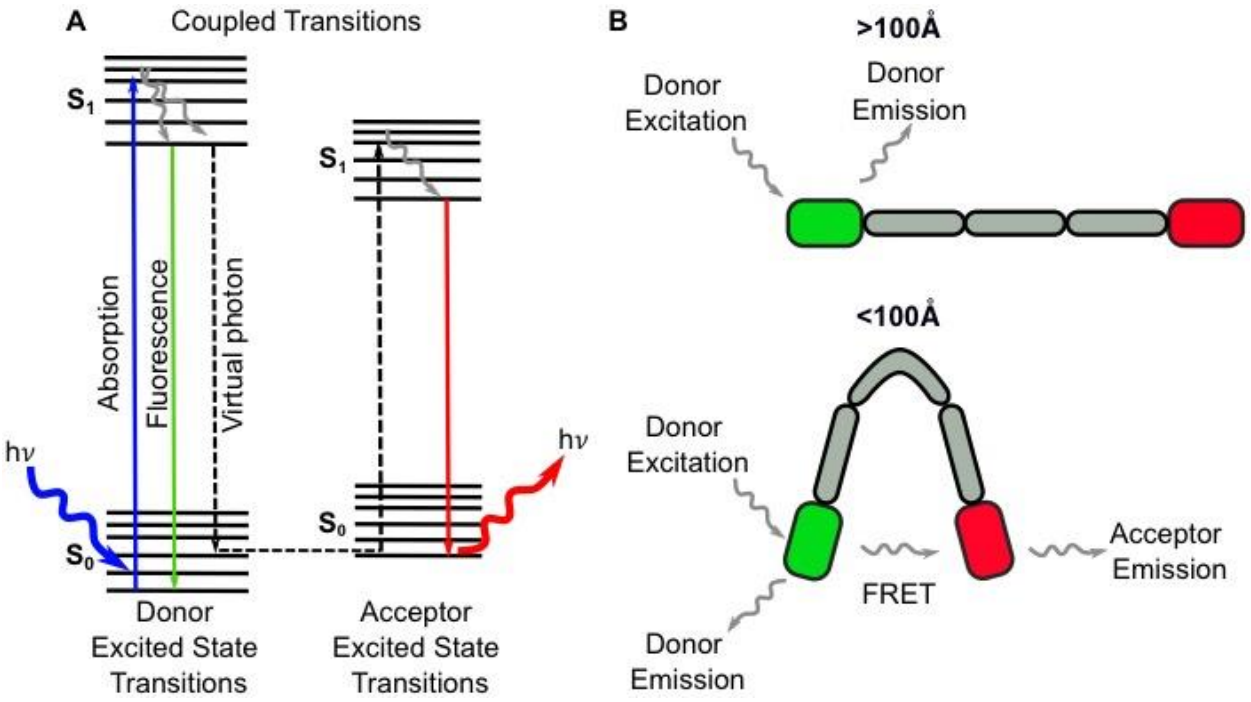

Figure 2–13 FRET mechanism and distance dependency.
A) FRET Jablonski Diagram. Upon donor excitation, the chromophore moves into the first excited state (blue). The excited chromophore can then return to the ground state through internal conversion, quenching, fluorescence, or intersystem crossing to the triplet state (solid green line). In some cases, when distance is optimal between donor and acceptor chromophores, energy transfer can occur from donor to acceptor (virtual photon). The excited acceptor chromophore can then return to the ground state through the same pathways as the donor molecule (red line). B) Using fluorescent proteins as an example, when the distance between proteins is greater than 100Å, energy transfer cannot occur and the donor emits fluorescence. When the distance between proteins is less than 100Å, energy transfer can occur. Some energy is then emitted by the acceptor protein at a longer wavelength than the donor.

FRET occurs over a distance of 1-10 nm (10-100Å) (Figure 2–13B). Due to biological processes taking place on a length-scale of less than 8 nm, FRET can applied to study the interaction of bodies of interest *in vivo*, such as the biological processes of calcium signaling, cyclic di-GMP sensing, and how subunits of an enzyme interact.[117,139,140] The FRET technique applied in this study is sensitized emission FRET, the most common method of FRET used.

Sensitized emission FRET is the technique commonly used on conventional wide-field or confocal microscopes. Also called filterFRET, sensitized emission uses of the fluorescence emission of the acceptor molecule in the system as a result of the energy transfer from the donor to determine the distance change between two FRET pair molecules.[127] A set of filters and controls

are necessary in order to properly measure the acceptor fluorescence following energy transfer from the donor. We used filterFRET to measure FRET on a widefield microscope using a specific filter set, an image splitter, and a split camera chip. Here we outline that method used to capture a FRET image on our microscope.

2.1.7 filterFRET on a widefield, epifluorescence microscope

To use sensitized emission FRET to image samples, we had to take certain considerations into account. These considerations include: direct excitation of the acceptor, cross-talk of the acceptor into the donor emission, and spectral bleed through of the donor emission into the acceptor channel.[127] To overcome these problems, three constructs were created for imaging: Donor only, acceptor only, and a double-fusion construct labeled with both the donor and acceptor. Each construct is imaged under the same donor excitation conditions. Sequential imaging overcomes the need to use a fast filter wheel to capture both emissions. The tool that was used to simultaneous image a FRET pair was the image splitter. We used a Hamamatsu W-VIEW Gemini Image splitting optic in order to do sequential imaging of our samples (Figure 2–14).

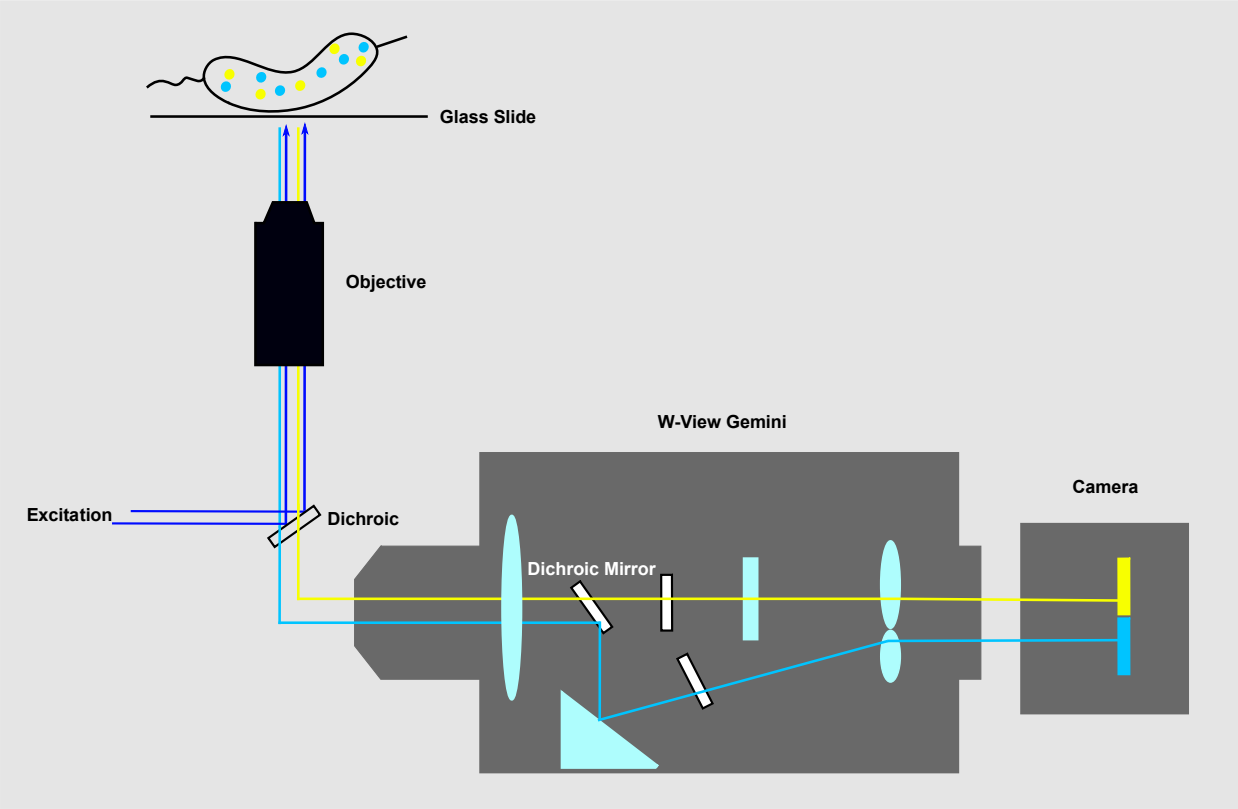

Figure 2–14 Light path through the W-VIEW Gemini splitter.
A sample containing ECFP and EYFP fluorescent proteins was excited using the donor emission wavelength (dark blue). Upon excitation, ECFP is excited resulting in ECFP emission and if FRET occurs, EYFP emission. The ECFP and EYFP emission as well as excitation reflected from the sample is passed through an excitation dichroic to remove excitation from the light path. The remaining emission is the sent to the W-VIEW Gemini where it passes through a lens and a dichroic mirror that separates EYFP and ECFP emission. The ECFP and EYFP emission then passes through cleanup filters and a correction lens. Emission is collected on separate halves of the charged-coupled device (CCD) camera chip. This results in two separate images, ECFP and FRET (EYFP).

But in order to collect simultaneous images, precise registration of both channels had to be done. Manual alignment of the mirrors used to direct the light path was done for each filter set (enhanced yellow fluorescent protein (EYFP)/enhanced cyan fluorescent protein (ECFP), enhanced green fluorescent protein (EGFP)/mCherry) when using the W-VIEW Gemini. Ratiometric imaging is a form of sensitized emission that can be used in a quantitative manner to determine the distance between FRET pairs. It is considered easier to use than typical sensitized emission, because it is not necessary to image the acceptor only, the donor only, and the dual label constructs under the same conditions. To perform ratiometric FRET, the subject must be labeled

with both donor and acceptor to control the stoichiometry of the molecules. Following imaging, the acceptor emission collected is divided by the donor emission to report the ratio of FRET/Donor. Biological conclusions can be drawn from these methods.

2.2 Results and discussion

2.2.1 Development of FRET standards and first generation sensor using ECFP/EYFP

EYFP and ECFP have been a commonly used FRET pair due to their early development by the Tsien group and the wide spectral overlap between ECFP emission and EYFP excitation.[141] We originally started with the EYFP/ECFP FRET pair in our first generation CckA-FRET biosensor, but issues arose with low signal-to-noise ratios. We transitioned early on to the mClover3/mRuby3 FRET pair that was developed in order to increase the brightness, photostability and quantum yields of a FRET pair.[142] mClover3 is a green fluorescent protein (GFP) derivative with a quantum yield of 0.78 and greater than two-fold brightness over EGFP.[142] mRuby3 is a variant of the red fluorescent protein eqFP611 that has been engineered to have a two-fold quantum yield versus mCherry and twice as bright.[142,143] This FRET pair results in a Förster radius (R_0 (nm)) of 6.5 compared to 5.4 for EGFP/mCherry pair and 4.9 for YFP/CFP.[142] Due to an increase in R_0 we can expect to detect FRET changes over a larger distance. Because of the lack of published FRET sensors using this pair we decided to design controls to test the FRET ratiometric imaging of this sensor.

To accomplish this, we constructed two controls consisting of mClover3 and mRuby3 attached by rigid linkers of known lengths. Work done by Ohashi confirmed that the protein

fibronectin (FN) was rigid enough to effectively separate FRET pairs at distances that allowed for more FRET to occur (less than R_0) and blocked FRET from occurring (greater than R_0).[144] Fibronectin is a dimeric glycoprotein composed of disulfide-linked subunits that consists of three domain types.[145] Using this strategy we designed the two constructs using two forms of type III fibronectin spacers, a short and long spacer. The long fibronectin spacer was directly attached to mClover3 and mRuby3 to create the 7.4 nm construct. This spacer is long enough to put the FRET pairs outside of their R_0 radius and decrease the amount of ratiometric FRET. The short fibronectin spacer was also directly attached to mClover3 and mRuby3 in order to place the FRET pair at 3.4 nm, within their R_0 radius and allow for a higher ratiometric FRET to occur (Figure 2–15).

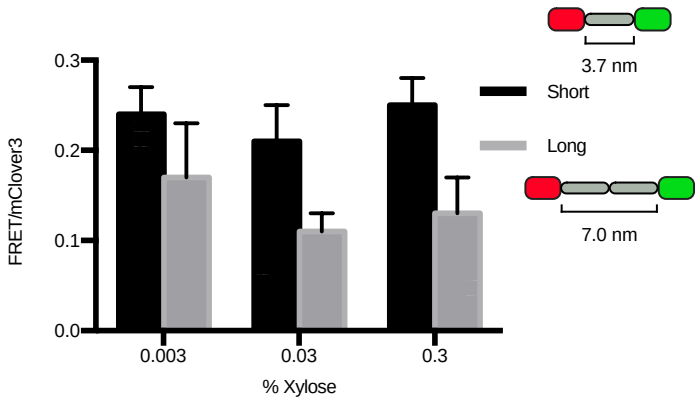

Figure 2–15 Fibronectin standards of mClover3 and mRuby3.
Comparison of short and long FRET standards expressed from the xylose locus in *C. crescentus* after 3 hours. Cells were grown overnight medium shaking at 28ºC to OD_{600} of 0.1. Expression was done using final concentrations of xylose listed for 3 hours. Imaged using FRET imaging protocol (see Methods). Standards were created using fibronectin (FN) 7 domain for the short standard and FN8-10 domains for the long standard. Bars represent standard deviation of the mean. Data represents 2 replicates, N>50 for each condition.

We expressed these constructs in the *C. crescentus* NA1000 using an integrated plasmid at the xylose promoter with concentrations ranging from 0.003 to 0.3% xylose inducer (Figure 2–15). We observed that the average FRET ratio was 0.11 ± 0.02 for the long FRET standard, and 0.21 ± 0.04 for the short FRET standard at 0.03% xylose (Figure 2–15). As a result of these controls we were confident in our FRET ratios for mClover3 and mRuby3 constructs at an induction concentration of 0.03% xylose or higher.

We next needed to generate a functional fusion of CckA that was fused to both fluorescent proteins. As our wild-type control for CckA localization, we used a CckA-mClover3 fusion under the control of its native promoter (Figure 2–16A,B).

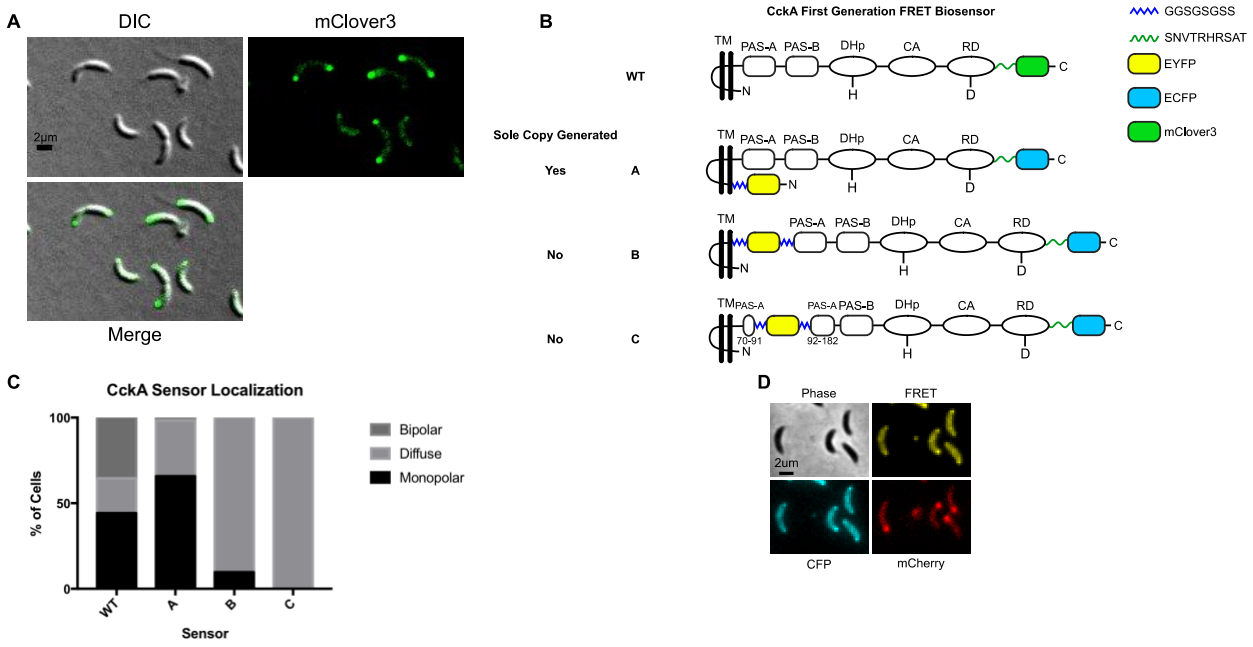

Figure 2–16 CckA-FRET biosensor designs and localization screens.
Cells were grown overnight at 28ºC with shaking in M2 plus glucose (M2G) containing antibiotics to an OD_{600} of 0.1. Cells requiring xylose were induced with a final concentration of 0.03% xylose. Cells were then grown for 3 hours at 28ºC with shaking and imaged on a 1% agarose pad. A) *cckA::cckA-mClover3* cells imaged under DIC and GFP filter settings (See Methods). Scale bar is 2 μm. B) Panel of first-generation FRET sensors designed using ECFP and EYFP as the fluorescent protein pair. The C-terminal ECFP remained static across all designs while the N-terminal EYFP was moved to generate three sensors. C) Localization pattern of all three sensors compared to NA1000, *cckA::cckA-mClover3* cells, with all unsynchronized populations. Represents average of two biological replicates, N>50 for each condition. D) Sensor A cells imaged under FRET imaging conditions also expressing *tipN::tipN-mCherry* in order to visualize the new cell pole (See Methods for imaging details). Scale bar is 2 μm.

An earlier study where we used an EYFP/ECFP pair resulted in fusions that only localized in a monopolar fashion (Figure 2–16B,C). In this group of subjects, we fused ECFP to the C-terminus. We moved the position of EYFP to the N-terminus and between the transmembrane tether and PAS A (Figure 2–16B). Only the N-terminal fusion showed localization (Figure 2–16B,C). Cells were able to be imaged under FRET conditions (Figure 2–16D). Due to these fusion constructs not producing bipolar localization in cells we decided to generate a new group of fusion constructs where the donor fluorescent protein was moved between PAS A and PAS B.

2.2.2 Design of functional CckA-FRET biosensor

CckA contains a tandem-PAS sensory domain.[76,113,130] PAS B contains the predicted DITE motif at residues 293-296 as DVSE. PAS A does not contain this motif which means it is likely not transmitting signals through its C-terminal linker region. In fact, CckA's linking region between PAS A and PAS B is proline-rich, containing 5 proline residues in a 12 amino acid region (PAPVAERAAPPP) (Figure 2–17A). Proline-rich regions have not been identified as signal transduction elements in PAS sensory domains.

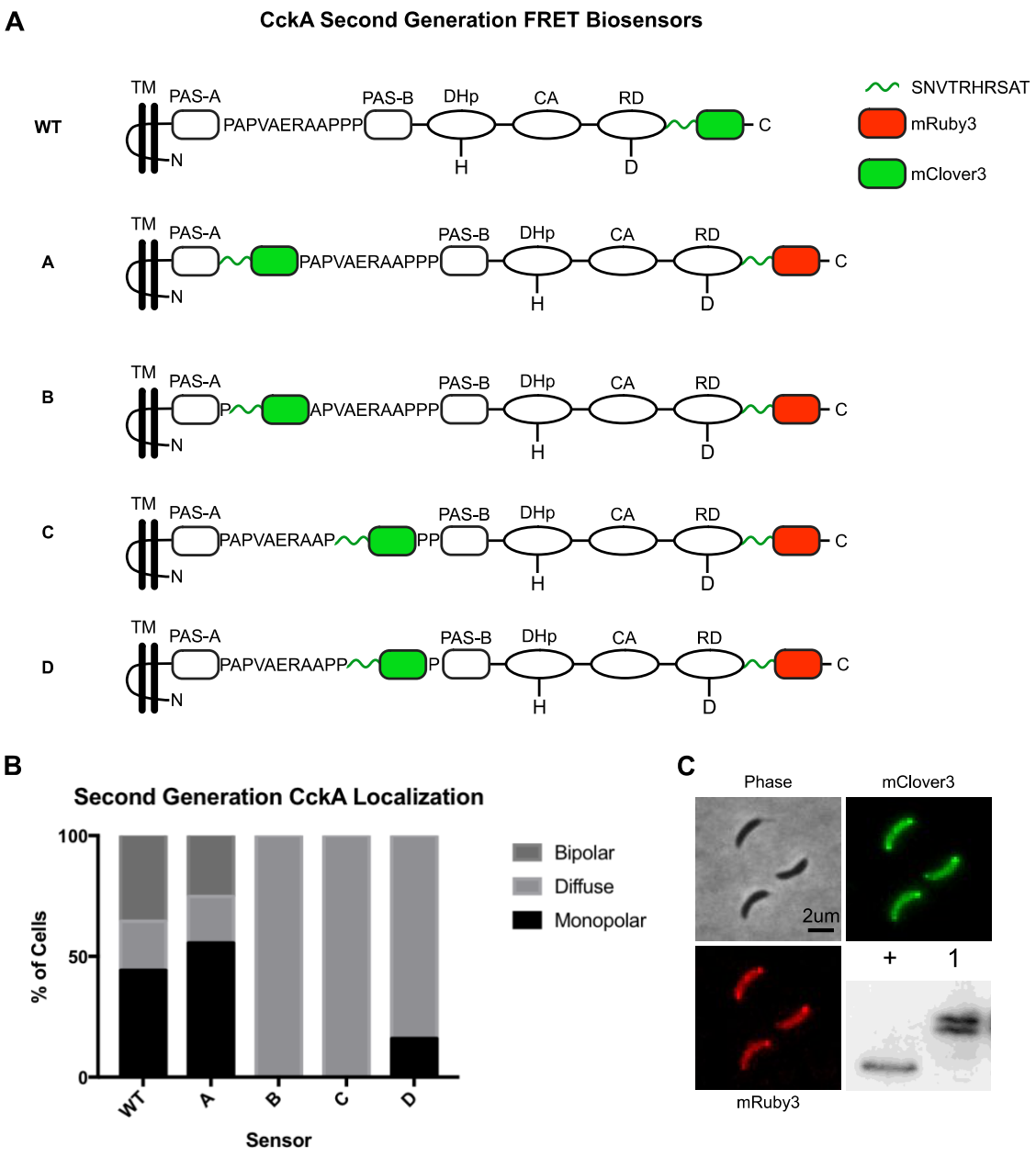

Figure 2–17 Second generation CckA-FRET biosensor produces a sensor that mimics wild-type localization. Cells were grown overnight at 28ºC with shaking in M2G containing antibiotics to an OD_{600} of 0.1. Cells requiring xylose were induced with a final concentration of 0.03% xylose. Cells were then grown for 3 hours at 28ºC with shaking and imaged on a 1% agarose pad. A) Second-generation FRET sensor design panel using mClover3 and mRuby3 as the fluorescent protein pair. The C-terminal mRuby3 position remained fixed and the mClover3 was inserted at varied positions with the linker between PAS A and PAS B. B) Localization of second-generation FRET sensor panel compared to NA1000 *cckA::cckA-mClover3*. Data represents the average of two biological replicates. C) Second-generation Sensor A imaged under GFP and mCherry non-FRET imaging conditions to visualize localization of sensor using mCherry and GFP filters and settings. Scale bar is 2 µm. Inset is a western blot using GFP (ProteinTech) primary antibody to blot for mClover3. + lane is CckA-mClover3 under control of its promoter. 1 is the CckA-FRET biosensor A expressed from the xylose locus. See Methods for Western Blot details.

Because of this linker's composition we decided the space between PAS A and PAS B was a better spot for a fluorescent protein fusion than after PAS B. We generated a panel where we moved the mClover3 protein to different positions within the proline-rich linker (Figure 2–17A). We identified a fluorescent protein fusion within the proline-rich linker between PAS A and PAS B sensory domains at residue 182 (before the linker) that maintained localization at both cell poles like CckA-mClover3 (Figure 2–17A,B). After checking the expression level by western blot (Figure 2–17C) we aimed to determine the FRET ratio values in cells.

Our initial analysis of the FRET sensor indicated the CckA-FRET biosensor displayed FRET/mClover3 ratio values that vary between 0.15-0.25 (Figure 2–18A,C).

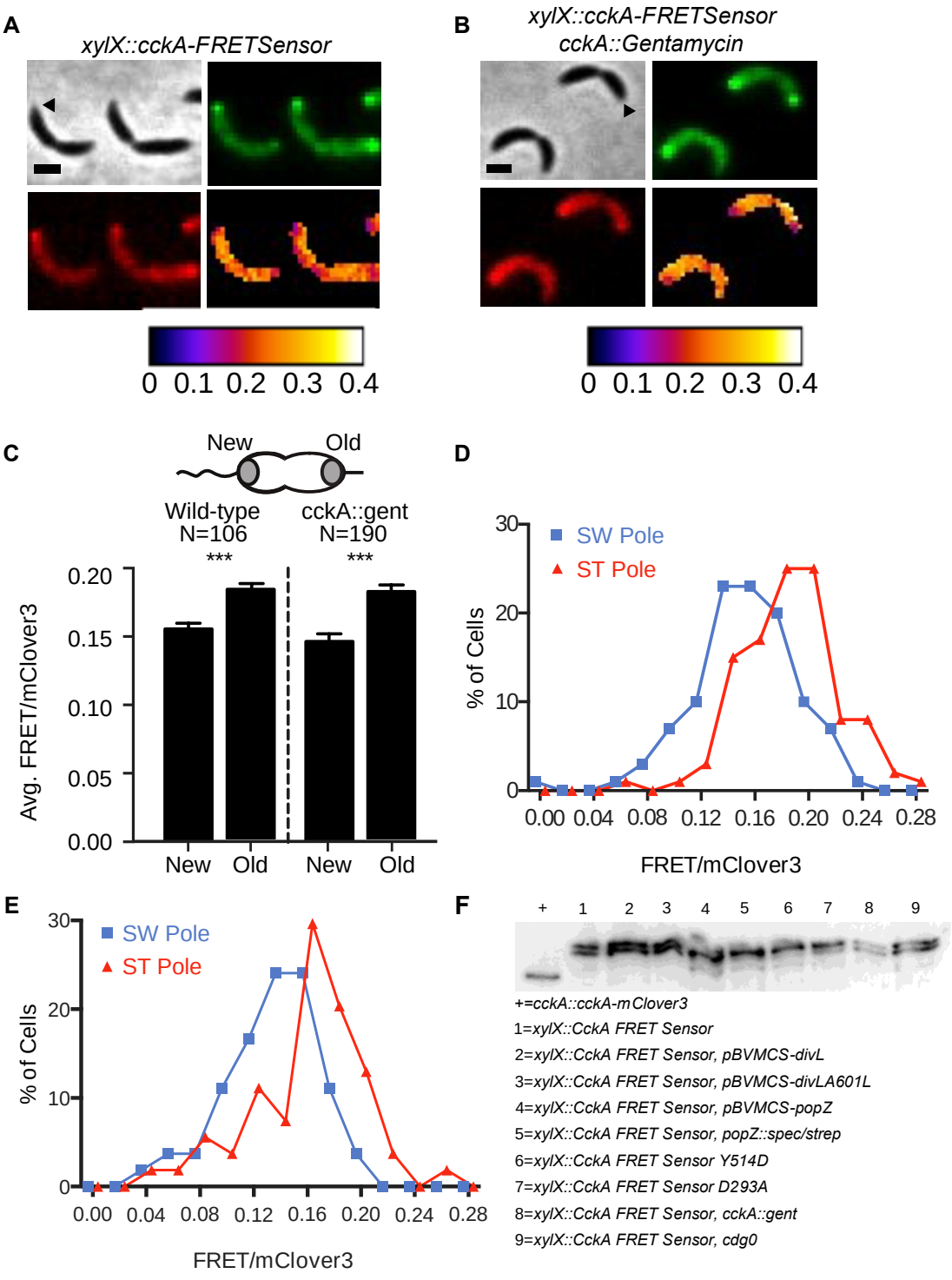

Figure 2–18 CckA-FRET biosensor displays spatial differences in meridiploid and as a sole copy.
Cells were grown overnight at 28ºC with shaking in M2G containing antibiotics to an OD_{600} of 0.1. Cells requiring xylose were induced with a final concentration of 0.03% xylose. Cells were then grown for 3 hours at 28ºC with shaking and imaged on a 1% agarose pad. Imaging was done using FRET imaging conditions (See Methods for details). Black triangles identify the new cell pole. A) CckA-FRET biosensor expressed in wild-type *C. crescentus* strain. Scale bar is 2 µm. The top left panel is the phase-contrast image, top right is the mClover3 fluorescence channel

(green), bottom left is the FRET image (mRuby3, red), and the bottom right is the average FRET ratiometric analysis. The scale is for the average FRET ratio analysis. The panels have been false-colored and all subsequent panels follow the same format. B) CckA-FRET biosensor shown in *cckA* deletion *C. crescentus* strain, in which the CckA-FRET biosensor serves as the sole functional copy of the essential gene CckA. The ability of the CckA-FRET biosensor to serve as the sole copy indicates that kinase has sufficient catalytic function to support cell viability. Scale bar is 2 µm. C) Average new and old cell pole average FRET ratio for a population of *C. crescentus* pre-divisional cells that includes endogenous levels of unlabeled CckA to limit intermolecular FRET. Bar graph comparing the old and new cell pole and display a significant difference (*** indicates $p<0.0005$, N=106, three replicates). CckA-FRET biosensor, as the sole copy of the essential *cckA* gene, shows a similar difference in FRET at the new and old cell pole to merodiploid cells. (*** indicates $p<0.0005$, N=190, two replicates). D) Histogram of swarmer (new) and stalk (old) cells pole average corresponding to bar graphs in C. E) Histogram of CckA-FRET biosensor in *cckA::gentamycin* cells corresponding to bar graph in C. F) Western blot analysis of CckA-FRET biosensor in different genetic backgrounds. This western blot can be referred to for all figures where a CckA-FRET biosensor is shown. The CckA-FRET biosensor shows similar doubling banding in all backgrounds.

FRET/mClover3 is an intensity-based measurement calculated by dividing the intensity of the FRET signal by the donor mClover3 emission signal (see Methods for details). These values fell near the average FRET ratio for the long (0.11 ± 0.02) and short (0.21 ± 0.04) FRET standards. Therefore, we were confident in the measurements of FRET ratio from the CckA-FRET biosensor using our system.

2.2.3 CckA-FRET biosensor can serve as the sole functional copy in cells

Within pre-divisional cells, the CckA-FRET biosensor exhibited differences in the average FRET ratio between the old and new cell pole in bipolar, pre-division cells (Figure 2–18). To determine if the sensor could replicate CckA function, we deleted the essential endogenous copy of CckA. We observed that the CckA-FRET biosensor could support cell viability (Figure 2–18B). Compared to conditions with no CckA that displayed a 400-minute doubling time, the induction of the CckA-FRET biosensor as the sole copy resulted in a 161-minute doubling time in minimal media (data not shown, wild-type doubling time is 180 minutes). The CckA-FRET biosensor regulated signaling in a manner that does not exhibit aberrant phenotypes such as cell filamentation that would be expected for CckA mutations that have lost function.[113,129] This sole copy sensor also displayed similar average FRET ratio differences between the new and old cell poles of

bipolar, pre-division cells indicating similar response at the cell poles when CckA was present (Figure 2–18C-E). To determine that the measurements made were due to conformational changes of the CckA-FRET sensor and not due to other sources of FRET , we next tested whether changes in FRET were due to inter or intramolecular FRET.

2.2.4 CckA-FRET biosensor is not sensitive to intermolecular FRET sources

We next aimed to investigate the contributions from intermolecular FRET versus intramolecular FRET, or both. CckA is known to form dimers and tetramers *in vitro* and localizes to cell poles *in vivo*. This crowding could indicate that we are only observing changes in FRET due to changes in oligomeric states and crowding at the cell poles. While still useful, this would mean we are not reporting on conformational changes of a population of the CckA-FRET sensor. To determine the effect of intermolecular FRET, we co-expressed two copies of a CckA-FRET biosensor: one with only mClover3 and the other with only mRuby3 (Figure 2–19A).[146]

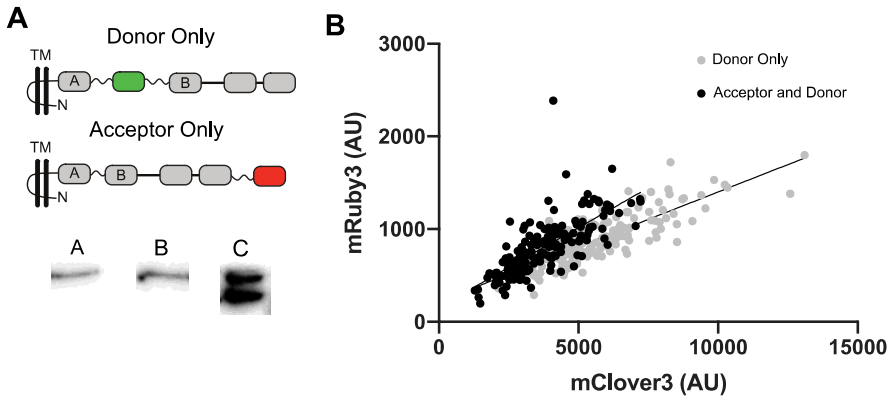

Figure 2–19 CckA-FRET biosensor is not sensitive to intermolecular FRET.
A) Cartoon representations of donor only (green represents mClover3) and acceptor only (red represents mRuby3. The donor only construct was blotted using an anti-GFP antibody (ProteinTech). The acceptor only contained a Flagtag and was blotted using an anti-Flagtag antibody (Sigma). Western blots: A is the donor only, B is the donor in a strain expressing donor and acceptor, and C is the acceptor in the strain expressing both donor and acceptor constructs. See Methods for Western Blot details. B) Plot of acceptor (mRuby3) intensity vs. donor (mClover3) intensity for strains expressing donor only (gray) R^2=0.6723, donor and acceptor (black) R^2=0.5329. Cells were grown under overnight at 28ºC with shaking to OD_{600} of 0.1. Protein expression was induced with either 0.03% final concentration of xylose (donor) or 0.5 mM vanillate and 0.03% xylose (acceptor and donor). Cells were grown for 3 hours more and imaged

using standard conditions (See Methods). Analysis was done using standard FRET imaging analysis (See Methods). Plot represents two pooled, biological replicates R^2 was calculated using Prism.

To determine if intermolecular FRET was occurring, we first imaged cells expressing the mClover3 only sensor. We measured mRuby3 intensities in order to set a baseline for mRuby3 intensity when no acceptor is present. We observed mRuby3 intensity values between 290-1800 AU for this condition (Figure 2–19). When we coexpressed the mRuby3 only and mClover3 only sensors, we did not observe an increase in mRuby3 intensity relative to mClover3 expression alone (200-1650 AU, Figure 2–19B). If FRET were occurring between the separately labeled copies, we would have expected an increase in the mRuby3 signal compared to the mClover3 labeled copy alone. This suggests that the majority of our FRET signal is coming from intramolecular sources when both labels are on the same sensor. Because the engineered sensor displayed low intermolecular signal, we next tested whether FRET would change in response to CckA signals.

2.2.5 CckA-FRET biosensor is responsive to overexpression of the pseudokinase DivL

To identify factors that impact the subcellular variation in observed average FRET ratio, we examined the CckA-FRET biosensor within genetic backgrounds that perturb CckA signaling inputs. Previous studies have demonstrated that CckA interaction with the pseudokinase DivL leads to an increase in CckA kinase activity.[76,94,128] In contrast, CckA interaction with the DivL-DivK~P complex[147] resulted in an increase in phosphatase activity.[113,116,148] Therefore, we tested if the CckA-FRET biosensor was sensitive to DivL overexpression. Compared to uninduced conditions, confirmed by western blot, we observed a significant increase in the average FRET ratio upon DivL overexpression (Figure 2–20A-C,E).

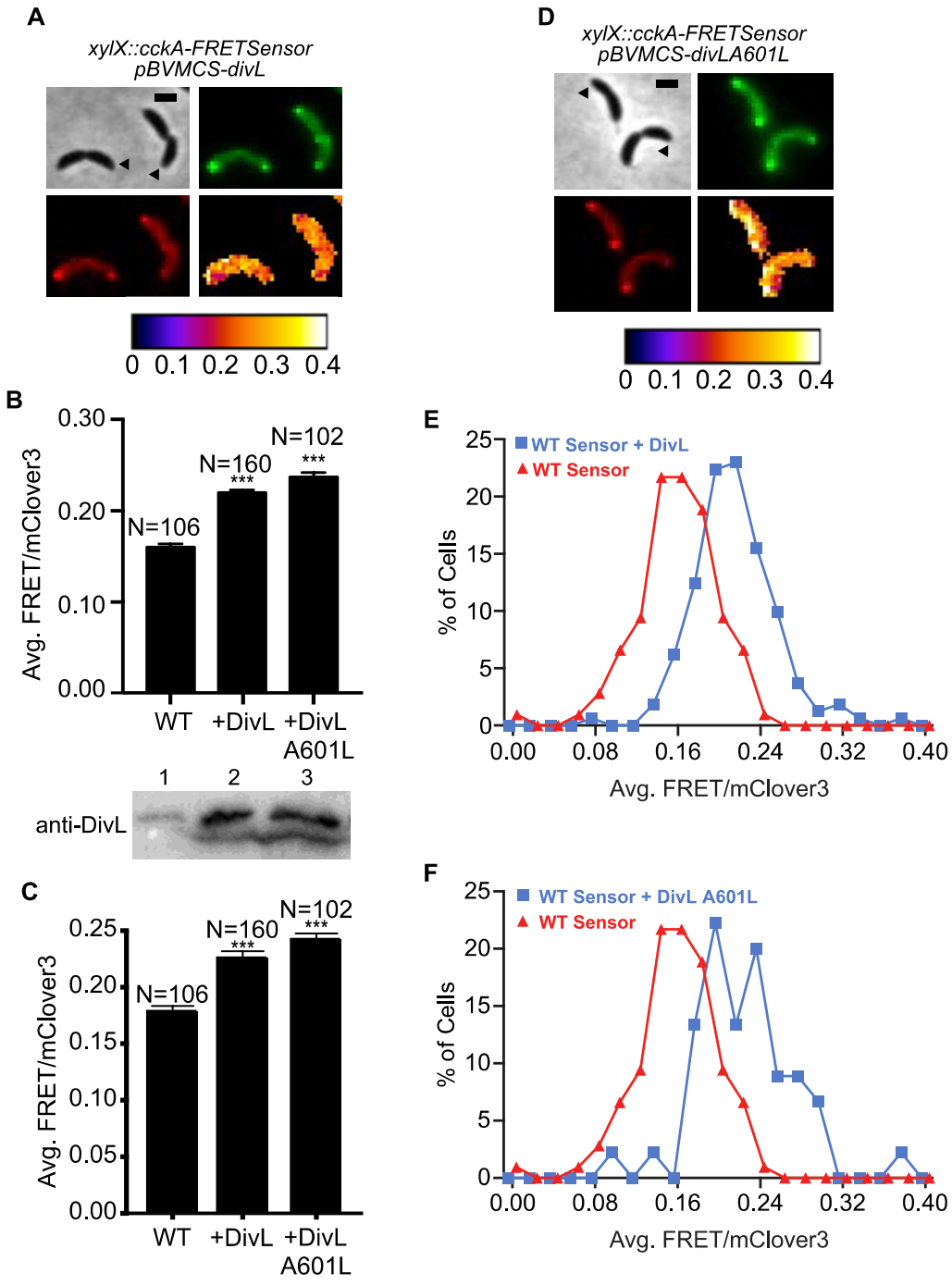

Figure 2–20 DivL overexpression leads to increase in average FRET/mClover3 *in vitro*.
Cells were grown overnight at 28ºC with shaking in M2G containing antibiotics to an OD_{600} of 0.1. Cells requiring xylose were induced with a final concentration of 0.03% xylose. Cells requiring vanillate were induced with a final concentration of 0.5 mM vanillate. Cells were then grown for 3 hours at 28ºC with medium shaking and imaged on a 1% agarose pad. Imaging was done using FRET imaging conditions (See Methods for details). Black triangles identify the new cell pole. Error bars represent starndard error of the mean. A) CckA-FRET biosensor with DivL overexpressed in wild-type cells. Scale bar is 2 µm. B) Bar graphs of CckA-FRET biosensor at the new cell pole in wild-type, DivL overexpression, and DivLA601L overexpression (*** indicates $p<0.0005$ relative to wild-type, three biological replicates). Western blot for DivL in wild-type cells (1), DivL overexpression (2), and DivLA601L (3) using the anti-DivL antibody. See Methods for details. C) Old cell pole average FRET/mclover3 for cells expressing CckA-FRET

biosensor in *C. crescentus* wild-type strain, DivL overexpression cells, and DivL A601L overexpression cells (*** indicates p<0.0005, relative to wild-type, three biological replicates). D) CckA-FRET biosensor expressed with DivLA601L overexpressed in wild-type cells. Scale bar is 2 μm. E) New cell pole histogram of CckA-FRET biosensor in cells overexpressing DivL compared to CckA-FRET biosensor with wild-type levels of DivL corresponding to bar graph in B. F) New cell pole histogram of CckA-FRET biosensor in cells overexpressing DivL compared to CckA-FRET biosensor with wild-type levels of DivLA601L corresponding to bar graph in B.

Given that the overexpressed DivL can either activate CckA kinase activity in its free form or promote CckA phosphatase function when bound to DivK~P, we evaluated a DivL variant that cannot bind DivK~P (DivL A601L). Studies have demonstrated that *C. crescentus* strains that express the DivL A601L variant exhibits a 5-fold activation of the CckA signaling pathway.[76,94] Upon overexpression of the DivL A601L variant we observed an increase in the average FRET ratio at both the new cell pole (Figure 2–20B,D,F) and the old cell pole in predivisional cells that contain bipolar CckA accumulation (Figure 2–20C,D,F). We used a western blot confirm that DivL and DivLA601L were both overexpress compared to wild-type levels (Figure 2–20B). The responsiveness of the CckA-FRET biosensor to the DivL A601L variant indicated that overexpression of the free form of DivL can lead to a high CckA average FRET ratio state. Moreover, these studies revealed that DivL A601L could impact the average FRET ratio state in both the new and old cell pole populations of the CckA-FRET biosensor.

2.2.6 CckA-FRET biosensor detects absence of cellular cyclic di-GMP levels

A second signal that regulates CckA activity is the secondary messenger cyclic di-GMP, which binds directly to CckA's CA domain[116,148] and PAS B sensor.[113] We observed that a *C. crescentus* strain lacking cyclic di-GMP diguanylate cyclases[118], termed *cdg*^{0}, resulted in a decrease in the average FRET ratio at the new cell pole to 0.09±0.003 when compared to wild-type cells (0.15±0.005) (Figure 2–21A-D).[118]

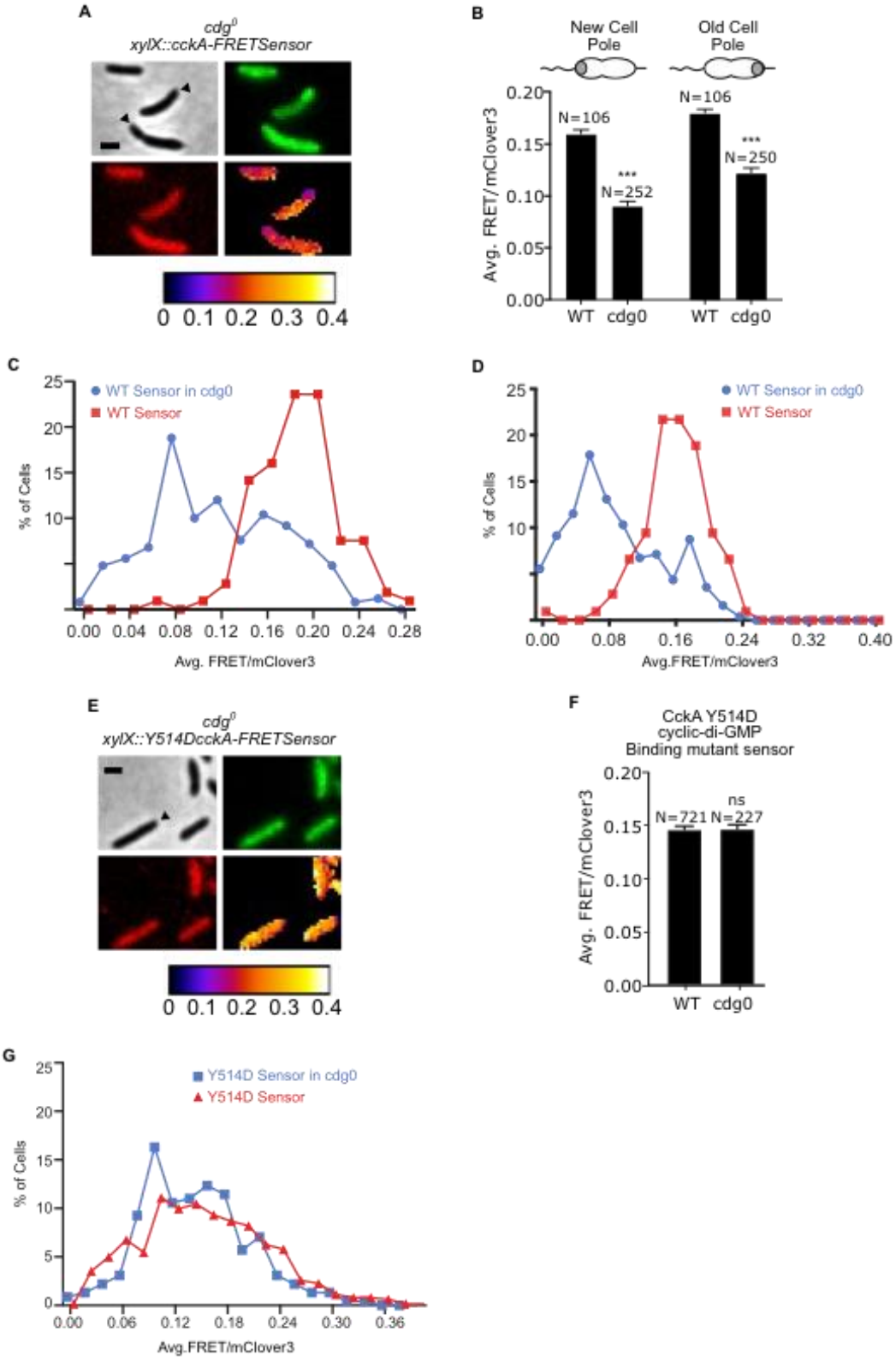

Figure 2–21 CckA-FRET biosensor is responsive to the removal of cyclic di-GMP from cells.
Cells were grown overnight at 28ºC with medium shaking in M2G containing antibiotics to an OD_{600} of 0.1. Cells requiring xylose were induced with a final concentration of 0.03% xylose. Cells were then grown for 3 hours at 28ºC

with shaking and imaged on a 1% agarose pad**.** Black triangles mark the new cell pole. WT stands for wild-type. A) CckA-FRET biosensor expressed in *cdg*^{0} cells, a strain lacking diguanylate cyclases. Scale bar is 2 µm. B) Average FRET ratio at the new and old cell poles for wild-type versus *cdg*^{0}. Lack of cellular cyclic di-GMP results in a reduction of the average FRET ratio (*** indicates $p<0.0005$, three biological replicates). C) Histogram of CckA-FRET biosensor in wild-type cells and *cdg*^{0} cells (n=252) at the new cell pole corresponding to bar graph in B. D) Histogram of CckA-FRET biosensor in wild-type cells and *cdg*^{0} cells (n=250) at the old cell pole corresponding to bar graph in B. E) Cells expressing the CckA-FRET biosensor Y514E in the *cdg*^{0} strain. Scale bar is 2 µm. (F) Cells expressing CckA-FRET biosensor Y514D in wild-type and *cdg*^{0} cells show no difference in average FRET ratio at the new cell pole. Represents three biological replicates. G) Histogram of CckAY514D FRET sensor in wild-type cells (n=721) and *cdg*^{0} (n=227).

To test if this change in FRET ratio was due to the absence of cellular cyclic di-GMP, we used a previously characterized Y514D substitution that lies within the CA domain and disrupts cyclic di-GMP binding.[116,148] We observed that the Y514D CckA-FRET biosensor was no longer responsive to changes in the cellular levels of cyclic di-GMP in the *cdg*^{0} strain (Figure 2–21E-G). This indicated that the changes in the average FRET ratio in the *cdg*^{0} strain were cyclic di-GMP dependent.

2.2.7 PAS-HK DITE motif is required for DivL and cyclic di-GMP responsiveness

To investigate the role of intramolecular conformational change, we incorporated mutations into the CckA-FRET gene that disrupt allostery between the sensor and kinase domains. HKs contain a conserved PAS-specific signal transmission motif that mediates conformational changes between the PAS sensory domain and the HK domain through an intervening coiled-coil region (Figure 2–22A).[15,28]

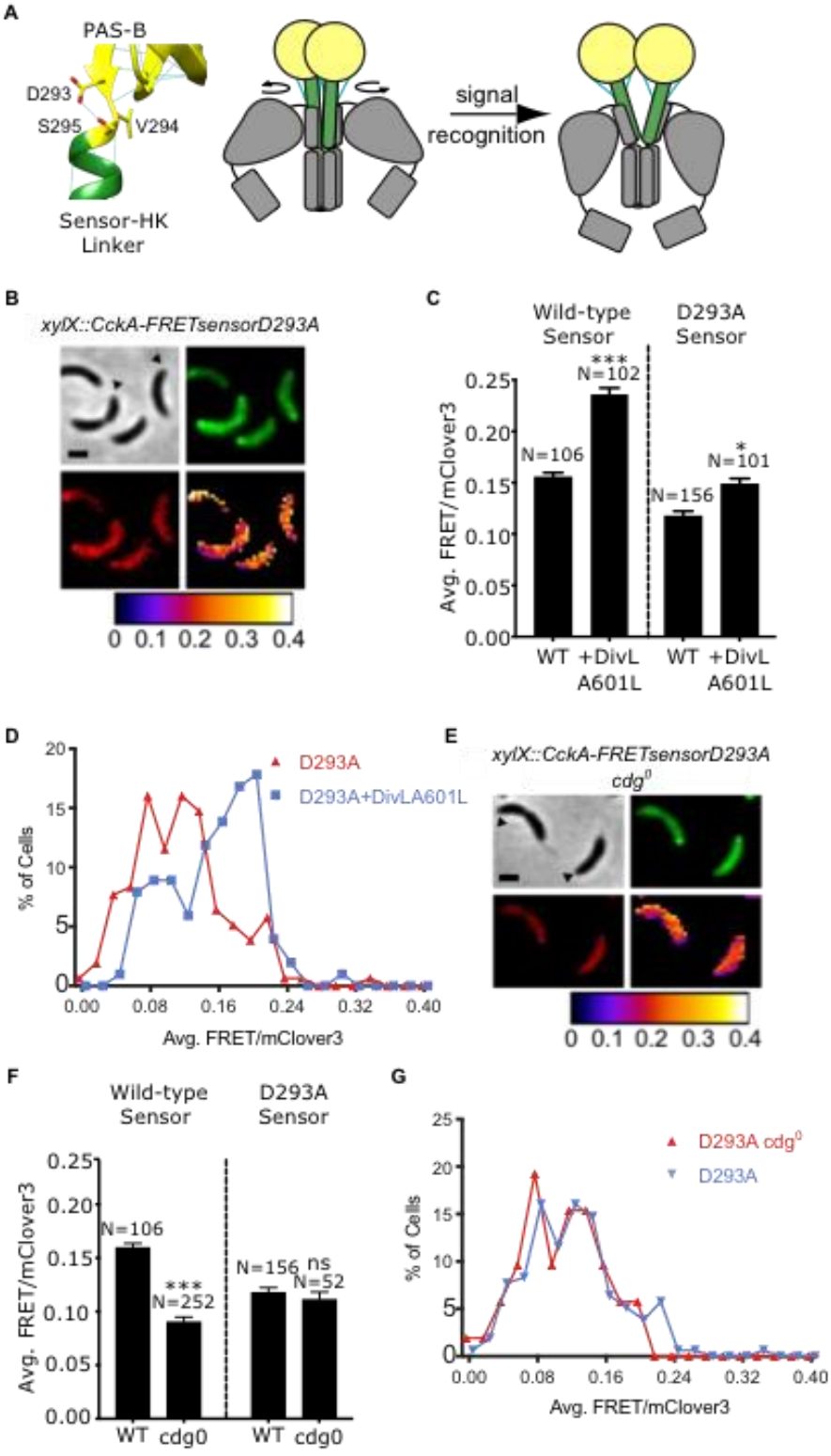

Figure 2–22 CckA-FRET biosensor requires the PAS sensor transmission motif to be responsive to DivL A601L and cyclic di-GMP.

Cells were grown overnight at 28ºC with medium shaking in M2G containing antibiotics to an OD_{600} of 0.1. Cells requiring xylose were induced with a final concentration of 0.03% xylose. Cells requiring vanillate were induced with

a final concentration of 0.5 mM vanillate. Cells were then grown for 3 hours at 28ºC with medium shaking and imaged on a 1% agarose pad. Black triangles mark the new cell pole. A) A signal transmission motif at the C-terminus of PAS domains regulates large-scale conformational changes in PAS-HK sensor. HK was modeled after YF1 crystal structure PDB:4GCZ. B) Cells expressing CckA-FRET biosensor D293A in the wild-type strain. Scale bar is 2 μm. C) The average FRET ratio of the D293A CckA-FRET biosensor containing the signal transmission mutant is less responsive to overexpressed DivL A601L compared to the wild-type sensor (*** indicates $p<0.0005$, * indicates $p<0.05$, three biological replicates). D) Histogram of D293A CckA-FRET biosensor in wild-type and DivLA601L overexpression backgrounds corresponding to bar graph in C. E) Cells expressing D293A CckA-FRET biosensor in the cdg0 background. Scale bar is 2 μm. F) Average FRET ratio of D293A CckA-FRET biosensor in wild-type and cdg0 backgrounds. D293A CckA-FRET biosensor is unresponsive to the removal of cyclic di-GMP from cells (*** indicates $p<0.0005$, three biological replicates). G) Histogram of D293A CckA-FRET biosensor in wild-type and *cgd*^{0} background corresponding to bar graph in F.

Previous mechanistic studies of the engineered YF1 light-sensitive kinase demonstrated that mutations of this PAS domain (DITE) motif prevented light-dependent kinase activity[15]. CckA contains this motif (as DVSE) so we tested if DivL and cyclic di-GMP sensitivity required a sensor-HK conformational change mediated by this signal transmission motif by introducing a D293A mutation into the CckA-FRET biosensor.

In contrast to the wild-type CckA-FRET biosensor, *C. crescentus* expressing the D293A CckA-FRET biosensor was less responsive to the overexpression of DivL A601L (Figure 2–22B-D). In the same manner, the D293A CckA-FRET biosensor displayed identical levels of average FRET ratio at the cell poles in both wild-type and *cdg*^{0} strains (Figure 2–22E-G). Further biochemical analysis of CckA D293A is needed to understand how the D293A mutation impacts kinase and phosphatase activity. However, the lack of responsiveness of the D293A sensor indicates that DivL and cyclic di-GMP-mediated changes to the FRET ratio require a functional PAS signal transmission motif.

2.2.8 CckA-FRET biosensor detects subcellular and temporal changes as cells develop

Given that our CckA-FRET biosensor exhibited a high average FRET ratio state upon stimulation by DivL and a lower average FRET ratio in the absence of cyclic di-GMP, we tracked

FRET/clover3 ratio throughout the cell cycle in a synchronized population.[149] We inspected pre-divisional cells that exhibited bipolar accumulation of the CckA-FRET biosensor and observed that the sensor was in a higher FRET state at the old cell pole than at the new cell pole (Figure 2–23A).

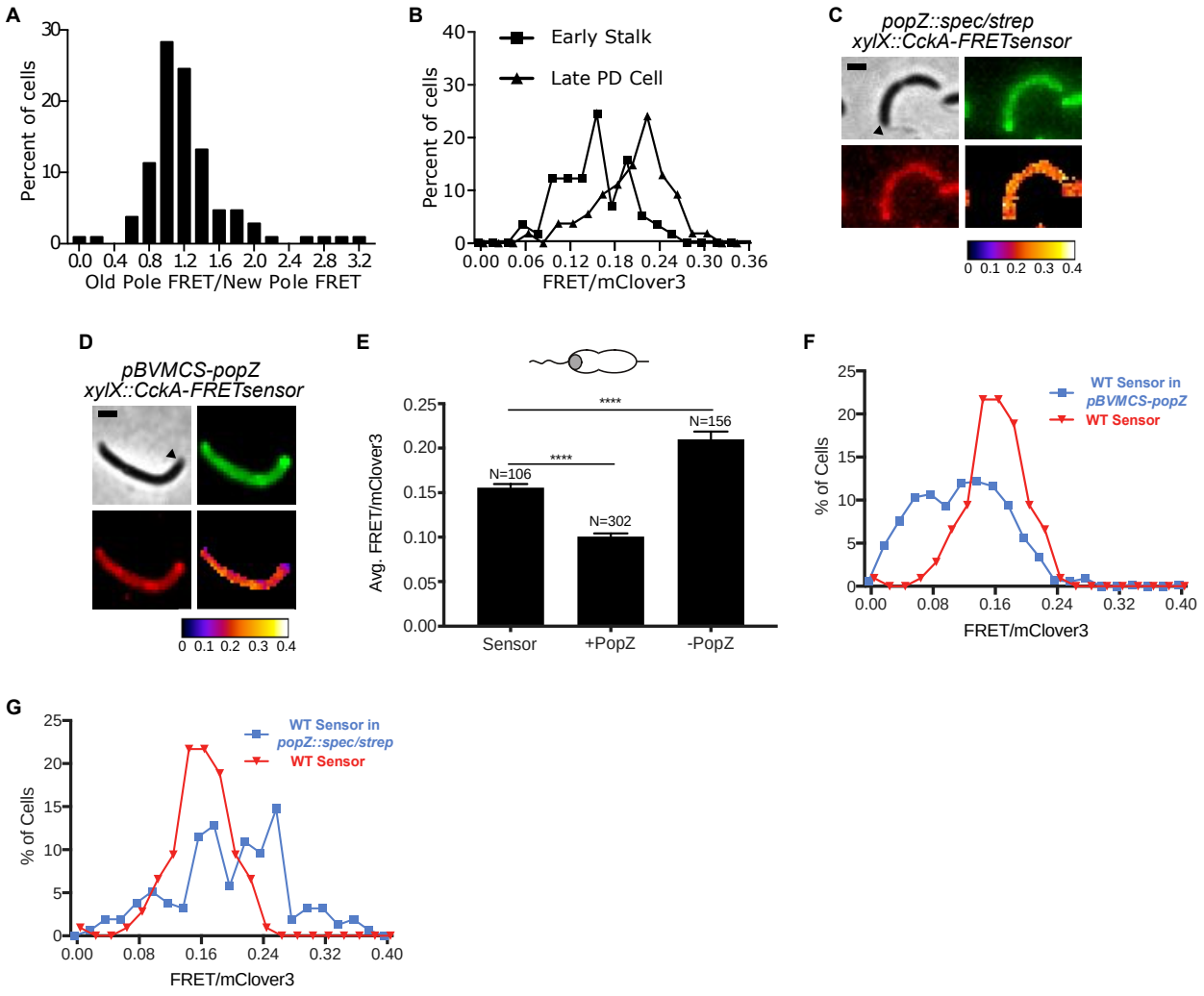

Figure 2–23 CckA-FRET biosensor detects subcellular changes in CckA conformation or as cells progress through the cell cycle.
Cells were grown overnight at 28ºC with medium shaking in M2G containing antibiotics to an OD_{600} of 0.1. Cells requiring xylose were induced with a final concentration of 0.03% xylose. Cells requiring vanillate were induced with a final concentration of 0.5 mM vanillate. Cells were then grown for 3 hours at 28ºC with medium shaking and imaged on a 1% agarose pad. Black triangles mark the new pole. A) The ratio of old/new cell pole FRET in pre-divisional cells. Each value was derived by dividing the average FRET ratio of a single cell's poles. B) Average FRET ratio for early stalk cells (45 min post-synchrony) and pre-divisional (PD) cells (105 min post-synchrony) indicate a significant increase in average FRET ratio as the new cell pole signaling complex matures. C) CckA-FRET biosensor in cells where *popZ* has been deleted. Scale bar is 2 µm. D) Cells expressing the CckA-FRET biosensor and overexpressing PopZ from a replicating vanillate inducible plasmid. Scale bar is 2 µm. E) CckA-FRET biosensor new cell pole

measurement in cells where *popZ* has been deleted compared with a PopZ overexpression from a vanillate inducible replicating plasmid (+PopZ) and the CckA-FRET biosensor in wild-type cells shows a significant difference (*** indicates $p<0.0005$, two biological replicates for + and – PopZ). F) Histogram of PopZ overexpression from bar graph E. G) Histogram of Δ*popZ* from bar graph E.

Previous studies have shown that CckA localizes to the new cell pole at approximately 45 min post-synchrony[129]; however, it does not reach significant levels of phosphorylation until 105 min post-synchrony[150]. We examined whether the CckA-FRET biosensor could detect differences between these cell-cycle stages. We observed that the CckA-FRET biosensor accumulated at the new cell pole at approximately 45 min post synchrony (Figure 2–23B), consistent with previous CckA-EYFP time-lapse studies.[129] We also observed that the average FRET ratio at the new cell pole was initially in the range of 0.08-0.22 in early stalked cells (45-min post synchrony), while in pre-divisional cells (105 min post synchrony) the average FRET ratio increased to 0.14-0.27 (Figure 2–23B). As cells develop the CckA-FRET biosensor may have increased interactions with free DivL or cyclic di-GMP at the new cell pole. However, measurements of cyclic di-GMP levels from early stalk cells to pre-divisional indicate a decrease from 150 to 90 nM.[118] Therefore, the increase in average FRET ratio are likely not due to the rise in cyclic di-GMP levels but may be due to increased DivL-CckA interaction.[118] These results suggest that CckA may arrive at the new cell pole before DivL in early stalked cells, and at later stages may form a complex with DivL.

CckA contains another binding partner, PopZ[134], that assists its new cell pole localization. Interestingly, we observed that strains overexpressing PopZ resulted in a reduction of the CckA average FRET ratio from 0.16 ± 0.01 to 0.10 ± 0.01 (Figure 2–23C,E,G). In contrast, deletion of *popZ* resulted in an increase in the CckA average FRET ratio from 0.160 ± 0.004 to 0.21 ± 0.01 (Figure 2–23D,E,F). These observations suggest that the PopZ-CckA interaction may modulate the FRET sensor conformation and change as cells develop. However, we note that changes to PopZ could have pleotropic effects and impact the sensor via modulation of cyclic di-GMP levels

or DivL localization. These results support a model in which the new cell pole undergoes a gradual compositional remodeling, that we observe as an increase in FRET.

2.3 Discussion

In summary, for the first time, we used FRET to detect HK inputs that occur upon protein-protein interactions (Figure 2–20) and protein-small molecule interactions (Figure 2–21) in a bacteria. The addition of CckA-specific signals stimulates intramolecular conformational changes that lead to changes in FRET ratio (Figure 2–22). We found that the addition of signals that upregulate kinase activity (DivL) and phosphatase activity (cyclic di-GMP) each led to increases in the average FRET ratio. In contrast, overexpression of the PopZ scaffolding protein led to a decrease in the average FRET ratio (Figure 2–23D-F). Upon understanding how CckA stimuli impacted the FRET ratio, application of the sensor revealed that at the new cell pole, the CckA-FRET biosensor transitions from a low average FRET ratio state to a high average FRET ratio state (Figure 2–23A,B). We propose a model in which the new cell pole signaling complex undergoes a compositional remodeling of interaction partners. In this model, at early stages of the cell-cycle CckA initially interacts with PopZ predominately at the new cell pole. While, at the predivisional stage there is increased interaction with DivL that enables CckA kinase activity.

To understand the mechanistic underpinnings of this CckA-FRET biosensor, we observed that sensor stimulation by DivL and cyclic di-GMP required both a functional PAS sensor transmission motif (D293) and the cyclic di-GMP-binding residue (Y514). Analysis of mutations of these sites that regulate conformational change suggests that domain rearrangements within the PAS B sensor, DHp, and CA domains occur upon DivL and cyclic di-GMP binding. Future

structural studies of CckA in complex with DivL, PopZ and cyclic di-GMP will be needed to correlate the observed FRET/mClover3 ratio with CckA's structural state.

An ideal HK sensor would be able to distinguish a HK that is active from one that is inactive. Past analysis of crystallized of HKs observed that kinase-equivalent conformational state is symmetric, while those in the phosphatase-equivalent conformational state are asymmetric.[151] A limitation of the CckA-FRET biosensor is that it cannot distinguish between kinase and phosphatase states, as signals that mediate kinase and phosphatase functions both lead to increased average FRET ratio levels. Rather, in this study we demonstrated the CckA-FRET biosensor reported on its binding with CckA specific signals. Future *in vitro* studies will be aimed at quantifying how signals and HK biochemical states directly impact the FRET ratio. Future studies applying electron paramagnetic resonance (EPR) may offer a potential to detect asymmetry conformations in bulk live cells.

Even with these initial limitations, the ability to track and visualize HK signal integration mechanisms may be useful in dissecting individual kinase contributions to larger multi-kinase networks. We envision the kinase FRET sensor approach could be applied to the HKs involved in processes that range from pathogenesis to symbiosis.[1] These types of FRET sensors may provide unique access to the broad range of signals detected by HKs. We note that hybrid HKs that sense multiple signals may exhibit a range of similar conformational states that prevents functional annotation as kinase or phosphatase state. In contrast, other HKs that are only involved in sensing single signals may provide simpler systems with capabilities to distinguish kinase and phosphatase function.

A second consideration of this approach is the selection of internal fluorescent protein fusion sites within the HK. The HK C-terminus appears to tolerate fluorescent protein fusions

without perturbing function. In the case of CckA, we screened a set of 8 insertions within the N-terminal sensory domain and identified one fusion that maintained CckA's localization pattern and served as a sole functional copy in living cells. We suspect that select insertions within the sensory domain or between the kinase and sensory domain could disrupt sensory mediated allostery. Therefore, given the potential uniqueness of each HK insertion site, future strategies might utilize high-throughput protein engineering technologies[152] to isolate variants that retain function and maximize the FRET dynamic range.

2.4 Future directions

We can apply design principles from working on the CckA-FRET biosensor to other HKs due to the conservation of the DHp and CA domains. We aim to broaden this HK FRET sensor technology to other types of HKs by designing, building, and testing FRET sensors of the HK PhoQ which is linked to virulence in *Salmonella typhimurium* and *P. aeruginosa*.[153,154] This will broaden the use of HK FRET sensor technology and will give us a test case for applying design rules learned from the CckA-FRET biosensor.[155] We envision these new biosensors will enable tracking pathway activity, detecting protein-protein interactions, and screening new HK inhibitors in a broadly studied bacterium, *E. coli*, which also contains the HK PhoQ.[156]

2.4.1 Design and testing of a PhoQ HK conformational FRET sensor

One well-studied HK is PhoQ, which mediates adaptation to Mg^{2+} depleted condition.[154,156] PhoQ also utilizes a prevalent HK domain architecture: TM-calcium channel and chemotaxis receptors (Cache)-TM-HAMP-DHp-CA (Figure 2–24).

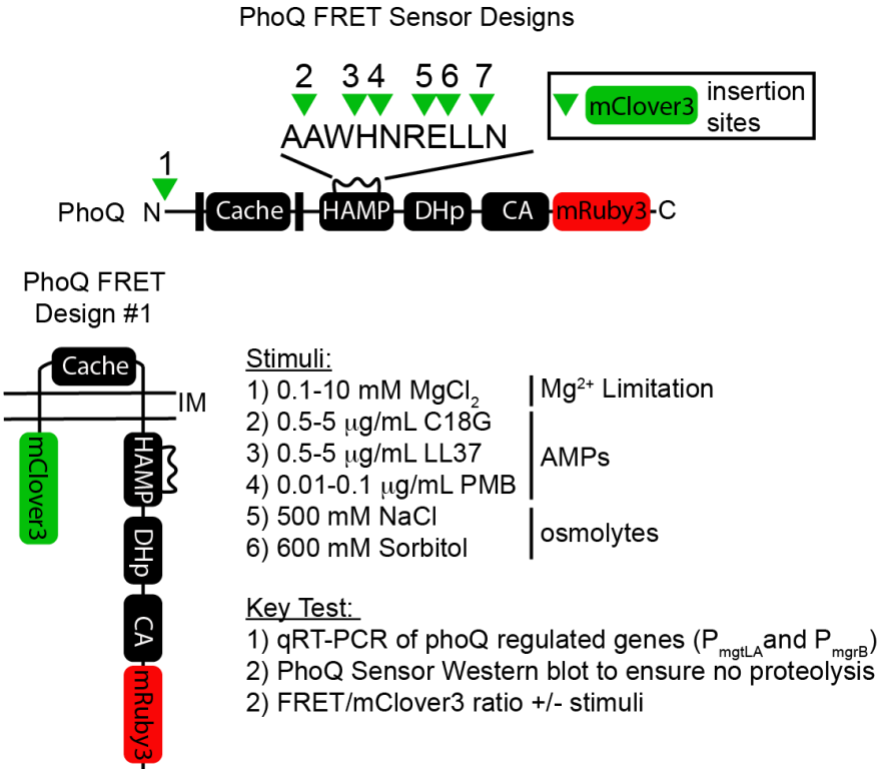

Figure 2–24 Generation of a FRET sensor using PhoQ for expanding HK FRET sensor design rules.
PhoQ is a multisensor HK with a periplasmic Cache domain and a cytosolic HAMP domain. Numbers 1-7 represent potential insertion sites for the fluorescent protein mClover3 in the HAMP domain structural loop. Using the N and C-terminally tagged PhoQ FRET sensor as an example, different stimuli that impact PhoQ kinase activity are listed and broken down by type (Mg^{2+} sensing, antimicrobial peptides (AMPs), and osmolytes). Assays to determine if the PhoQ FRET sensor is functional include qRT-PCR of PhoQ regulated genes, western blots to ensure intact protein, and FRET imaging experiments to measure FRET change upon stimulus.

Therefore, design principles learned from the construction of a PhoQ FRET sensor may also apply to other HKs that use the same domain architecture. Within the HK family, C-terminal protein fusions commonly have little effect upon kinase function.[129] Therefore, our initial designs will utilize a mRuby3 fusion at the C-terminus of PhoQ. A key consideration will be the placement

of the corresponding FRET donor, mClover3. The linker regions connecting each domain are coiled-coil and may play a role in signal transmission, making then non-ideal spots for insertion. Analysis of HAMP domain structures has shown that a HAMP domain structural loop could tolerate insertion of up to 10 glycine residues.[157] Therefore, our initial seven designs include inserts at the N-terminus and a flexible disordered loop within the HAMP domain (Figure 2–24). Linker length impact on FRET will also be considered. For example, short linkers may introduce steric clashes and disrupt the PhoQ structure. Therefore, we will optimize the linker length between the PhoQ protein and the fluorescent proteins inserted into the structure.

2.4.2 Evaluate functionality and dynamic range

A key criterion for an acceptable PhoQ FRET sensor includes the ability to function as a single copy in *E. coli.* For this assay, we will utilize qRT-PCR to track previously characterized PhoQ regulated genes: *mgTLA* and *mgrB.*[156] Past work has shown that the stimulation of PhoQ with low Mg^{2+}, antimicrobial peptides (AMPs), or osmolytes leads to an increase in transcripts or reporter gene GFP expression.[156] In this experiment, wild-type cells will serve as the positive control, while the *E. coli* Δ*phoQ* strain will serve as a negative control. Successful PhoQ FRET sensors will be sensitive to PhoQ-specific stimuli. The second criterion will identify FRET sensors that yield substantial differences in FRET/mClover3 ratio with and without stimulation. We will measure the whole-cell FRET/mClover3 ratio at low (1 mM $MgCl_2$) versus high (10 mM $MgCl_2$) magnesium.[158] We will also characterize the PhoQ sensor's osmolarity sensing capabilities by comparing no osmolyte, 300 mM NaCl [156], 600 mM sucrose [156], and 600 mM sorbitol (Figure 2–24).[156] A third screen will be PhoQ FRET sensors ability to sense cationic α-helical antimicrobial peptides by comparing 5 mg/mL of LL-37 peptide with 1mM $MgCl_2$[159], 5 mg/mL of C18G[159] with

1 mM $MgCl_2$ versus media lacking the cationic antimicrobial peptide with 1 mM $MgCl_2$ (Figure 2–24). For each of these conditions, the FRET/mClover3 ratio will be measured by fluorescence microscopy. Western blot analysis will be performed to ensure accumulation of comparable levels of the PhoQ-FRET sensor protein and a lack of FRET sensor degradation. Additionally, western blot analysis will be carried out to detect any sensor proteolysis. After the initial PhoQ FRET sensor characterization, we will analyze the impact of mutations that disrupt the PhoQ function. These will include mutations that disrupt PhoQ's Mg^{2+} sensing (PhoQ E184K, T156K[159] and H157A[160,161]), cationic peptide sensing (PhoQ D51-181[159]), and osmolarity sensing (PhoQ N202A[162]).

2.4.3 Expected results

We expect to identify a PhoQ FRET sensor that is responsive to PhoQ stimulation and can be disrupted by point mutations that impact PhoQ's function. We also expect that our combined efforts engineering PhoQ-FRET and past CckA-FRET biosensor design work [163] will outline general HK-FRET sensor design principles. For example, we anticipate identifying a possible HAMP insertion point that could be utilized for other HAMP containing HKs. More broadly, the construction of a PhoQ FRET sensor would be available as a FRET imaging tool to the bacterial signaling community. In future work, we aim to use the PhoQ-FRET sensor to test if PhoQ activity is homogenous across cells within biofilm communities. We may observe that regions within PhoQ's HAMP domain are critical for function. In these scenarios, we will take a high-throughput library screening approach, such as domain insertion profiling [152], to screen each insertion point within PhoQ for function.

2.5 Methods

Growth Conditions: *E. coli* strains were grown at 37 °C with shaking overnight in LB media supplemented with antibiotics (SI Table 6). *C. crescentus* strains were grown in PYE or M2G media supplemented with antibiotics (SI Table 6) at 28 °C with shaking overnight or for specified times for imaging.

Electroporation: *C. crescentus* were electroporated by centrifuging 4 mL for 5 minutes at 21,100 x g. Supernatant was removed and cells were washed in 100 µL of cold, sterile water and centrifuged for 1 minute at 21,100 x g. This step was repeated 2 more times, followed by suspension of cells in a final volume of 80 µL. Integrating plasmids (12.5 µL) or replication plasmids (3 µL) were then added to the cells and electroporated on the *E. coli* setting of a BioRad GenePulser using 0.1 cm electroporation cuvettes (BioRad). Cells were then resuspended in 1 mL of 2xPYE and shaken at 28 °C for 3 hours, then 100 µL of cells were then plated on PYE/antibiotic plates. The remaining cells were pelleted, resuspended in 100 µL of 2xPYE, and plated on PYE/antibiotic plates. Cells were grown at 28 °C for 3 days and colonies were streaked onto a PYE/antibiotic plate. Colonies that grew after streaking were screened for using colony PCR (DreamTaq Green) using primers for integration at the xylose locus (RecUni-1, RecXyl-2), vanillate locus (RecUni-1, RecVan-2), or for replicating plasmids (Pvan-for, M13-for) according to the manufacturer's protocol with 5 minute extension times.

Phage Transduction: Phage transduction followed a previously published protocol from Bert Ely and co-workers[164]. In order to delete *cckA* from strain WSC1413 containing the CckA-FRET biosensor expressed from the xylose inducible promoter, a strain containing a gentamycin replacement of CckA was grown overnight in PYE (WSC1149). 5 µL of three concentrations of phage (1x, 10x dilution, 100x dilution) were each added to 0.5 mL of cells and incubated at room

temperature for 15 minutes. Cells were then added to 2 mL of PYE in a 15 mL conical. 500 µL of warm PYE top agar (1.5% PYE agar) was then added to cells and the mixture was added and nutated on a PYE plain agar plate. Plates were incubated overnight at 28 °C right-side-up. Plates with confluent lysis were recovered by scraping top agar layer into 50 mL conical, washing plate with 5 mL of PYE, and adding 100 µL of chloroform followed by vortexing. The tube was shaken for 10 minutes at room temperature. After centrifuging for 30 minutes at 8000 rpm, supernatant was transferred to a new tube. 100 µL of chloroform was added and the tube was vortexed. Phage was aliquoted and stored at 4 °C. The strain WSC1413 was grown in PYE/chloramphenicol overnight. 100 µL of prepared phage was added to 500 µL of cells. Cells were incubated at room temp for 45 minutes to allow phage to attach to cells. Cells were centrifuged at 21,100 x g for 5 minutes, supernatant was removed, and cells were resuspended in 100 µL of PYE. After 2 hours of incubation at room temperature cells were plated on PYE/gentamycin/chloramphenicol/0.003%xylose media to select for the deletion of *cckA.* Replacement was confirmed using colony PCR (DreamTaq) using primers nSWD35 and nSWD36.

Imaging Conditions: *C. crescentus* strains for single time point imaging were grown overnight in M2G media supplemented with antibiotics to an OD_{600} 0.1-0.2. Cells were then induced with either xylose (0.03% w/v) or vanillate (0.5 mM) or both for 3 hours. 2 µL of cells were deposited on a 1% agarose/M2G pad on a glass slide and covered with a glass coverslip. For intermolecular experiments, 0.03% xylose was used and 0.15 mM van was used to avoid increasing levels of CckA too much.

Time-lapse And Time-course Synchrony: This method adapted was from Schrader, et al[149]. Synchronized *C. crescentus* cells for time-lapse or time-course imaging were grown

overnight in M2G media supplemented with antibiotics to a cell density between OD_{600} 0.1 and 0.2 before being induced with either xylose (0.03% w/v) or vanillate (0.5 mM) or both for 3 hours. Cells were then spun down at 4000 rpm for 17 minutes at 4 °C. Supernatant was removed and pellet was resuspended in 1mL of cold 1xM2. Cells were transferred to a 2 mL Eppendorf tube and spun for 3 minutes at 4 °C at 13000 rpm. Supernatant was removed and the pellet was resuspended in 900 µL of cold 1xM2. 900 µL of Percoll was then added. Cells were then spun at 11000 rpm for 20 minutes at 4 °C in order to density centrifugate stalk from swarmer cells. The top band (stalk cells) was then removed and the bottom band (swarmer cells) was isolated and washed with 1 mL of 1xM2. Cells were spun at 7500rpm for 3 minutes at 4 °C. Cells were then washed again with 1xM2. Pelleted cells were resuspended in M2G and incubated with shaking at 28 °C for 5 minutes. 2 µL of cells were deposited on a 0.75% agarose/M2G pad on a glass slide and covered with a glass coverslip. Wax was then used to seal pad to prevent evaporation for time-lapses. For time-courses 2 µL of cells were deposited on a 1% agarose/M2G pad on a glass slide and covered with a glass coverslip. Cells were incubated at 28 °C with shaking during the duration of the time-course.

Microscopy: Images were taken on a Nikon T*i*E inverted setup using an APO Lambda 100X oil objective with phase-contrast or differential interference contrast (DIC) using Zeiss Immersol 518F Immersion Oil using Nikon Element AR software to control the setup. A halogen lamp was used for the white light source. Spectra X light engine was used for all fluorescence excitation. An Andor Ixon Ultra 897 EMCCD camera was used for all imaging. All filter sets used were purchased from Chroma. CFP/YFP/mCherry (77074157) and GFP (77074160) filter cubes were used with emission filter sets GFP (77074161) and CFP/YFP/mCherry (77074158).

FRET Microscopy and Image Processing: Simultaneous FRET imaging was done by placing a Hamamatsu W-View Gemini Image Splitter in the light path between the Nikon T*i*E and the camera. A GFP/mCherry dichroic mirror, GFP emission filter, and mCherry emission filter were used. Alignment of the channels was done using the supplied alignment slide. Alignment of the channels was done before each imaging event. Each strain was imaged under the same conditions (600 millisecond Autoexposure, 100 Gain, 2x2 binning for capture, and 15% power). Background from the fluorescent channels was subtracted in the Nikon software and images were exported as TIFFs for processing in ImageJ.[165] In ImageJ a mask was generated by thresholding cell signal above background. The original image was then multiplied by the masked image to remove background signal and the mCherry emission channel image was divided by the GFP emission channel (32 bit image) to generate a ratiometric FRET image.

Image Analysis: For each experiment, 4 images were uploaded into MicrobeJ[166] (Phase, GFP channel, mCherry channel, and ratiometric image). The phase image was used to generate a cell outline using the Medial Axis setting. Cell poles were outlined using the MicrobeJ automatic pole settings which to draw a shape around the cell pole. MicrobeJ was preset to mark the stalk pole as the pole with higher intensity in the GFP channel. After software chose the poles, manual adjustment was done by choosing cells with a visible stalk and cells with incorrect pole alignment were corrected manually. MicrobeJ data analysis tool was then used to average the intensity of the cell pole and body. Data was exported to Prism in order to generate histograms and average data. Student's t-test was used to determine significant difference in populations. Error bars are reported as standard error of the mean.

Western Blot: Western blots were done by centrifuging 1 mL of cells of a known OD_{600}, removing the supernatant and resuspending in 100 µL of 4x Sample Buffer containing 40%

glycerol, 24% 6.8 M Tris/HCl, 8% weight by volume sodium dodecyl sulfate (SDS), 5% β-mercaptoethanol, and 30% bromophenol blue solution. Samples were then heated at 95 °C for 10 minutes. Samples were loaded onto a 10% resolving SDS-PAGE gel with a 4% stacking gel. Loading volumes were normalized using OD_{600} of the culture at the time of sampling. The ladder used was ThermoFisher Page Ruler Pre-Stained Ladder. Transfer was done using ThermoFisher Mini Blot Module with a polyvinylidene difluoride (PVDF) transfer membrane (ThermoFisher) for 2 hours at 20 V and 4 °C. Blotting for DivL was done by blocking overnight at 4 °C in blocking buffer (0.1% Tween-20, 1xtris buffered saline (TBS), 5% milk). The blot was rinsed 3x5 minutes in tris buffered saline plus Tween-20 (TBST) (1xTBS, 0.1% Tween-20). It was then incubated in primary rabbit polyclonal antibody solution (TBST, 1:10000 anti-DivL antibody dilution) for 1 hour at 4 °C. The blot was then rinsed 3x5 min in TBST and incubated in secondary antibody solution (TBST, 1:10000 goat anti-rabbit IgG HRP antibody, Sigma) for 1 hour at 4 °C. The blot was then rinsed 1x15 min, 2x5 min in TBST, brought to room temperature and exposed to chemiluminescent substrate (SuperSignal West Pico PLUS Chemiluminescent Substrate) and imaged using the Chemi Hi Resolution setting on a BioRad ChemiDoc with auto exposure for intense bands. Blotting for mClover3 was done using the same procedure for SDS-PAGE and transfer. The resulting blot was blocked in 1xTBST (0.2% Tween-20) with 5% milk for 2 hours at 4 °C. After two hours the solution was changed to 1xTBST (0.2% Tween-20) with 5% milk with a 1:2000 dilution of GFP Rabbit Polyclonal Antibody (ProteinTech) and incubated overnight at 4 °C. The blot was then washed in 1xTBST (0.2% Tween-20) 3x10 minutes. It was then incubated for 1 hour in 1xTBST (0.2% Tween-20) with 5% milk with 1:5000 dilution of goat anti-rabbit IgG HRP antibody for 1 hour at 4 °C. The blot was then washed 3x10 minutes in 1xTBST (0.2% Tween-20) and treated with chemiluminescent substrate the same way as the DivL blot. Blotting

for FLAG epitope was completed with same SDS-PAGE and transfer as above. Blots were incubated in 1xTBST (0.2% Tween-20), 5% milk overnight at 4 ºC. The blot was then washed in 1xTBST (0.2% Tween-20) 3x5 minutes. It was then incubated for 1 hour in 1xTBST (0.2% Tween-20) with 5% milk with 1:5000 dilution of anti-Flagtag antibody (Sigma) for 1 hour at 4 °C. The blot was then washed 3x5 minutes in 1xTBST (0.2% Tween-20) and 1xTBST (0.2% Tween-20) with 5% milk with 1:10000 dilution of goat anti-rabbit IgG HRP was added and incubated for one hour at 4ºC. The blot was then washed 3x5 minutes in 1xTBST (0.2% Tween-20) and treated with chemiluminescent substrate the same way as the DivL blot.

Construction Of Plasmids: The plasmids used in this study can be found in Table 2–1. Detailed plasmid construction is described below and can be found in Table 2–2. Site-directed mutagenesis primers and annealing temperatures can be found in Table 2–3. The lists of oligonucleotides used in this study can be found in Table 2–4. All oligos were ordered from IDT. The strains used can be found in Table 2–5 and methods to generate strains are listed below. Phusion polymerase (ThermoFisher) was used for amplification of PCR products used in Gibson assembly and amplicons were isolated using gel electrophoresis using a 1% agarose, 1xTAE gel with ethidium bromide added for visualization by UV light. Band sizes were determined using a GeneRuler 1 kb DNA Ladder (ThermoFisher). Bands were excised from the gel and extracted using a GeneJet Gel Extraction Kit (ThermoFisher) following manufacturer's protocols, with the addition of a 100 µL binding buffer wash step following the spin through of DNA/agarose/binding buffer. Water was used for elution. DNA concentrations were determined using a NanoDrop 2000 spectrophotometer (Thermo Scientific). All reactions were done according to the manufacturer's protocols with annealing temperature at 55 °C for 30 seconds, unless otherwise noted. KOD Hot Start Polymerase (Millipore) was used for site-directed mutagenesis PCR according the

manufacturer's protocols with annealing temperatures noted (Table 2–3) and 10 minute extension times. DpnI (Thermofisher) was used to degrade template after reaction was finished. 5 µg of vector was digested at a time using the manufacturer's protocol and isolated the same way as PCR products (above). If a single restriction enzyme was used, FastAP (ThermoFisher) was used to decrease occurrence of reannealing.

Plasmids: Below is an example of the generation of a plasmid using the Gibson assembly method for table Table 2–2. This can be used as a guide to understand the remainder of plasmids constructed using the Gibson assembly method. Plasmids for Gibson assembly method were designed using J5.[167] All Gibson reaction buffers were made using Phusion polymerase (ThermoFisher), Taq ligase (NEB), and T5 exonuclease (NEB).[168] The plasmid pSWD95 encodes a xylose-inducible copy of CckA-mRuby3 with mClover3 inserted between codons for amino acids 182 and 183. *mClover3* was linked to the *cckA* N-terminal using a GGSGS linker and was directly fused to the C-terminal of *cckA*. *mRuby3* was linked to *cckA* using an SNVTHRSAT linker. The vector pXCFPC-6 was linearized by double digestion with the restriction endonucleases NheI and NdeI. PCR products with overhangs for Gibson assembly were generated following the schematic below at a 100 ng scale Gibson reaction scale. Four inserts were generated by PCR that include codons 1-182 of *cckA* were amplified by PCR using plasmid pMT383 as a template with primers SWD160 and SWD305, and codons 183-691 were amplified as a separate PCR product using primers SWD308 and SWD309. Additionally *mclover3* was amplified by PCR using plasmid pSWD14 as a template with primers SWD306 and SWD307. The 3'-insert, *mruby*3 was amplified by PCR using plasmid pSWD14 as a template with primers SWD310 and SWD311. The linearized pXCFPC-6 and each of the four inserts were combined at 100 ng reaction scale and incubated at 50°C for 60 min in a reaction mixture containing T5 exonuclease, Phusion DNA

polymerase, and Taq ligase (NEB). 5 µL of the reaction mixture was transformed into KCM competent DH5*α E. coli* cells and plated on LB/agar supplemented with the appropriate antibiotic. Colonies were screened using primers Pxyl-for Thanbichler, *et al.* [169] and M13-for[169] using DreamTaq PCR with a 5 minute extension time. The first generation CckA-FRET biosensor contained EYFP that was joined to the *cckA* residue 69 using a GGSGSGSS linker (in primer) and to CckA residue 70 using codons for linker GGSGSGSS linker. CckA residue 691 was joined using codons for SNVTRHRSAT.

Site-Directed Mutagenesis (SDM): Site-directed mutagenesis was performed to generate point mutants that alter CckA function. Each reaction was performed at a 10 ng scale using pMT383 as a template. KOD PCR reactions were performed using the manufacturer's protocol with a 10-minute extension time. Reactions were DpnI treated for 1 hour at 37 °C followed by 80 °C for 5 minutes for enzyme inactivation. 20 µL of reaction were transformed into KCM competent DH5*α E. coli* competent cells. Colonies were isolated, grown, and DNA was isolated by miniprep. Plasmids were sequenced to determine correct mutation. Plasmids were then used as templates for PCR product amplification for Gibson assembly reactions.

2.6 Tables

Table 2–1 Plasmids utilized in this study.

Name	Description	Reference/Addgene #
pSWD95	2nd Gen CckA-FRET biosensor	This work
pSWD155	DivL overexpression plasmid	This work
pSWD156	DivL A601L overexpression plasmid	This work
pSWD95Y514D	CckA-FRET Y514D Mutant sensor	This work
pSWD95D293A	CckA-FRET D293A Mutant sensor	This work
pSWD94	PopZ overexpression plasmid	This work

pSWD109	2nd Gen CckA 183/184 FRET Sensor	This work
pSWD110	2nd Gen CckA 192/193 FRET Sensor	This work
pSWD111	2nd Gen CckA 193/194 FRET Sensor	This work
pWSC10011	1st Gen CckA 69/70 FRET Sensor	This work
pWSC10012	1st Gen CckA 91/92 FRET Sensor	This work
pWSC10013	1st Gen CckA N-terminal FRET Sensor	This work
pSWD55	Short Fibronectin FRET Standard	This work
pSWD56	Long Fibronectin FRET Standard	This work
pSWD275	mRuby3 Intermolecular Sensor	This work
pSWD276	mClover3 Intermolecular Sensor	This work
pSWD14	mClover3/mRuby3	Bajar, *et al.* [142], Addgene# 74252
pSWD63	cckA::cckA-mClover3	This work
pMT383	CckA template	Shapiro Lab
pXCFPC-6	Xylose inducible Vector	Thanbichler, *et al.* [169]
pVMCS-1	Vanillate inducible Vector	Thanbichler, *et al.* [169]
pBVMCS-2	Vanillate inducible high copy plasmid	Thanbichler, *et al.* [169]
pXYFPC-1	Xylose inducible Vector	Thanbichler, *et al.* [169]
pXCFPC-2	Xylose inducible Vector	Thanbichler, *et al.* [169]
FN_7-8_FN_10	Fibronectin Gene Block	Ohashi, *et al.* [144]

Table 2–2 Gibson assembly of plasmids for this study.

Plasmid, Description	**Insert Description**	**Forward Primer**	**Reverse Primer**	**Template**	**Screening primers**
pSWD95 CckA-FRET biosensor	cckA_1-182	SWD160	SWD305	pMT383	Pxyl-for Thanbichler, *et al.* [169], M13-for[169]
	mClover3	SWD306	SWD307	pSWD14	
	cckA_183-691	SWD308	SWD309	pMT383	
	mRuby3	SWD310	SWD311	pSWD14	
	pXCFPC6, Digested with NheI and NdeI	n/a	n/a	pXCFPC-6	
pSWD155 DivL overexpression	pVMCS-1	SWD485	SWD486	pVMCS-1	Pvan-for[169], M13-for
	DivL	SWD487	SWD488	divL	
pSWD156 DivLA601L overexpression	pVMCS-1	SWD489	SWD486	pVMCS-1	Pvan-for[169], M13-for
	DivL1-600	SWD487	SWD490	divL	
	DivL602-769	SWD491	SWD488	divL	

pSWD95Y514D CckA Y514D sensor	cckA_1-182	SWD160	SWD305	pMT383	Pvan-for[169], M13-for
	mClover3	SWD306	SWD307	pSWD14	
	cckA_183-691(Y514D)	SWD308	SWD309	pMT383(Y514D)	
	mRuby3	SWD310	SWD311	pSWD14	
	pXCFPC6, Digested with NheI and NdeI	n/a	n/a	pXCFPC-6	
pSWD95D293A D293A sensor	cckA_1-182	SWD160	SWD305	pMT383	Pxyl-for[169] and M13-for[169]
	mClover3	SWD306	SWD307	pSWD14	
	cckA_183-691(D293A)	SWD308	SWD309	pMT383(D293A)	
	mRuby3	SWD310	SWD311	pSWD14	
	pXCFPC-6, digested with NheI and NdeI	n/a	n/a	pXCFPC-6	
pSWD94 PopZ overexpression	popZ	SWD303	SWD304	popZ	Pvan-for[169], M13-for
	pBVMCS-2, digested with NdeI_FastAP			pBVMCS-2	
pSWD109 CckA 183/184 FRET Sensor	cckA_1-183	SWD357	SWD358	pMT383	Pxyl-for and M13-for
	mClover3	SWD213	SWD359	pSWD14	
	cckA_184-691	SWD319	SWD360	pMT383	
	mRuby3	SWD361	SWD189	pSWD14	
	pXCFPC-6, digested with SacI and NdeI	n/a	n/a	pXCFPC-6	
pSWD110 CckA 192/193 FRET Sensor	cckA_1-192	SWD357	SWD362	pMT383	Pxyl-for and M13-for
	mClover3	SWD213	SWD323	pSWD14	
	cckA_193-691	SWD324	SWD348	pMT383	
	mRuby3	SWD294	SWD189	pSWD14	
	pXCFPC6 digested with SacI and NdeI	n/a	n/a	pXCFPC-6	
pSWD111 CckA 193/194 FRET Sensor	cckA_1-193	SWD357	SWD325	pMT383	Pxyl-for and M13-for
	mClover3	SWD213	SWD363	pSWD14	
	cckA_194-691	SWD327	SWD348	pMT383	
	mRuby3	SWD294	SWD189	pSWD14	
	pXCFPC-6_SacI_NdeI	n/a	n/a	pXCFPC-6	

pWSC10011 CckA 69/70 FRET Sensor	cckA_1-69	WSC10026	WSC10027	pMT383	Pxyl-for and M13-for
	EYFP	WSC10028	WSC10029	pXYFPC-1	
	cckA_70-691	WSC10030	WSC10031	pMT383	
	pXCFPC-2_EcoRI	n/a	n/a	pXCFPC-2	
pWSC10012 CckA 91/92 FRET Sensor	cckA_1-91	WSC10026	WSC10032	pMT383	Pxyl-for and M13-for
	EYFP	WSC10028	WSC10033	pXYFPC-1	
	CckA	WSC10034	WSC10035	pMT383	
	pXCFPC-2_EcoRI	n/a	n/a	pXCFPC-2	
pWSC10013 CckA N-terminal FRET Sensor	EYFP	WSC10036	WSC10037	pXYFPC-1	Pxyl-for and M13-for
	cckA_1-691	WSC10038	WSC10031	pMT383	
	pXCFPC-2_EcoRI	n/a	n/a	pXCFPC-2	
pSWD55 Short FRET Standard	mClover3	SWD184	SWD185	pSWD14	Pxyl-for and M13-for
	FN_10	SWD186	SWD187	FN_7-8_FN_10	
	mRuby3	SWD188	SWD189	pSWD14	
	pXCFPC-6_NheI_SacI	n/a	n/a	pXCFPC-6	
pSWD56 Long FRET Standard	mClover3	SWD184	SWD190	pSWD14	Pxyl-for and M13-for
	FN_7-8	SWD191	SWD192	FN_7-8_FN_10	
	mRuby3	SWD193	SWD189	pSWD14	
	pXCFPC-6_NheI_SacI	n/a	n/a	pXCFPC-6	
pSWD275 CckA mRuby3 intermolecular	CckA	SWD160	SWD309	pMT383	Pxyl-for and M13-for
	mRuby3	SWD361	SWD523	pSWD14	
	flagtag	SWD542	SWD528	flagtag	
	pXCFPC-6_NdeI_NheI	n/a	n/a	pXCFPC-6	
pSWD276 Ccka mClover3 intermolecular	CckA(1-182)	SWD818	SWD305	pMT383	Pvanl-for and M13-for
	mClover3	SWD306	SWD307	pSWD14	
	CckA(183-691)	SWD308	SWD815	pMT383	
	flagtag	SWD816	SWD528	flagtag	
	pVCFPC-1_NdeI_NheI	n/a	n/a	pVCFPC-1	

Table 2–3 Site directed mutagenesis primers for introduction of CckA point mutations.

Template	**Mutation**	**Forward Primer**	**Reverse Primer**	**Annealing Temperature (°C)**

pMT383	Y514D	nSWD98	nSWD99	68
pMT383	D293A	nSWD104	nSWD105	65

Table 2–4 DNA primers utilized in this study.

Name	Sequence (5'-3')
SWD160	CGCTCGAGTTTTGGGGAGACGACCATATGGCCGACTTGCAGCTCCAG
SWD184	ATATGCATGGTACCTTAAGATCTCGAATGAGCAAGGGCGAGGAGC
SWD185	GGACGTCCGACACGCTCACCATCGGATCTTCGCCG
SWD186	TCCGATGGTGAGCGTGTCGGACGTCCCGCGC
SWD187	GCTCTTCGCCCTTAGAGGTGCGATAGTTGATGGAGATCGGC
SWD188	CCATCAACTATCGCACCTCTAAGGGCGAAGAGCTGATCAAGGA
SWD189	ACTAGTGGATCCCCCGGGCTGCAGCTTTACTTGTACAGCTCGTCCATG CCACCA
SWD190	GGGGCGACAGCGGGCTCACCATCGGATCTTCGCCG
SWD191	TCCGATGGTGAGCCCGCTGTCGCCCCCCACC
SWD192	CTTCGCCCTTAGAGGTCTTTTGGCGCCCGCG
SWD193	GGGCGCCAAAAGACCTCTAAGGGCGAAGAGCTGATCAAGGA
SWD213	CCGGTCGGCCACCAGCAAGGGCGAGGAGCTGTTCACC
SWD294	CCGGTCGGCCACCTCTAAGGGCGAAGAGCTGATCAAGGA
SWD303	CGAGGAAACGCATATGTCCGATCAGTCTCAAGAACCTACAATGG
SWD304	GGCCCGTTTTCATTTAGGCGCCGCGTCCCCG
SWD305	GCGTAACGTTCGACGACGCGTCTTCCACAACCGG
SWD306	GGAAGACGCGTCGTCGAACGTTACGCGTCACCGG
SWD307	CCTTGCTCATCTCGGTGGCCGACCGGTGACG
SWD308	CCGGTCGGCCACCGAGATGAGCAAGGGCGAGGAGC
SWD309	ACCGGGGCCGGGCTCACCATCGGATCTTCGCCG
SWD310	GATCCGATGGTGAGCCCGGCCCCGGTCGCCGAG
SWD311	CGTAACGTTCGACGCCGCCTGCAGCTGCTG
SWD319	CGAAGATCCGATGGTGAGCGCCCCGGTCGCCGAGCGC
SWD323	GCTGGGTGGGCTCACCATCGGATCTTCGCCGC
SWD324	CGAAGATCCGATGGTGAGCCCACCCAGCTCGCTGGACGC
SWD325	CCTCGCCCTTGCTGGTGGCCGACCGGTGACGCGTAACGTTCGATGGC GGGGCGGCGCGCTC
SWD327	CGAAGATCCGATGGTGAGCCCCAGCTCGCTGGACGCC
SWD348	CTTCGCCCTTAGAGGTGGCCGACCGGTGACGCGTAACGTTCGACGCC GCCTGCAGCTGCTG

SWD357	ATATGCATGGTACCTTAAGATCTCGAATGGCCGACTTGCAGCTCCAGG
SWD358	CCTCGCCCTTGCTGGTGGCCGACCGGTGACGCGTAACGTTCGACGGCGACGCGTCTTCCACAACC
SWD359	ACCGGGGCGCTCACCATCGGATCTTCGCCGC
SWD360	TTCGCCCTTAGAGGTGGCCGACCGGTGACGCGTAACGTTCGACGCCGCCTGCAGCTGCTGC
SWD361	ACCGGTCGGCCACCTCTAAGGGCGAAGAGCTGATCAAGGA
SWD362	CCTCGCCCTTGCTGGTGGCCGACCGGTGACGCGTAACGTTCGACGGGGCGGCGCGCTCGGC
SWD363	CGAGCTGGGGCTCACCATCGGATCTTCGCCGC
SWD485	GCCCGAACTCGGCTTCTAGCTCTTAAGATCTACGTACCGGTGCTAGCTG
SWD486	CGTACGAAGTCATCTCACCACGTGGTACCTCGAGAATTCATATGC
SWD487	GGTACCACGTGGTGAGATGACTTCGTACGACCTGATCCTCGCG
SWD488	CGTAGATCTTAAGAGCTAGAAGCCGAGTTCGGGCTGC
SWD489	CGAACTCGGCTTCTAGCTCTTAAGATCTACGTACCGGTGCTAGCTG
SWD490	CGGCGTCGATCTGCAGCATGTCCAGCACGTCGTCGATCG
SWD491	GCTGGACATGCTGCAGATCGACGCCGGCGAAATGG
SWD523	CGTGGTCCTTGTAGTCCTTGTACAGCTCGTCCATGCCACC
SWD528	GAACTAGTGGATCCCCCGGGCTGCAGCTTCACTTATCGTCGTCGTCCTTG
SWD542	GGACGAGCTGTACAAGGACTACAAGGACCACGACGGC
SWD818	CCGAACCACGATGCGAGGAAACGCATATGGCCGACTTGCAGCTCCAGG
SWD815	GTCCTTGTAGTCCGCCGCCTGCAGCTGCTGCTTGACG
SWD816	AGCTGCAGGCGGCGGACTACAAGGACCACGACGG
WSC10026	CCTTAAGATCTCGAGCTCCGGAGAATATGGCCGACTTGCAGCTC
WSC10027	CCTTGCTCACCATCGAGCTCCCGCTACCACTGCCACCAATGGCGACAAGGCCCAAC
WSC10028	TAGCGGGAGCTCGATGGTGAGCAAGGGCGAGG
WSC10029	GCTGAGCCGCGCGAGCTCCCGCTACCACTGCCACCCTTGTACAGCTCGTCCATGC
WSC10030	GGTAGCGGGAGCTCGCGCGGCTCAGCGCTTTCC
WSC10031	GCCGACCGGTGACGCGTAACGTTCGACGCCGCCTGCAGCTGCTG
WSC10032	CCTTGCTCACCATCGAGCTCCCGCTACCACTGCCACCCTCGGCCAGCGCCTCGATG

WSC10033	AGGGCGGCCGGCGAGCTCCCGCTACCACTGCCACCCTTGTACAGCTC GTCCATGC
WSC10034	GGTAGCGGGAGCTCGCCGGCCGCCCTGGCCGCC
WSC10035	GCCGACCGGTGACGCGTAACGTTCGACGCCGCCTGCAGCTGCTGC
WSC10036	CCTTAAGATCTCGAGCTCCGGAGAATATGGTGAGCAAGGGCGAGG
WSC10037	GCAAGTCGGCCATCGAGCTCCCGCTACCACTGCCACCCTTGTACAGC TCGTCCATGC
WSC10038	TAGCGGGAGCTCGATGGCCGACTTGCAGCTC
nSWD084	GCCGCCGACCTCCCGCGCAAGCTCTTG
nSWD085	CAAGAGCTTGCGCGGGAGGTCGGCGGC
nSWD086	CCAATCCGGCGCCGACCACGATGAC
nSWD087	GTCATCGTGGTCGGCGCCGGATTGG
nSWD088	CTGCAGCTGTCCCGCGCCCAGAAGATG
nSWD089	CATCTTCTGGGCGCGGGACAGCTGCAG
nSWD090	GAGGTCTTGCTGTGCCGCCTGCTGC
nSWD091	GCAGCAGGCGGCACAGCAAGACCTC
Pxyl-for	CCCACATGTTAGCGCTACCAAGTGC
M13-for	GCCAGGGTTTTCCCAGTCACGA
Pvan-for	GACGTCCGTTTGATTACGATCAAGATTGG
RecUni-1	ATGCCGTTTGTGATGGCTTCCATGTCG
RecVan-2	CAGCCTTGGCCACGGTTTCGGTACC
RecXyl-2	TCTTCCGGCAGGAATTCACTCACGCC
nSWD035	CCAAGGTCATCAGCTTCATCC
nSWD036	CGCTGGTGCGTAATCCG

Table 2–5 Strains used in this study.

Name	**Genotype**	**Plasmid**	**Reference**
WSC1119	*E. coli*, DH5*α*	none	Novagen
WSC1411	*C. crescentus*, NA1000	none	Lucy Shapiro
WSC1412	*E. coli*, DH5*α*	pSWD95	This work
WSC1413	NA1000	pSWD95	This work
WSC1414	NA1000, *cckA::gent*	pSWD95	This work
WSC1415	*E. coli*, DH5*α*	pSWD155	This work
WSC1416	NA1000	pSWD155, pSWD95	This work
WSC1417	*E. coli*, DH5*α*	pSWD156	This work
WSC1418	NA1000	pSWD156, pSWD95	This work
WSC1419	*C. crescentus*, cdg^0	none	Abel, *et al.* [118]

WSC1420	cdg^0	pSWD95	This work
WSC1421	cdg^0	pSWD95, pSWD156	This work
WSC1422	*E. coli*, DH5*α*	pSWD94	This work
WSC1423	NA1000	pSWD94, pSWD95	This work
WSC1424	NA1000, *popZ::spec/strep*	none	Bowman, *et al.* [132]
WSC1425	NA1000, *popZ::spec/strep*	pSWD95	This work
WSC1426	*E. coli*, DH5*α*	pSWD95D293A	This work
WSC1427	NA1000	pSWD95D293A	This work
WSC1428	cdg^0	pSWD95D293A	This work
WSC1429	*E. coli*, DH5*α*	pSWD95Y514D	This work
WSC1430	NA1000	pSWD95Y514D	This work
WSC1431	cdg^0	pSWD95Y514D	This work
WSC1432	*E. coli*, DH5*α*	pSWD63	This work
WSC1433	NA1000, *cckA::cckA-mClover3*	pSWD63	This work
WSC1434	*E. coli*, DH5*α*	pWSC10011	This work
WSC1435	NA1000	pWSC10011	This work
WSC1436	*E. coli*, DH5*α*	pWSC10012	This work
WSC1437	NA1000	pWSC10012	This work
WSC1438	*E. coli*, DH5*α*	pWSC10013	This work
WSC1439	NA1000	pWSC10013	This work
WSC1440	*E. coli*, DH5*α*	pSWD109	This work
WSC1441	NA1000	pSWD109	This work
WSC1442	*E. coli*, DH5*α*	pSWD110	This work
WSC1443	NA1000	pSWD110	This work
WSC1444	*E. coli*, DH5*α*	pSWD111	This work
WSC1445	NA1000	pSWD111	This work
WSC1446	*E. coli*, DH5*α*	pSWD55	This work
WSC1447	NA1000	pSWD55	This work
WSC1448	*E. coli*, DH5*α*	pSWD56	This work
WSC1449	NA1000	pSWD56	This work
WSC1450	*E. coli*, DH5*α*	pSWD14	This work
WSC1027	*E. coli*, DH5*α*	pWSC1027	This work
WSC1149	NA1000, *cckA::gent*	pMR10cckAover	Jacobs, *et al.* [107]
WSC1451	*E. coli*, DH5*α*	pXCFPC-6	Thanbichler, *et al.* [169]

WSC1452	*E. coli*, DH5α	pVMCS-1	Thanbichler, *et al.* [169]
WSC1453	*E. coli*, DH5α	pBVMCS-2	Thanbichler, *et al.* [169]
WSC1454	*E. coli*, DH5α	pXYFPC-1	Thanbichler, *et al.* [169]
WSC1455	*E. coli*, DH5α	pXCFPC-2	Thanbichler, *et al.* [169]
WSC1459	*E. coli*, DH5α	pSWD275	This work
WSC1460	*E. coli*, DH5α	pSWD276	This work
WSC1461	NA1000	pSWD275	This work
WSC1462	NA1000	pSWD276	This work
WSC1463	NA1000	pSWD275,pSWD276	This work

3.0 Determining DivL/CckA domain interactions using LZ and FRET technologies

3.1 Introduction

Bacteria have evolved two-component systems in order to regulate processes with spatial and temporal control in contexts like biofilm formation and chemotaxis (EnvZ/OmpR), virulence (GacS/RetS), and cell division (CckA).[106,107,111,154] Two-component systems consist of a histidine kinase that senses signals and converts them to phosphorylation events upon a response regulator that is able to change activity, commonly through regulation of gene transcription[170,171]. Histidine kinases have evolved to maintain a conserved catalytic domain for autophosphorylation and phosphotransfer (DHp/CA) that maintains specificity with downstream partners.[6,108,109] Where diversity commonly occurs is within the signaling domains of histidine kinases. PAS, HAMP, and GAF domains are all common as single domains, or in combinations that facilitate integration of a number of different signal inputs.[20,28,59,172] Small molecule ligands, oligomerization, temperature, pH, and protein-protein interactions are all different types of signals that can be sensed by these domains. When signals bind the domains, the binding event results in a conformational change that propagates from the signaling domains to the catalytic domain.[21] Because histidine kinases often have more than one domain, it can be difficult to understand how signals are integrated. To add to this complexity, a newer group of signaling proteins known as pseudokinases have recently been shown to act as mediators of cell-signaling cross-talk.[71,80,124]

3.1.1 The pseudokinase DivL transmits signal in a reverse manner

Pseudokinases share homology with histidine kinases, but lack the phosphorylatable histidine within the catalytic domain. One example of a pseudokinase is DivL in the alphaproteobacterium *C. crescentus*.[71,94,124] DivL is transmembrane tethered and contains four signaling domains (one DUF and three PAS) followed by the DHp/CA domain without the catalytic histidine residue (Figure 3–1A-C).

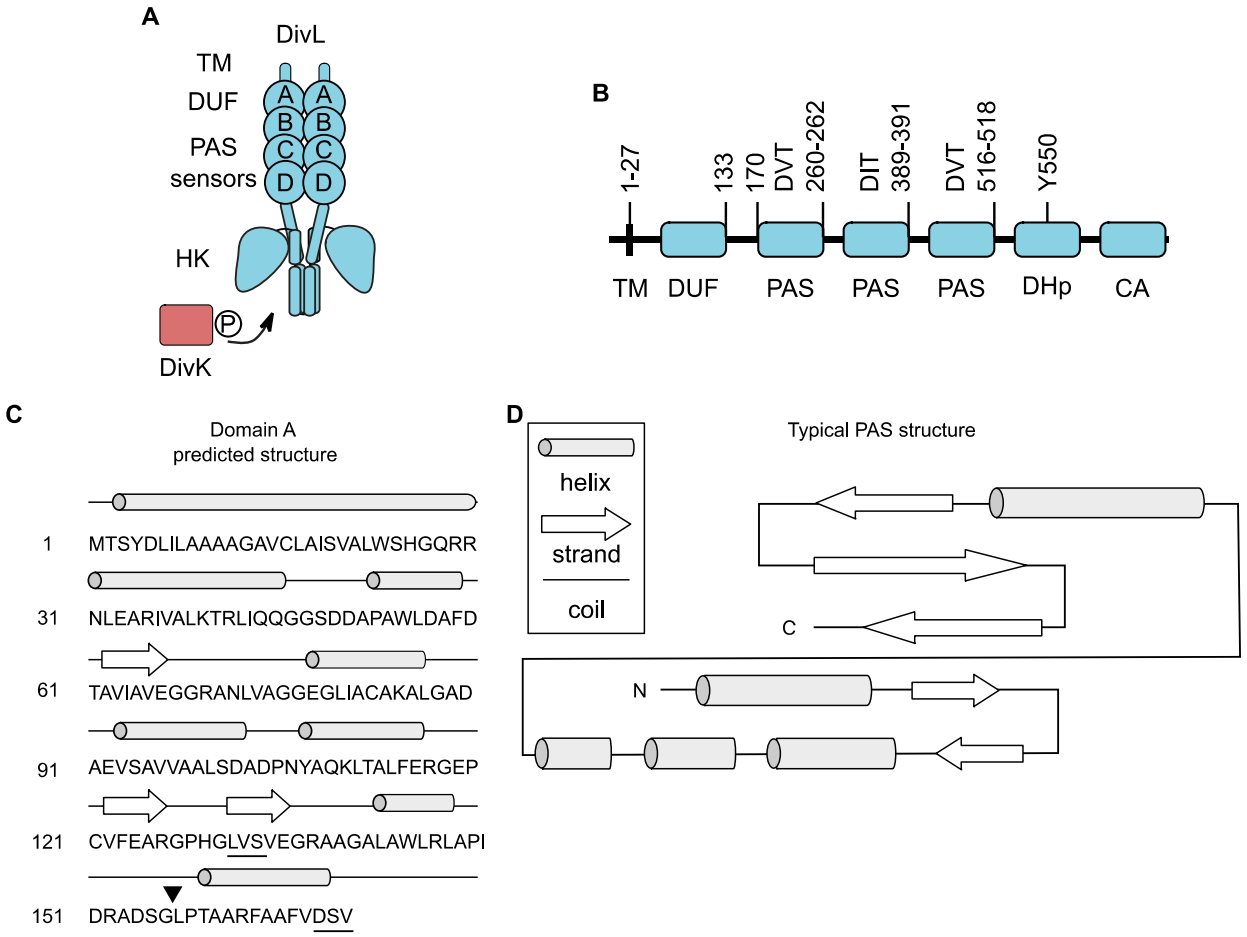

Figure 3–1 DivL contains a DUF at the N-terminus and three PAS signaling domains.
A) DivL is transmembrane tethered and contains four signaling domains, Domain A (DUF), PAS B, PAS C, and PAS D. It if followed by the catalytic domain which no can no longer autophosphorylate and instead binds to DivK~P. B) Detailed breakdown of cutoffs for each domain. Note that Domain A (DUF) does not contain the conserved DITE motif. Y550 would be the site of phosphorylation before substituting tryrosine. C) Domain A (DUF) predicted structure using secondary structure prediction software. D) Typical PAS structure. Key represents both C and D. Topology of PAS domains adapted from Moglich, *et al. Cell Struct. Funct.* **2009**, 17(10), 1282-1294.

DivL is essential in *C. crescentus'* and is important for maintaining asymmetric cell division. It's role in signaling is to act as a mediator between two orthogonal signaling pathways, DivJ/PleC and CckA. DivL is recruited to the new cell pole by the scaffolding protein PopZ, which also recruits CckA.[134,173] In order to accomplish this, DivL has evolved to no longer transmit sensory signals from its sensory domains to its catalytic domains. DHp and CA domains of DivL are now involved in binding to phosphorylated DivK (DivK~P), the RR of both HKs PleC and DivJ (Figure 3–2).[33,71,94]

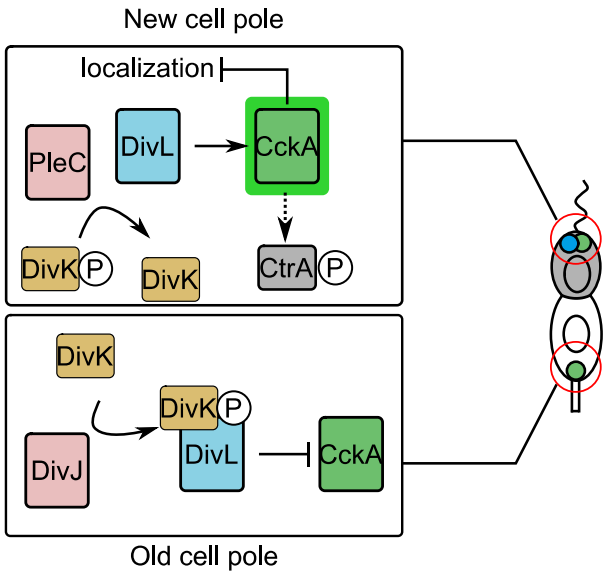

Figure 3–2 DivL/DivK~P binding dictates CckA kinase activity.
At the new cell pole, the HK PleC dephosphorylates DivK~P. Unphosphorylated DivK cannot bind DivL, resulting in activation of the CckA-CtrA pathway. At the old cell pole, the HK DivJ phosphorylates DivK to generate DivK~P, which binds DivL. DivL bound to DivK~P is unable to activate the CckA-CtrA pathway.

DivL does not bind unphosphorylated DivK (Figure 3–1A). A mutant of DivL, DivLA601L, that no longer binds phosphorylated DivK activates CckA kinase activity 5-fold higher than DivL.[33] In order to bind DivK~P, DivL requires at least two of its sensory domains.[71] In addition to being required for binding the DivK~P, the sensory domains are used to transmit signal to the HK CckA.[124] Former lab member Kim Kowallis established that DivL uses its sensory

domains to transmit signal in a reverse signaling manner (Figure 2–11).[124] This reverse signaling requires only the sensory domains in order to transmit signal.

Kim Kowallis also used leucine zippers (LZs), discussed in Chapter 1, to establish that this reverse signaling is dependent not just on the domains themselves, but also the confirmational state they were in. The LZs were fused to the α-helical region between PAS D and the DHp. The PAS D DITE motif was required for this reverse signaling to occur. By deleting, one residue at a time, from the helix between PAS D and DHp, she was able to modulate the confirmation of DivL. This resulted in changes in swarm size in a swarm motility assay with a periodic trend. To follow up on these changes in swarm size, she expressed two DivL leucine zipper (DivL-LZ) fusions in a strain that does not express DivK. DivL531-LZ successfully rescued this strain indicating it mimicked a DivK~P bound confirmation. DivL534-LZ induced a more severe phenotype in this strain due to being locked in a confirmation similar to free DivL, resulting in likely overactivation of the CckA-CtrA pathway.

What remained to be understood is how DivL is able to activate or deactivate CckA. Due to the reverse signaling manner of DivL, DivL/CckA interactions are likely mediated through the sensory domains of both proteins. While both Domain A in DivL and PAS A in CckA are unlikely to be involved in signal transduction due to lack of DITE motifs, that left PAS B in CckA and PAS B-D in DivL.

DivL does not activate CckA kinase activity *in vitro* in solution or on the membrane-like architecture of a liposome while the DivLA601L mutant is still able to activate kinase activity on liposomes and in solution.[76,113] This difference in activities led to the need to further understand the specific interactions that facilitate DivL-CckA *in vivo* and *in vitro* in order to understand the underlying mechanisms that regulate CckA. To answer these questions we took an approach using

the tools developed in our lab (CckA-FRET biosensor and DivL-LZ) to screen domain deletions of DivL in order to identify the domain interactions responsible for DivL mediation of CckA activity. We then coupled this *in vivo* work with biochemistry to identify how those domains impacted CckA kinase activity *in vitro*.

3.2 Results

3.2.1 Domain A of DivL is required for localization

In order for DivL function at the new cell pole to occur, it needs to be able to accumulate there in sufficient quantities. To answer what domain or domains are required for DivL localization at the new cell pole, we used a DivL domain deletion screen. DivL variants were tagged on the C-terminus with mCherry and expressed in *C. crescentus* (Figure 3–3A).

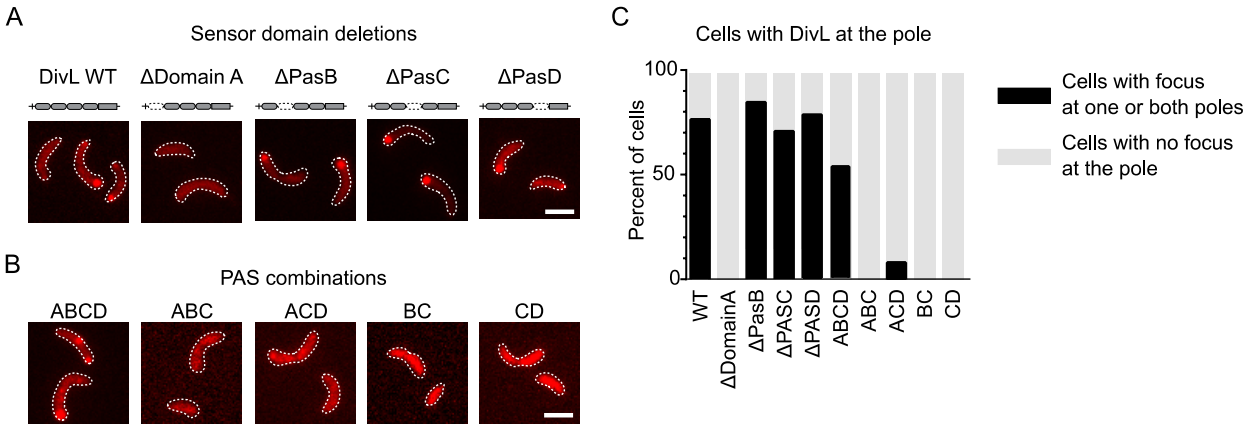

Figure 3–3 Domain A is required, but not sufficient, for DivL inducible localization.
The variants in A-B were induced from the chromosomal xylose promoter in M2G supplemented with 0.03% xylose for 4 hours. Scale bar denotes 2 μm. A) Fluorescence microscopy was used to visualize the subcellular localization of DivL-mCherry domain deletion variants and B) A panel of PAS domain combinations. C) Quantification of the percent of cells with DivL localization at the cell pole. N>36 cells for each condition. Experiment and figure provided by Kim Kowallis.

DivL wild-type forms foci at one or both poles in ~75% of cells. Out of the domain deletions, only the deletion of Domain A results in a full loss of localization at one or both cell poles (Figure 3–3A,C). To test whether only the domains were required for localization, we deleted the DHp/CA domain (HK domain) from DivL. We expressed combinations of the sensory domains A-D and observed that the full A-D was able to localize (Figure 3–3B,C). Deletion of any of the domains resulted in a complete loss of localization, with ACD being the exception (~10% localization, Figure 3–3C). This result identified that the HK domain of DivL may also be required for DivL to localize in the absence of Domain A. To answer this, we constructed minimal versions of DivL Domain A and HK domain. Domain A alone, or combined with either the transmembrane tether or HK domain, was unable to form foci (Figure 3–4A,C).

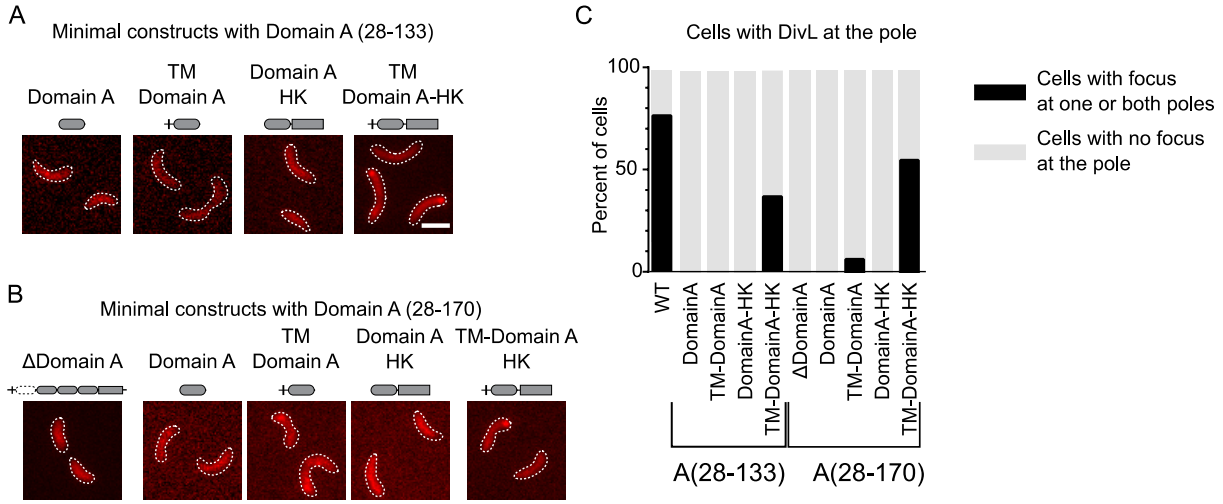

Figure 3–4 TM-Domain A-HK is the minimal DivL inducible localization form.
The variants in A-B were induced from the chromosomal xylose promoter in M2G supplemented with 0.03% xylose for 4 hours. Scale bar denotes 2 μm. A) a panel of potential minimal localization constructs in *C. crescentus* using Domain A (28-133). B) A panel of potential minimal localization constructs using Domain A (28-170). C) Quantification of the percent of cells with DivL localization at the cell pole. N>36 cells.

All three together (TM-Domain A-HK) were able to form foci at the cell poles, though reduced from wild-type levels (Figure 3–4A,C). We also tested a larger variant of Domain A, 28-170, which is predicted to contain a larger helical region in order to identify if this influenced localization. This construction of Domain A showed low levels of foci formation with only the

transmembrane tether (TM-Domain A) and higher levels for TM-Domain A-HK than Domain A (28-133) (Figure 3–4B,C). These results point towards a combination of the transmembrane tether, Domain A, and the HK domain being required for localization. Additionally, PAS B-D may be able to replicate some of the HK domain localization functions, as evidenced by the localization of ABCD in Figure 3–3B,C. This points at redundancies in localization mechanisms for DivL and likely a cooperative process for localizing DivL at the new cell pole.

3.2.2 PodJ and PopZ can both recruit DivL in *E. coli*

Scaffolding proteins play a major role in cells by localizing proteins in order to increase the speed of cellular processes.[88] An example of this in *C. crescentus* is the polar localization of CckA by PopZ.[134,174] PopZ has also been identified as a scaffold for DivL.[134] In addition to PopZ, the scaffolding protein PodJ also localizes to the new cell pole. To test if Domain A or the HK domain could be scaffolded by PopZ, PodJ, or both we used a heterologous expression system in *E. coli*. By expressing these proteins in *E. coli* we removed other factors related to localization in *C. crescentus* and try to isolate specific domain interactions. We expressed three variants of DivL all labeled with msfGFP: full-length DivL (DivL WT), DivL with the transmembrane tether and Domain A deleted (ΔTMΔDomain A), and Domain A alone (Figure 3–5A).

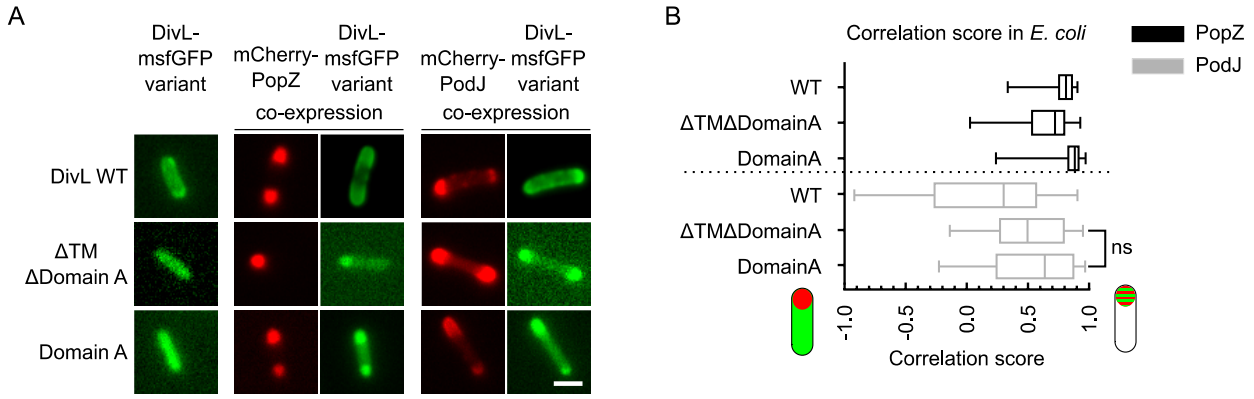

Figure 3–5 DivL is recruited by PodJ and PopZ on arabinose inducible promoters by multiple interactions. DivL variants were induced from the pBAD plasmid with 10 mM arabinose for 2 hours. mCherry-PopZ and mCherry-PodJ were induced from the *lac* promoter with 0.05 mM IPTG for 2 hours. Scale bar denotes 2 μm. A) Heterologous expression of DivL-msfGFP variants with mCherry-PopZ or mCherry-PodJ in *E. coli*. B) Quantification of co-localization between the DivL variants and PopZ or PodJ. A correlation score of +1 indicates complete co-localization and a score of - 1 indicates no co-localization. The center line is the median and the box extends to the 25th and 75th percentiles. The whiskers lie at the minimum and maximum values. Significance was determined using Tukey's multiple comparisons tests. Comparing the three DivL variants combined with the same scaffold have P-value<0.0037 except for the difference between DivL-ΔTM ΔDomain A compared to DivL-Domain A when co-expressed with PodJ. N>72 cells for all samples.

We then coexpressed either mCherry-PopZ or mCherry-PodJ and measured the correlation between protein localization. When the DivL variants were expressed alone, all displayed diffuse patterns (Figure 3–5A). All three DivL variants frequently colocalized with PopZ (Figure 3–5A,B). Upon coexpression with PodJ, all variants displayed some colocalization (Figure 3–5A,B). The localization of ΔTMΔDomain A and Domain A only were not significantly different from wild-type (Figure 3–5B). These results indicate that DivL may have multiple binding sites for PodJ and PopZ, which is consistent with the localization screen in *C. crescentus*.

3.2.3 DivL PAS B and PAS D are required for DivL-mediated regulation of the cell cycle

Once DivL is localized to the cell pole, it must interact in some way with CckA, likely through its sensory domains. To monitor which domains may affect CckA activity, we used a

swarm motility assay to detect changes in the CckA-CtrA pathway. Swarming by *C. crescentus* can be impacted by changes in motility, division, or replication, all processes related to CtrA activity.[175] In this assay, empty vector does not contain a *divL* gene and represents wild-type motility. Expression of DivL variants containing a C-terminal FLAG tag sequence was observed using a western blot with an anti-FLAG antibody (Figure 3–6A).

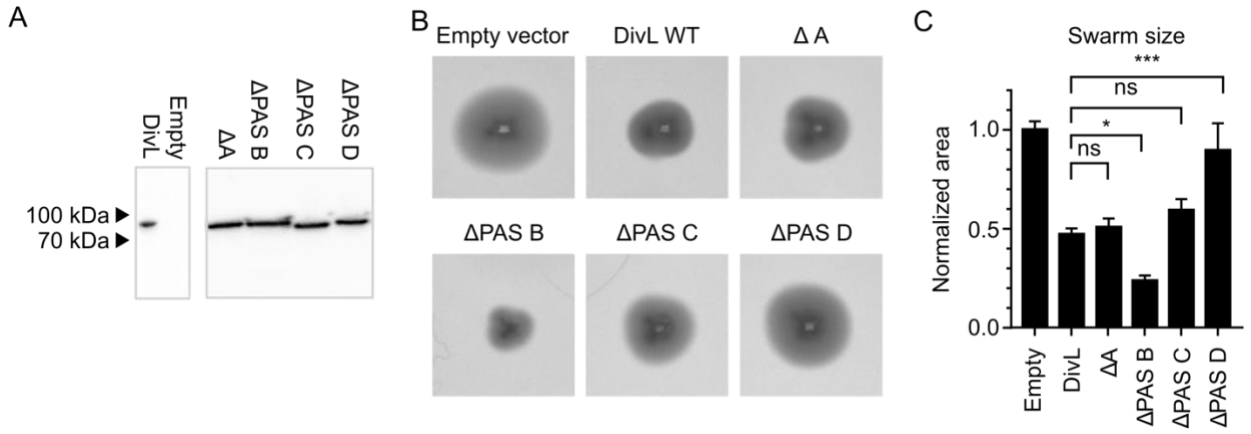

Figure 3–6 DivL's PAS B and PAS D are required for DivL mediated regulation of cell motility.
A) Western blot analysis was performed to confirm expression of DivL variants in the strains used in the PAS domain deletion swarm assays. B) Motility assay of *C. crescentus* strains expressing DivL-FLAG domain deletions. *C. crescentus* were stabbed into 0.3% PYE agar supplemented with 0.3% xylose and incubated at 28ºC for 3 days. C) Quantification of the motility assay of *C. crescentus* strains expressing DivL-FLAG domain deletions.

When DivL is overexpressed compared to wild-type, the swarm size decreases significantly to 47 ± 3% of the empty vector (Figure 3–6B,C). We next evaluated which DivL domains were needed for the DivL mediated reduction in swarm size and overexpressed DivL domain deletion variants individually and measured impact on swarm size. Deletion of Domain A and PAS C did not impact swarm size (Figure 3–6B,C). This indicates that diffuse DivL is still able to regulate swarm size reductions that are mediated by the CckA signaling pathway. Deletion of PAS B resulted in a smaller swarm size 24 ± 3% of the empty vector control (Figure 3–6B,C). PAS D deletion resulted in a larger swarm size 90 ± 1% of the empty vector control (Figure 3–6B,C). The PAS B and PAS D results show that these domains are likely required for interaction with CckA. Deletion of PAS B results in a greater reduction in swarm size, while removal of PAS

D results in loss of swarm size reduction. The ability of DivL to still regulate swarm size without Domain A shows that PAS domains B-D are likely regulating CckA activity. PAS B and PAS D had opposite effects on swarm size indicating they are both involved in CckA regulation, but both may regulate CckA in different ways. Additionally, removal of protein domains could impact the overall folding and structure of DivL, resulting in changes in regulation.

To follow up on this we made mutations to the DITE motifs of PAS B and PAS C (Figure 3–7A). We had previously shown that the DITE motif of PAS D was required for reverse signaling in the swarm plate assay.[124] Both D and T variants were made for PAS B and PAS C independently and expression was monitored by western blot (Figure 3–7B).

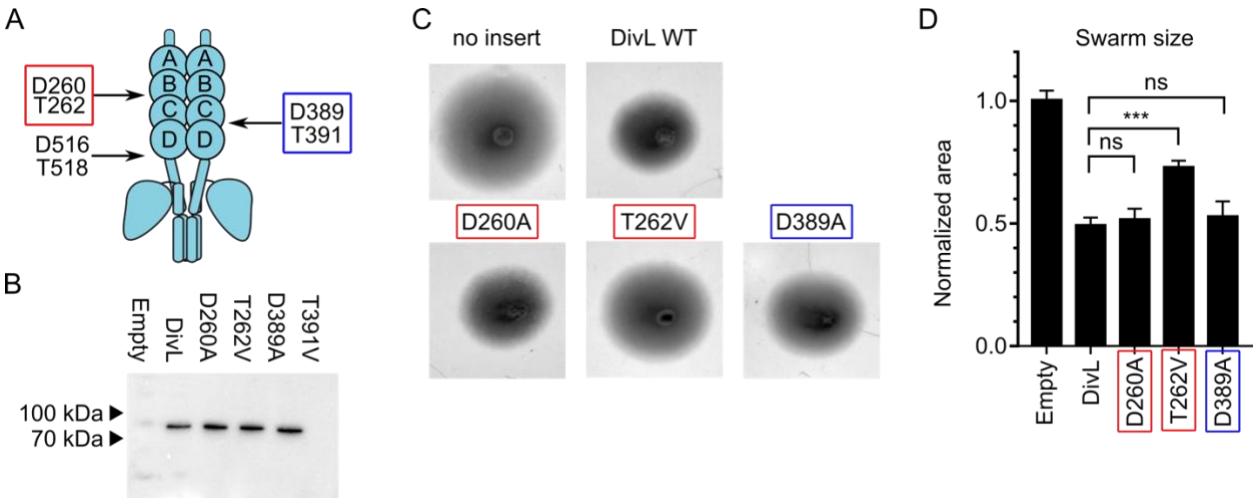

Figure 3–7 An intact PAS B signal transmission motif is required for swarm size reduction.
A) Cartoon of DivL with the signal transmission motif residue numbers labelled. B) Western blot analysis were performed to confirm over- expression of DivL variants in the strains used in the DITE motif mutation swarm assays. C) Motility assay of *C. crescentus* strains expressing DivL-DITE variants. *C. crescentus* were stabbed into 0.3% PYE agar supplemented with 0.3% xylose and incubated at 28ºC for 3 days. (D) Quantification of the motility assay of *C. crescentus* strains expressing DivL-DITE variants. Error bars represent SD (n=3). Significance was determined with a Dunnett's multiple comparisons test by comparing the mean area of each strain to the mean area of DivL-WT (ns: $P>0.05$, *: $P \leq 0.05$, **: $P \leq 0.01$, ***: $P \leq 0.001$).

PAS C T391V variant did not accumulate and was not assayed for swarm size. The T262V mutation to PAS B was able to knockout some of the effect of DivL overexpression on swarm size (Figure 3–7C,D). The PAS C mutant did not disrupt the effect of DivL overexpression (Figure 3–7C,D). These results show that PAS B is required for impact on the CtrA driven swarm phenotype

and requires its signal transduction motif intact. Combined with previous work that showed a similar effect for PAS D, we can point to PAS B and PAS D as the primary domains for regulating swarm size reduction that is likely mediated through CckA as evidenced by change in swarm size.

3.2.4 PAS D is required to mediate CckA-FRET biosensor interaction

Now that we had narrowed down the domains likely to interact with CckA to PAS B and PAS D, we wanted to a more specific approach that could demonstrate the observed swarm size reductions were mediated through CckA. We turned to the CckA-FRET biosensor assay, which increased its FRET signal in response to DivL overexpression (Figure 2–20). We overexpressed domain deletions of DivL in the strain expressing the CckA-FRET biosensor and compared changes in FRET ratio. As a control for sensory domain mediated FRET changes, we used a sensory domain only DivL, DivL-565 and observed no significant difference from DivL overexpression (Figure 3–8A,F).

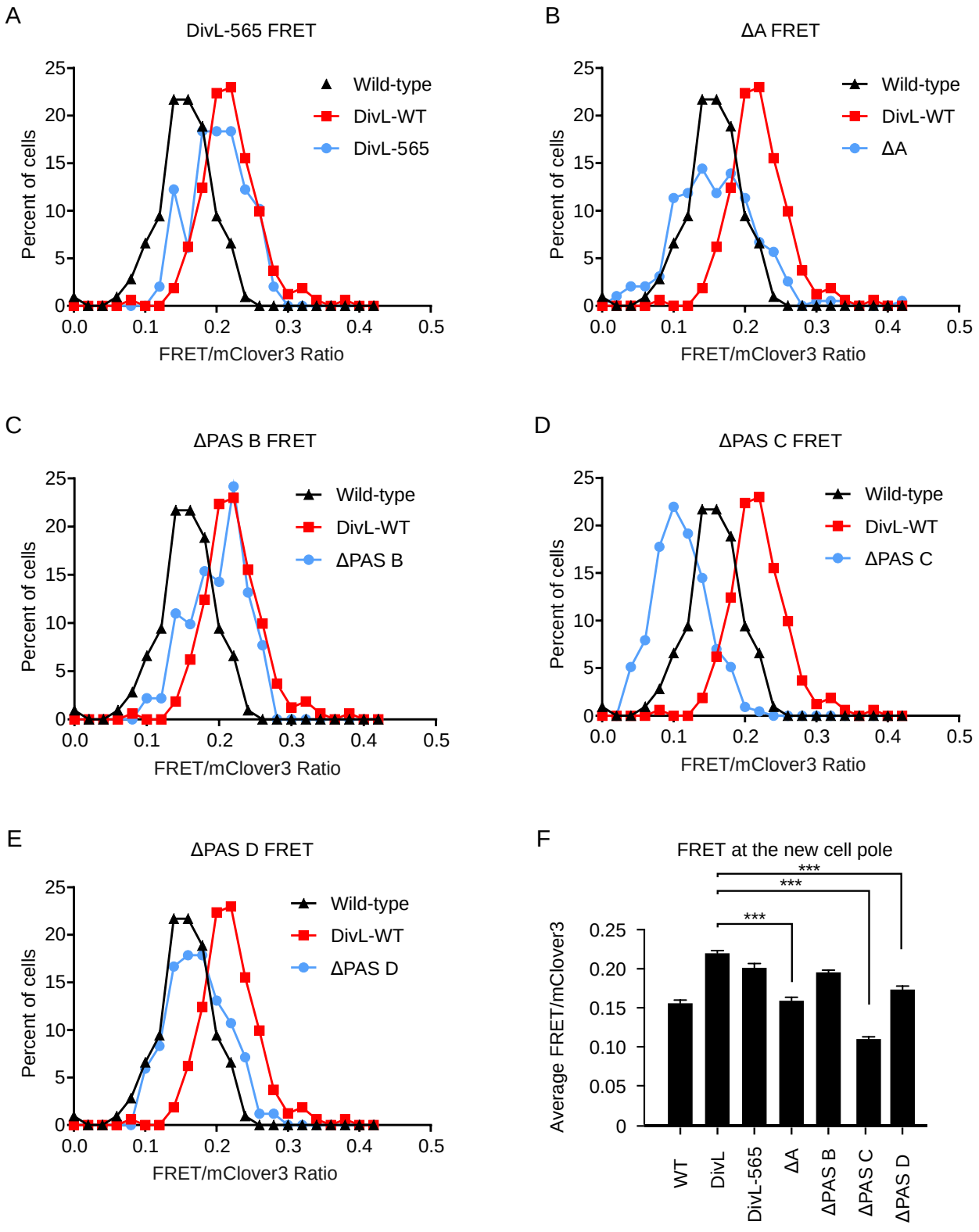

Figure 3–8 PAS A, PAS C, and PAS D regulate the CckA-FRET biosensor conformation.
Cells were grown overnight at 28ºC with medium shaking in M2G containing antibiotics to an OD_{600} of 0.1. Cells were induced with a final concentration of 0.03% xylose and 0.5 mM vanillate. Cells were then grown for 3 hours at 28ºC with medium shaking and imaged on a 1% agarose pad. Imaging and analysis were done using FRET imaging

and analysis conditions (See Methods for details). A)-E) Histograms of the FRET/mClover3 ratio at the new cell pole in N>84 cells. Wild-type *C. crescentus* cells expressed the CckA-FRET biosensor induced with 0.03% xylose and over-expressing the DivL domain deletion variants induced with 0.5 mM vanillate for 3 hours. Fluorescence microscopy was used to visualize the subcellular localization of the CckA-FRET biosensor and to measure FRET intensities. F) Average of the FRET ratio of the cells shown in the histograms in A-E.

These results indicate that the HK domain of DivL is not needed to mediate an impact upon the CckA-FRET biosensor. This result is consistent with past studies that indicate that the CckA-DivL interaction is mediated by sensory domain interactions.[33,76,113,173]

We observed that overexpression of the DivL ΔDomain A variant led to no change in the CckA-FRET biosensor. This is likely due to our measurements only being recorded at the cell pole (Figure 3–8B,F). Domain A deletion in the localization assay did not form foci at the cell poles so the effect of DivL accumulation likely no longer occurs at the cell poles. We next observed that overexpression of DivL ΔPAS B did not result in a significant decrease when compared to DivL (Figure 3–8C,F). In contrast, overexpression of DivL ΔPAS C resulted in a lower average FRET than wild type cells (Figure 3–8D,F). This observed reduction in FRET may mean that DivL ΔPAS C is required to allosterically regulate the CckA/DivL interaction. In agreement with swarm assay observations, deletion of PAS D resulted in the loss of the effect of DivL variant overexpression, resulting a significantly lower average FRET similar to wild type (Figure 3–8,F). These results, combined with the requirement of the DITE motif of PAS D for reverse signaling indicate the PAS D is required for interaction with CckA.

3.2.5 DivL-LZ fusions show periodic trend with CckA-FRET biosensor

The drawback to swarm plate assays is that the swarm size phenotype can be the culmination of replication, motility, and cell length changes. While these are all related to the CckA-CtrA pathway, we wanted to identify if the DivL-LZ fusions could directly impact CckA.

To do this, we used the CckA-FRET biosensor to report on the overexpression of different DivL-LZ fusions (Figure 3–9A).

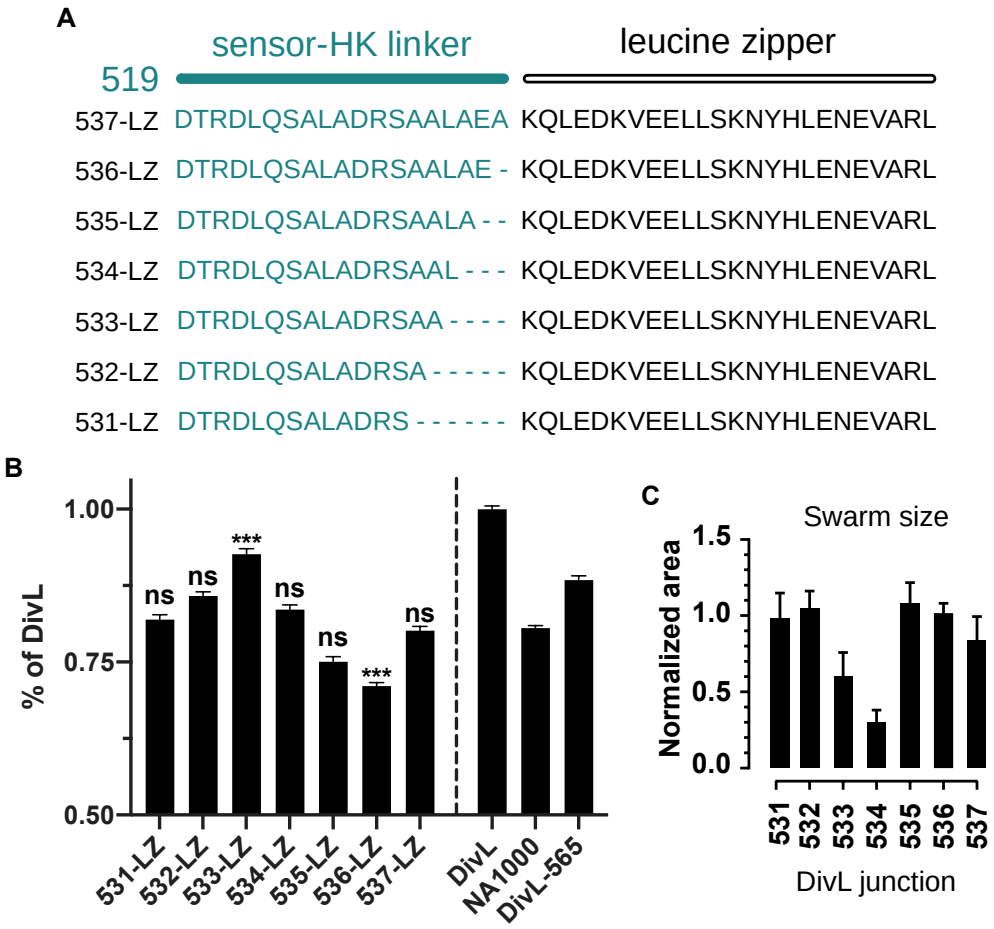

Figure 3–9 DivL-LZ fusions generate periodic trend on CckA-FRET biosensor.
Cells were grown overnight at 28ºC with shaking in M2G containing antibiotics to an OD_{600} of 0.1. Cells were induced with a final concentration of 0.03% xylose and 0.5 mM vanillate. Cells were then grown for 3 hours at 28ºC with shaking and imaged on a 1% agarose pad. Imaging and analysis were done using FRET imaging and analysis conditions (See Methods for details). A) DivL to leucine zipper fusion sites. A residue from DivL was deleted to generate different fusion while the leucine zipper was kept constant. B) Graph of average FRET ratio of the CckA-FRET biosensor at the old cell pole. All measurements were scaled such that DivL overexpression was equal to 1 and all others were represented as a percent of DivL. NA1000 represents no DivL overexpression, DivL-565 is shown as a sensory domain only control. Data for DivL-LZ fusions represents two biological replicates. N>65 for each variant. *** indicates p<0.001 compared to NA1000. C) Analysis of swarm motility assay of *C. crescentus* strains expressing DivL-LZ variants. *C. crescentus* were stabbed into 0.3% PYE agar supplemented with 0.3% xylose and incubated at 28ºC for 3 days. Figure provide by Kim Kowallis.

We imaged cells using the established FRET protocol and measured old cell pole average FRET in predivisional cells. We then scaled the FRET ratios to the overexpression of full-length DivL such that full-length is equivalent to 1.00 (Figure 3–9B). We observed that the DivL-LZ

fusions had a periodic trend similar to the swarm sizes when DivL-LZs were overexpressed (Figure 3–9C). Compared the empty vector, the following DivL LZ fusions displayed little change in observed FRET from the CckA-FRET biosensor: DivL 531-LZ, DivL 534-LZ, DivL 537-LZ. Interestingly, overexpression of DivL 533-LZ exhibited an increase in the observed FRET ratio compared to NA1000, and may suggest a correlation of increased FRET ratio and reduction of swarm size. In the swarm assay, DivL 533-LZ and DivL 534-LZ exhibited reductions in swarm size (Figure 3–9C). However, we observed no change in the FRET sensor upon expression of DivL 534-LZ which produced the smallest swarm size (Figure 3–9C,D).

DivL 535-LZ and DivL 536-LZ displayed decreases in the FRET ratio (Figure 3–9B) but had no change in the swarm assay (Figure 3–9C). Consistent with these observations we also observed that overexpression of DivL ΔPAS C resulted in a lower average FRET than wild type cells. This is a second example of a correlation where reduction in CckA-FRET biosensor (Figure 3–9B) correlates with no changes in swarm size (Figure 3–9C).

While these trends do not match perfectly to the swarm assay trend, this is a key result because this reports directly on the conformational change of CckA due to changes in the conformation of DivL. These observations may indicate that regulation downstream of CckA may be able to overcome the changes that occur in CckA to ultimately lead to no change in swarm size in these experiments. In contrast, it may also suggest that changes in the CckA-FRET biosensor alter the tertiary or quaternary structure CckA, without impacting its function as kinase or phosphatase.

This result also confirms that the DivL/CckA interaction is DivL sensor domain mediated. This coincides well with our observation that certain PAS domains (PAS D) are required for DivL/CckA interactions (Figure 3–6). We plan to conclude this experiment using DivL-537 and

DivL-518 with no leucine zipper fusions in order to control for the activity of the PAS domains when not locked into a particular confirmation. The DivL-565 control used here does contain a sizeable portion of the DHp helical region, that may retain some binding to DivK~P. This expression of DivL-LZ fusions and CckA-FRET biosensor will also be confirmed using western blots to ensure protein accumulation.

3.2.6 DivL/DivK~P binding may be regulated by CckA's RD domain

The DivL/CckA interaction is a direct event for DivL reverse signal propagation. What remains to understand is how does DivL bound to DivK~P impact CckA activity. The DivL/DivK~P complex is an inhibitor of CckA kinase activity.[71,94] What is not well understood is how this occurs. DivL and CckA could always be in a complex where kinase activity is on, but upon binding of DivK~P to DivL, the change in conformation of DivL results in CckA kinase activity turning off. Additionally, DivK~P binding could disrupt the DivL/CckA complex entirely. To answer this we used a fluorescence polarization (FP) assay where purified DivK was labeled with boron-dipyrromethene (BODIPY). Labeled DivK~P was generated by introducing DivK to its kinase DivJ then isolating DivK~P. DivK~P was then mixed with DivL and a change in FP was measured (Figure 3–10A).

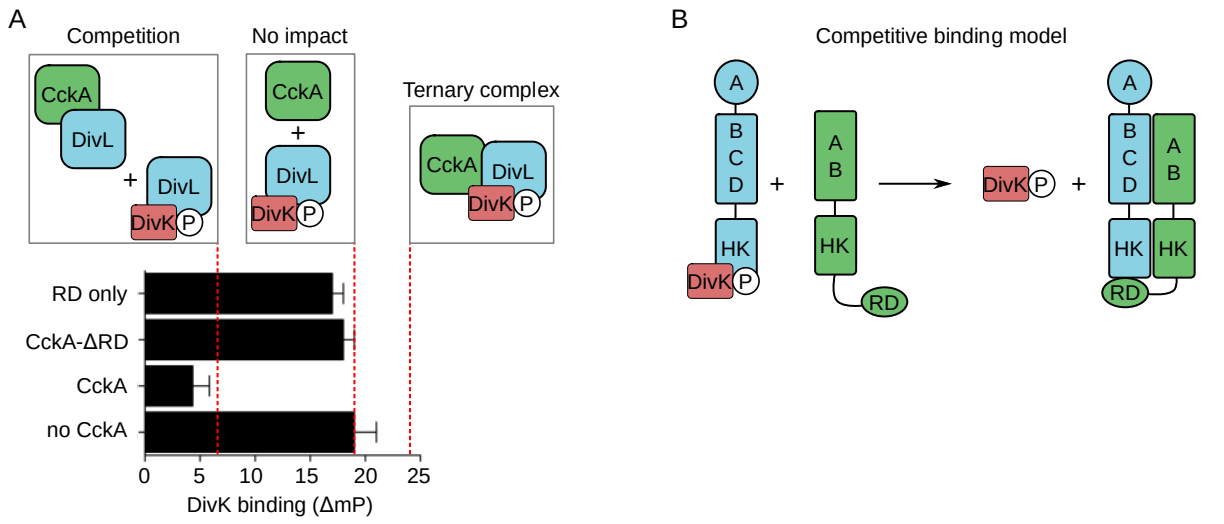

Figure 3–10 CckA disrupts the DivL-DivK~P complex *in vitro*.
A) An FP binding assay determining if DivL binds DivK~P and CckA in a ternary complex or if DivK~P and CckA compete for DivL binding. BODIPY-labelled DivK was phosphorylated by its kinase DivJ and combined with DivL in solution. Each CckA variant was added to the existing mixture and FP was measured. Error bars represent SD (n=3). B) A model showing that the receiver domain is important for the displacement of DivK~P from DivL.

DivK~P was able to bind to DivL (no CckA, Figure 3–10A). Upon addition of CckA to this complex a decrease in fluorescence polarization was measured (Figure 3–10A). Addition of CckA-ΔRD or RD only were not able to disrupt the DivL/DivK~P complex (Figure 3–10A). This experiment points to a model where CckA competes with DivK~P for the RR binding interface. Biologically, this may mean that DivL/DivK~P can in fact bind to CckA and results the formation of DivL/CckA complex which is kinase active. This model is strengthened by the fact that DivLA601L, which cannot bind DivK~P, is a 5-fold activator of CckA kinase activity. DivLA601L is likely in a frequent complex with CckA.[94] Why would the CckA RD domain be involved in DivL binding? We know that the CckA RD domain is required for phosphotransfer to ChpT[114] and the RD domain of CckA is required for maintaining dimerization *in vitro*.[76] If the RD domain is busy binding DivL, how is it able to perform these functions? We will explore this more in the future using DivK mutants that impair binding to DivL (D90G) and or enhance binding to DivL (Q55A) and use FP on the RD domain of CckA.

3.3 Discussion

In this chapter we have identified a number of ways for how DivL is able to connect two orthogonal signaling pathways in a bacterium. We have identified parts of DivL that mediate three key functions: how DivL localizes to the cell pole (Figure 3–3), the function of its PAS domains in relation to CckA activity (Figure 3–8), and the role of DivK~P in CckA binding (Figure 3–10). DivL localizes to the cell pole in *C. crescentus* through a combination of its transmembrane tether, Domain A, and HK domain (Figure 3–4). This result showed that the DivL localization may occur though both PopZ and PodJ recruitment to the cell pole as observed in *E. coli* (Figure 3–5). This multivalent binding may have an impact on the regulation of DivL that needs to be further explored. The function of PAS domains was then mapped to identify PAS B as a regulator of swarm size through its DITE motif (Figure 3–7). This implicates PAS B as a regulator of CckA kinase activity. In the CckA-FRET assay, deleting PAS B did not remove the DivL overexpression FRET change, which shows that PAS B may not be the only regulator of DivL/CckA interaction. PAS C did not impact swarm size even when its DITE motif was disrupted. PAS C did show a decrease in the CckA-FRET biosensor assay that will be explored more in the future. Deletion of PAS D and variants to the DITE motif of PAS D were both viable ways to knock out the impact of DivL on swarm size (Figure 3–7). Additionally, the PAS D deletion also removed the DivL overexpression effect in the CckA-FRET biosensor assay providing more evidence that PAS D is required for interaction with CckA. This is likely due to the reverse signaling mechanism of DivL. The reverse signaling impact of DivL had been shown by attaching a leucine zipper to the sensory domains in a swarm motility assay.[124] We further confirmed that the reverse signaling mechanism was propagated by directly interacting with CckA using the CckA-FRET biosensor to report the periodic change with each leucine zipper fusion. DivL LZ variants mediate two key changes in the

CckA-FRET biosensor: either a decrease (e.g. DivL 536-LZ) or increase (e.g. DivL 533-LZ). While our two assays designed to test the DivL/CckA interaction (swarm and FRET sensor) do not always correlate we can identify some trends between them. We have summarized the results of both assays for ease of comparison (Figure 3–11).

DivL Variant	Δ Domain A	Δ PAS B	Δ PAS C	Δ PAS D	531-LZ	532-LZ	533-LZ	534-LZ	535-LZ	536-LZ	537-LZ
Swarm Size[a]	+/–	–	+/–	+	+	+	+/–	–	+	+	+
FRET Impact[b]	–	+/–	–	–	–	–	+/–	–	–	–	–

Figure 3–11 DivLdomain function summary table.
For entire table, +/– indicates no change, + means increase and – means decrease. [a]For swarm size, domain deletions and LZs variants are compared to DivL overexpression swarm size. [b]For FRET impact, domain deletions and LZ variants are compared to the DivL overexpression FRET ratios.

Finally, we have showed that the DivL/CckA complex is likely mediated in some fashion through the RD domain of CckA, which can outcompete DivK~P binding to DivL. Overall this points to a model where at the old cell pole, a combination of high DivK~P levels and another PAS domain-specific signal inhibits CckA/DivL interactions so CckA maintains phosphatase activity, dephosphorylating CtrA (Figure 3–12).

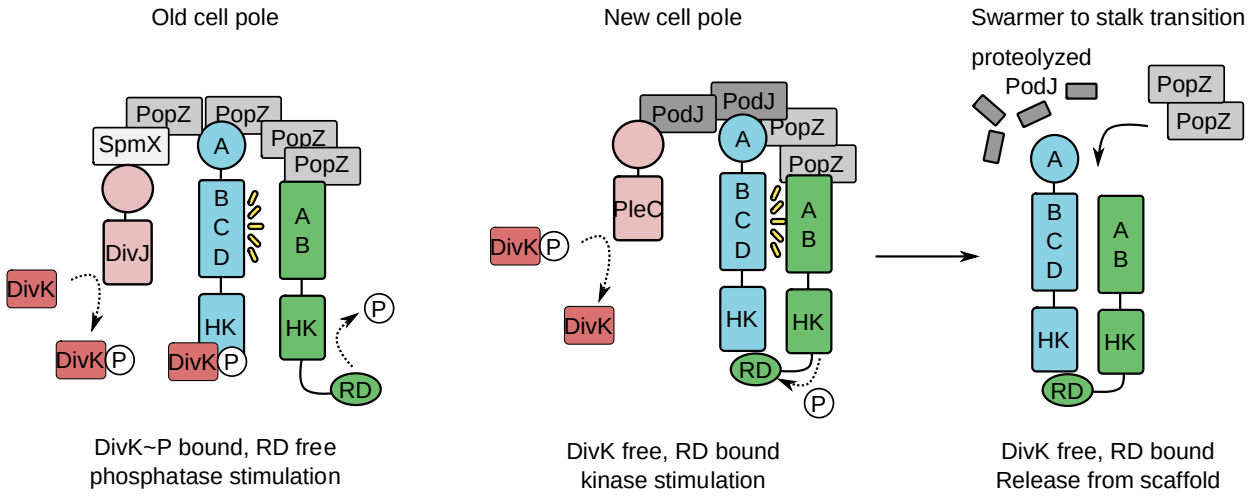

Figure 3–12 Model of DivL's pseudokinase functions regulating asymmetric localization and CckA pathway activity.

At the new cell pole, both PodJ and PopZ recruit DivL, PleC, and CckA. PleC keeps DivK~P levels low such that CckA gains an additional binding site for its RD domain and kinase activity remains high (Figure 3–12). Once cells have divided, PodJ is proteolyzed and the PopZ remains the only scaffold for both DivL and CckA (Figure 3–12). At this point CckA kinase activity is low in order for CtrA to be degraded to block the next cycle of replication from occurring. This model will require refinement in the future, but sets the foundation for understanding of how two multidomain signaling proteins work together to control the cell-cycle.

3.4 Future directions

3.4.1 CckA kinase activity *in vitro* is also impacted by DivL-LZ fusions

Now that we have evidence of direct interaction between the DivL-LZ fusions and CckA, we next wanted to use biochemistry to answer how DivL-LZ fusion impacts CckA kinase activity. Numerous studies on CckA kinase activity *in vitro* have been completed. Mann and coworkers established liposomes, lipid membranes containing Ni^{2+} groups that simulate the impact of the membrane on membrane-bound proteins, as a way to assay the impact of DivL on CckA activity.[76,113] Coupling liposome based assays with radiography, it was established the CckA kinase activity is density dependent and high densities result in higher kinase activity. The addition of DivL results in a decrease in kinase activity, either due to decreasing the packing of CckA on the liposome or a specific DivL/CckA interaction, as evidenced by the increase in activity seen when DivLA601L is used instead of DivL. Mann and coworkers work also identified PAS B as a potential DivL regulator of kinase activity.[76] Work by Blair[114] and Vo[176] optimized the use of the

coupled-enzyme assay for measuring CckA kinase kinetics *in vitro* without liposomes.[177] In order to measure more kinetics, we have decided to use the coupled-enzyme assay to report on DivL-LZ impact on CckA kinase activity. The assay works by mixing the coupled-enzymes (L-lactate dehydrogenase and pyruvate kinase), nicotinamide adenine dinucleotide, reduced form (NADH), phosphoenol pyruvate (PEP), and an ATPase, in our case CckA. Upon addition of ATP, CckA will generate ADP upon autophosphorylation. The pyruvate kinase will generate ATP and pyruvate from ADP and PEP. ATP can subsequently be reused by the kinase. Pyruvate can be converted to lactate by the L-lactate dehydrogenase which oxidizes NADH in the process. As NADH, which absorbs at 340 nm, is converted to nicotinamide adenine dinucleotide, oxidized form ($NAD^{+)}$, a decrease in absorbance can be monitored by plate reader, making this assay high throughput (Figure 3–13A).

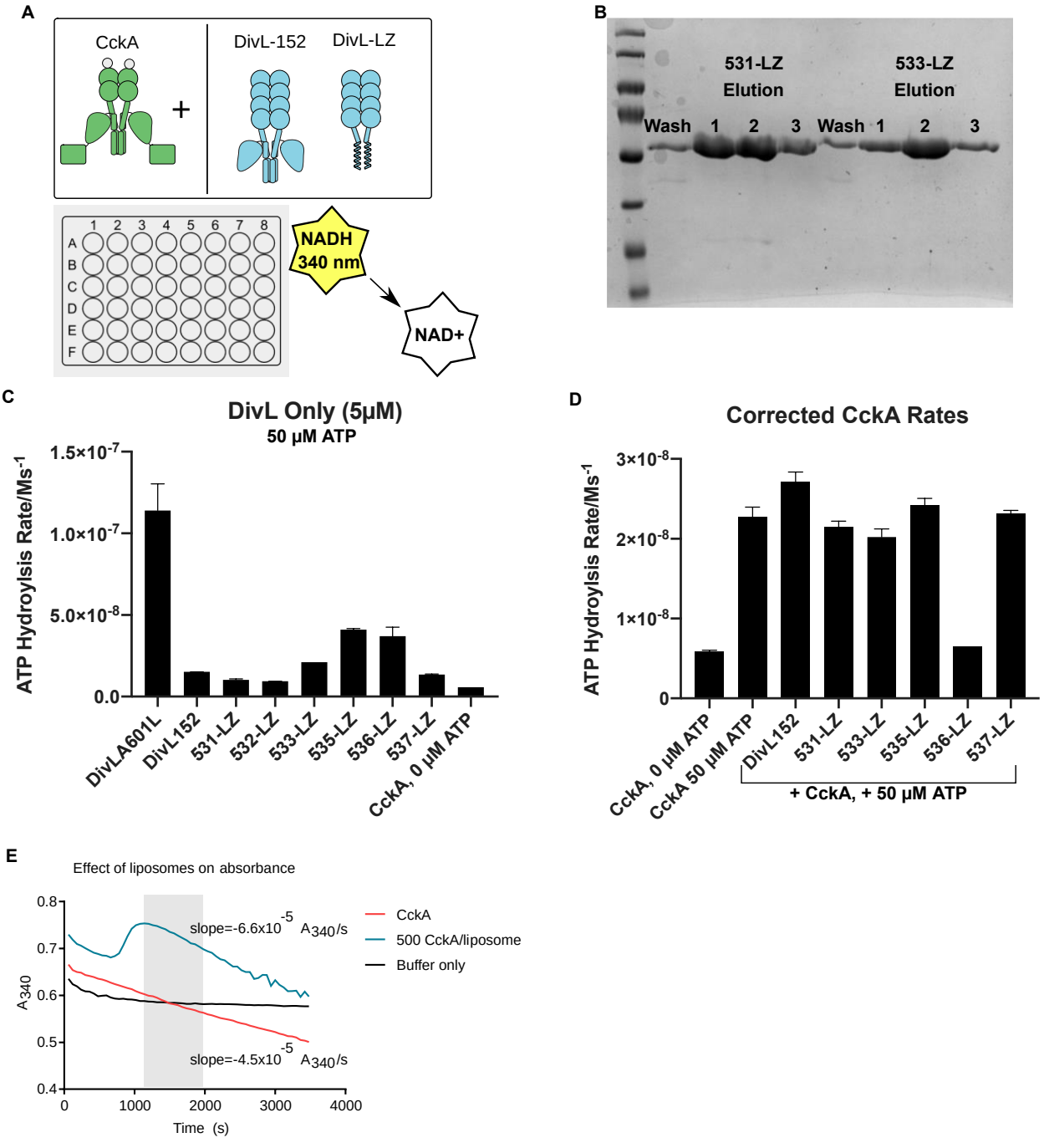

Figure 3–13 DivL-LZ fusions interact directly with CckA-FRET biosensor.
A) Schematic showing that CckA were mixed with either DivL-152 or DivL-LZ fusions. Assays were done in a 96-well plate format with a decrease in NADH absorbance measured. B) SDS-PAGE example of protein purification with protein stained using Coomassie G-250 Safe Stain. Wash indicates first wash after incubating protein with nickel resin. Elutions represent three separate elutions from the nickel resin. All bands appear at the correct molecular weight. C) Coupled-enzyme assay using purified DivL variants only at 5 μM concentration. See Methods for ATP Hydrolysis Rate calculation details. Data represents average of two trials. Bars indicate standard deviation of the mean. D) Corrected CckA ATP hydrolysis rates. DivL variant bars were generated by measuring the rates of DivL variants + CckA, then subtracting out the rates of DivL only. CckA 0 μM ATP and CckA 50 μM ATP are shown for background NADH oxidation and baseline kinase activity. Bars represent standard deviation of the mean. 536-LZ represents one

trial. E) Raw absorbance data over time for 5 μM CckA in solution alone or assembled at a half-maximum density of 500 molecules/liposome. Slopes used to determine ATP hydrolysis rates were calculated within the linear region shaded in gray.

Rates for kinase activity can then be calculated for steady-state ATP hydrolysis using the slope of absorbance.

We began by purifying DivL-LZ fusions using protocols developed in our lab by Kim Kowallis.[124] Nickel-affinity purification of His-tagged fusions followed by dialysis was used to purify the DivL-LZ fusions. DivL-LZ fusions were checked for purity by gel, a typical gel is shown for reference in Figure 3–13B. We did not identify any bands corresponding to high concentration of contaminating ATPases, a common problem when using purified protein in the coupled-enzyme assay. We subsequently tested the activity of the DivL-LZ fusions alone along with DivLA601L and DivL152 which had been purified previously under the same conditions. We noted that these proteins showed levels of ATP hydrolysis well above CckA containing no ATP (Figure 3–13C). These rates above CckA with no ATP could indicate either the contamination of protein preps with ATPases, or less likely the DivL constructs have inherent kinase activity which is very unlikely. Even with this setback, we did follow up by completing trials to compare CckA activity with and without DivL variants. We accomplished this by subtracting the observed rates for DivL alone from the rates including CckA. We were not able to measure DivLA601L in this manner due to the almost immediate loss of NADH upon addition of ATP.

Amongst this data set, we were able to determine that 536-LZ decreased kinase activity at 2:1, DivL (5 μM): CckA (2.5 μM) conditions (Figure 3–13D). Interestingly, we observed that overexpression of DivL-536-LZ resulted in a decrease in the FRET ratio *in vivo*. This preliminary data is evidence for us to purify the DivL variants again, this time adding an extra steps of gel filtration and ion-exchange to minimize co-purification of an ATPase. Additionally, we will use the liposomes in the coupled-enzyme assay platform. Those preliminary results are provided by

former lab mate Kim Kowallis who identified that liposomes impact the readout of the coupled-enzyme assay in the presence of liposomes.

3.4.2 FRET binding assays to study DivL/CckA interactions

The model in Figure 3–10 could be refined if it was known how DivL and CckA interact throughout the cell cycle. CckA can disrupt the DivL-DivK~P complex, but does DivK~P similarly disrupt a DivL-CckA interaction? Here we propose a FRET-based *in vitro* binding assay in which purified DivL-mClover3 and CckA-mRuby3 are allowed to incubate in solution before the addition of DivK~P. A predicted loss of FRET upon DivK~P addition would indicate that DivL and CckA were bound together, but disrupted by DivK~P. In contrast, DivK~P may only disrupt the interaction between the CckA RD domain and the DivL HK domain. In this model, the addition of DivK~P would not disrupt DivL-CckA sensory domain interactions. Therefore, DivL-mClover3 and CckA-mRuby3 would exhibit high FRET. The proposed FRET experiment will play a critical role in distinguishing these DivK-CckA-DivL competition models. An additional condition we can test is the addition of cyclic di-GMP. Cyclic di-GMP promotes phosphatase activity in CckA. Addition of this small molecule could also create a disruption between CckA and DivL.

3.4.3 Domain deletion biochemistry

Due to domain deletions in DivL having an impact on swarm size and CckA-FRET biosensor response, it is likely that certain domains in DivL have an impact on CckA activity *in vivo*. It has already been seen *in vitro* by Mann and coworkers that deletion of certain DivL domains could reduce CckA kinase activity.[76] We intend to do our own DivL domain deletion

panel in which each domain is deleted individually and mixed with CckA in the coupled-enzyme assay with and without liposomes. We expect that deletion of PAS B and PAS D will each give a change in kinase activity. It is likely deletion of PAS B will result in a higher kinase activity while the PAS D deletion will result in a lower kinase activity. These results would help to better understand the changes we observed in the swarm and CckA-FRET biosensor assays.

3.4.4 *in vitro* characterization of the CckA-FRET biosensor

In addition to the discussed optimization of purification methods of DivL variants for use in the coupled-enzyme assay, we aim to expand the use of the coupled-enzyme assay to the CckA-FRET biosensor. We have already been able to purify and do some quantification of the FRET sensor *in vitro*, but the kinase activity is over 5-fold lower than wild-type. We plan to optimize the activity of the CckA-FRET biosensor in order to make *in vitro* FRET measurements. We plan to mix the CckA-FRET biosensor with unlabeled CckA in order to form heterodimers that may retain a higher kinase activity. Once this is established, we will use the fluorimeter or plate reader to measure FRET under kinase and phosphatase conditions. For controls, we will also purify single fluorescent tagged CckA similar to our intermolecular FRET controls in Chapter 2. We can then mix fluorescently labeled variants together or with unlabeled CckA then measure FRET in kinase and phosphatase conditions.

3.5 Methods

Western Blot: Western blot analysis was used to determine protein levels of each DivL-FLAG variant. Cells were grown in 2 mL peptone yeast extract (PYE) medium to early log phase at 28°C. Overnight induction with 0.3% xylose began at inoculation. 1 mL cells were harvested by centrifugation and resuspended in SDS 100 µL sample loading dye. Samples were treated by heating (75°C for 10 min). Samples volumes were normalized to the lowest OD_{600} upon collection and separated by 10% SDS–PAGE. Proteins were transferred onto a PVDF membrane (GE Healthcare). The membrane was blocked in 5% milk (AmericanBio) overnight at 4°C. The anti-FLAG antibody (Sigma-Aldrich) (1:5000 in TBST for 1 hour at 4°C) was used with a goat anti-rabbit IgG-peroxidase secondary antibody (Sigma-Aldrich) (1:10,000 in TBST for 1 hour at room temperature). PVDF membranes were treated with an ECL western blotting kit (Thermo Scientific) and visualized using a ChemiDoc XRS+ system (Bio-Rad). Colorimetric imaging was used to visualize the protein ladder (Thermo Scientific), which was aligned with the blots to assign the size labels.

Swarm Plate Assay: Cells were grown to mid-log phase at 28 °C overnight in PYE medium and the appropriate antibiotic. Cells were normalized by dilution in PYE medium to the culture with the lowest OD_{600}. Cells were stabbed into 0.3% PYE agar with the appropriate antibiotic and 0.3% xylose in 15 cm diameter culture plates using a Boekel replicator. Plates were incubated at 28 °C for 3 days. Plates were visualized using a ChemiDoc XRS+ system (Bio-Rad). Three replicate plates were analyzed. Swarm area was measured using ImageJ[178]. Swarm areas were normalized to the empty vector control on each plate. The error for the empty vector control was calculated by dividing the standard deviation of the areas by the average area. The error for the experimental areas was calculated as the standard deviation of the areas after normalization to

the empty vector control. Significance was determined using Prism (GraphPad) with a Dunnett's multiple comparisons test by comparing the mean area of each strain to the mean area of DivL-WT (ns, P>0.05, *,P ≤ 0.05, **, P ≤ 0.01, ***, P ≤ 0.001).

Fluorescence Microscopy: *C. crescentus* cells were grown in M2G medium with the appropriate antibiotics at 28 °C overnight to OD_{600} of 0.2-0.8. DivL-mCherry variants were induced with 0.03% xylose for 4 hours. Cells were diluted as needed and immobilized on a 1.5% agarose in M2G pad. $DivK^{cs}$ strains were grown overnight in PYE medium and diluted in PYE supplemented with 0.03% xylose to induce over-expression. Cells were grown again overnight at 28 or 20 °C. Phase microscopy was performed by using a Nikon Eclipse T*i*-E inverted microscope equipped with an Andor Ixon Ultra DU897 EMCCD camera and a Nikon CFI Plan-Apochromat 100X/1.45 NA Oil objective and intermediate 1.5x magnification. DIC (differential interference contrast) microscopy was performed with a Nikon CFI Plan-Apochromat 100X/1.45 NA Oil DIC objective with a Nikon DIC polarizer and slider in place. Carl Zeiss Immersol 518 oil was used. Excitation source was a Lumencor SpectraX light engine. Chroma filter cube CFP/YFP/MCHRY MTD TI was used to image mCherry (630/60M). Chroma filter cube DAPI/GFP/TRITC was used to image EGFP, and mClover3 (515/30M). Images were acquired with Nikon NIS-Elements AR software.

Fluorescence Image Analysis: ImageJ[178] was used to adjust LUT, pseudocolor, and crop images. ImageJ Cell Counter and Nikon-NIS Elements AR were used to manually count cells and foci. ImageJ and MicrobeJ[166] were used for manual cell counting, cell length analysis and correlation scores. White outlines of the *C. crescentus* cell body were based on DIC or phase contrast imaging.

FRET Microscopy and Image Processing: Simultaneous FRET imaging required a Hamamatsu W-View Gemini Image Splitter in the light path between the Nikon T*i*E and the camera. A GFP/mCherry dichroic mirror, GFP emission filter, and mCherry emission filter were used. Alignment of the channels was done using the supplied alignment slide. Alignment of the channels was done before each imaging event. Each strain was imaged under the same conditions (600 millisecond Autoexposure, 100 Gain, 2x2 binning for capture, and 15% power). Background from the fluorescent channels was subtracted in the Nikon software. In ImageJ a mask was generated by thresholding cell signal above background. The original image was then multiplied by the masked image to remove background signal and the mCherry emission channel image was divided by the GFP emission channel (32-bit image) to generate a ratiometric FRET image. Image Analysis for each experiment, 4 images were uploaded into MicrobeJ (Phase, GFP channel, mCherry channel, and ratiometric image). The phase image was used to generate a cell outline using the Medial Axis setting. Cell poles were outlined using the MicrobeJ automatic pole settings which to draw a shape around the cell pole. MicrobeJ was preset to mark the stalk pole as the pole with higher intensity in the GFP channel. After software chose the poles, manual adjustment was done by choosing cells with a visible stalk and cells with incorrect pole alignment were corrected manually. MicrobeJ data analysis tool was then used to average the intensity of the cell pole and body. Data was exported to Prism (GraphPad) in order to generate histograms and average data. Student's t-test was used to determine significant difference in populations. Error bars are reported as standard error of the mean.

Protein Purification: Expression plasmids were transformed into BL21 cells, and plated onto 100 µg/mL ampicillin LB plates and grown overnight at 37 °C. From a single colony, an overnight 10 mL 50 µg/mL ampicillin LB culture was inoculated and grown to saturation

overnight. From this saturated culture two 1 L LB cultures were inoculated and grown to mid-log phase (OD_{600} of 0.6). Expression of the DivL-LZ fusions was induced with 333 µM isopropyl-b-D-thiogalactopyranoside (IPTG) for 4 hours at 25 °C. The cells were harvested by centrifugation (4 °C for 20 minutes at 3,700 g). The resulting pellet was resuspended in 50 ml 50 mM HEPES pH=8, 0.5 M KCl and centrifuged (3,700 g at 4 °C for 20 minutes) to yield a cell pellet stored at -80 °C. Cells were thawed on ice and resuspended in 50 ml of lysis buffer (50 mM HEPES pH 8.0, 0.5 M KCl, 1 mM DTT, 25 mM imidazole, 10% glycerol, and 200 U of Benzonase Nuclease (Sigma) supplemented with SIGMAFAST protease inhibitor tablets (Sigma)). The cell suspension was lysed with three passes through the Emulsiflex at 20,000 psi. Insoluble cell debris was pelleted via centrifugation (30,000 g, 50 min at 4 °C). The resulting supernatant was incubated with 2 ml of a 50% slurry of HisPur Ni-NTA agarose resin (Thermo Fisher Scientific) at 4 °C for 2 hours. The Ni-NTA agarose was pelleted and washed with 30 ml of Ni-NTA wash buffer (50 mM HEPES pH=8), 0.5 M KCl, 1 mM DTT, 25 mM imidazole, and 10% glycerol). Then the DivL-LZ fusion was eluted from the agarose with Ni-NTA elution buffer (50 mM HEPES pH=8.0, 0.5 M KCl, 1 mM DTT, 250 mM imidazole, and 10% glycerol) and concentrated using Amicon Centrifugal Filter Units (30 kDa cutoff), aliquoted and frozen at 80 °C. The concentration was determined using the predicted molecular weight of 58 kDa and an extinction coefficient of 78,630 $M^{-1}cm^{-1}$.

Fluorescence Polarization Assay: DivK was labeled at Cys-99 using thiol-reactive BODIPY FL N-aminoethyl maleimide (Invitrogen). DivK was mixed together with 10-fold excess BODIPY FL N-aminoethyl maleimide and allowed to react for 2 hours at room temperature, and unreacted dye was quenched with mercaptoethanol. BODIPY-DivK was purified via dialysis to remove unreacted fluorescent dye. BODIPY-DivK~P was generated by mixing 250 nM DivJ with 1 mM ATP and 5 mM $MgCl_2$ and incubated for 40 min. For binding assays using unphosphorylated

DivK, 1 mM nonhydrolyzable AMPPNP and 5 mM $MgCl_2$ were included in the buffer. BODIPY-DivK~P or BODIPY-DivK was then incubated with varying kinase concentrations for 45 minutes to reach binding equilibrium. Fluorescent DivK was excited at 470 nm and emission polarization was measured at 530 nm in a Molecular Devices SpectraMax M5 plate reader. Fluorescent polarization measurements were performed in triplicates, and three independent trials were averaged with error bars representing the standard deviation.

Coupled Enzyme Assay: ATPase activity was measured using a coupled-enzyme assay CckA was mixed in kinase buffer (50 mM HEPES pH=8, 50 mM KCl) supplemented with 0.1 mM ATP, 10 mM $MgCl_2$, 3 mM phosphoenolpyruvate, 0.2 mM NADH, 2 units of pyruvate kinase (P0294, Sigma), and 6.6 units of lactate dehydrogenase (P0294, Sigma). DivL constructs and/or liposomes were added to the reported concentrations. Reactions were performed in duplicate in a 200 µL volume and loaded into a clear polystyrene 96 well-plate. Each reaction was initiated by the addition of ATP, and 340 nm absorbance was recorded every 60 s for 60 min on a Tecan Infinite 200 Pro plate reader. The slope of a stable, linear absorbance decay was measured to calculate ATP hydrolysis rates using a NADH extinction coefficient of 6220 $M^{-1}s^{-1}$.[176] Background rates of ATP hydrolysis and NADH oxidation were measured and subtracted from observed CckA construct ATP hydrolysis rates. The mean observed rates were determined and analyzed using Prism (GraphPad).

Construction of Plasmids and Strains: All experiments were performed using *C. crescentus* NA1000 (also known as CB15N) and *E. coli* DH5α (Invitrogen) and BL21 DE3 (Novagen). *C. crescentus* NA1000, WSC11311 *DivK341* ($DivK^{cs}$), and the ϕCR30 phage were kind gifts from Dr. Lucy Shapiro (Stanford University School of Medicine). Plasmids, plasmid

construction methods, oligos, and strains used in this study can be found in Table 3–1, Table 3–2, Table 3–3, and Table 3–4, respectively.

Plasmid Construction: Restriction enzymes were purchased from Thermo Scientific or Invitrogen. PCR reactions were performed in 50 µL reaction mixtures containing 3% (v/v) DMSO, 1.3 M betaine, 0.3 µM each primer, and 0.2 mM each dNTP, and 1U Phusion High-Fidelity DNA Polymerase (Thermo Scientific). Gibson assembly reactions were performed in 20 µL with 100 ng backbone and typically a 1:5 backbone:insert ratio, with 0.08 U T5 Exonuclease (New England Biolabs), 1 U Phusion High-Fidelity DNA Polymerase (Thermo Scientific), and 80U Taq DNA Ligase (New England Biolabs). An annealing temperature of 55 °C was used for most reactions. Plasmids and primers were designed using the J5 device editor software. Oligonucleotides were synthesized by IDT (Coralville, IA) and all DNA sequencing reactions were performed by The University of Pittsburgh Genomics Research Core or Genewiz (South Plainfield, NJ). Further Gibson assembly procedures can be found below.

DivL-mCherry Variants: Plasmid WSC10153-pXCHYC6-divL was made by Gibson assembly of full-length *divL* into pXCHYC-6 and served as the template for all further DivL plasmid designs. Full length *divL* was amplified from the template cosmid 2G1 using primers KAK1 and KAK2. pXCHYC-6 was digested with SacI. This backbone and the insert were assembled using the Gibson assembly method resulting in an integrating plasmid at the *C. crescentus* chromosomal xylose locus encoding 3' mCherry-tagged DivL. *C. crescentus* cells were transformed by electroporation. Briefly, cells were grown in PYE medium overnight and rinsed three times with cold sterile water. Cells were resuspended in water and 80 µL of cells plus 10 µL of plasmid were electroporated with a time constant of 3.5-5.0 ms. Colonies were screened for

integration at the xylose locus using RecUni-1, a primer that anneals to the plasmid, and RecXyl-2, a primer that anneals to the 5' region of the chromosomal promoter.

DivL Point Mutants: DivL point mutants were designed as two-fragment Gibson assemblies with the point mutant embedded in the fragment amplification primers. pKAK0001-pXCHYC6-SacI-DivL-F292A was made by amplifying Insert 1 using primers KAK1 and WSCp89 and Insert 2 using primers WSCp88 and KAK2 from plasmid WSC10153 as a template. pXCHYC-6 was digested with SacI. This backbone and the inserts were assembled using the Gibson assembly method resulting in an integrating plasmid at the *C. crescentus* chromosomal xylose locus encoding the 3' mCherry-tagged DivL mutant.

DivL-FLAG Variants: pBXMCS-2 backbone was amplified by PCR using the primers KAK9 and KAK10. Fragments were amplified from WSC10153 or an already existing construct in pXCHYC-6. The backbone and insert were assembled using the Gibson assembly method resulting in a *C. crescentus* high-copy plasmid for the xylose-inducible expression of the 3' FLAG-tagged DivL variant.

pBAD-DivL-msfGFP Variants: The pBAD-DivL-msfGFP plasmid was isolated from a strain generously provided by Dr. Grant Bowman (University of Wyoming, Department of Molecular Biology)[179]. The pBAD backbone, excluding DivL, was amplified using the primers KAK321 and KAK322. A *divL* fragment encoding 134-769 was amplified from plasmid WSC10153. The backbone and insert were assembled using the Gibson assembly method resulting in an *E. coli* arabinose-inducible plasmid encoding 3' msfGFP-tagged DivL 134-769.

pTEV-His-DivL Variants: The pTEV-5 backbone was digested with NheI. Fragments were amplified from WSC10153 or an already existing construct in pXCHYC-6. The backbone

and insert were assembled using the Gibson assembly method resulting in an IPTG-inducible His-tagged DivL variant.

DivL-LZ Fusions for CckA-FRET Biosensor Assay: pBVMCS-1 backbone was amplified by PCR using primers SWD952 and SWD486. Each insert was amplified from already existing DivL-LZ plasmids using primers SWD487 and SWD953. Plasmids were assembled using Gibson assembly method and screened using primers pVanfor and M13for.

3.6 Tables

Table 3–1 Plasmids utilized in this study.

Plasmid	Description	Reference
pET-28b(+)	bacterial expression vector	Novagen
pTEV5	bacterial expression vector	[180]
pTEV6	bacterial expression vector with MBP solubilization tag	[180]
pXCHYC-6	C. crescentus integrating C-terminal mCherry fusion vector	[181]
pBXMCS-2	C. crescentus high-copy replicating C-terminal FLAG fusion vector	[181]
N/A	pBAD DivL (1-769), msfGFP	[179]
pWZ013-30	pCDFDuet1-mcherry-PodJ	[182]
WSC10153	pXCHYC-6 DivL (1-769)	This Study
pWSC10159	pXCHYC-6 DivL (1-27, 134-769)	This Study
pWSC10160	pXCHYC-6 DivL (1-170, 264-769)	This Study
pWSC10161	pXCHYC-6 DivL (1-262, 392-769)	This Study
pWSC10162	pXCHYC-6 DivL (1-391, 519-769)	This Study
pKAK0001	pXCHYC-6 DivL F292A	This Study
pKAK0003	pXCHYC-6 DivLV418A	This Study
pKAK0016	pBXMCS-2 DivL (1-27, 134-769)	This Study
pKAK0017	pBXMCS-2 DivL (1-170, 264-769)	This Study
pKAK0018	pBXMCS-2 DivL (1-262, 392-769)	This Study
pKAK0019	pBXMCS-2 DivL (1-391, 519-769)	This Study

pKAK0033	pBXMCS-2 DivL D260A	This Study
pKAK0034	pBXMCS-2 DivL T262V	This Study
pKAK0035	pBXMCS-2 DivL D389A	This Study
pKAK0036	pBXMCS-2 DivL T391V	This Study
pKAK0045	pXCHYC-6 DivL (1-170)	This study
pKAK0046	pXCHYC-6 DivL (1-133)	This study
pKAK0047	pXCHYC-6 DivL (28-170)	This study
pKAK0048	pXCHYC-6 DivL (28-133)	This study
pKAK0049	pXCHYC-6 DivL (1-170, 519-769)	This study
pKAK0050	pXCHYC-6 DivL (1-133, 519-769)	This study
pKAK0051	pXCHYC-6 DivL (28-170, 519-769)	This study
pKAK0052	pXCHYC-6 DivL (28-133, 519-769)	This study
pKAK0072	pXCHYC-6 DivL (1-170, 263-518)	This study
pKAK0073	pXCHYC-6 DivL (1-391)	This study
pKAK0088	pXCHYC-6 DivL (171-391)	This study
pKAK0089	pXCHYC-6 DivL (263-518)	This study
pKAK0096	pXCHYC-6 DivL (1-170, LZ)	This Study
pKAK0137a	pTEV-5 DivL (54-537, GCN4)	This Study
pKAK0137b	pTEV-5 DivL (54-536, GCN4)	This Study
pKAK0137c	pTEV-5 DivL (54-535, GCN4)	This Study
pKAK0137e	pTEV-5 DivL (54-533, GCN4)	This Study
pKAK0137g	pTEV-5 DivL (54-531, GCN4)	This Study
pKAK0207	pBAD DivL (134-769), msfGFP	This Study
pKAK0208	pBAD DivL (33-133), msfGFP	This Study
pWSC10036	pTEV5-DivL(152-769)	[71]
pWSC10038	pTEV5-DivL(152-769) A601L	[71]
pJAB27	pET-28b(+) CckA(70-691) expression vector	[71]
pWSC29	pET-28b(+) DivJ(195-596)	[71]
pWSC31	pET-28b(+) DivK	[71]
pSWD63	pGFPC-4 CckA (1500bp), mClover3	[155]
pSWD209	pVMCS-1 DivL (1-27, 134-769)	This Study
pSWD210	pVMCS-1 DivL (1-170, 264-769)	This Study
pSWD228	pVMCS-1 DivL (1-262, 392-769)	
pSWD211	pVMCS-1 DivL (1-391, 519-769)	This Study
pSWD208	pVMCS-1 DivL (1-565)	This Study
pSWD329	pBVMCS-1 DivL 1-531-GCN4	This Study
pSWD330	pBVMCS-1 DivL 1-532-GCN4	This Study
pSWD331	pBVMCS-1 DivL 1-533-GCN4	This Study

pSWD332	pBVMCS-1 DivL 1-534-GCN4	This Study
pSWD333	pBVMCS-1 DivL 1-535-GCN4	This Study
pSWD334	pBVMCS-1 DivL 1-536-GCN4	This Study
pSWD335	pBVMCS-1 DivL 1-537-GCN4	This Study

Table 3–2 Gibson cloning strategy to generate plasmids expressing DivL variants.

Plasmid	**Plasmid Description**	**First Insert Forward Primer**	**First Insert Reverse Primer**	**Second Insert Forward Primer**	**Second Insert Reverse Primer**
pWSC10159	pXCHYC-6 DivL (1-27, 134-769)	WSC10297	WSC10304	WSC10305	WSC10171
pWSC10160	pXCHYC-6 DivL (1-170, 264-769)	WSC10297	WSC10306	WSC10307	WSC10171
pWSC10161	pXCHYC-6 DivL (1-262, 392-769)	WSC10297	WSC10308	WSC10309	WSC10171
pWSC10162	pXCHYC-6 DivL (1-391, 519-769)	WSC10297	WSC10310	WSC10311	WSC10171
pKAK0001	pXCHYC-6 DivL F292A	KAK1	WSCp89		
pKAK0003	pXCHYC-6 DivLV418A	WSCp88	KAK2		
pKAK0016	pBXMCS-2 DivL (1-27, 134-769)	KAK3	KAK7		
pKAK0017	pBXMCS-2 DivL (1-170, 264-769)	KAK3	KAK7		
pKAK0018	pBXMCS-2 DivL (1-262, 392-769)	KAK3	KAK7		

pKAK0019	pBXMCS-2 DivL (1-391, 519-769)	KAK3	KAK7		
pKAK0033	pBXMCS-2 DivL D260A	KAK10	KAKqc0011	KAKqc0010	KAK9
pKAK0034	pBXMCS-2 DivL T262V	KAK3	KAKqc0013	KAKqc0012	KAK7
pKAK0035	pBXMCS-2 DivL D389A	KAK3	KAKqc0015	KAKqc0014	KAK7
pKAK0036	pBXMCS-2 DivL T391V	KAK10	KAKqc0017	KAKqc0016	KAK7
pKAK0045	pXCHYC-6 DivL (1-170)	KAK1	KAK31		
pKAK0046	pXCHYC-6 DivL (1-133)	KAK1	KAK32		
pKAK0047	pXCHYC-6 DivL (28-170)	KAK33	KAK31		
pKAK0048	pXCHYC-6 DivL (28-133)	KAK33	KAK32		
pKAK0049	pXCHYC-6 DivL (1-170, 519-769)	KAK1	KAK34	KAK35	KAK2
pKAK0050	pXCHYC-6 DivL (1-133, 519-769)	KAK1	KAK36	KAK37	KAK2
pKAK0051	pXCHYC-6 DivL (28-170, 519-769)	KAK33	KAK34	KAK35	KAK2
pKAK0052	pXCHYC-6 DivL (28-133, 519-769)	KAK33	KAK35	KAK37	KAK2
pKAK0072	pXCHYC-6 DivL (1-170, 263-518)	KAK1	WSC10306	WSC10307	KAK63
pKAK0073	pXCHYC-6 DivL (1-391)	KAK1	KAK64		
pKAK0088	pXCHYC-6 DivL (171-391)	KAK91	KAK92		

pKAK0089	pXCHYC-6 DivL (263-518)	KAK93	KAK94		
pKAK0096	pXCHYC-6 DivL (1-170, LZ)	KAK1	KAKqc0108		
pKAK0137g	pTEV5-DivL (54-531, GCN4	KAK155	KAK158		
pKAK0137f	pTEV-5-DivL (54-532, GCN4)	KAK155	KAK158		
pKAK0137e	pTEV-5-DivL (54-533, GCN4)	KAK155	KAK158		
pKAK0137c	pTEV-5-DivL (54-535, GCN4	KAK155	KAK158		
pKAK0137b	pTEV-5-DivL (54-536, GCN4)	KAK155	KAK158		
pKAK0137a	pTEV-5-DivL (54-537, GCN4	KAK155	KAK158		
pKAK0207	pBAD DivL (134-769),msfGFP	KAK323	KAK234		
pKAK0208	pBAD DivL (33-133), msfGFP	KAK325	KAK326		
pSWD63	pGFPC-4 CckA (1500bp), mClover3	SWD211	SWD212	SWD213	SWD214
pSWD208	pVMCS-1 DivL (1-565)	SWD649	SWD486	SWD487	SWD660
pSWD209	pVMCS-1 DivL (1-27, 134-769)	SWD485	SWD486	SWD487	SWD488

pSWD210	pVMCS-1 DivL (1-170, 264-769)	SWD485	SWD486	SWD487	SWD488
pSWD211	pVMCS-1 DivL (1-391, 519-769)	SWD485	SWD486	SWD487	SWD488
pSWD228	pVMCS-1 DivL (1-262, 392-769)	SWD485	SWD486	SWD487	SWD488
pSWD329	pBVMCS-1 DivL 1-531-GCN4	SWD487	SWD953		
pSWD330	pBVMCS-1 DivL 1-532-GCN4	SWD487	SWD953		
pSWD331	pBVMCS-1 DivL 1-533-GCN4	SWD487	SWD953		
pSWD332	pBVMCS-1 DivL 1-534-GCN4	SWD487	SWD953		
pSWD333	pBVMCS-1 DivL 1-535-GCN4	SWD487	SWD953		
pSWD334	pBVMCS-1 DivL 1-536-GCN4	SWD487	SWD953		
pSWD335	pBVMCS-1 DivL 1-537-GCN4	SWD487	SWD953		

Table 3–3 DNA pimers used in this study.

Name	Description
RecXyl-2	TCTTCCGGCAGGAATTCACTCACGCC
RecUni-1	ATGCCGTTTGTGATGGCTTCCATGTCG
WSCp88	CCGTGGCGATCGCCAGCCAGACGCG
WSCp89	CGCGTCTGGCTGGCGATCGCCACGG
WSC10295	TGGTACCTTAAGATCTCGAGCTATGACTTCGTACGACCTGATCCTCGC
WSC10296	TCGAATTCTCCGGGAAGCCGAGTTCGGGCTGCATGG

WSC10297	TGCATGGTACCTTAAGATCTCGAGCTATGACTTCGTACGACCTGATCCTCG CG
WSC10304	CGCGACCCTCGACCCCGTGGGACCACAGGGC
WSC10305	GTGGTCCCACGGGGTCGAGGGTCGCGCGGCG
WSC10306	GGACATCCTCGATCTCCACGCTGTCGACGAAGGCGG
WSC10307	CGTCGACAGCGTGGAGATCGAGGATGTCCGCGACGC
WSC10171	TGACGCGTAACGTTCGAATTCTCCGGGAAGCCGAGTTCGGGCTGC
WSC10306	GGACATCCTCGATCTCCACGCTGTCGACGAAGGCGG
WSC10307	CGTCGACAGCGTGGAGATCGAGGATGTCCGCGACGC
WSC10308	GGCGCAGCTCGCCGGTGACGTCGGCGCAGAACAC
WSC10309	CGCCGACGTCACCGGCGAGCTGCGCCTGAAAGC
WSC10310	GGTCTCGGGTGTCGGTGATGTCGGAATAGATCAGCAGC
WSC10311	TATTCCGACATCACCGACACCCGAGACCTGCAGAGCG
KAKqc0010	GTGTTCTGCGCCGCCGTCACCGAGATC
KAKqc0011	GATCTCGGTGACGGCGGCGCAGAACAC
KAKqc0012	CTGCGCCGACGTCGTCGAGATCGAGGATG
KAKqc0013	CATCCTCGATCTCGACGACGTCGGCGCAG
KAKqc0014	CTGATCTATTCCGCCATCACCGGCGAG
KAKqc0015	CTCGCCGGTGATGGCGGAATAGATCAG
KAKqc0016	CTATTCCGACATCGTCGGCGAGCTGCG
KAKqc0017	CGCAGCTCGCCGACGATGTCGGAATAG
KAKqc0108	TGACGCGTAACGTTCGAATTCTCCGGCAGACGGGCGACCTCATTCTCGAGG TGGTAGTTCTTCGAGAGGAGTTCTTCGACCTTGTCTTCGAGTTGCTTCACGC TGTCGACGAAGGC
KAK1	TGCATGGTACCTTAAGATCTCGAGCTATGACTTCGTACGACCTGATCCTCG C
KAK2	TGACGCGTAACGTTCGAATTCTCCGGGAAGCCGAGTTCGGGCTGCATGG
KAK3	CGAGGTCGACGGTATCGATAAGCTTGATATGACTTCGTACGACCTGATCCT CGCG
KAK7	CGGCGCTTTTCCATCGAGAATTCGATGAAGCCGAGTTCGGGCTGCATGG
KAK9	ATCGAATTCTCGATGGAAAAGCGCCG
KAK10	ATCAAGCTTATCGATACCGTCGACCTCGAG
KAK31	TGACGCGTAACGTTCGAATTCTCCGGCACGCTGTCGACGAAGGC
KAK32	TGACGCGTAACGTTCGAATTCTCCGGCGAAACAAGGCCATGGGG
KAK33	TGCATGGTACCTTAAGATCTCGAGCTATGCAGCGACGGAACCTGGAGGC
KAK35	CGTCGACAGCGTGGACACCCGAGACCTGCAGAGCG
KAK36	GGTCTCGGGTGTCCGAAACAAGGCCATGGGG
KAK37	TGGCCTTGTTTCGGACACCCGAGACCTGCAGAGCG
KAK63	TGACGCGTAACGTTCGAATTCTCCGCGGTGACGTCGGCGAAGGCG

KAK64	TGACGCGTAACGTTCGAATTCTCCGCGGTGATGTCGGAATAGATCAGCAGC
KAK91	TGCATGGTACCTTAAGATCTCGAGCTATGGTCGAGCCGTGCTGGATCGC
KAK92	TGACGCGTAACGTTCGAATTCTCCGGGGTGATGTCGGAATAGATCAGCAGC
KAK93	TGCATGGTACCTTAAGATCTCGAGCTATGGAGATCGAGGATGTCCGCGACG C
KAK94	TGACGCGTAACGTTCGAATTCTCCGGGGTGACGTCGGCGAAGGCG
KAK155	CCAACTAGTGAAAACCTGTATTTTCAGGGCGCTATGGCCTGGCTCGACGCC TTCGA
KAK158	GCTCGAGAATTCCATGGCCATATGGCTTCACAGACGGGCGACCTCATTCTC GA
KAK323	TTTTTGGGCTAACAGGAGGAATTAACCAATGGTCGAGGGTCGCGCGGCG
KAK324	TTACTGCCGCCGCCGCCGCTCTCGAGGAAGCCGAGTTCGGGCTGCATGG
KAK325	TTTTTGGGCTAACAGGAGGAATTAACCAATGGAGGCGCGTATCGTCGCGC
KAK326	TTACTGCCGCCGCCGCCGCTCTCGAGCGAAACAAGGCCATGGGGACCG
SWD211	GGTACCTTAAGATCTCGAGCTCCGGAGAACCCGCCACCCAGCTCGCTG
SWD212	CCTCGCCCTTGCTGGTGGCCGACCGGTGACGCGTAACGTTCGACGCCGCCT GCAGCTGCTG
SWD213	CCGGTCGGCCACCAGCAAGGGCGAGGAGCTGTTCACC
SWD214	CTAGTGGATCCCCCGGGCTGCAGCTATTAGCTCACCATCGGATCTTCGCCG C
SWD485	GCCCGAACTCGGCTTCTAGCTCTTAAGATCTACGTACCGGTGCTAGCTG
SWD486	CGTACGAAGTCATCTCACCACGTGGTACCTCGAGAATTCATATGC
SWD487	GGTACCACGTGGTGAGATGACTTCGTACGACCTGATCCTCGCG
SWD488	CGTAGATCTTAAGAGCTAGAAGCCGAGTTCGGGCTGC
SWD659	CGGCTATTCGGAGCTGTAGCTCTTAAGATCTACGTACCGGTGCTAGCTG
SWD660	GGTACGTAGATCTTAAGAGCTACAGCTCCGAATAGCCGATGATCGTCG
SWD952	GGTCGCCCGTCTGTAGCTCTTAAGATCTACGTACCGGTGCTAGCTG
SWD953	CGTAGATCTTAAGAGCTACAGACGGGCGACCTCATTCTCGAGG

Table 3–4 Strains used in this study.

Strain	Description	Plasmid Number	Reference
E. coli DH5α	bacterial cloning strain		Invitrogen
E. coli BL21 (DE3)	bacterial expression strain		Novagen
C. crescentus NA1000	laboratory Caulobacter crescentus strain		Lucy Shapiro
JH42	BL21 (DE3) pACYC-mCherry-PopZ		[179]

JH79	BL21 (DE3) pACYC-mCherry-PopZ + pBAD-DivL-msfGFP		[179]
WSC0300	*C. crescentus* pBXMCS-2		[181]
WSC0302	*C. crescentus* pBXMCS-2 DivL (1-769)		This study
WSC1233	DH5α pCDFDuet1-mcherry-PodJ	pWZ013-30	[182]
WSC1368	BL21(DE3) pCDFDuet1-mcherry-PodJ	pWZ013-30	[182]
WSC0458	*C. crescentus* pXCHYC-6 DivL (1-27, 134-769)	pWSC10159 NA1000	This study
WSC0459	*C. crescentus* pXCHYC-6 DivL (1-170, 264-769)	pWSC10160 NA1000	This study
WSC0460	*C. crescentus* pXCHYC-6 DivL (1-262, 392-769)	pWSC10161 NA1000	This study
WSC0461	*C. crescentus* pXCHYC-6 DivL (1-391, 519-769)	pWSC10162 NA1000	This study
KAK15	DH5α pXCHYC-6 DivL (1-27, 134-769)	pWSC159	This study
KAK16	DH5α pXCHYC-6 DivL (1-170, 264-769)	pWSC160	This study
KAK17	DH5α pXCHYC-6 DivL (1-262, 392-769)	pWSC161	This study
KAK18	DH5α pXCHYC-6 DivL (1-391, 519-769)	pWSC162	This study
KAK20	DH5α pXCHYC-6 DivL (1-769)	WSC10153	This study
KAK23	DH5α pBXMCS-2 DivL D260A	pKAK0033	This study
KAK26	DH5α pXCHYC-6 DivL F292A	pKAK0001	This study
KAK27	DH5α pBXMCS-2 DivL T262V	pKAK0034	This study
KAK28	DH5α pXCHYC-6 DivLV418A	pKAK0003	This study
KAK43	NA1000 pXCHYC-6 DivL (1-769)	WSC10153	This study
KAK48	DH5α pBXMCS-2 DivL (1-27, 134-769)	pKAK0016	This study
KAK49	DH5α pBXMCS-2 DivL (1-391, 519-769)	pKAK0019	This study
KAK51	DH5α pBXMCS-2 DivL (1-170, 264-769)	pKAK0017	This study
KAK52	DH5α pBXMCS-2 DivL (1-262, 392-769)	pKAK0018	This study
KAK66	NA1000 pBXMCS-2 DivL (1-262, 392-769)	pKAK0018	This study

KAK67	NA1000 pBXMCS-2 DivL (1-391, 519-769)	pKAK0019	This study
KAK68	NA1000 pBXMCS-2 DivL (1-27, 134-769)	pKAK0016	This study
KAK69	NA1000 pBXMCS-2 DivL (1-170, 264-769)	pKAK0017	This study
KAK88	NA1000 pXCHYC-6 DivL F292A	pKAK0001	This study
KAK89	NA1000 pXCHYC-6 DivLV418A	pKAK0003	This study
KAK117	DH5α pXCHYC-6 DivL (28-170)	pKAK0047	This study
KAK119	DH5α pXCHYC-6 DivL (28-133)	pKAK0048	This study
KAK122	DH5α pXCHYC-6 DivL (1-170)	pKAK0045	This study
KAK123	DH5α pXCHYC-6 DivL (1-133)	pKAK0046	This study
KAK124	DH5α pXCHYC-6 DivL (1-170, 519-769)	pKAK0049	This study
KAK125	DH5α pXCHYC-6 DivL (1-133, 519-769)	pKAK0050	This study
KAK126	DH5α pXCHYC-6 DivL (28-170, 519-769)	pKAK0051	This study
KAK127	DH5α pXCHYC-6 DivL (28-133, 519-769)	pKAK0052	This study
KAK130	DH5α pBXMCS-2 DivL D389A	pKAK0035	This study
KAK137	NA1000 pBXMCS-2 DivL D260A	pKAK0033	This study
KAK138	NA1000 pBXMCS-2 DivL T262V	pKAK0034	This study
KAK139	NA1000 pBXMCS-2 DivL D389A	pKAK0035	This study
KAK140	NA1000 pXCHYC-6 DivL (1-170)	pKAK0045	This study
KAK141	NA1000 pXCHYC-6 DivL (1-133)	pKAK0046	This study
KAK142	NA1000 pXCHYC-6 DivL (28-170)	pKAK0047	This study
KAK143	NA1000 pXCHYC-6 DivL (28-133)	pKAK0048	This study
KAK144	NA1000 pXCHYC-6 DivL (1-170, 519-769)	pKAK0049	This study
KAK145	NA1000 pXCHYC-6 DivL (1-133, 519-769)	pKAK0050	This study
KAK146	NA1000 pXCHYC-6 DivL (28-170, 519-769)	pKAK0051	This study
KAK147	NA1000 pXCHYC-6 DivL (28-133, 519-769)	pKAK0052	This study
KAK149	NA1000 pBXMCS-2 DivL T391V	pKAK0036	This study
KAK174	*divL*::*spec* pXCHYC-6 DivL (1-769) *cckA::cckA-mclover3*	WSC10153	This study

KAK186	DH5α pXCHYC-6 DivL (1-170, 263-518)	pKAK0072	This study
KAK188	DH5α pXCHYC-6 DivL (171-391)	pKAK0088	This study
KAK191	DH5α pXCHYC-6 DivL (171-391)	pKAK0089	This study
KAK215	NA1000 pXCHYC-6 DivL (1-170, 263-518)	pKAK0072	This study
KAK221	NA1000 pXCHYC-6 DivL (171-391)	pKAK0088	This study
KAK222	NA1000 pXCHYC-6 DivL (263-518)	pKAK0089	This study
KAK228	NA1000 pXCHYC-6 DivL (1-391)	pKAK0073	This study
KAK253	DH5α pTEV-5 DivL (54-537, GCN4)	pKAK0137a	This study
KAK254	DH5α pTEV-5 DivL (54-536, GCN4)	pKAK0137b	This study
KAK255	DH5α pTEV-5 DivL (54-535, GCN4)	pKAK0137c	This study
KAK256	DH5α pTEV-5 DivL (54-533, GCN4)	pKAK0137e	This study
KAK270	DH5α pTEV-5 DivL (54-532, GCN4)	pKAK0137f	This study
KAK271	DH5α pTEV-5 DivL (54-531, GCN4)	pKAK0137g	This study
KAK322	BL21 pTEV-5 DivL (54-535, GCN4)	pKAK0137c	This study
KAK331	BL21 pTEV-5 DivL (54-537, GCN4)	pKAK0137a	This study
KAK332	BL21 pTEV-5 DivL (54-536, GCN4)	pKAK0137b	This study
KAK333	BL21 pTEV-5 DivL (54-533, GCN4)	pKAK0137e	This study
KAK334	BL21 pTEV-5 DivL (54-532, GCN4)	pKAK0137f	This study
KAK335	BL21 pTEV-5 DivL (54-531, GCN4)	pKAK0137g	This study
KAK392	DH5α pBAD DivL (134-769), msfGFP	pKAK0207	This study
KAK393	DH5α pBAD DivL (33-133), msfGFP	pKAK0208	This study
KAK406	BL21 pBAD DivL (33-133), msfGFP+ pACYC-mCherry-PopZ	pKAK0208, pACYC-mCherry-PopZ	This study
KAK411	BL21 pBAD DivL (33-133), msfGFP	pKAK0208	This study
KAK423	BL21 pBAD DivL (134-769), msfGFP +pCDFDuet1-mcherry-PodJ	pKAK0207, pWZ013-30	This study
KAK424	BL21 pBAD DivL (33-133), msfGFP +pCDFDuet1-mcherry-PodJ	pKAK0208, pWZ013-30	This study
KAK427	BL21 pBAD DivL (134-769), msfGFP	pKAK0207	This study
KAK428	BL21 pBAD DivL (134-769), msfGFP +pACYC-mCherry-PopZ	pKAK0207, pACYC-mCherry-PopZ	This study
SWD193	DH5α pGFPC-4 CckA (1500bp), mClover3	pSWD63	[155]

SWD491	DH5α pVMCS-1 DivL (1-27, 134-769)	pSWD209	This study
SWD485	DH5α pVMCS-1 DivL (1-170, 264-769)	pSWD210	This study
SWD557	DH5α pVMCS-1 DivL (1-262, 392-769)	pSWD228	This study
SWD492	DH5α pVMCS-1 DivL (1-391, 519-769)	pSWD211	This study
SWD504	DH5α pVMCS-1 DivL (1-565)	pSWD208	This study
SWD212	NA1000 *cckA::cckA-mClover3*	pSWD63	[155]
SWD513	NA1000 FRET+pVMCS-1 DivL (1-27, 134-769)	pSWD95, pSWD209	This study
SWD510	NA1000 FRET+pVMCS-1 DivL (1-170, 264-769)	pSWD95, pSWD210	This study
SWD611	NA1000 FRET+pVMCS-1 DivL (1-262, 392-769)	pSWD95, pSWD228	This study
SWD509	NA1000 FRET+pVMCS-1(1-391, 519-769)	pSWD95, pSWD211	This study
SWD525	NA1000 FRET+pVMCS-1 DivL (1-565)	pSWD95, pSWD208	This study
SWD608	NA1000 FRET Sensor only	pSWD95	[155]
SWD770	DH5α pVMCS-1 DivL-1-531-GCN4	pSWD329	This study
SWD771	DH5α pVMCS-1 DivL-1-532-GCN4	pSWD330	This study
SWD772	DH5α pVMCS-1 DivL-1-533-GCN4	pSWD331	This study
SWD773	DH5α pVMCS-1 DivL-1-534-GCN4	pSWD332	This study
SWD774	DH5α pVMCS-1 DivL-1-536-GCN4	pSWD334	This study
SWD775	DH5α pVMCS-1 DivL-1-537-GCN4	pSWD335	This study
			This study
SWD783	NA1000 FRET+ pVMCS-1 DivL-1-531-GCN4	pSWD95, pSWD329	This study
SWD784	NA1000 FRET+ pVMCS-1 DivL-1-532-GCN4	pSWD95, pSWD330	This study
SWD785	NA1000 FRET+ pVMCS-1 DivL-1-533-GCN4	pSWD95, pSWD331	This study
SWD786	NA1000 FRET+ pVMCS-1 DivL-1-534-GCN4	pSWD95, pSWD332	This study
SWD787	NA1000 FRET+ pVMCS-1 DivL-1-536-GCN4	pSWD95, pSWD334	This study

SWD788	NA1000 FRET+ pVMCS-1 DivL-1-537-GCN4	pSWD95, pSWD335	This study

4.0 Histidine kinase inhibitors as a next generation antibiotic

4.1 Introduction

The appearance of rapid antibiotic resistance in bacteria has led to increased risk of chronic infection, economic burden, and deaths associated with antibiotic resistant bacteria.[183,184] Different strategies have been used to combat antibiotic resistance including the discovery of new classes of antibiotics that target signaling systems in bacteria, rather than traditional antibiotics that target essential cell functions such as translation or cell wall biogenesis.[4,176,183,184] Bacterial signaling systems make an attractive target for antibiotic development not only because specific bacteria can be targeted, but also because they can alter bacterial behavior rather than destruction of the bacteria, which often leads to the development of bacterial antibiotic resistance due to destruction putting pressure on the bacteria to evolve resistance.[183,184] Two categories of bacterial signaling systems are attractive candidates for antibiotic development: quorum sensing systems[185] and two-component systems. Quorum sensing is a viable target due to the widespread nature of inter and intraspecies quorum sensing systems, making it possible to target specific pathogenic bacteria.[186] These systems also rely on small molecules for communication between bacteria.[187] These small molecule signals can be taken of advantage of by designing competitive inhibitors than could lock the bacteria in a non-virulent state. Two-component systems are more widespread. While different quorum sensing systems exist in certain bacteria, all bacteria use the catalytic HK for two-component signaling, making it a more attractive target for a new class of antibiotics.

Two-component systems are composed of a HK that can sense a signal and, upon signaling integration, phosphorylate a RR that will carry out an activity such as transcription or enzyme

regulation.[1,91,109] Bacterial HKs contain an ATP-binding domain in the GHKL (gyrases, heat shock protein 90 (Hsp90), histidine kinase, MutL) superfamily of proteins.[188] The GHKL superfamily of ATPases/kinases uses the ATP-binding Bergerat fold as a nucleotide-binding site consisting of a 3-part motif.[188] Using an HK as an example, the three motifs identified in the Bergerat fold are the N, G1, and G2 conserved boxes (Figure 4–1).[188]

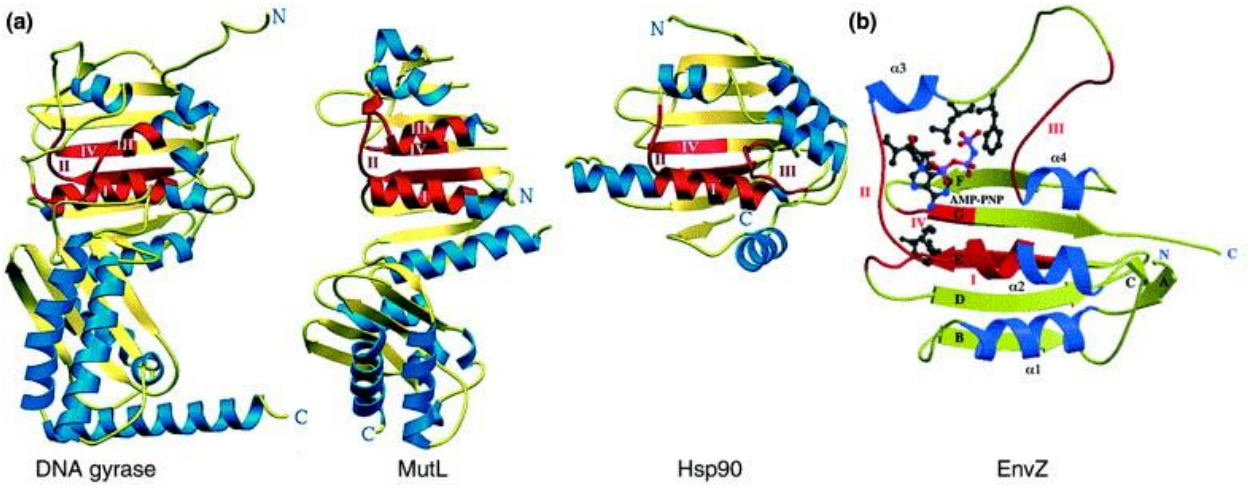

Figure 4–1 Comparison of GHKL ATP-binding domains.
A) ATP-binding domains of DNA gyrase, MutL, Hsp90, and EnvZ. Protein secondary structures involved in ATP-binding are color coded red. B) EnvZ is shown as the energy-minimized average structure bound to non-hydrolyzable AMPPNP. Conserved amino acids are shown as ball-and-stick models. Figure used with permission from Dutta, *et al. Trends Biochem. Sci.* **2000**, 25(1), 24-28.

Due to this shared motif, inhibitors designed to target Hsp90[189], gyrases[190], and MutL[191] have the potential to target HK ATP-binding sites. Issues with orthogonality can arise due to the shared Bergerat fold. Specific targeting of HKs can be improved using structure-activity relationship (SAR) studies.[176,192] A limited number of HKs are encoded in the human genome meaning off-target effects may be limited.[82,193] This makes HKs a potential orthogonal target to signaling proteins of higher order Eukaryotic cells, which are typically serine/threonine and tyrosine kinases.[194] These classes of kinases use different folds for ATP-binding than HKs.[194]

4.1.1 Gyrase inhibitors redesigned to inhibit HKs

DNA gyrase is a member of the GHKL superfamily and is classified as topoisomerase IIA, an ATP-dependent enzyme that plays roles in transcription, replication, and chromosome segregation.[190] Since DNA gyrases are only found in bacteria, they constitute a target for an antibiotic. Inhibition of DNA gyrases in bacteria can lead to single and double-stranded breaks in DNA, resulting in loss of chromosome stability and ultimately cell death.[195] Due to the vast amount of work done to develop inhibitors for DNA gyrases, a wide array of inhibitors are available to test for binding and inhibition of the GHKL fold in HKs in bacteria.[190]

One method of searching for potential HK inhibitors is comparative computational docking studies of the DNA gyrase with the target HK ATP-binding domain. This method was used as an early-stage screen to determine what features would be required to transition a compound from a DNA gyrase inhibitor to an HK inhibitor, owing to the HKs flexible ATP lid (Figure 4–2).[188]

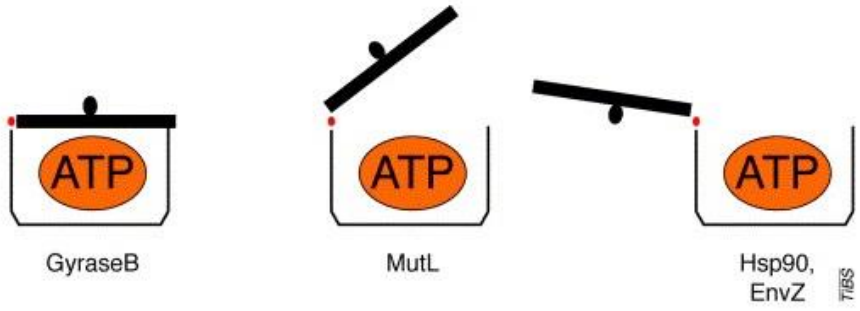

Figure 4–2 ATP-lid confirmations in GHKL superfamily.
The ATP-lid confirmation is one feature that sets the GHKL family apart. In GyrB, the ATP-lid fully encloses ATP upon binding. In MutL, the ATP-lid is partially open so ATP is exposed. In Hsp90 and EnvZ (HKs), ATP is fully exposed to solvent when bound. Figure used with permission from Dutta, *et al. Trends Biochem. Sci.* **2000**, 25(1), 24-28.

Ligands designed for DNA gyrases had been known to bind HKs, but further optimization of the ligand is required to ensure high binding affinity.[196] The *B. subtilis* HK WalK was chosen due to the availability of a crystal structure of high resolution.[197] DNA gyrase was bound to a

pyrrolamide inhibitor (Figure 4–3) that made contacts through the -NH of the pyrrole, and the carbonyl of the amide bond through a water molecule in the binding pocket.

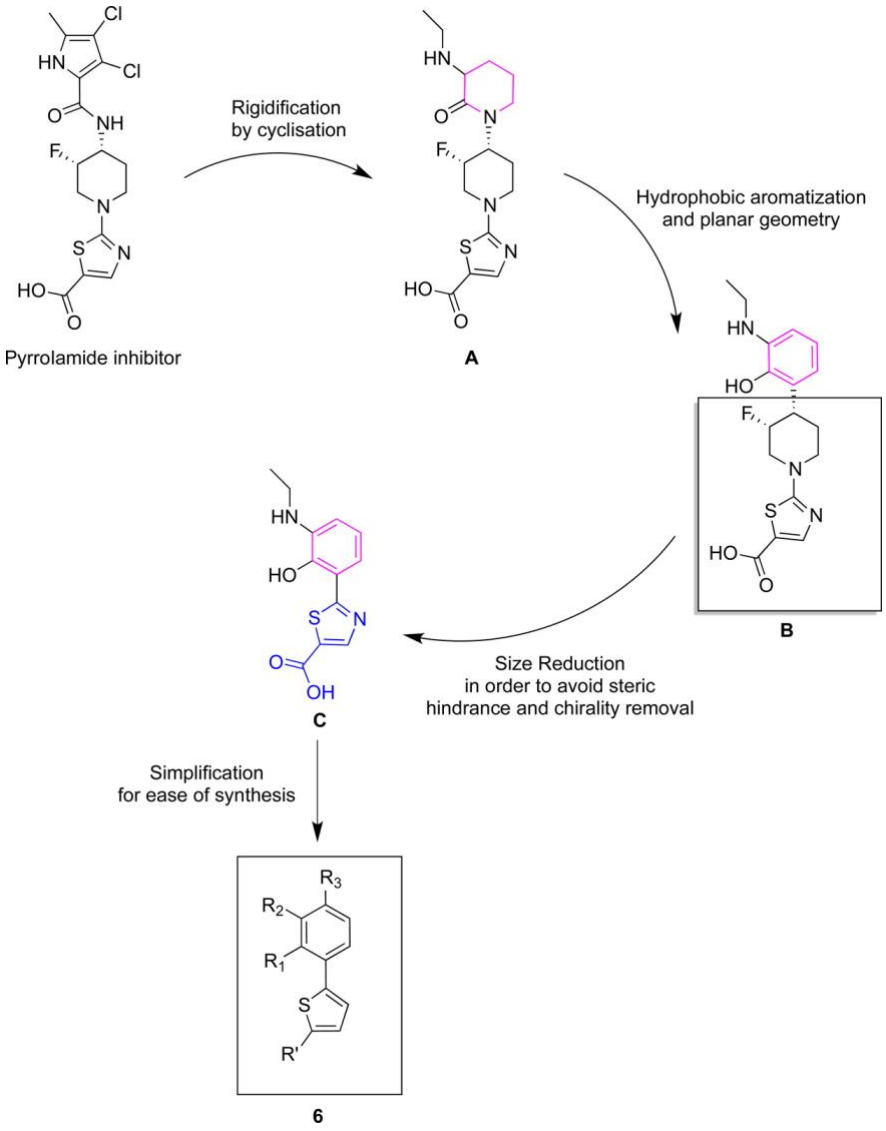

Figure 4–3 Pyrrolamide inhibitor and subsequent design strategies to produce phenyl thiopene based inhibitors.
The original pyrrolamide inhibitor scaffold (IC_{50} of 4 nM against Gyrase B) was superimposed into WalK's ATP-binding domain. The pyrrole moiety was rigidified in order to maintain hydrogen bond contacts. Aromaticity was introduced in order to generate hydrophobicity and impose a planar geometry. Size was reduced to decrease steric hinderance by removal of the piperidine ring. Chirality was removed to ease synthesis. The thiazole was replaced with thiophene in order to unlock functionalization potential. Figure used with permission from Boibessot *et al. J. Med. Chem.* **2016,** *59*(19), 8830-8847.

After docking studies and superimposing the crystal structure, rational design was used to fit three criteria to increase the ligand binding affinity to WalK.[197] The ligand was made more rigid

via cyclization of the amide bond, an aromatic ring was added to increase hydrophobicity and for its planar geometry, and the overall ligand size was reduced to decrease hindrance in the binding pocket by removing the piperidine ring (Figure 4–3). A thiophene ring was substituted for the thiazole to increase the amount of modifications that could easily be made to the compound (Figure 4–3).[197] Derivatizations of this structure were then designed to access different binding modes in the pocket and then docked to determine which ones were suitable for synthesis. This approach produced ligands that inhibited autokinase activity of WalK by ^{32}P assay, but also other histidine kinases. The ligands showed varying strengths of inhibition against different kinases, highlighting the potential specificity of designing ligands this way. The ligand 6e (Figure 4–3, 6, R_1=NO_2, R_2=H, R_3=OH, R'=H) also showed no activity against DNA gyrase or the serine/threonine kinase IreK, providing evidence for orthogonality.[197] 6e and others were further characterized and found to be bactericidal, non-hemolytic, and able to increase the antibiotic susceptibility of bacteria against other antibiotics.

4.1.2 ATP derived and serine/threonine kinase inhibitors

ATP competitive inhibitors of HKs share similar contacts with residues in the ATP-binding pocket as ATP. Naturally, one class of inhibitors designed to inhibit HKs is derived from the adenosine scaffold.[198] Great care has to be taken when designing inhibitors based off the nucleobase of ATP due to potential losses of orthogonality to other ATPases in bacteria or eukaryotes. The Carlson lab used SAR study to identify principles for designing adenine scaffold inhibitors.[198] The original screen using $HK853^6$ to identify lead compounds used FP of a non-hydrolyzable ADP-BODIPY analogue with a K_d of 6.79 ± 0.11 μM.[199] FP was measured in the absence and presence of the inhibitor (Figure 4–4).

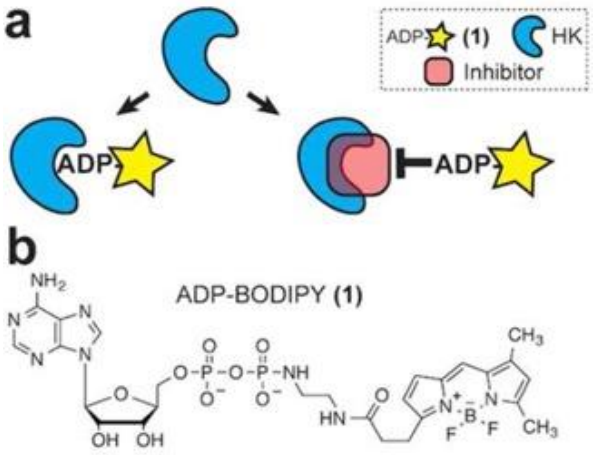

Figure 4–4 Use of ADP-BODIPY FP to identify HK inhibitors.
A) Fluorescence polarization schematic. HK (blue) is mixed either with inhibitor or no inhibitor (pink). If ADP-BODIPY binds the HK, Brownian motion of the ADP-BODIPY will be reduced and produce high fluorescence polarization readout. If ADP-BODIPY binding is blocked by an inhibitor, it will produce low fluorescence polarization readout. B) ADP-BODIPY fluorescence polarization probe. Figure used with permission from Wilke *et al. ACS Chem. Biol.* **2015**, *10*(1), 328-335.

This high-throughput screen identified inhibitors that were able to inhibit multiple HKs (HK853, CheA, VicK).[199] They built off these results by returning to 4 of the hit compounds (Figure 4–5) with low μM affinity and functionalization of the 6-position on the purine ring.[198] A second SAR study was conducted and expanded to include Eukaryotic kinase inhibitors and Hsp90 inhibitors based off the purine scaffold (Figure 4–5).

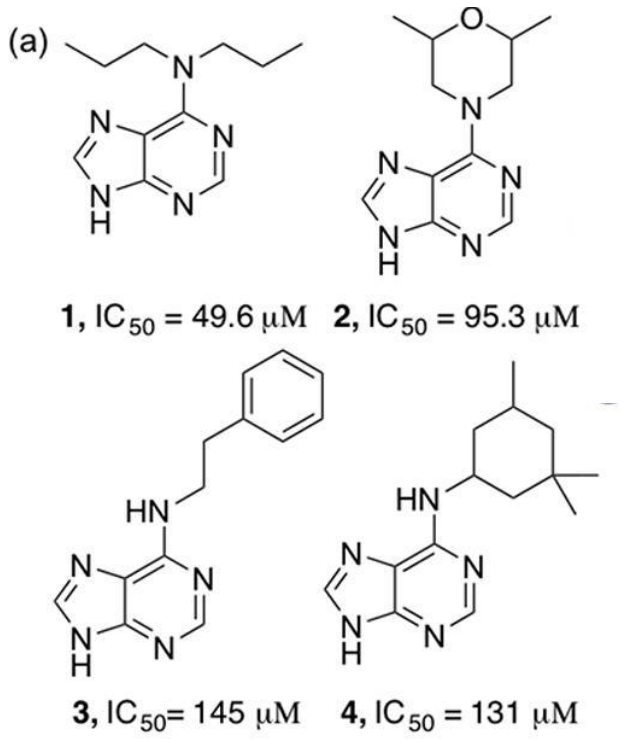

Figure 4–5 Four adenosine derivatives with functionalization at the 6-position of the purine ring.
IC_{50} refers to inhibition of HK853. Figure used with permission from Goswami *et al. J. Med. Chem.* **2017**, *60*, 8170-8182.

Idelalisib and Ibruntinib were unable to inhibit HK853 at 1.25 mM concentrations and showed distinct purine interaction differences from HK inhibitors (Figure 4–6).

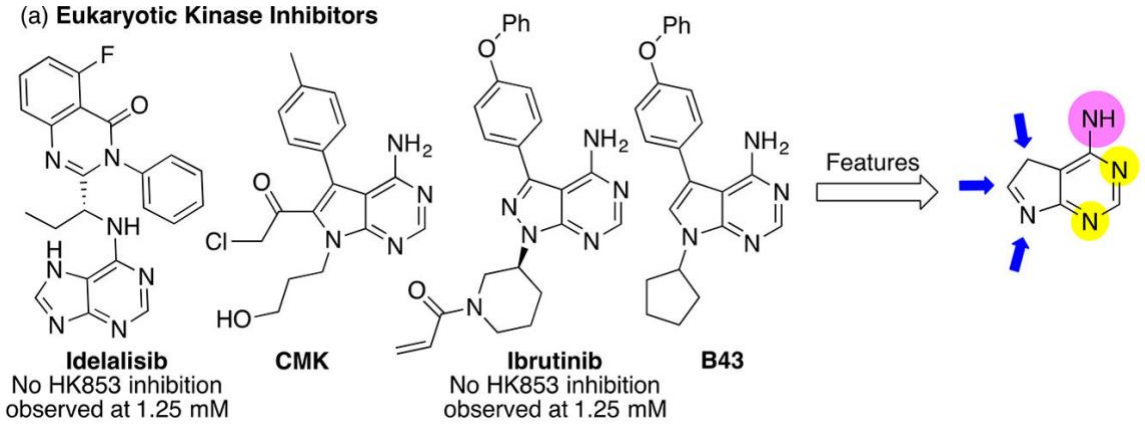

Figure 4–6 FDA approved eukaryotic kinase inhibitors Idelalisib and Ibrutinib.
Features highlighted by yellow indicate similar N-scaffold, pink spheres indicate conserved $–NH_2$ which forms an H-bond with an Asp residue, and blue arrows indicate common substitutions. Figure used with permission from Goswami *et al. J. Med. Chem.* **2017**, *60*, 8170-8182.

Hsp90 inhibitors were frequently derived from purine scaffolds and had high binding affinities for HKs. This led them to determine a set of rules to predict the inhibition strength and selectivity for Hsp90 inhibitors which enables better prediction abilities for designing future compounds (Figure 4–7A).[198]

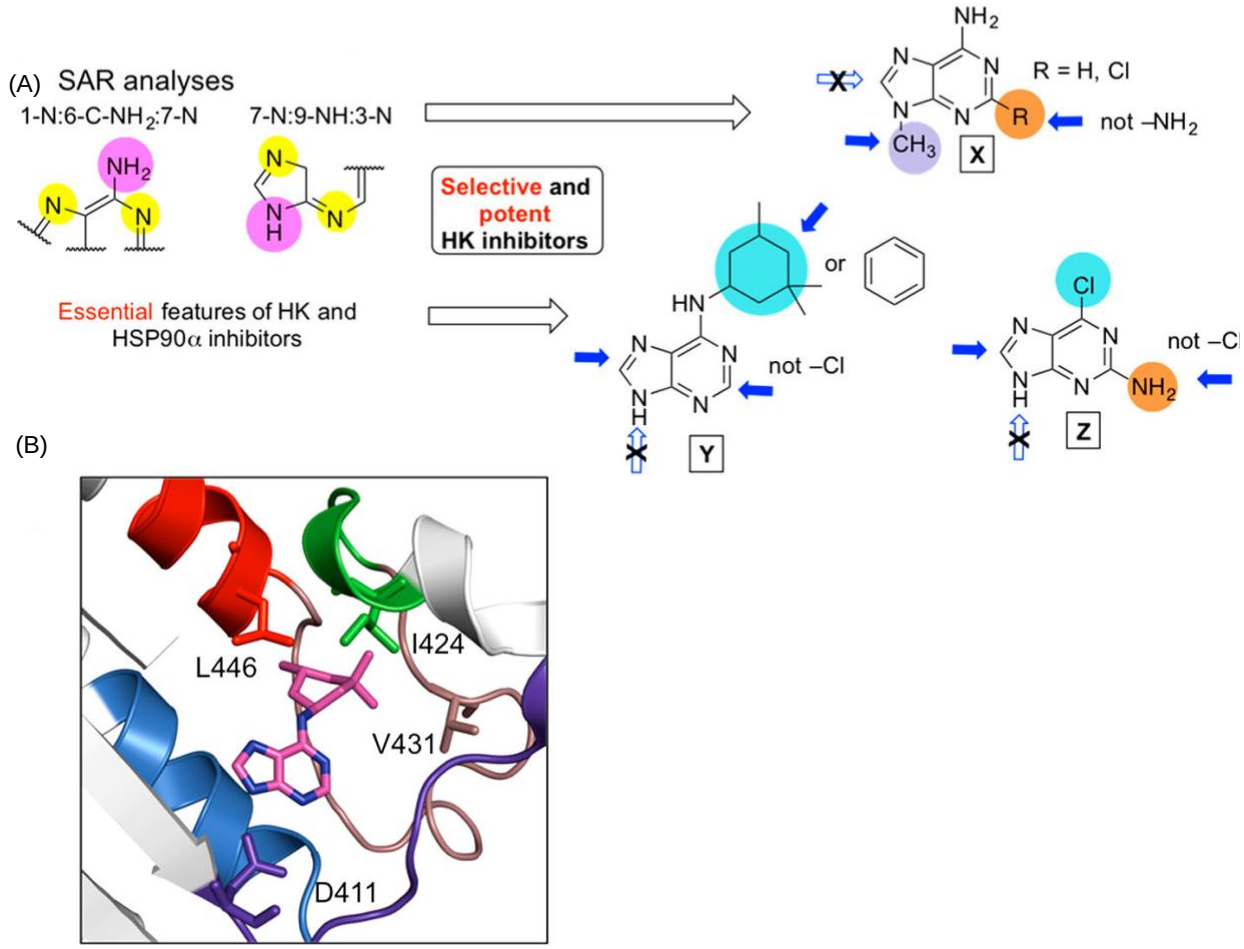

Figure 4–7 Hsp90 inhibitor rules and contacts with HK ATP-binding domain crystal structure.
A) For SAR analysis, yellow spheres indicate similar N-scaffold, pink spheres indicate –NH that contacts Asp, and blue arrows indicate substitution positions for achieving selectivity. Blue arrows with X's indicate substitution positions that produce poor HK inhibitors. B) Docked pose of compound 4. Residues belonging to N-box are colored blue, G-1 box are purple, G-2 box are red, F-box is green, and the flexible loop is brown. Figure used with permission from Goswami *et al. J. Med. Chem.* **2017**, 60, 8170-8182.

Of note, they determined the key amine residue required to interact with the aspartic acid in the active site (pink sphere), as well as which residues were interacting with different parts of the Bergerat fold: N box, G1 box, G2 box, F-box, and the flexible loop (Figure 4–7B).[198]

Because these inhibitors work off the same purine scaffold that mimics ATP in the binding pocket, it raises the question of whether inhibitors designed to inhibit other ATP-binding proteins are available to draw from. The sheer amount of work already done to develop inhibitors for serine/threonine kinases, which have been implicated in diseases from Parkinson's[200] to Alzheimer's[201], has generated a large variety of ligands to test for HK inhibition. Serine/threonine kinases (STKs) do not share the ATP-binding Bergerat fold that HKs do, meaning any inhibitors found from screening libraries of STKs would likely bind with lower affinities, but could unlock new HK inhibitor scaffolds. Using a FP-based assay[199], Wilke, *et al.* were able to screen the Roche Published Kinase Set, 222 published inhibitors that bind to STKs (Hoffmann-La Roche, Inc.).[192] Out of this set, only one hit compound was found to bind and inhibit the ATP-binding domain of HK853. Compound 32 was unable to inhibit cell growth or biofilm development in either *Staphylococcus aureus* or *Pseudomonas aeruginosa*, as measured by OD_{600} and crystal violet staining, respectively, indicating it may not be potent enough to inhibit the kinases that control virulence (Figure 4–8).

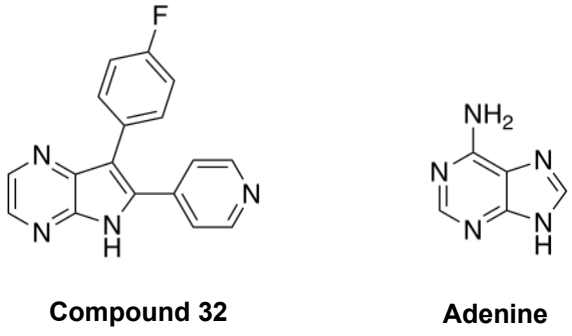

Figure 4–8 STK inhibitor screened against HK853.
Compund 32 was the only compound to displace ADP-BODIPY in fluorescence polarization assay. Compound 32 contains a pyrrolopyrazine core. Adenosine has a purine core.

Other potential issues, such as poor cell permeability, are possible. Though this was a negative result, it opens up the potential for HK inhibitors to be developed off of a pyrrolopyrazine core as opposed to a purine core (Figure 4–8).

4.1.3 Alternative library screening approaches for HK inhibitors

In addition to FP screening approaches[199,202] that look for a decrease in FP upon competitive inhibitor binding, differential scanning fluorimetry (DSF) has also been used to screen large libraries of compounds.[203] DSF works by introducing a small molecule, such as SYPRO Orange, that binds to exposed hydrophobic residues and increases in fluorescence as the protein unfolds upon heating.[204] If a ligand with strong binding affinity is added to the protein before heating, the temperature at which it unfolds will be higher compared to the non-ligand bound state. This assay is also commonly referred to as a thermal shift assay due to the thermal shift that occurs when a ligand binds to the protein of interest.[205,206] Fluorescence change by DSF is typically measured in real-time.[203]

DSF was used to screen a library of compounds (Chem-X-Infinity, Romanville, France) against two CA domains of HKs, WalK[207] and NblS[208] from *Streptococcus pneumonia* and *Synechococcus sp.* PCC7942, respectively. DSF enabled fast screening of the library against two CA domains. Due to the flexible ATP-lid of the CA domain[188], finding compounds that could potentially work independent of the ATP-lid would enable generation of rules for broad HK inhibitors. Successful fragments were labeled F1 and F2 (Figure 4–9).

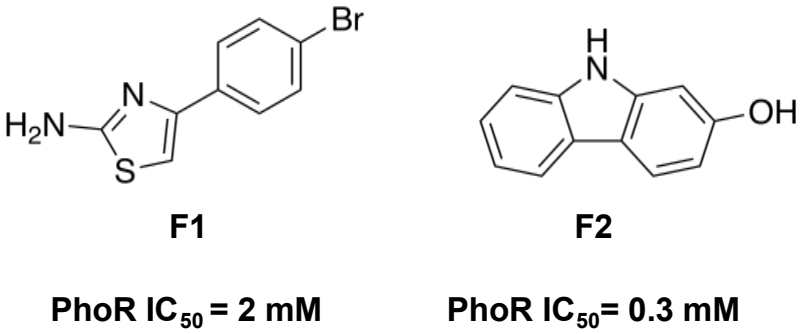

Figure 4–9 Fragments identified to inhibit HK autophosphorylation activity.
F1 and F2 were identified using differential scanning fluorimetry (DSF) as ligands of HK CA domains. IC_{50} for inhibition of the HK PhoR are included.

These compound hits were then followed up with autokinase ^{32}P assays to test for inhibition against both WalK and NblS with both inhibiting autokinase activity *in vitro*.[209] Coupled with this approach, Velikova *et al.* used an *in silico* screen called structure-based virtual screening using an ensemble of HK CA domains to overcome the flexibility in the domain.[210] Using three crystallized CA domains *T. maritima* HK853 (PDB: 3DGE)[17], *T. maritima* CheA (PDB: 1I58)[211], and *G. stearothermophilus* KinB (PDB: 3D36)[212] that were solved in the presence of a nucleotide, screening for general HK inhibitors could be completed. Hits S5 and S6 were added to a pool with F1 and F2 and similar compounds to both sets were then identified using extended connectivity fingerprinting.[213] Compounds identified this way will share high similarity with parent compounds, only small changes will occur to the structures that could cause increased or decreased effects (i.e. activity cliffs). Compounds showing strong inhibition were used for treatment of Gram-negative and Gram-positive bacterial cultures to test for antibiotic activity. Successful antibiotics were then tested against multi-drug resistant clinical isolates including MRSA (methicillin-resistant *Staphylococcus aureus*) and showed varying amounts of success.[209] Using these inhibitors, docking studies were also performed and compared to the binding capabilities of ADP. Like other HK inhibitors, successful docking showed that compounds with high success of inhibition, for example, S1.14 from the extended connectivity fingerprinting, make contact with the conserved aspartate residue located in the G1 box.[209] This conserved aspartate forms a hydrogen bond with the N6 amino group of the pyrimidine group of adenine when bound to ATP/ADP. This bond helps to give specificity for ATP/ADP in the binding pocket, so it follows that stronger inhibitors would be able to access this residue. This work overall has helped to establish that precise recognition of the essential aspartate interaction in the G1 box are required for high binding affinity.

4.1.4 Hsp90 inhibitors

The molecular chaperone Hsp90 has been a popular target as a cancer drug therapy target for over 20 years due to its role in maintaining stability of proteins related to cell proliferation and cell cycle regulation.[189] Inhibitors of Hsp90 have used a variety of scaffolds including diarylisoxazole[214], diarylpyrazole[215], 2-amino-6-halopurine[216], and imidazopyridine[217] (Figure 4–10).

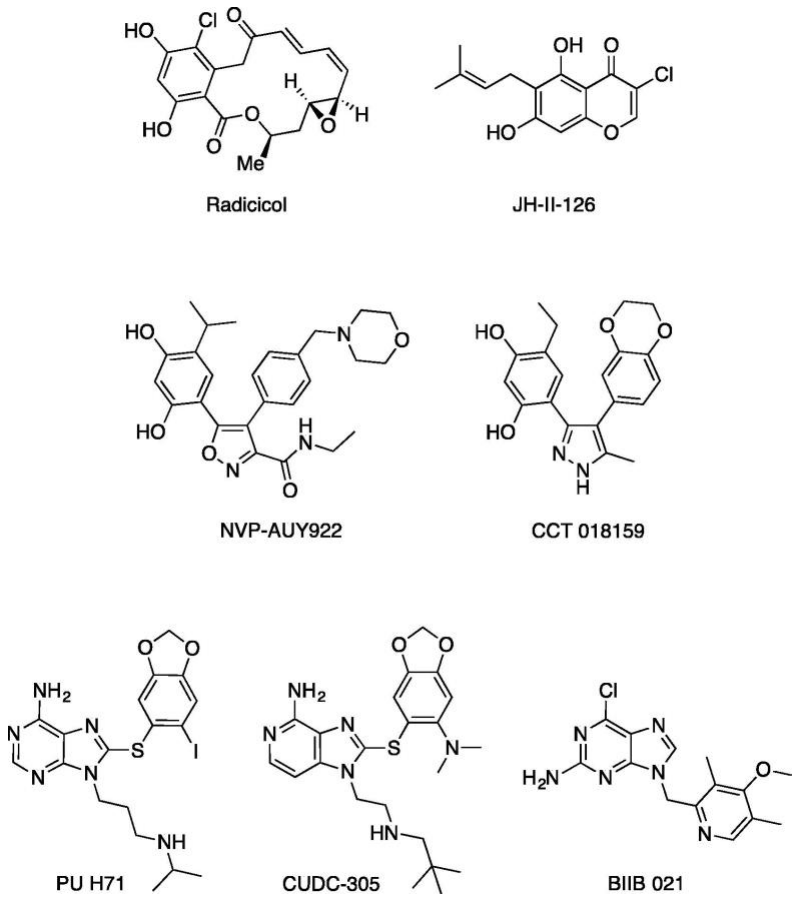

Figure 4–10 Commercially available Hsp90 inhibitors.
Figure used with permission from Vo *et al. Bioorg. Med. Chem.* **2017**, *27*(23), 5235-5244.

Drug compounds based off of these scaffolds have shown strong binding kinetics and in some cases efficacy against different types of cancer.[217] Due to the wide range of compounds available, Hsp90 inhibitors have provided an array of starting points for developing HK inhibitors.

Early working transitioning Hsp90 compounds to bacterial HKs showed promise testing the compound Radicicol on the HK PhoQ, found in the major food-borne pathogen *Salmonella*.[196] PhoQ was chosen because it is the sensor kinase of the PhoP/PhoQ two-component system which is linked the virulence of *Salmonella*.[218] Radicicol had a K_d of 715 ± 78 µM, determined by monitoring changes in chemical shifts using Nuclear Magnetic Resonance (NMR).[196] Radicicol binds to Hsp90 at a much lower affinity (K_d = 19 nM)[219] indicating that there was likely differences around the ATP-binding pocket not related to the Bergerat fold. In order to answer this, the PhoQ ATP-binding domain was crystallized in the presence of Radicicol and the crystal structure was compared Hsp90 bound to Radicicol (Figure 4–11A).

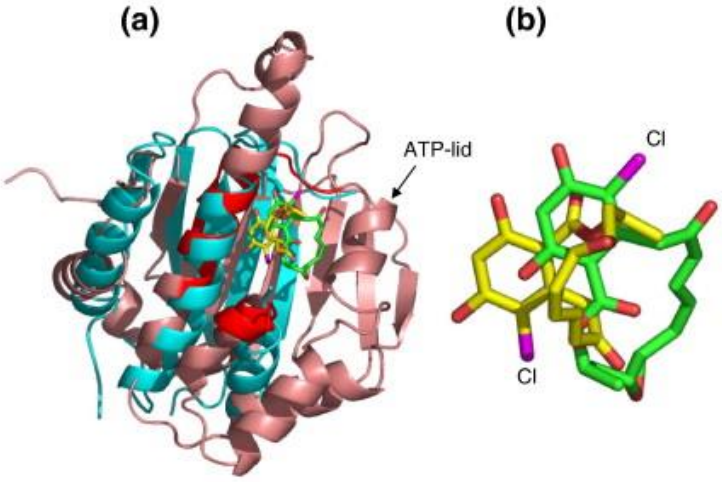

Figure 4–11 Comparison of radicicol binding to Hsp90 and PhoQ's CA domain.
A) Hsp90 bound to radicicol (PDB 1BGQ) (pink) was superimposed on PhoQ CA domain bound to radicicol (PDB 3CGY) (blue). B) Configuration of radicicol in Hsp90 (yellow) and PhoQ (green). Figure used with permission from Guarnieri, *et al. J. Mol. Biol.* **2008**, *379*(1), 82-93.

It was determined that Radicicol did in fact bind the pocket of PhoQ differently, resulting in an almost 180º flip in the orientation of the macrocycle in the binding pocket (Figure 4–11B).[196] The orientation difference accounts of the different binding affinities and further, it was determined that PhoQ did not share a similar ATP-lid relative to Hsp90. This was not surprising as the GHKL family comprises a diverse set of ATP-lid conformations.[188] This difference in ATP-

lid conformation showed that these compounds could eventually be tuned to bind HKs over other members of the GHKL family, therefore increasing specificity for the HK. Increased specificity could make it a more viable clinical drug in the future.

As a high-throughput method for screening compounds that bind the HK ATP-binding domain, an assay was developed using PhoQ where a fluorescent ATP analog, TNP-ATP [2'(3')-*O*-(2,4,6-trinitrophenyl)adenosine 5'-triphosphate], was displaced from the ATP-binding domain by competitive inhibitors.[220] TNP-ATP had been previously shown to bind to the HK CheA, and functions by increasing in fluorescence when it is stabilized in a hydrophobic environment, such as the ATP-binding pocket of a protein.[202,221] PhoQ showed weak affinity for the probe (~294 μM), and therefore high concentrations of protein and probe were required to detect changes in binding by fluorescence limiting its utility in screening compounds.

Vo, *et al.*, working under our collaborator Jimmy Blair at Williams College, designed additional studies motivated by radicicol binding to PhoQ[196] and earlier work with thiophene-based DNA gyrase inhibitors that also showed affinity for the HK WalK.[197] Using six commercially available inhibitors and the HK CckA from *C. crescentus*[107], a thermal shift assay[206] was used to screen compounds against CckA. Two test compounds, NVP-AUY922[214] and CCT018159[215], (Figure 4–10) displayed binding to CckA.[222] They followed up these results using a coupled-enzyme assay which is designed to measure ATPase activity *in vitro*.

The coupled enzyme assay utilizes pyruvate kinase and lactate dehydrogenase. Upon addition of ATP, the ATPase of interest dephosphorylates ATP resulting in one molecule of ADP being produced. The pyruvate kinase can use one molecule of ADP and PEP to generate pyruvate and ATP. The ATP can then be reused as a substrate by the ATPase resulting in a cycling of product until the PEP is depleted. As the pyruvate is generated, the lactate dehydrogenase is able

to oxidize NADH (absorbance 340 nm) to NAD^+ (absorbance 260 nm) (Figure 3–13).[177] The decrease in absorbance at 340 nm as a function of time can be readout in a plate reader format and the kinetics and the volume of the reaction can be adapted to fit a range of ATPase rates.

Using the coupled enzyme assay, inhibition of CckA autophosphorylation activity occurred in the presence of both NVP-AUY922 and CCT018159 at concentrations below 50 μM.[176] Due to the similarities in the two compounds (two aromatic rings, one of which is a resorcinol ring, connected to a pyrazole ring or an isoxazole), a SAR study was completed using CCT018159 due to ease of synthesis and tighter binding affinity. The library was designed to test the impact of changing the ethyl group in the 6-position of the resorcinol ring on Hsp90 activity.[215] Substitution of the pyrazole and benzo were also explored to test sterics and electronics.[176]

In order to test the SAR in the context of a broad spectrum antibiotic, two other HKs, PhoQ[153] and DivJ[223] were chosen for coupled-enzyme assays because of diversity in the ATP-binding sites. Though both HKs share the Bergerat fold for ATP-binding, variety in residues in the ATP lid and around the ATP-binding site can differ between HKs. For PhoQ, a tyrosine at position 394 (Y394) is involved in the π-π stacking interactions, and in DivJ, a phenylalanine is involved. However, CckA has an alanine at position 438 (A438), eliminating π-π stacking (Figure 4–12).

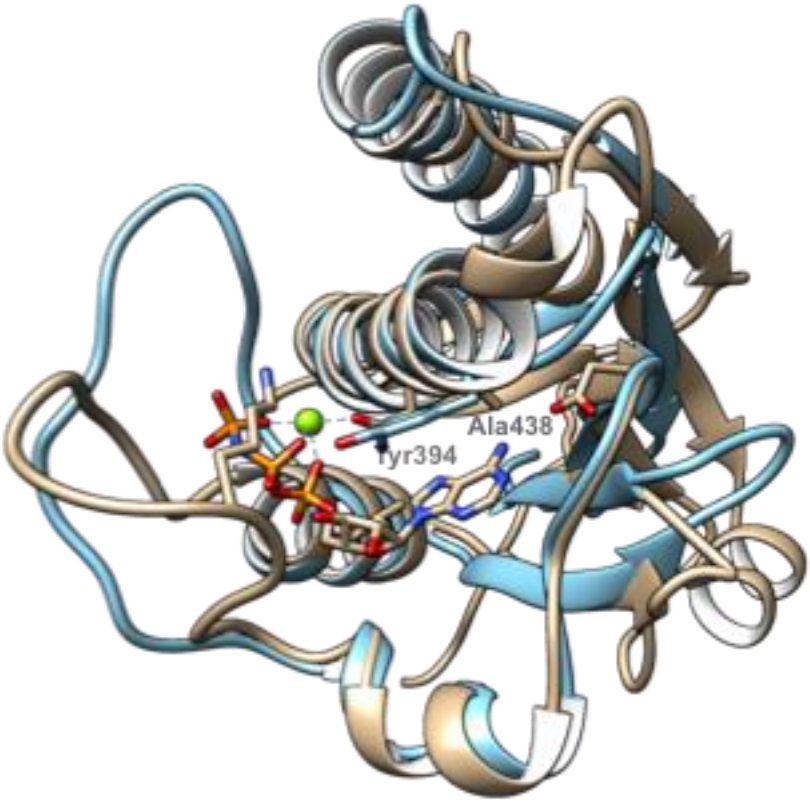

Figure 4–12 Overlay of PhoQ (PDB 1ID0) and CckA (5IDM) CA domains bound to AMP-PNP.
CckA (brown) and PhoQ (blue) are overlaid to show the position of Tyr394 (PhoQ) and Ala438 (CckA). AMPPNP bound to PhoQ is shown. Tyr394 of PhoQ makes π-π stacks with the adenosine nucleobase while the Ala438 of CckA does not. Crystal structures overlayed using Chimera.[7]

This suite of residues could help to identify SARs and properties that make for a broad spectrum HK antibiotic.

Using a ^{32}P dot blot radiolabeling assay, inhibition of DivJ and PhoQ by select compounds was determined. Of note, NVP-AUY922 did not inhibit DivJ autophosphorylation while CCT018159 was able to inhibit both PhoQ (9% activity) and DivJ (70% activity) at 500 µM compound.[176] CckA was inhibited fully by both compounds in this assay, which may have to do with the alanine in the CckA ATP-binding pocket. Hsp90 shares an alanine in this same position indicating that the steric bulk of the tyrosine and phenylalanine of PhoQ and DivJ, respectively, may interfere with compound binding to the same degree as Hsp90 and decreasing effectiveness

as a broad-spectrum antibiotic. The differences in this position may also make it possible to design HK inhibitors that target kinases containing an alanine over ones with an aromatic group.

To determine the mechanism of action of one of the inhibitors, CckA autophosphorylation using the coupled enzyme assay was performed by varying concentrations of ATP and the inhibitor CDV009, an analogue of CCT018159 where the benzodioxine moiety has been replaced with a 4-methoxyphenyl moiety (Figure 4–13).[176]

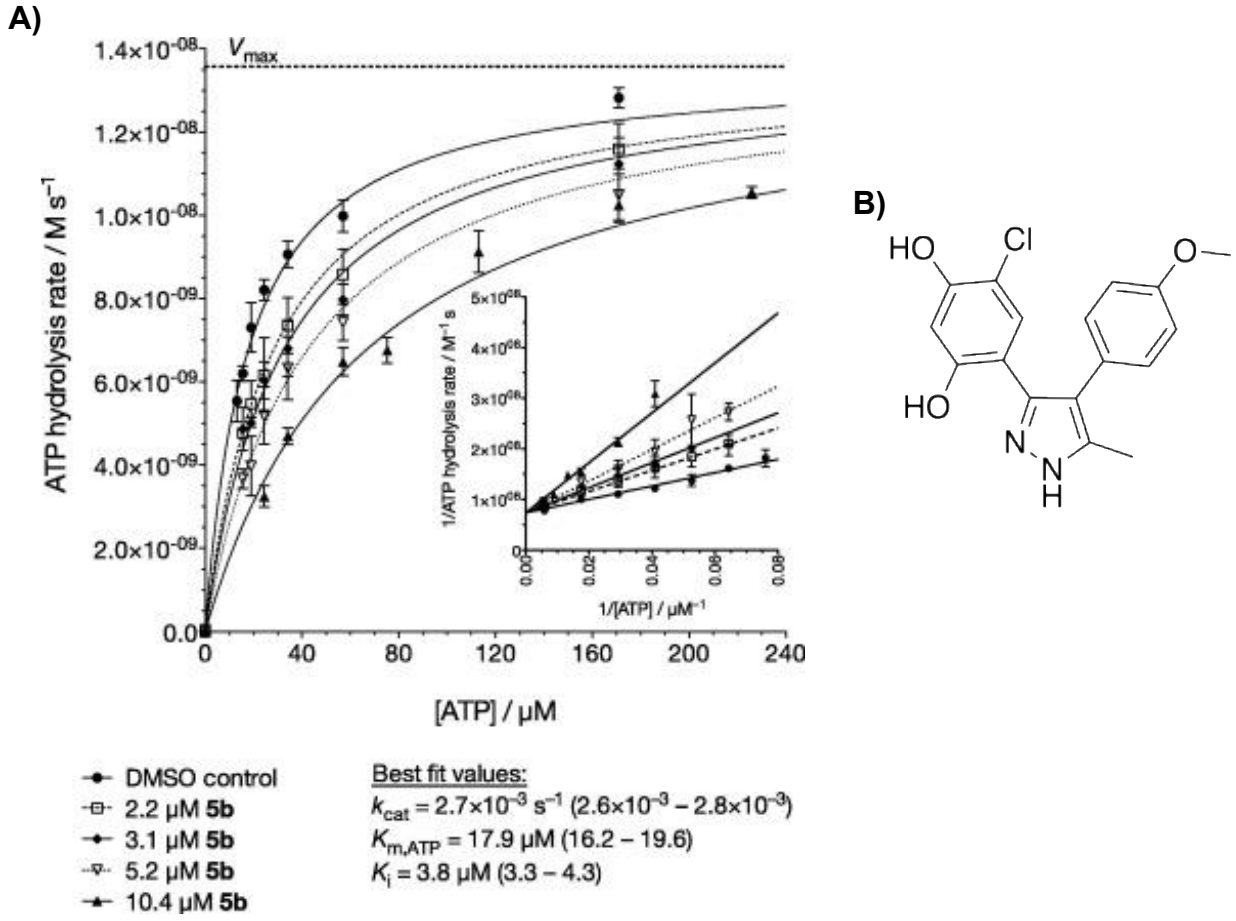

Figure 4–13 CckA inhibition by compound CDV009.
A) Plot of rate vs. substrate concentration for CckA using the ATPase coupled enzyme assay. CDV009 was added to inhibit CckA autophosphorylation. Inset is the Lineweaver-Burk plot of outer graph. B) Compound CDV009 (5b) used in inhibition study in A). Figure used with permission from Vo *et al. Bioorg. Med. Chem.* **2017**, *27*(23), 5235-5244.

CDV009 was generated through a panel of compounds based off the work done by Dymock, *et al.* (Figure 19B).[224] Dymock *et al.* generated new analogues of the Hsp90 inhibitor

CCT018159 by using guided design based off CCT018159 cocrystallized with the N-terminal domain of Hsp90.[225] By measuring the initial velocity of the reaction at the varied ATP and inhibitor concentrations, the data was fit to a competitive model of inhibition. Docking studies suggest that the compounds interacted with the conserved aspartate via the N6 amine hydrogen bond for both CckA and PhoQ. CCT018159 contained an ethyl group, whereas CDV009 substituted a chlorine in that position, a better group for sharing space near the asparagine lid of CckA due to favorable electronics. Therefore, future design of HK inhibitors could revolve around the protein-ligand contacts in the N-box. The diversity shown here between CckA (alanine), DivJ (phenylalanine), and PhoQ (tyrosine) demonstrates that future inhibitor design can be broad enough to target all three types of kinases, or specifically target only one group.

To determine if these compounds were able to inhibit activity *in vivo*, broth dilution assays were conducted using *C. crescentus* (NA1000) and *E. coli* (DC2). DC2 was used to differentiate between antibiotic activity from HK inhibition and activity from membrane disruption. DC2 has membrane defects that make it more susceptible to antibiotics that must be cell permeable.[226] CCT018159, the Hsp90 inhibitor, was able to inhibit bacterial growth at lower concentrations (150-225 µM MIC) than CDV009 (225 µM MIC), although CDV009 is better stabilized in CckA *in vitro* (IC_{50} of 28 µM vs. 12.5 µM, respectively). To gain a better understanding of the mechanism of action, we worked with our collaborator Jimmy Blair, previously of Williams College, to test a small panel of inhibitors from this study (CCT018159, CDV008, CDV009) as well as new inhibitors based off a triazole ring rather than a pyrazole ring. We chose *C. crescentus* NA1000 as a model because its signaling pathways are well-understood.[137] We set out to test the ability of the compounds to enter the cell and target the HK CckA using a FRET sensor approach and compound effects on downstream signals such as chromosome replication and CtrA phosphorylation.

4.2 Results

4.2.1 *In vivo* screening of HK inhibitors using the CckA-FRET biosensor

Described in Chapter 2, the CckA-FRET biosensor was designed using CckA from *C. crescentus* in order to study impact of different signals into CckA. Because the CckA-FRET biosensor was functional and able to replace wild-type CckA in cells, we suspected that the FRET sensor could be used to determine if HK inhibitors bind CckA within living *C. crescentus* cells. Before testing for changes in FRET using the sensor, we first determined the impact the inhibitors had upon cell growth. At a concentration of 300 µM, both CDV008 and CDV009 showed reduced cell growth, while NVP-AUY22 did not which is consistent with Vo *et al.* (Figure 4–14).[176]

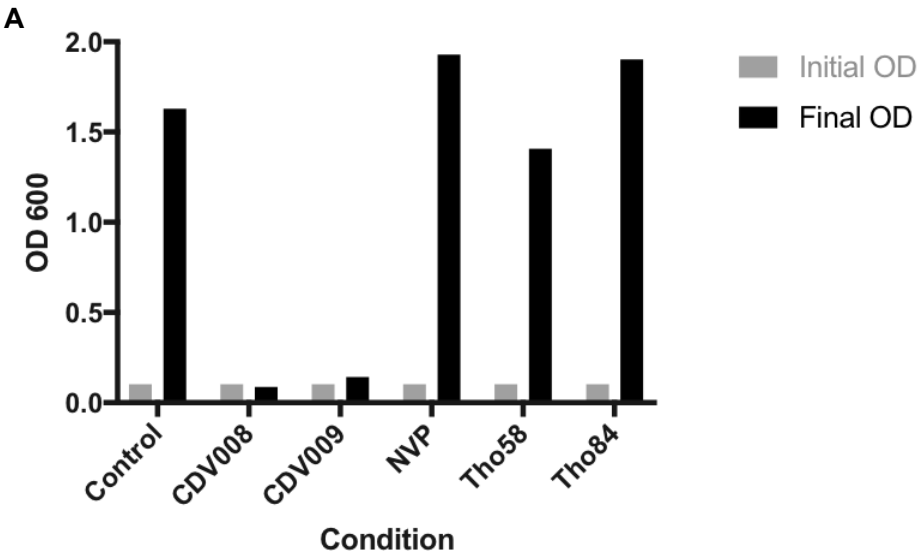

Figure 4–14 Inhibition of cell growth by HK targeting antibiotics.
A) NA1000 cultures were grown to an OD_{600} of ~0.1 in M2G, split, then 0.3 mM concentrations of each condition were added and OD was taken 24 hours later. The control was DMSO. CDV008 and CDV009 showed inhibition of growth while NVP, Tho58, and Tho84 did not inhibit growth. NVP-AUY22 is commercially available. Our collaborator Jimmy Blair at Williams College synthesized all other compounds.

Compounds Tho84 and Tho58, which utilize diaryltriazole rather than diarylpyrazole did not show inhibitory effects (Figure 4–14), however morphological phenotypes became prevalent

after incubation with either inhibitor at 0.3 mM for 130 minutes. Five phenotypes were catalogued: Alive with no granules, alive with granules, dead with no granules, dead with granules, and dead and swollen (Figure 4–15).

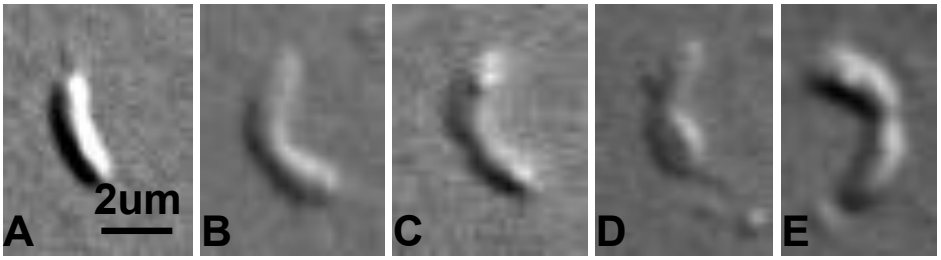

Figure 4–15 Cell phenotypes induced by inhibitors.
A) Alive cell with no granules (normal). B), Dead cell with no granules. C), Dead cell with granules. D), Dead cell that is swollen. E), Alive cell with granules.

The CDV008 and CDV009 both showed an increase in percentage of dead cells in the population relative to DMSO only from 0% to ~75% (Data not shown). The most commonly observed granules in *C. crescentus* are phosphate granules, which often form under stress conditions.[227] Previous work has shown a similar phenotype to occur in cells when the response regulator that regulates genes involved in cell wall envelope synthesis (*i.e.* CenR) is overexpressed in cells as either the wild-type sequence or phosphomimetic.[91] CenR is regulated by the histidine kinase CenK.[91] This led us to speculate that the observed phenotypes occur through histidine kinase targeting.

Past studies have relied upon *in vitro* tests to confirm inhibitor binding to CckA in aqueous buffer, however we hypothesized that our designed CckA-FRET biosensor may be able to detect inhibitor binding to CckA in the context of the cell. We tested if our CckA-FRET biosensor was sensitive to the addition of HK-directed inhibitors to culture media (Figure 4–16).

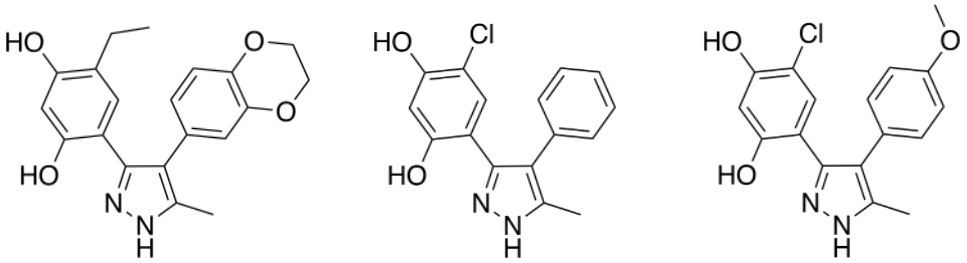

Figure 4–16 Chemical inhibitors used on CckA-FRET biosensor.

The CckA-FRET biosensor retains the ATP-binding domain required for inhibitor binding, making it a good candidate to test for binding *in vivo.* We followed the standard imaging conditions for the antibiotic assay but included an extra growth period for incubation with the inhibitor. After 210 minutes of incubation, CCT018159 and CDV009 both resulted in increased FRET compared to the DMSO control (Figure 4–17).

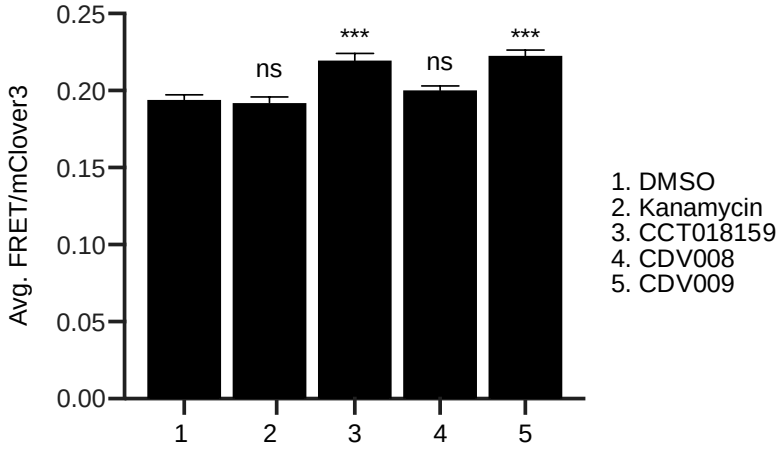

Figure 4–17 CckA-FRET biosensor can be used to detect histidine kinase antibiotics *in vivo*.
Cells with CckA-FRET biosensor expressed were grown overnight at 28ºC to OD_{600} of 0.1. A final concentration of 0.03% xylose was used to induce CckA-FRET biosensor expression. Cells were imaged to verify expression then inhibitors were added at these final concentrations: 28 µM CCT018159, 17.5 µM CDV008, 12.5 µM CDV009, 2 µL DMSO, and 2.5 µg/mL Kanamycin. DMSO and kanamycin were used as controls that should not impact the CckA-FRET biosensor. N>100 for all trials, comprised of three separate biological replicates. *** indicates $p<0.0005$.

Kanamycin, the negative control, did not cause a change in FRET, which is consistent with its inhibitory effects on the 30S ribosomal subunit (Figure 4–17).[228] Interestingly, CDV008 did not

cause a change in FRET (Figure 4–17). The difference in CDV008 and CDV009 is the presence of a methoxy group in the para position of the phenyl ring (Figure 4–16). Both compounds have similar IC_{50} values (CDV008 = 17.5 µM, CDV009 = 12.5 µM) for CckA. Based off docking studies done by Vo, *et al.*, the phenyl ring is pointed toward the ATP lid and G-box. The methoxy of CDV009 may be better stabilized in the binding pocket due to interactions with H-bond residues of the ATP-lid and G-box. The lack of methoxy may also open CDV008 as a scaffold to inhibiting other HKs as a less-bulky alternative to CDV009. CDV008 could also be inhibited from crossing the cell membrane. We did see membrane defects at high concentrations similar to what observations made by Vo *et al.*, so CDV008 may be exerting antibiotic activity through membrane disruption rather than HK inhibition though this is unlikely due to being well below the concentrations where membrane disruption was observed.[176] These results using the CckA-FRET biosensor indicate that CCT018159 and CDV009 are both able to target CckA, while CDV008 may be inhibiting another target (other GHKL fold proteins).

4.2.2 Evaluating impact of Hsp90 analogs on downstream signals *in vivo*

The CckA-FRET biosensor indicates binding interaction between Hsp90 analogs and CckA, so we next asked if this resulted in misregulation of downstream CckA-mediated phenotypes (Figure 4–18).

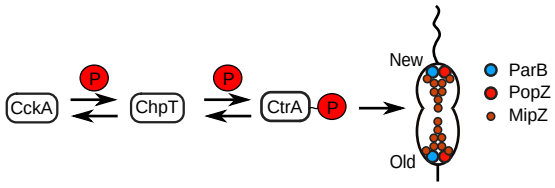

Figure 4–18 CckA regulation of CtrA phosphorylation and downstream effects.
CckA is able to autophosphorylate and transfer a phosphate to ChpT, which then transfers the phosphate to CtrA. This process can also go in reverse. When phosphorylation is properly regulated, PopZ and ParB localization at the new and old cell poles occurs, and Mipz is able to form a gradient within cells.

We focused on CckA outputs related to CtrA phosphorylation. CtrA phosphorylation is the output of CckA kinase activity so we chose factors related to CtrA phosphorylation to observe. A group of polarly localized proteins are controlled by CtrA~P levels in the cell. The chromosome partioning protein ParB binds the *parS* centromere near the origin of replication and segregates the chromosome to both cell poles (Figure 4–18).[229] The polar organelle protein PopZ is a self-assembled scaffolding protein that localizes to the old and new cell poles.[132] PopZ is required for ParB to localize to both cell poles (Figure 4–18). The partitioning of these proteins is controlled downstream of CckA by CtrA~P levels in the cell.[112] One more protein related to CtrA~P levels in the cell that can be studied is MipZ. MipZ, the division site placement protein, maintains localization at the cell poles and decreases in concentration towards the midcell where it ensures placement of FtsZ, the division ring protein (Figure 4–18).[230] MipZ localization is controlled by CtrA~P through the localization of ParB[230]. We began by screening CCT018159 using the Phos-tag method to determine impact of the inhibitor on CtrA~P phosphorylation levels in cells through CckA.

4.2.3 Effect of inhibitor on CtrA~P levels *in vivo*

Phos-tag is a magnesium-chelating small molecule that reversibly binds phosphomonoester dianions (Figure 4–19A).[231]

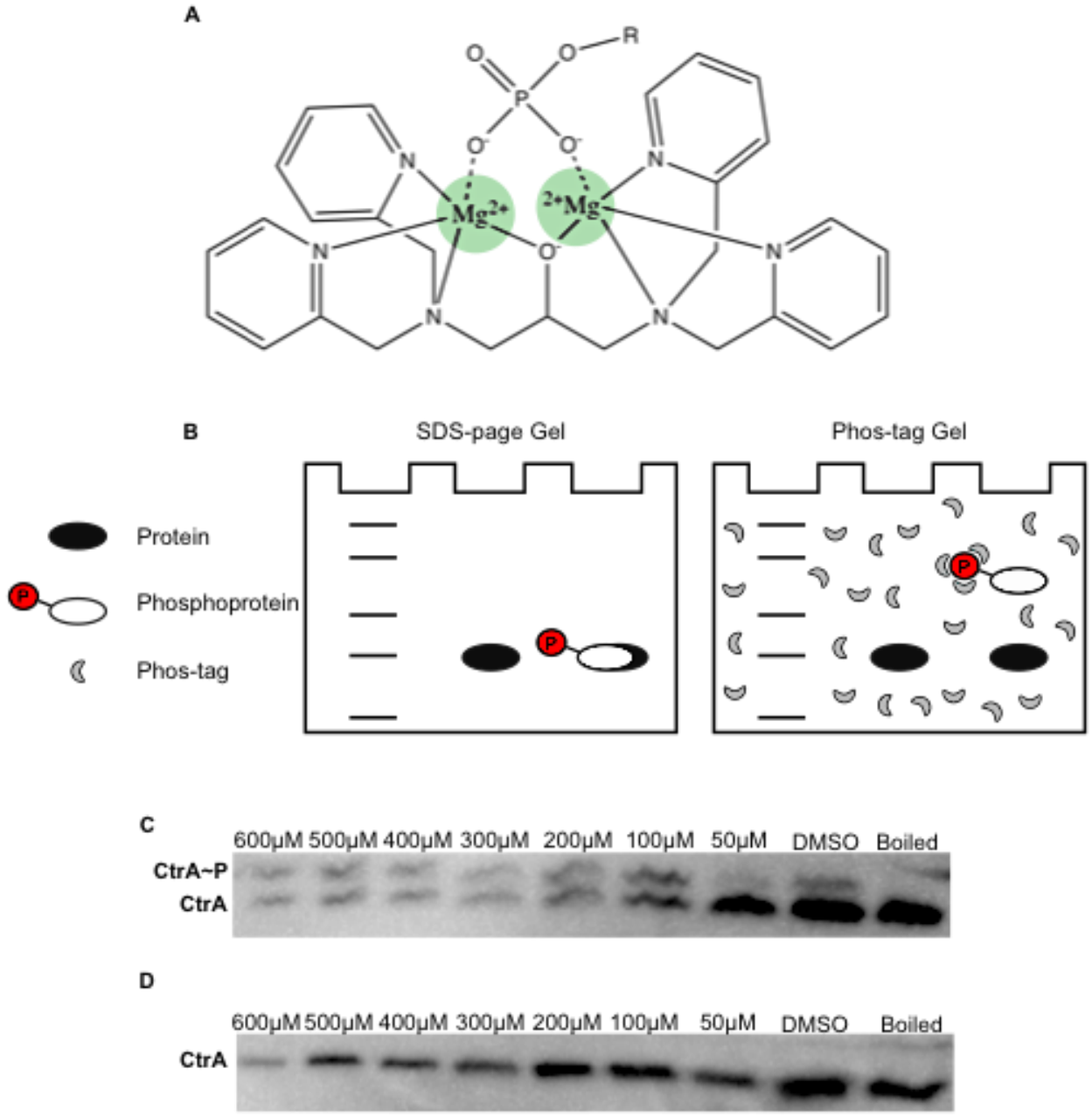

Figure 4–19 CtrA Phostag to measure CtrA~P levels upon addition of CCT018159.
A) Phos-tag reagent uses Mg^{2+} to reversibly bind a phospomonoester dianion linked to a protein. B) Phos-tag schematic depicting how proteins that are unphosphorylated or phosphorylated will run at the same rate on a gel. Upon addition of Phos-tag to a gel, phosphorylated proteins will run at a slower rate and bands of phosphorylated and unphosphorylated proteins can be resolved. C) A DivK cold sensitive mutant was grown overnight at 28ºC in M2G to an OD_{600} of 0.2. The culture was split and inhibitor or control was added. Cells were grown at 20ºC for three hours with inhibitor. Phos-tag gel of NA1000 grown in inhibitor at specified concentrations ranging from 600 μM to 50 μM. See Methods for CtrA SDS-PAGE and Western Blot conditions. DMSO was used as a negative control. Boiled samples were made to dephosphorylate CtrA. Higher bands are phosphorylated CtrA, lower bands are unphosphorylated CtrA. D) CtrA Western blot (no Phos-tag gel) for loading control of CtrA. See Methods for details.

Addition of this compound to an SDS-PAGE gel can separate phosphorylated protein from non-phosphorylated protein (Figure 4–19B). We used a DivK cold sensitive strain (DivKcs) to increase basal levels of CtrA~P in cells.[119] We then measured the effect of CtrA~P levels upon addition of CCT018159 using a Phos-tag gel coupled with a western blot. A western blot of CtrA was also done to confirm CtrA levels in samples. At inhibitor concentrations less than 100 µM, the inhibitor causes a decrease in CtrA~P to less than 5%, compared to the DMSO control, which is about 15% CtrA~P (Figure 4–19C). At concentrations of 100 µM and greater, the amount of CtrA~P increases to 50%. Therefore, inhibitor concentrations below 100 µM decrease in kinase activity, and inhibitor concentrations above 100 µM increase in kinase activity. We can conclude that the increase in FRET signal upon addition of CCT018159 (Figure 4–17) was a result of decreased CckA kinase activity. 12.5 µM CCT01819 for the CckA-FRET biosensor assay was between the DMSO and 50 µM condition in the Phos-tag assay, in which we saw a decrease in CtrA~P levels. A decrease CckA kinase activity could result from either direct competition by the inhibitor or indirect effects due to changes in cyclic di-GMP upregulation. Direct competition is viable because CCT018159 can bind and inhibit CckA *in vitro*.[176] Cyclic di-GMP dependent inhibition could occur if the inhibitor is leading to the activation of diguanylate cyclases (cyclic di-GMP producing proteins) or downregulation of phosphodiesterases. Both sets of enzymes can be directly controlled by histidine kinase phosphorylation.[136]

When levels of CCT018159 are above 100 µM, CtrA~P levels become almost even with CtrA levels (Figure 4–19C). This high concentration effect could be due to a loss of CckA phosphatase activity or a general inactivation of cellular processes due to cell death caused by the inhibitor. To further test the effect of CtrA~P levels increasing above 100 µM of CCT018159, we chose to look at CtrA~P-dependent degradation in cells.

4.2.4 Addition of CCT018159 inhibitor results in loss of CtrA degradation at the old cell pole upon cell division

In vitro confirmation has proven that CCT018159 does inhibit CckA kinase activity. If CckA kinase activity is inhibited, phosphorylation of CtrA downstream will also be inhibited. To directly test for inhibition of CckA phosphotransfer we used a strain of CtrA in *C. crescentus* where YFP was inserted before the last 15 amino acids of the CtrA sequence (CtrA-YFP-15aa). Upon expression, CtrA-YFP-15aa appears to localize to only new cell (swarmer) pole.[232] This asymmetric distribution of CtrA occurs due to the localized activity of ClpXP protease at the old cell (stalk) pole. Upon division, the stalk-localized ClpXP begins degrading CtrA-YFP-15aa resulting in a loss of fluorescence. CpdR triggers ClpXP localization at the stalked cell pole and is phosphorylated by the same pathway as CtrA (Figure 4–20A).[233]

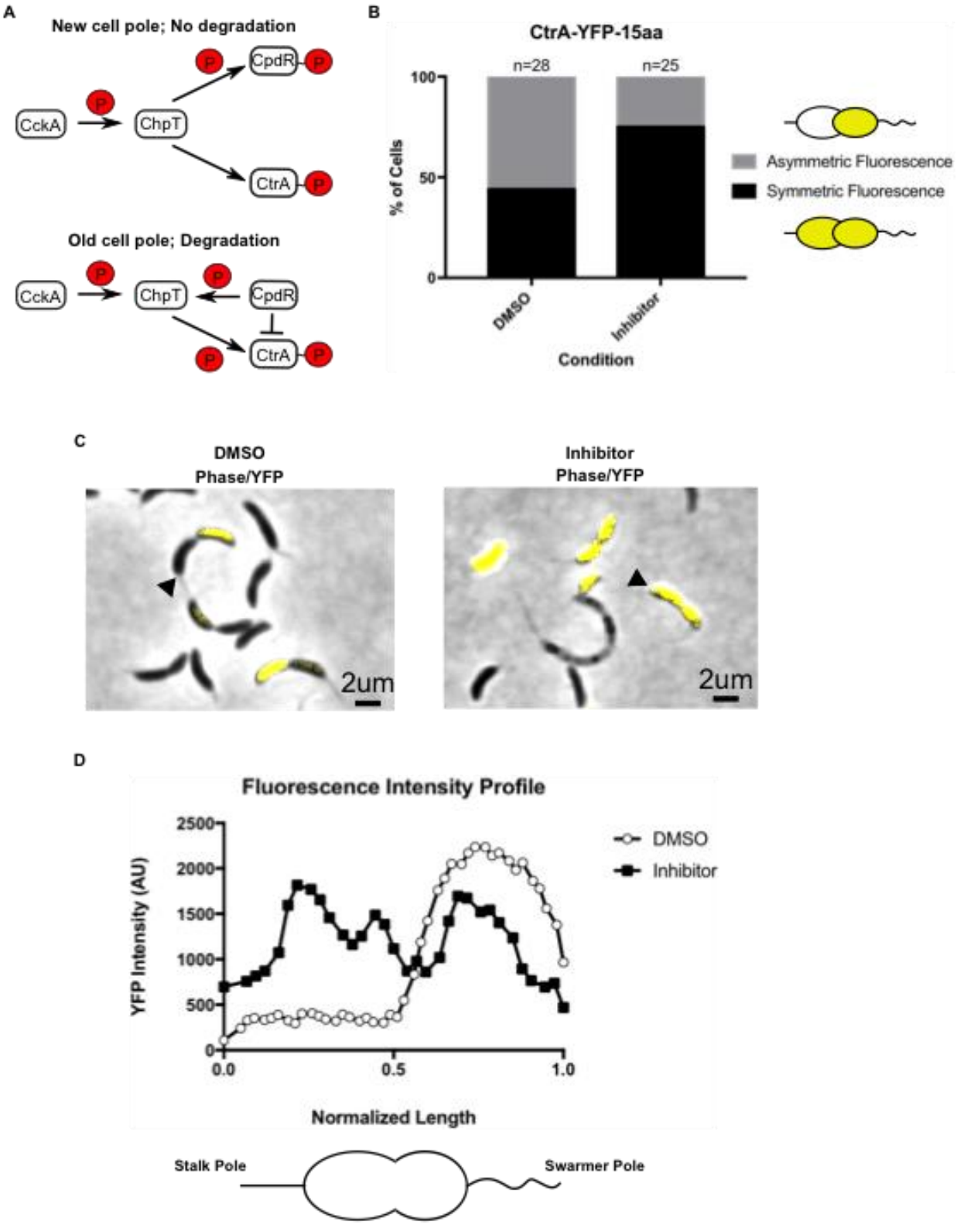

Figure 4–20 CtrA asymmetry is lost when grown with CCT018159.
Cells containing the low copy plasmid pCtrA-YFP-15aa were grown overnight in M2G containing antibiotics to OD_{600} of 0.2. DMSO or 140 µM CCT018159 were added and cells were grown for 3 hours then imaged on 1% agarose pads

using Phase and YFP filters and settings (See Methods). A) The histidine kinase CckA phosphorylates ChpT, which then phosphorylates CpdR and CtrA. When CpdR is phosphorylated CtrA~P remains active at the new cell pole. When CpdR is unphosphorylated CtrA~P is degraded at the stalk cell pole. B) CtrA in predivisional cells favors being asymmetric with higher intensity concentrated in the new cell due to degradation of CtrA in the old cell compartment. Upon addition of CCT018159 CtrA maintains similar fluorescent levels in both cell compartments. CtrA-YFP in DMSO displays asymmetric intensity in predivisional cells. C) Addition of inhibitor causes loss of asymmetrical intensity in predivisional cells. D) Fluorescence intensity profile of CtrA-YFP-15aa along the medial axis of the cell. DMSO only cells maintain an over 4-fold increase in YFP intensity in the new cell body compared to the old cell body. Addition of inhibitor causes a loss in the asymmetric distribution in the cell bodies.

Our hypothesis was that if the inhibitor was affecting CckA phosphorylation activity, we would observe a loss of asymmetric degradation of CtrA-YFP-15aa due to the inability of CckA to phosphorylate CpdR. Unphosphorylated CpdR leads to CtrA~P degradation (Figure 4–20A). In the DMSO control, the cells display asymmetric degradation upon compartmentalization of the cells (Figure 4–20B,C). Upon growth in 140 µM CCT018159, cells display similarly high levels of CtrA-YFP-15aa in both cell compartments (Figure 4–20B,C). A fluorescence intensity profile of representative cells outlines this loss of asymmetric fluorescence (Figure 4–20D). Loss of asymmetry indicates that CtrA/CtrA~P is no longer being degraded in cells. This could be the result of steady phosphorylation of downstream factors. If the inhibitor blocks autophosphorylation, it may also be inhibiting phosphatase activity. If CckA can no longer dephosphorylate ChpT~P, a buildup of CpdR~P and CtrA~P could occur, resulting in an increase in symmetric fluorescence with the CtrA reporter. Future assays would need to be completed *in vitro* to test inhibition of phosphatase activity of CckA upon addition of an HK inhibitor.

4.2.5 CckA maintains localization upon addition of CCT018159

CckA activity has also been shown to be density dependent.[113] CckA localizes in predivisional cells as monopolar or bipolar populations (Figure 4–21A,B).

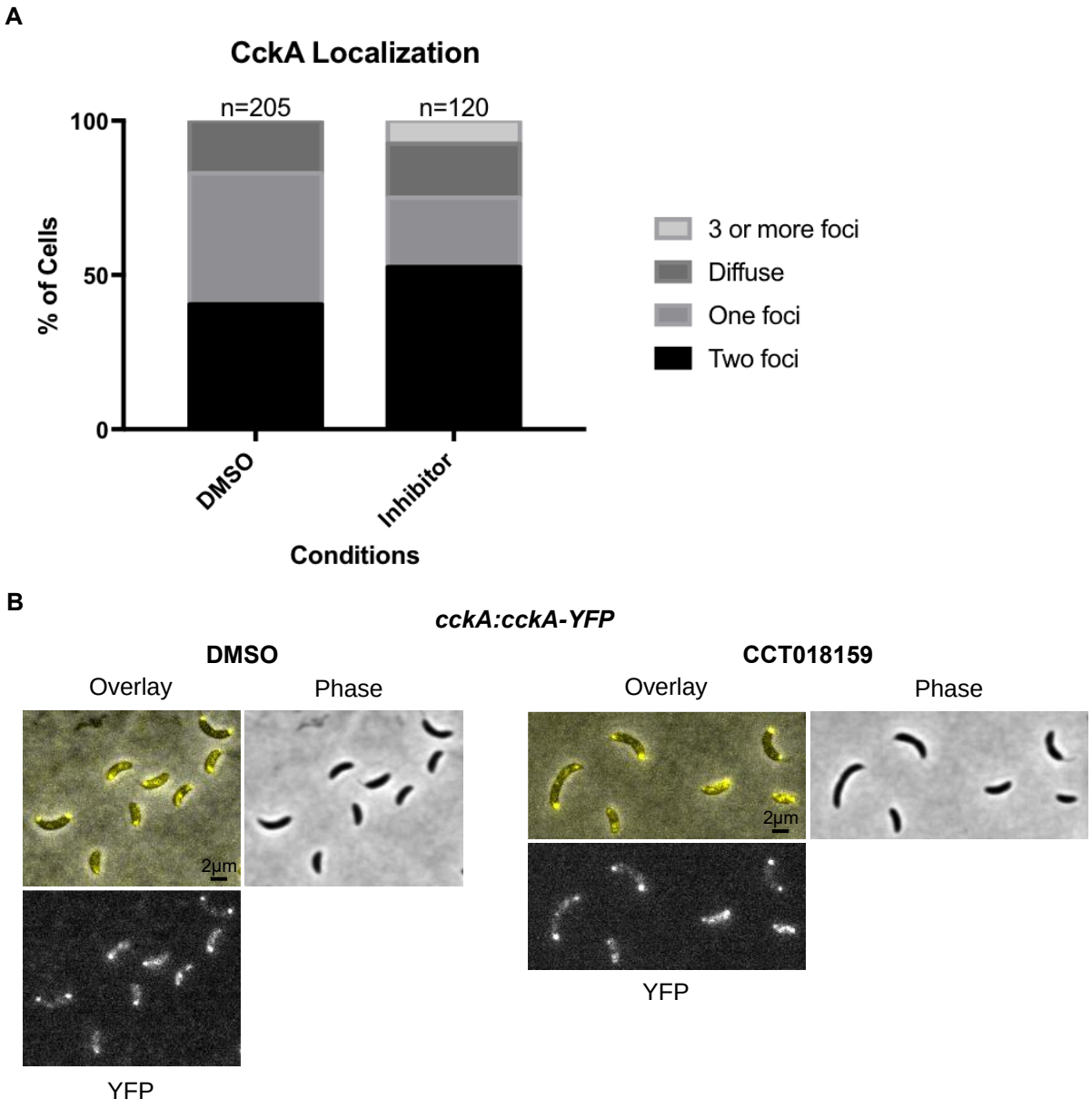

Figure 4–21 CckA localization is not impacted by inhibitor.
Cells expressing CckA-YFP from its native locus, *cckA::cckA-YFP*, were grown overnight in M2G at 28ºC to OD_{600} of 0.2. Cells were then treated with DMSO or 140 µM CCT018159 final concentration. After three hours of growth, cells were imaged on a 1% agarose pad using Phase and YFP filters and settings (See Methods). A) CckA localization in DMSO and CCT018195 conditions. Foci counts were done manually. B) Cell images of DMSO and CCT018159 conditions.

In order for CckA kinase activity to occur, CckA needs to be localized in predivisional cells. A CckA-YFP strain was used to determine if the inhibitor caused a loss of localization of CckA. CckA did not become more diffuse upon addition of 140 µM CCT018159 (Figure 4–21A,B). In fact, the opposite effect occurred with a 10% increase in bipolar populations as well as

the appearance of 3 or more foci in cells (Figure 4–21A). The CckA diffuse model as a mode for loss of CtrA~P degradation in cells can be eliminated following this result.

4.2.6 CCT018159 inhibits ParB localization at the cell poles

To further test the effect of CtrA~P levels decreasing below 100 µM CCT018159, we chose to look at ParB and PopZ localization due to their regulation by CtrA~P. Given that we observed changes in CtrA~P phosphorylation upon exposure to 140 µM CCT018159, we investigated the impact of chromosome count given that CtrA serves as a replication inhibitor protein. ParB is related to the number of chromosomes in the cell due to ParB binding the *parS* sequence near the origin of replication.[234,235] We decided to screen a *parB::CFP-parB C. crescentus* strain where the chromosomal copy expressing *parB* is labeled.[132] When a cell is functioning normally, two foci of CFP-ParB are seen at the new and old cell poles (Figure 4–18). If CckA kinase activity is being inhibited in cells, there should be an increase in cells containing 3 or more foci due to replication no longer being repressed by CtrA~P.[123]

Upon addition of inhibitor to the ParB-CFP strain, complete loss of localization of ParB-CFP was seen (Figure 4–22).

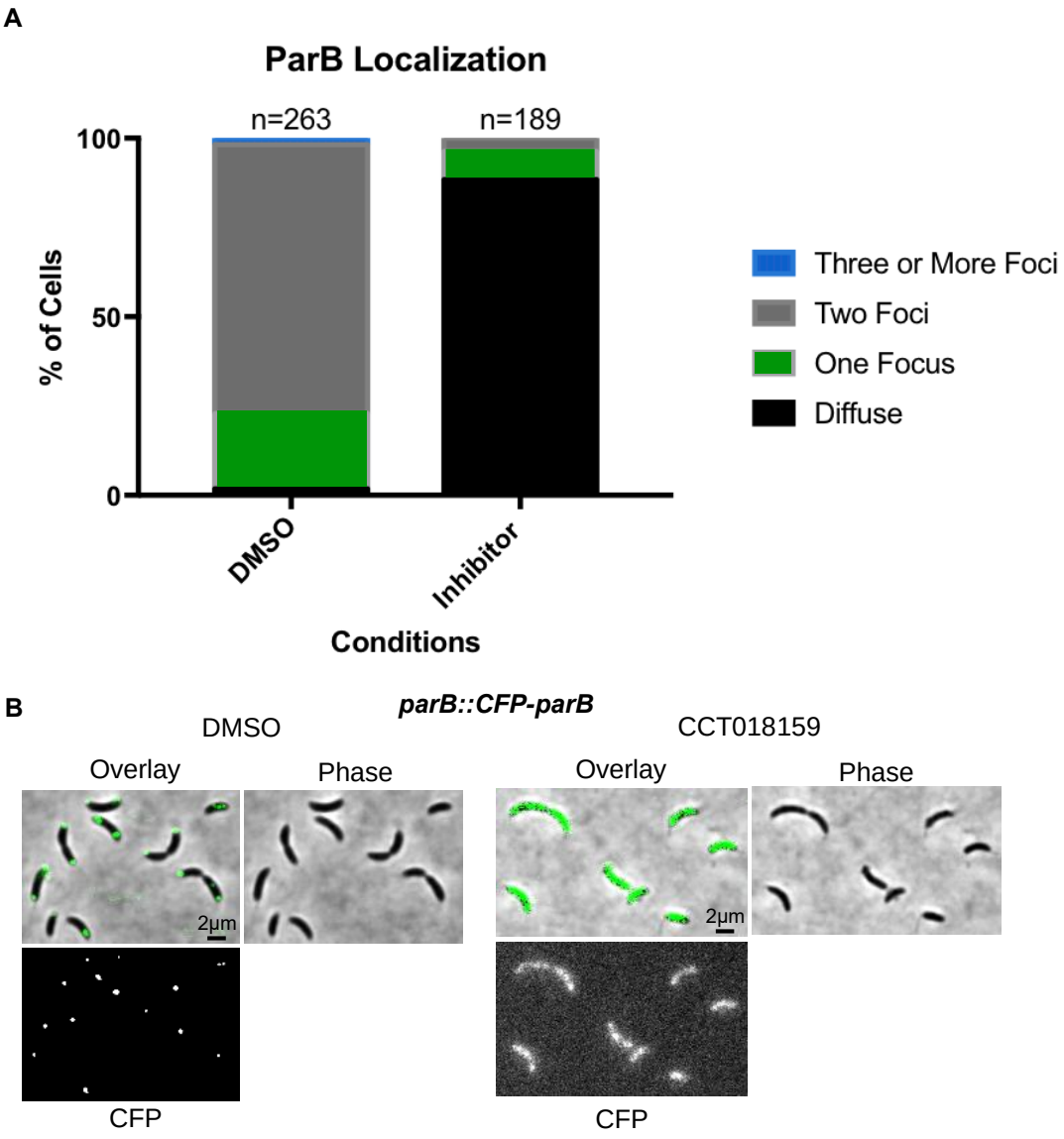

Figure 4–22 ParB localization is disrupted by CCT018159.
Cells expressing CFP-ParB from its native locus, *parB::CFP-parB*, were grown overnight in M2G at 28ºC to OD_{600} of 0.2. Cells were then treated with DMSO or 140 μM CCT018159 final concentration. After three hours of growth, cells were imaged on a 1% agarose pad using Phase and CFP filters and settings (See Methods). A) CFP-ParB typically forms two foci in cells. Addition of inhibitor caused loss of foci formation for CFP-ParB. B) Representative cells of CFP-ParB (pseudocolored green) in DMSO or CCT018159 conditions.

This loss of ParB-CFP was striking due to ParB's function in cells. Loss of localization of ParB means the inhibitor could affect factors that localize ParB so we set out to test factors related to ParB localization.

PopZ is self-assembled scaffolding protein that anchors the chromosome to the cell pole by interacting with the centromere-binding protein ParB.[132,229] In the absence of the PopZ scaffold,

ParB is unanchored at the cell pole. Therefore, we hypothesized that the inhibitor may be directly or indirectly inhibiting the localization of the PopZ scaffold at the cell poles. To test this idea we added the inhibitor to a *C. crescentus* strain that expressed ParB-CFP and mCherry-PopZ. In the absence of inhibitor, ParB-CFP and mCherry-PopZ form bipolar populations in cells (Figure 4–23A, B).

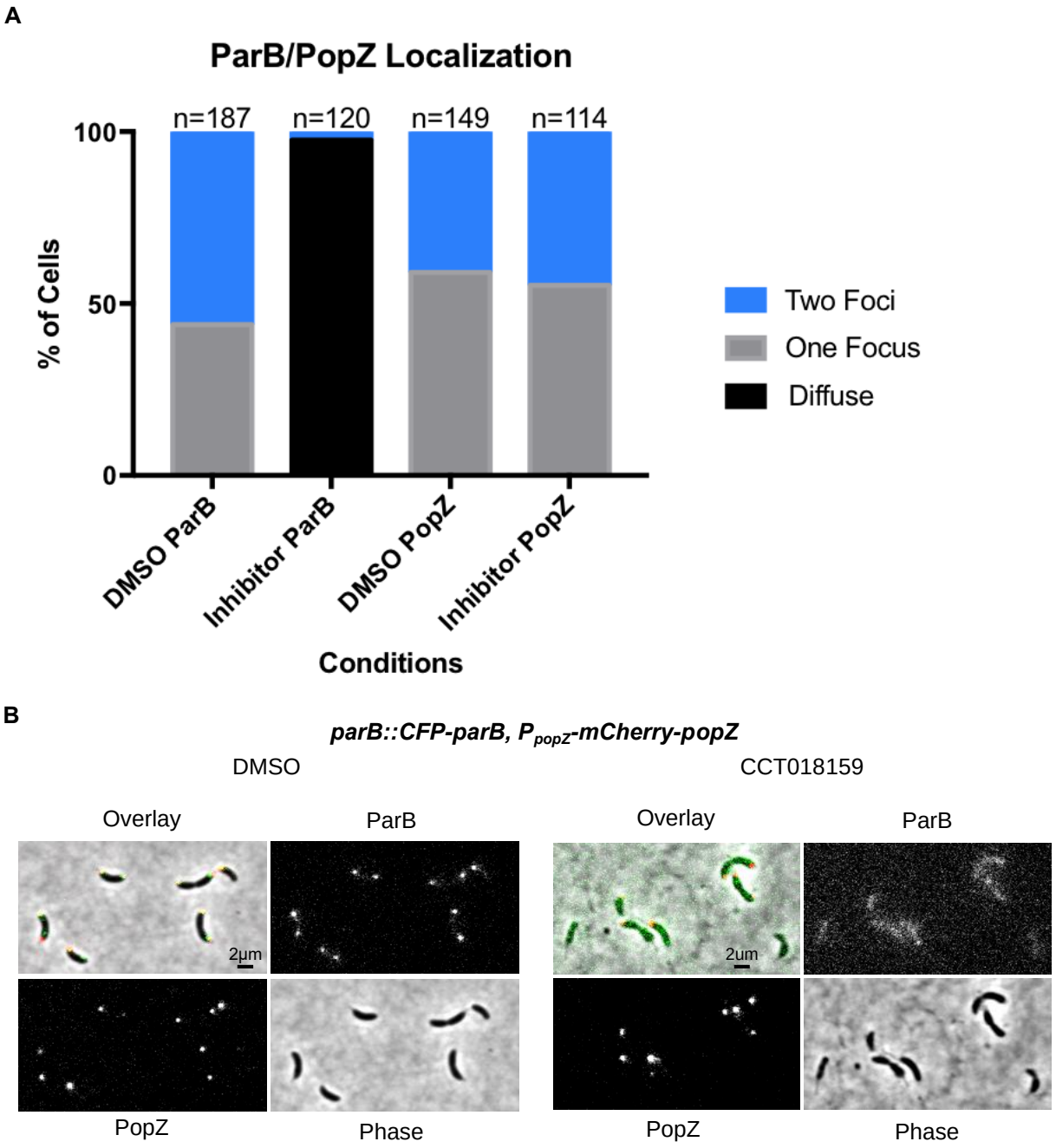

Figure 4–23 PopZ is not diffuse upon addition of CCT018159.
Cells expressing CFP-ParB, mCherry-PopZ, *parB::CFP-parB* and P_{popZ}*-mCherry-popZ*, were grown overnight in M2G at 28ºC to OD_{600} of 0.2. Cells were then treated with DMSO or 140 µM CCT018159 final concentration. After three hours of growth, cells were imaged on a 1% agarose pad using Phase, CFP, and mCherry filters and settings (See Methods).A) ParB/PopZ localization graph. ParB is CFP labeled and PopZ is mCherry labeled. Upon addition of CCT018159, ParB becomes diffuse while PopZ localization does not change indicating ParB diffusion is not due to a loss of interaction with PopZ. B) PopZ and ParB colocalize due to ParB being pulled to the new cell pole by PopZ from the old cell pole. Upon addition of CCT018159, ParB signal becomes diffuse while PopZ stays localized meaning loss of PopZ localization is not the cause of ParB diffusion.

Upon addition of the CCT018159 inhibitor, ParB-CFP subcellular localization is disrupted, while mCherry-PopZ maintains localization at the cell poles (Figure 4–23A,B).This eliminates a PopZ disruption as the cause for loss of ParB foci.

To evaluate the consequences of loss of ParB binding to the centromere, we examined downstream targets of ParB. One target is the division site placement protein MipZ, which is an ATPase responsible for positioning the division plane at the center of the cell.[230] Central to the function of MipZ localization to both cell poles due to an interaction with the centromere-binding protein ParB (Figure 4–24).[230]

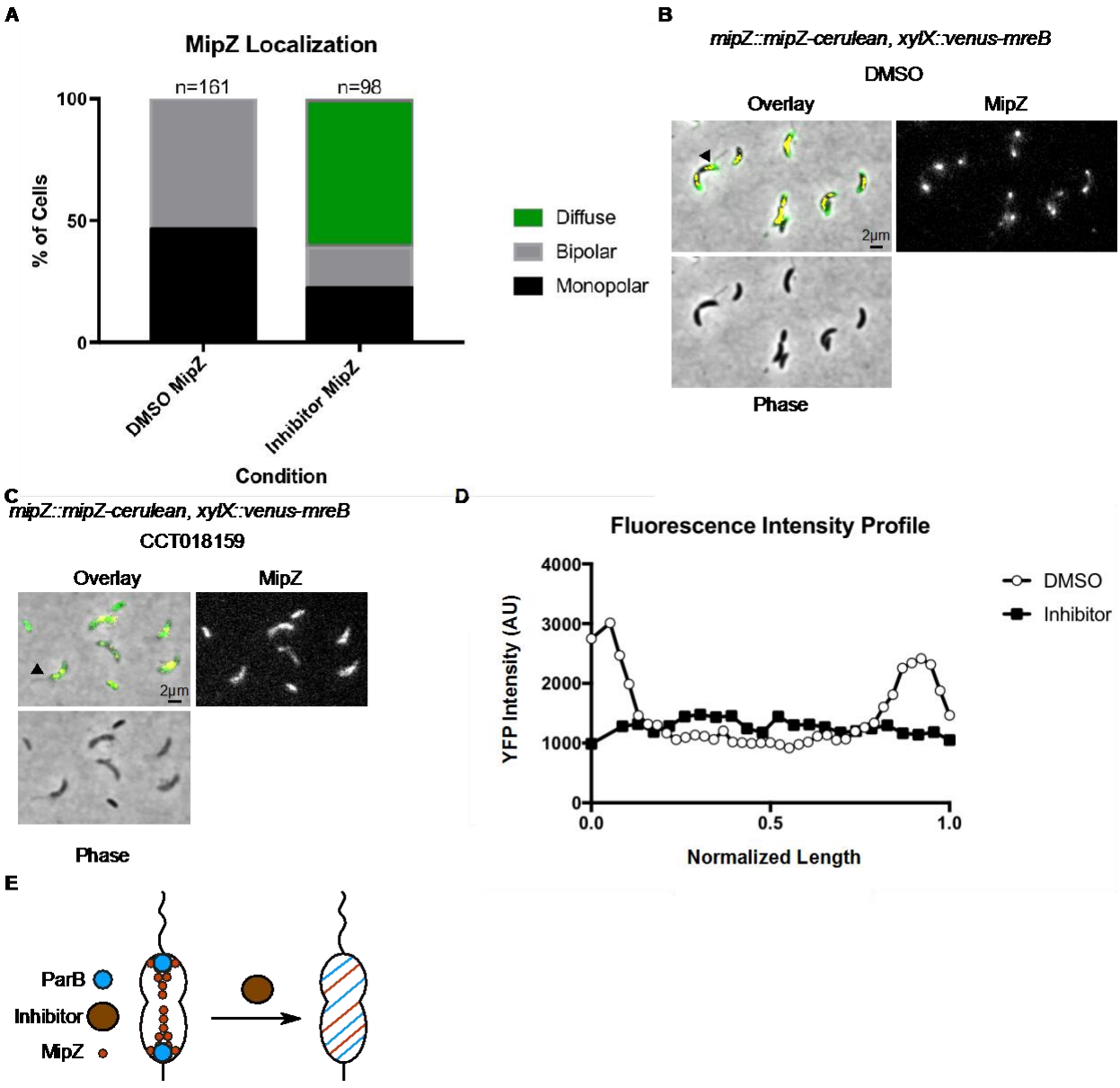

Figure 4–24 MipZ-GFP localization is disrupted by CCT010159 addition.
Cells expressing MipZ-cerulean (pseudocolored green for clarity) from *mipZ::mipZ-cerulean* and venus-MreB from the xylose locus were grown overnight in M2G at 28ºC to OD_{600} of 0.2. 0.03% xylose was added to induce venus-MreB expression. Venus-MreB is not shown for clarity. Cells were then treated with DMSO or 140 μM CCT018159 final concentration. After three hours of growth, cells were imaged on a 1% agarose pad using Phase, CFP, and YFP filters and settings (See Methods). A) MipZ-cerulean localization data with and without inhibitor. B) MipZ-cerulean in DMSO forms bipolar foci and extends towards the midcell as a gradient. C) Upon addition of inhibitor MipZ-GFP becomes diffuse. D) Fluorescence intensity profile of MipZ-GFP of representative cells. Foci formation is seen in the DMSO condition as peaks at 0.0 and 1.0 on the graph (cell marked with black arrow in B). With inhibitor, peaks at ends of the cell are lost (cell marked with black arrow in C). E) Cartoon representation of loss of ParB and MipZ phenotypes upon inhibitor addition.

MipZ normally forms a gradient from the poles to the midcell, which allows MipZ to inhibit FtsZ at the cell poles and allow FtsZ to assemble at the center of the cell. In DMSO, MipZ

forms one or two bright foci at the poles (Figure 4–24A,B). Upon addition of CCT018159, MipZ-GFP becomes diffuse with a small number of monopolar and bipolar populations remaining (Figure 4–24A,C). A fluorescence intensity profile of representative cells shows the loss of foci formation in the inhibitor assay (Figure 4–24D). Collectively these results indicate that the inhibitor disrupts ParB binding to the parS centromere and as a consequence impacts both chromosome replication and cell division (Figure 4–24E).

4.3 Discussion

We have been able to build off previous work with HK inhibitors to be the first to identify a direct *in vivo* binding interaction between an HK (CckA) and an HK targeting inhibitor (Figure 4–17). The CckA-FRET biosensor was selective for the HK inhibitor CDV009 and CCT018159 over CDV008, potentially due to the lack of H-bonding capabilities on the benzene ring (Figure 4–16). After we identified this binding result, we further explored the impact that inhibition of CckA, and likely other HKs, has on the cell-cycle and cell division. Use of Phos-tag identified a decrease in CtrA~P levels in the range of 0-50 µM CCT018159 (Figure 4–19). This decrease in CtrA~P is likely a result of decreased CckA kinase activity due to competitive inhibition by CCT018159. Furthermore, we identified CtrA related phenotypes that would be caused by a decrease in CtrA~P levels. CtrA asymmetric degradation was lost upon addition of CCT018159 due to lower CtrA~P levels or higher CpdR~P levels which could be the result of CckA phosphatase activity also being inhibited (Figure 4–20). When we turned to ParB subcellular localization to determine further downstream impact of CtrA~P levels, we found that rather than ParB foci number going up as expected, the ParB fusion was diffuse (Figure 4–22). After ruling

out PopZ as the reason for ParB localization becoming diffuse we also found a factor downstream of ParB, MipZ, to also be diffuse (Figure 4–24). This indicated that the loss of ParB localization was having an impact on downstream factors and points towards a potential new effect for the HK inhibitor. Cumulatively, this work is the first in-depth look at HK inhibition *in vivo* and exploration into other proteins that could be targeted by the HK inhibitors. Our future directions will be aimed at determining these potential off-targets and developing new uses for HK inhibitors.

4.4 Future directions

4.4.1 Determination of ParB or ParA inhibition by CCT018159

ParB has recently been discovered to contain cytidine triphosphate (CTP) hydrolase activity.[236-238] The *parS*-bindng site of ParB stimulates ParB CTP hydrolase activity and regulates ParB ability to spread across DNA flanking the *parS* site, generating a nucleoprotein complex. ParB bound to CDP (following CTP hydrolysis) was crystallized and revealed that CDP binds a GXXRXXA motif in the α-3 helix which results in dimerization of ParB.[236] The CDP β-phosphate forms hydrogen bonds with G77 (backbone) and R80 explaining the conservation of the GXXRXXA motif. ParB does not fall in the Bergerat fold family, but there is potential for inhibitor binding to ParB due to its similarity to ATP, which shares some structural similarities to CTP/CDP. An alternate hypothesis is that the inhibitor is binding to the ATPase ParA.[234,239] ParA is a member of the P-loop ATPase family and contains a Walker A motif. ParA plays a role in partitioning the ParB/chromosome complex from the site or replication to the new cell pole early in the cell cycle. ParA dimerizes upon binding ATP and hydrolyzes ATP, which is influenced by binding ParB.

Hydrolysis results in a return to monomeric ParA and then the dimerization cycle continues. PopZ can sequester monomeric ParA in order to decrease the local concentration that can bind ATP and dimerize.[240] Sequestration of ParA helps lead the ParB/*parS* complex to the new cell pole.[240] Because we observed that addition of the inhibitor does not impact the ability of PopZ to localize (**Error! Reference source not found.**), ParA is the other potential target that can bind the inhibitor and impact ParB binding to DNA.

Past studies from Ptacin *et al.* have shown that ParB's binding to PopZ is independent of *parS* and in addition, past DNA footprinting biochemical assays have shown that ParB can bind *parS* independent of PopZ.[229,240] Therefore, addition of the CCT0181159 inhibitor has prevented ParB from making either one or both of these two independent interactions. Overall we imagine a handful of mechanisms may explain this disruption of chromosome segregation. ParB binding directly to *parS* and PopZ, ParA dimerization and ATP hydrolysis, or ParC and ParE GHKL domain containing proteins could all be disrupted by CCT018159. ParC and ParE are subunits of topoisomerase (Topo IV) that plays a role in DNA upkeep during the segregation process.[241] ParC is also essential for the localization of the replication origin to the new cell pole.[241] Both ParC and ParE share homology with DNA gyrases, which is a GHKL family protein.[242]

4.4.2 Investigate CCT0181159 as a direct ParB inhibitor

In order to understand if the chemical inhibitor can bind ParB in its CTP/CDP binding site, biochemical assays will be completed to study inhibitor binding. ParB will be recombinantly expressed and purified using Ni^{2+} affinity purification, Heparin purification will be used to remove DNA and RNA, followed by gel filtration to remove aggregates. A malachite green phosphate assay will be used to determine the rate of CTP hydrolysis by ParB. The malachite green phosphate

assay works through a complex formation consisting of malachite green, molybdate, and free orthophosphate (Malachite Green Phosphate Assay Kit, Sigma Aldrich). The formation of this complex results in an increase in absorbance from 600-660 nm that can be measured in 96-well plate format. ParB will be incubated with CTP as a positive control to set a baseline for CTP hydrolysis rate. To study the potential inhibition of ParB CTP hydrolase activity we will add CCT018159 inhibitor to ParB, then add CTP and measure the rate of free phosphate generation by ParB. We can collect Michelis-Menten kinetics by varying CTP concentrations.

Further *in vivo* characterization of ParB will also include generation of a depletion strain of ParB where a ParB mutant, $ParB^{L12A}$, is expressed. $ParB^{L12A}$ cannot bind ParA, eliminating one potential interaction.[229] Incubating the inhibitor compound with this mutant will test for the ability of ParB to dimerize and bind *parS in vivo* independent of ParA.

4.4.3 Investigate CCT0181159 as a direct ParA inhibitor

ParA is a P-loop ATPase involved in segregating the ParB/*parS* complex to the new cell pole.[234] Because ParA helps promote ParB/*parS* nucleoprotein segregation to the new cell pole through its cycle of dimer to monomer through ATP hydrolysis, this segregation process could be interrupted if the ability of ParA to bind ATP is inhibited.[240] The loss of binding to ATP could also interrupt ParA interaction with PopZ which is also crucial to recruiting the ParB nucleoprotein complex to the new cell pole.[240] In order to understand if the inhibitor impacts ParA activity directly, we are proposing to study it using an mCherry-ParA fusion expressed from the xylose locus in *C. crescentus*. Cells expressing this fusion will be studied with and without inhibitor to determine if ParA is localizing when inhibitor is added. If localization at the new cell pole is not disrupted we can rule out the ParA-PopZ interaction as to why ParB-fusion localization is lost. As

a control for this experiment, we can express the fusion protein mCherry-ParA^{G16V}, a monomeric variant that associates only with PopZ and test for localization in the presence of the inhibitor.[229] This still leaves the possibility that ATP-binding to ParA is being disrupted as dimerization is not required for ParA to bind PopZ. We would next follow up with *in vitro* characterization of ParA/ATP-binding in the presence of the inhibitor to using the Malachite Green Phosphate assay to determine if ParA can hydrolyze ATP in with inhibitor present. If it can hydrolyze ATP we can rule out binding of the inhibitor to the ATP-binding site of ParA. This would not rule out disruption of ParA dimer binding to the nucleoid. If localization of mCherry-ParA is disrupted in the presence of the inhibitor, three hypotheses arise: (1) ParA binding to ATP is inhibited causing a disruption of binding to the nucleoid, (2) ParA binding to PopZ is being disrupted, or (3) loss of ParB localization impacts ParA localization. A combination of the two could exist, though unlikely due to the ATP-binding and dimerization not being required for PopZ binding ParA. Similar *in vitro* characterization will be completed to determine hydrolysis rate of ATP in the presence of the inhibitor. If hydrolysis is not inhibited, ParA DNA-binding assays using surface plasmon resonance (SPR) in with and without inhibitor can be used to test for disruption of ParA binding DNA.[229] The most difficult hypothesis to test is whether ParA localization is lost due to disruption of ParB activity.[229] Ptacin, *et al.* found that depletion of ParB from cells resulted in a loss of ParA localization. This result was confirmed by expressing an mCherry-ParB^{L12A} mutant that is unable to interact with ParA, resulting in a ParB foci with diffuse ParA.[229] This mutant will be used as a control to produce a phenotype where ParA is diffuse. The loss of ParA localization due to loss of ParB activity is a negative feedback loop, as ParB dimerization is lost, ParA will also become diffuse making it difficult to decouple effects of the inhibitor. *In vitro* characterization of both ParB and ParA will be important to decouple these effects.

4.4.4 Using CCT0181159 as a pull-down to identify targets

Due to the amount of results that could point toward different conclusions, we also want to employ a broader approach to identify direct targets of CCT018159. Our goal would be to create a biotinylated CCT018159 analog for doing pulldowns and coupling it with mass spectroscopy (Figure 4–25).

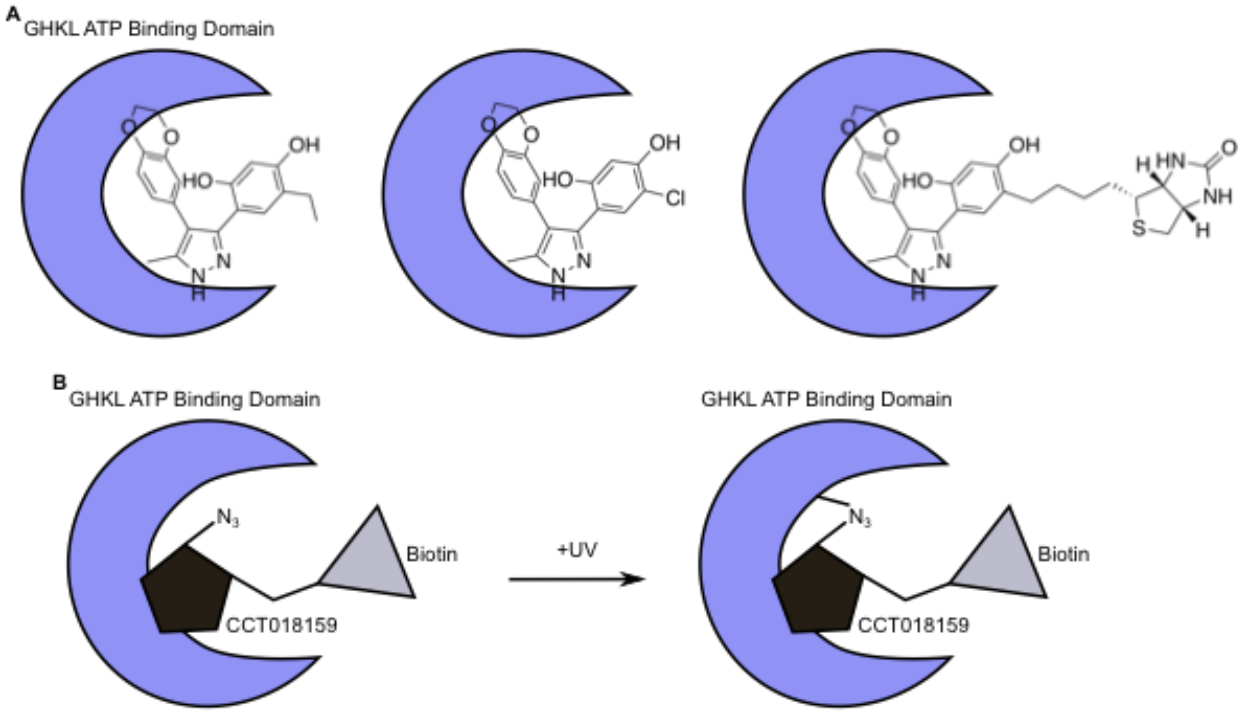

Figure 4–25 CCT018159 as a target pull-down analog.
A) CCT018159 (shown in a nonplanar configuration) can bind to GHKL ATP-binding domains of proteins (left, blue crescent). The ethyl position points out of the binding pocket and could be modified with a chlorine (middle), which would facilitate decarboxylative coupling reactions with biotin to generate a CCT018159-biotin analogue for use with a streptavidin pull-down assay (right). B) CCT018159 could be modified with arylazide to facilitate photo crosslinking with targets to increase success of pull-downs.

Biotinylated molecules have been previously used for pulling down histidine kinases using known binding partners.[243] Based off docking studies of CckA with CCT018159 and its synthetic derivatives by Vo *et al.*, we can make predictions of what chemical groups would be accessible for biotinylation. Using the docking of CCT018159, we predict that the ethyl group on the resorcinol ring would make a good candidate for biotinylation because that group points out of the

binding pocket (Figure 4–25A).[176] CDV008, which is based off the CCT018159 scaffold and inhibits cell growth, has this position accessible as well, but chlorine replaces ethyl group, opening the possibilities of decarboxylative coupling reactions with biotin (**Error! Reference source not found.**A).[244] Due to the low μM binding affinities of the inhibitors for CckA, we suspect that biotinylation may further decrease binding affinity. We will complete initial binding studies using purified CckA to access the affinity of biotinylated inhibitors. If affinity is lowered enough (3-fold or greater) that pull-down may not be possible without additional modifications, such as a photoprobe like arylazide or benzophenone (Figure 4–25B).[245] Once a suitable method for pull-down is optimized, we will be able to isolate proteins that bind our bait molecule using streptavidin. We can then follow up with mass spectrometry to identify any proteins enriched over controls.

4.4.5 High-throughput screening of inhibitors using the CckA-FRET biosensor

Currently, our methods of analysis of the CckA-FRET biosensor are low throughput microscopy image analysis. We aim to evaluate 96-well fluorescence plate reader and flow cytometry assays for their ability to detect FRET/mClover3 changes upon inhibitor addition. This analysis will include dose-response studies to assess the sensitivity and limit of detection of each method. We will use CCT018159 and CDV009 as positive controls to set a threshold for positive hits using flow cytometry and fluorescence plate reader assays and benchmark these results against the microscopy methods. If we are successful in screening these inhibitors over negative controls, we will then screen the full panel of published histidine kinase inhibitors[176] and a more extensive library of more than 75 molecules related to CCT018159 provided as a gift from Jimmy Blair.[176] Moreover, the most potent inhibitors will provide lead compounds that will motivate our design

of larger screens utilizing this new HK inhibitor screen technology. This new technique will be the first high-throughput, HK targeted, *in vivo* screen of HK inhibitors to date.

4.5 Methods

Growth Conditions: *E. coli* DH5*α* strains were grown at 37 °C with shaking overnight in LB media supplemented with antibiotics. *C. crescentus* strains were grown in PYE or M2G media supplemented with antibiotics at 28 °C with shaking overnight or for specified times for imaging.

Electroporation: Plasmids were introduced into *C. crescentus* by centrifuging 4 mL for 5 minutes at 21,100 x g. Supernatant was removed and cells were washed in 100 µL of cold, sterile water and centrifuged for 1 minute at 21,100 x g. This step was repeated 2 more times, followed by suspension of cells in a final volume of 80 µL of cold water. Integrating plasmid (12.5 µL DNA) or replication plasmid (3 µL DNA) were then added to the cells and electroporated on the *E. coli* setting of a BioRad GenePulser using 0.1 cm electroporation cuvettes (BioRad). Cells were then resuspended in 1 mL of 2xPYE and shaken at 28 °C for 3 hours, then 100 µL of cells were then plated on PYE/antibiotic plates. The remaining cells were pelleted, resuspended in 100 µL of 2xPYE, and plated on PYE/antibiotic plates. Cells were grown at 28 °C for 3 days and colonies were streaked onto a PYE/antibiotic plate. Colonies that grew after streaking were screened for using colony PCR (DreamTaq Green) using primers for integration at the xylose locus (RecUni-1, RecXyl-2), vanillate locus (RecUni-1, RecVan-2), or for replicating plasmids (Pvan-for, M13-for) according to the manufacturer's protocol with 5 minute extension times.

Imaging Conditions: *C. crescentus* strains for single time point imaging were grown overnight in M2G media supplemented with antibiotics to an OD_{600} 0.1-0.2. If cells required

expression from a xylose inducible vector, they were then induced with xylose (0.03% w/v) for 3 hours. 2 µL of cells were deposited on a 1% agarose pad on a glass slide and covered with a glass coverslip. For FRET experiments evaluating histidine kinase directed antibiotics, cells were grown for 3 hours with xylose, then for 2 hours with antibiotic and an image was taken (Time 0). The culture was then split and either DMSO, CCT018159 (28 µM) , Kanamycin (2.5 µg/mL), CDV008 (17.5 µM), or CDV008 (12.5 µM) were added to cultures. Cells were then imaged as a time-course for 210 minutes. For all other experiments where CCT018159 was used, 140 µM (in DMSO) final concentration was added.

Microscopy: Images were taken on a Nikon T*i*E inverted setup using an APO Lambda 100X oil objective with Phase-Contrast or Differential Interference Contrast (DIC) using Zeiss Immersol 518F Immersion Oil using Nikon Element AR software to control the setup. A halogen lamp was used for the white light source. Spectra X light engine was used for all fluorescence excitation. An Andor Ixon Ultra 897 EMCCD camera was used for all imaging. All filter sets used were purchased from Chroma. CFP/YFP/mCherry (77074157) and GFP (77074160) filter cubes were used with emission filter sets GFP (77074161) and CFP/YFP/mCherry (77074158).

FRET Microscopy and Image Processing: Simultaneous FRET imaging was done by placing a Hamamatsu W-View Gemini Image Splitter in the light path between the Nikon T*i*E and the camera. A GFP/mCherry dichroic mirror, GFP emission filter, and mCherry emission filter were used. Alignment of the channels was done using the supplied alignment slide. Alignment of the channels was done before each imaging event. Each strain was imaged under the same conditions (600 millisecond Autoexposure, 100 Gain, 2x2 binning for capture, and 15% power). Background from the fluorescent channels was subtracted in the Nikon software and images were exported at Tiffs for processing in ImageJ.[165] In ImageJ a mask was generated by thresholding cell

signal above background. The original image was then multiplied by the masked image to remove background signal and the mCherry emission channel image was divided by the GFP emission channel (32 bit image) to generate a ratiometric FRET image.

Image Analysis: For each FRET experiment, 4 images were uploaded into MicrobeJ[166] (Phase, GFP channel, mCherry channel, and ratiometric image). The phase image was used to generate a cell outline using the Medial Axis setting. Cell poles were outlined using the MicrobeJ automatic pole settings which to draw a shape around the cell pole. MicrobeJ was preset to mark the stalk pole as the pole with higher intensity in the GFP channel. After software chose the poles, manual adjustment was done by choosing cells with a visible stalk and cells with incorrect pole alignment were corrected manually. MicrobeJ data analysis tool was then used to average the intensity of the cell pole and body. Data was exported to Prism in order to generate histograms and average data. Student's t-test was used to determine significant difference in populations. Error bars are reported as standard error of the mean.

Phos-tag and Western Blot: Samples were generated by centrifuging 1 mL of cells of a known OD_{600} , removing the supernatant and resuspending in 100 µL of 4x Sample Buffer. Samples were then heated at 75 °C for 10 minutes. Samples were loaded onto a 12% resolving SDS-PAGE gel with a 4% stacking gel. Loading volumes were normalized using OD_{600}. The ladder used was ThermoFisher Page Ruler Pre-Stained Ladder. Samples were also loaded on Phos-tag 12.5% SDS-page gels, which were made using the SDS-page gel with the addition of 80 µL of 5.0 mM Phos-tag dissolved in methanol and 80 µL of 10 mM $MnCl_2$ for a total of 10 mL of gel. 3 mL of SDS-page stacking gel was made using the stacking gel recipes. Gels were poured and stored for up to 1 week. Gels were run at constant 150 mA for 1.5 hours in a 4ºC cold room. Phos-tag gels were incubated in EDTA/Transfer buffer for 15 minutes to remove the Phos-tag reagent.

A total of 3 wash incubations were performed. The gel was then incubated in 1x transfer buffer for 15 minutes (repeated three times). All incubations were performed with rocking. Western blots were completed by using the Life Science protocol for creating the transfer sandwich. Transfers were run at a constant 20 V for 3 hours. Transfer membranes were incubated in blocking buffer (5% non-fat milk in TBST). Membrane was washed in 1x TBST for 15 minutes and then incubated in primary antibody dilution buffer (10mL 1x TBST, 5% non-fat dry milk, 0.5 µL CtrA polyclonal antibody produced in rabbit (1:20000 dilution)) for one hour. Membrane was then washed in 1x TBST 3 times for 5 minutes. Membrane was then incubated in secondary antibody dilution buffer (10mL TBST, 5% non-fat dry milk, and 1 µL of anti-rabbit HRP secondary antibody (1:10000 dilution) for one hour followed by one 15 minute incubation in 1xTBST and 2 washes for 5 minutes in 1x TBST. Membrane was then incubated in chemiluminescent substrate (SuperSignal West Femto Maximum Sensitivity Substrate, Thermo, 1mL per membrane) for 5 minutes then imaged on a BioRad Chemidoc using the Hi sensitivity setting set for autoexposure. Images were exported into ImageLab.

Construction of Plasmids: Plasmids used can be found in Table 4–1. The lists of oligonucleotides used in this study can be found in Table 4–2. All oligos were ordered from IDT. The strains used can be found in Table 4–3 and methods to generate strains are listed above. Phusion polymerase (ThermoFisher) was used for amplification of PCR products used in Gibson assembly and isolated using gel electrophoresis using a 1% agarose, 1xTAE gel with ethidium bromide added for visualization by UV light. Band sizes were determined using a GeneRuler 1 kb DNA Ladder (ThermoFisher). Bands were excised from the gel and extracted using a GeneJet Gel Extraction Kit (ThermoFisher) following manufacturer's protocols, with the addition of a 100µL binding buffer wash step following the spin through of DNA/agarose/binding buffer. Water was

used for elution. DNA concentrations were determined using a NanoDrop 2000 spectrophotometer (Thermo Scientific). All reactions were done according to the manufacturer's protocols with annealing temperature at 55 °C.

Plasmids: See chapter 2 methods for plasmid construction of pSWD95. 5 µL of the Gibson reaction mixture was transformed into KCM competent DH5*α E. coli* cells and plated on LB/agar supplemented with the appropriate antibiotic. Colonies were screened using primers Pxyl-forThanbichler, *et al.* [169] and M13-for[169] using DreamTaq PCR with a 5 minute extension time.

4.6 Tables

Table 4–1 Plasmid utilized in this study.

Name	Description	Reference/Addgene #
pSWD95	2nd Gen CckA-FRET biosensor	[155]

Table 4–2 DNA primers used in this study.

Name	Sequence(5'-3')
SWD160	CGCTCGAGTTTTGGGGAGACGACCATATGGCCGACTTGCAGCTCCAG
SWD305	GCGTAACGTTCGACGACGCGTCTTCCACAACCGG
SWD306	GGAAGACGCGTCGTCGAACGTTACGCGTCACCGG
SWD307	CCTTGCTCATCTCGGTGGCCGACCGGTGACG
SWD308	CCGGTCGGCCACCGAGATGAGCAAGGGCGAGGAGC
SWD309	ACCGGGGCCGGGCTCACCATCGGATCTTCGCCG
SWD310	GATCCGATGGTGAGCCCGGCCCCGGTCGCCGAG
SWD311	CGTAACGTTCGACGCCGCCTGCAGCTGCTG

Table 4–3 Strains used in this study.

Name	Genotype	Plasmid	Reference
WSC1100	*C. crescentus, mipZ::mipZ–cerulean xylX::PxylX–venus–mreB*	none	LS4764

WSC1119	*E. coli*, DH5α	none	
WSC1131	*C. crescentus*, DivK cold sensitive (cs)	none	[175]
WSC1132	*C. crescentus*, *parB::CFP-parB*	none	[132]
WSC1133	*C. crescentus*, NA1000	MR-10 Pxyl-CtrA RD+15-YFP	[232]
WSC1139	*C. crescentus*, *cckA::gent*	pMR10cckAover	[107]
WSC1141	*C. crescentus*, *parB::CFP-parB*	P_{popZ}-mCherry-popZ	[240]
WSC1411	*C. crescentus*, NA1000	none	
WSC1412	*E. coli*, DH5α	pSWD95	This work
WSC1413	NA1000	pSWD95	This work
SWD018	*C. crescentus*, *cckA::cckA-YFP*	none	LS4473

5.0 Scaffold-scaffold interactions regulate cell polarity in a bacterium

This chapter was written in collaboration with Wei Zhao, Kim Kowallis, Chao Zhang, Dylan T. Tomares, Haley N. Petitjean, and W. Seth Childers. It contains data from the submitted manuscripts: "Scaffold-scaffold interactions regulate cell polarity in a bacterium" by Wei Zhao*, Samuel W. Duvall*, Kimberly A. Kowallis, Chao Zhang, Dylan T. Tomares, Haley N. Petitjean, W. Seth Childers. Some of this data appears in the pre-print entitled "A circuit of protein-protein regulatory interactions enables polarity establishment in a bacterium" by Wei Zhao, Samuel W. Duvall, Kimberly A. Kowallis, Dylan T. Tomares, Haley N. Petitjean, and W. Seth Childers, *bioRxiv* 503250.

5.1 Introduction

Time and space are two key factors that organisms take advantage of in order to regulate all aspects of their life-cycle. Because cells exist in 3D and range in sizes, space is important to consider when talking about the processes that a cell is carrying out. In the case of *Caulobacter crescentus*, space becomes an important factor due to the dimorphism of the daughter cells (Figure 5–1).

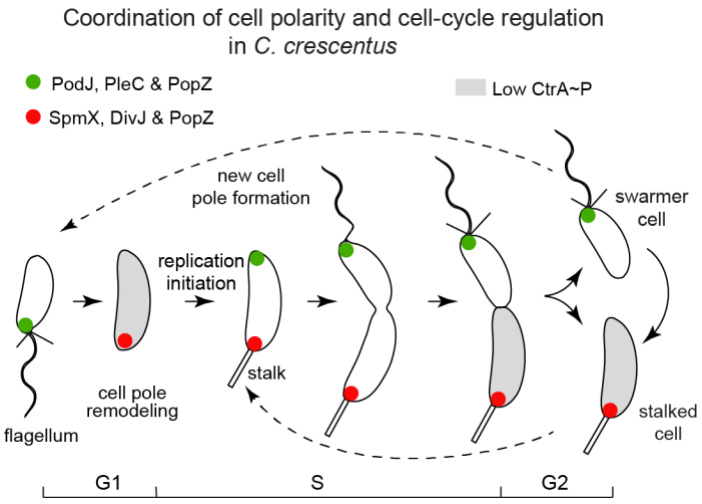

Figure 5–1 The PopZ and PodJ scaffold proteins are involved in the asymmetric accumulation of signaling proteins at the new cell pole.
Swarmer cells of *Caulobacter crescentus* differentiate into stalked cells, which is associated with cell pole remodeling of a PodJ-rich signaling hub (green) into a SpmX-rich signaling hub (red). At the new pole of the stalked cells, a PodJ-rich signaling hub with scaffolding protein PopZ accumulates gradually upon initiation of replication. Cell division results in daughter cells that involved unequal inheritance of a PodJ-rich signaling hub in swarmer cell and a SpmX-rich signaling hub in stalked cell.

This dimorphism is a result of different factors taking up residence at opposite cell poles. One may begin to ask how did the cell decide to position these factors? While we can point to evolution generating a cell type that thrives in its niche environment, we can also take a look at the subcellular level in order to answer why the cell poles end up with different results.

C. crescentus is not the first organism to be shown to differentiate into different cell types. The mammalian embryonic stem cell is the classic example which can even be forced to differentiate outside the body.[246] Stem cells are able to achieve differentiation through activation of different signaling pathways, but what enables them to divide into two different cell types is their ability to scaffold important signaling complexes at predetermined regions of the cell?[247] These scaffolding proteins can recruit multiple protein complexes[247] as well as allosterically regulate the signaling proteins they recruit[248], and can be dynamic in nature.[249] A great deal has been discovered about mammalian scaffolding proteins[88,248] and a majority of what has been learned has become applicable to understanding bacterial scaffold proteins.[250,251] The CtrA

signaling pathway is an example of the utility of scaffolding proteins to promote asymmetric division *C. crescentus*. The CtrA signaling pathway, whose regulation drives asymmetric division, is controlled by at least three known scaffolding proteins: PopZ, SpmX, and PodJ. Understanding how scaffolds help to regulate asymmetry can help us better understand the molecular mechanisms of bacteria that utilize asymmetry in virulence and biofilms.[252]

The CtrA signaling pathway, which has been thoroughly discussed in Chapter 2, is the primary driver for when the cell decides to replicate its chromosome and divide.[94,111,135,253-255] The HK CckA is recruited to the old and new cell pole by PopZ.[133,134] The cell poles are also occupied by two other scaffolding proteins: SpmX and PodJ (Figure 5–1).[256,257] SpmX scaffolds the HK DivJ to the old cell pole where it phosphorylates the response regulator DivK (Figure 5–1).[135,258] PodJ scaffolds the HK PleC, which dephosphorylates DivK~P (Figure 5–1).[135,259] This asymmetry in cell pole composition gives rise to the CtrA~P gradient that is likely to drive first chromosome replication and then differentiation(Figure of cell cycle with scaffolds).[120] One question that arises from this system of scaffolding proteins is why does a scaffold like PopZ, which is nucleoid occluded, need other scaffolds in order to perform its functions? More specifically, why does PopZ need PodJ for recruitment to cell pole when there are other factors like TipN[260] and ZitP[261] that are able to recruit it to the new cell pole. In this section we will investigate the structure and function of PodJ to better understand how it is able to recruit PopZ and other factors to the new cell pole and help maintain asymmetric polarity.

5.1.1 PodJ localization capabilities and domain architecture

In order to understand how PodJ is able to localize and recruit factors, it is important to look at its domain architecture. PodJ is a multidomain protein composed of an N-terminal coiled-

coil domain, a PSE (proline, serine, glutamic acid)-rich domain, a transmembrane tether flanked by two unique protease sites, and C-terminal domain that resides in the periplasm that is composed of tetracopeptide repeats (TPR) and a peptidoglycan binding (PG) domain (Figure 5–2).[262]

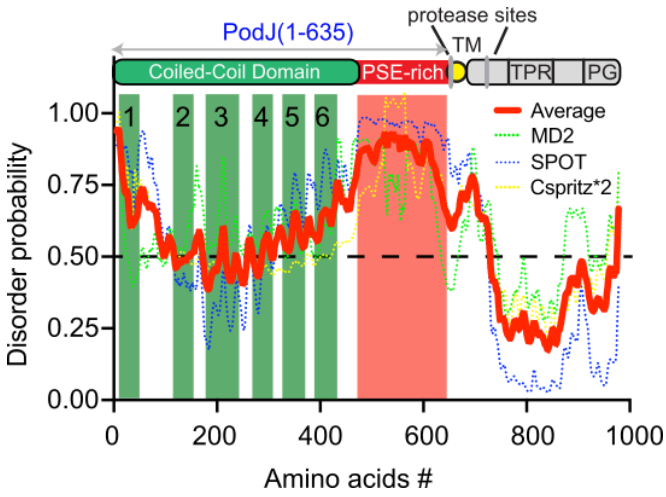

Figure 5–2 PodJ domain architecture and disordered prediction.
PodJ coiled-coil domain is composed of six independent coils that can also be treated as two groups of three coiled-coils (1-3 and 4-6). The PSE rich domain is the primary source of disorder in PodJ. The first protease site is recognized by MmpA, the second by PerP. The periplasmic domain is composed a TPR repeat domain and a PG binding domain. The probability of intrinsic disorder region over the primary sequence of PodJ was predicted by three independent programs, *i.e.*, Metadisorder MD2 [263] SPOT [264], and Cspritz [265]. The average scores of these programs were plotted against the PodJ sequence. We assumed the region as an intrinsic disorder with the probability > 75% in this study.

Lawler and coworkers were the first to look closely at the topology and function of different regions of PodJ. By doing a domain deletion study where PodJ was truncated gradually by starting at the C-terminus, they were able to score how different domains of PodJ impacted: 1. Holdfast synthesis, 2. ΦCbK sensitivity, 3. Swarming motility, 4. PodJ localization, and 5. PleC-GFP localization.[262] Holdfast synthesis and ΦCbK sensitivity are related to pili synthesis and positioning of PilA, the pili subunit protein (Figure 5–3).[266]

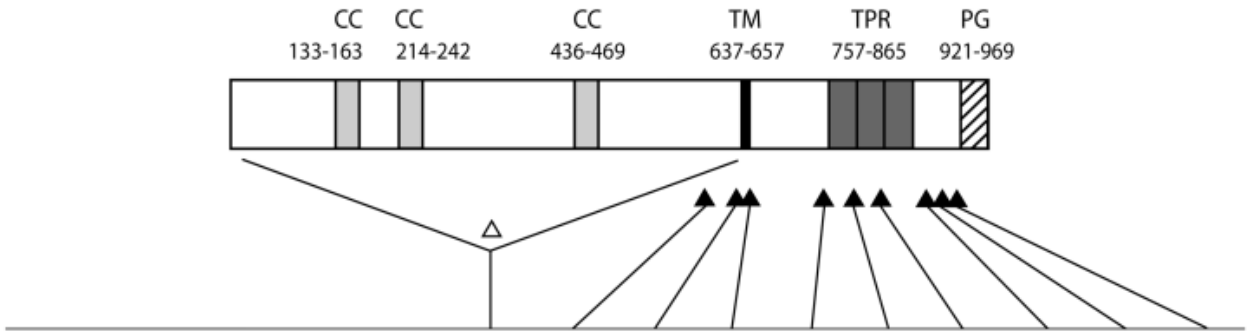

	Δ*podJ*	CB15 (974)	Δcyt	589	639	660	757	794	829	878	900	921
Holdfast synthesis	-	+	-	-	+	+	+	+	+	+	+	+
ϕCbK sensitivity	-	++	-/+	-	-/+	-/+	-/+	-/+	-/+	-/+	+	+/-
Swarming motility	+/-	+	+/-	+/-	+	+	+	+	+	+	+	+
PodJ localization	-	F	P/M	S	F/S	F/S	F	F	F/S	F/S	F	F
PleC-GFP localization	S	F	S	S	S/F	S	F	F	F	F/S	F	F

Figure 5–3 Summary of PodJ deletion on *C. crescentus* phenotypes.
For holdfast syntheis, + indicates formation of holdfast while – means lack of holdfast. For ΦCbK sensitivity, ++ means wild-type levels, – represents no titre increase (resistant), + represents significant titre production but less than wild-type, +/– represents a 300-fold increase in titre, and –/+ represents a two to four-fold titre increase. For swarm motility, + indicates swarm size greater than ΔpodJ, +/– represents swarm size equivalent to ΔpodJ. For PodJ and PleC-GFP localization, – indicates no localization, F is for flagellar pole localization, M represents midcell localization, S represents stalk pole localization, and P represents polar localization. Figure taken from Lawler, *et al. Mol. Micro.* **2005**, 59(1), 301-316.

PilA localization is disrupted when cells lacking *podJ* are no longer able to properly localize PleC at the swarmer cell pole.[267] Pili biogenesis and positioning in *Caulobacter crescentus* are important for surface recognition by motile swarmer cells to begin transitioning to stalked cells.[268] PodJ and PleC localization are both interconnected due to the ability of PodJ to recruit PleC to the new cell pole and the loss of proper PleC localization was lost when cytosolic portions of PodJ were deleted, indicating that PleC is likely recruited through cytosolic domains.[259,269] In addition to PilA and PleC recruitment/localization, PodJ is able to recruit a variety of different proteins to the cell pole including CpaE and CpaC which are important for pilus secretion and pilus assembly.[259] PodJ is able to recruit this variety of proteins through its cytosolic domains (PleC) and through its periplasmic domains (CpaE, CpaC, PilA). It still remains unclear the specific domains required for recruitment of these factors or how they interact with one another.

In order to answer this question, our lab has begun to further study the specific domain interactions of PodJ with its binding partners as well as with itself and the impact of losing PodJ throughout the cell-cycle.

5.2 Results

5.2.1 PodJ recruits PopZ to the new cell pole

PopZ forms a bipolar population in late stages of the cell-cycle. (Figure 5–1). The old cell pole PopZ is inherited by the daughter cell meaning the new pole PopZ could either be newly translated PopZ or old PopZ that has transitioned to the new cell pole. To test these models, we used a fluorescent timer attached to PopZ (Figure 5–4).[270]

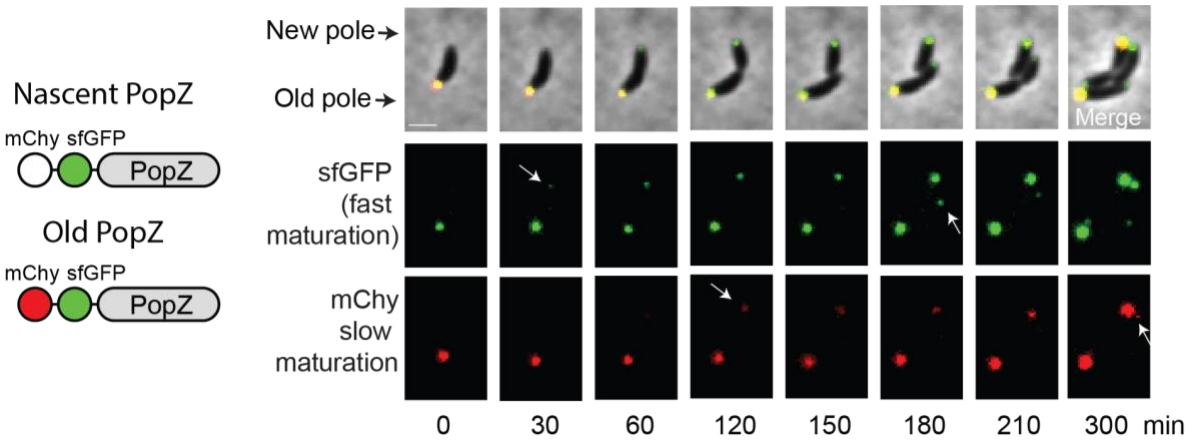

Figure 5–4 Newly translated PopZ localizes to the new cell pole in developing cells.
Expression of constructs was accomplished by growing cells overnight at 28ºC in M2G containing antibiotics to OD_{600} of 0.2. A final concentration of 0.03% xylose was used to induce expression for 3 hours. Cells were imaged on a 1% agarose pad on the Nikon T*i*E using Phase, GFP, and mCherry filter sets and settings (see Methods). mCherry (t_{50} maturation time of 45 min at 32ºC) and sfGFP (t_{50} maturation time of 19 minutes at 32ºC) chromophores mature at different rates so newly synthesized PopZ will appear green and older synthesized PopZ appears as yellow. At time 0 min, the old pole shows both green and red indicating it is older yellow PopZ. At times 30-60 min a green PopZ focus appears at the opposite pole. At time 120 min the new foci contain both green and red fluorescence, indicating the subsequent maturation of the mCherry chromophore. Subsequently, in the second round of cell division, a green PopZ

focus appears at the new cell pole of the divided cell at time 180 min as the newly translated PopZ appears at the new cell pole. Experiment, data analysis, and figure provided by Wei Zhao.

The fluorescent timer works due to the slower maturation time of mCherry (t_{50} maturation time of 45 min at 32ºC) compared to superfolder green fluorescent protein (sfGFP) (t_{50} maturation time of 19 minutes at 32ºC).[271] Older PopZ appeared as yellow foci (green/red overlay) and new PopZ appeared as green foci. When we tracked the PopZ labeled with the fluorescent timer, we observed that the old cell pole PopZ appeared yellow due to the maturation of both fluorescent proteins (Figure 5–4). As the cells continued its lifecycle, green labeled PopZ appeared at the new pole, indicating the new pole population was newly translated PopZ (Figure 5–4). After one cell division, this observation held true for the new daughter cells (Figure 5–4). There are two known factors that can recruit PopZ to the new cell pole: TipN[260], the cell pole marker protein and ZitP[261], a zinc finger domain protein. PopZ still accumulates at the new cell pole in the absence of these factors, so we wanted to see whether PodJ was yet another PopZ new pole scaffold. To test this we began by expressing mCherry labeled PopZ from a vanillate inducible promoter in wild-type, Δ*podJ*, and a sfGFP-PodJ complementary strain (Figure 5–5A).

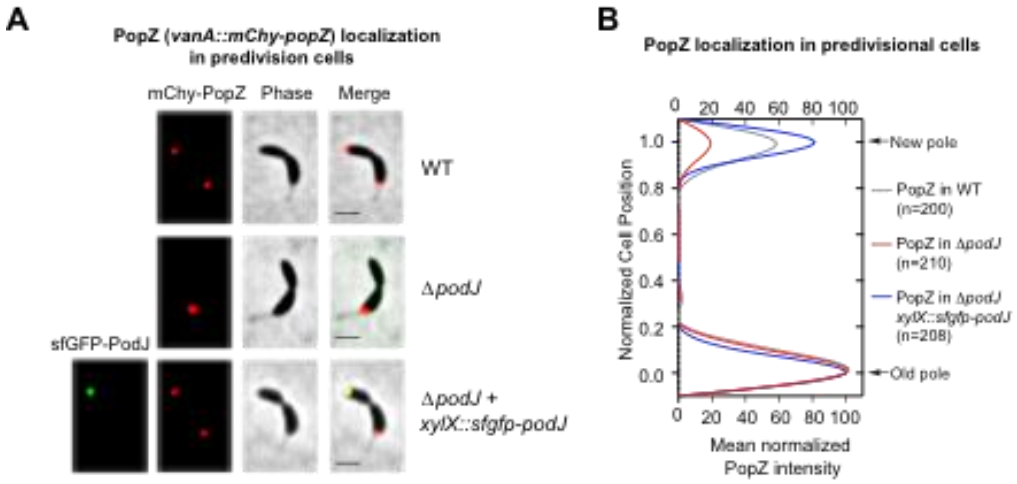

Figure 5–5 PodJ impact on PopZ localization expressed from an inducible promoter.
Expression of constructs was completed by growing cells overnight at 28ºC in M2G containing antibiotics to OD_{600} of 0.2. A final concentration of 0.03% xylose was used to induce expression for 3 hours. Cells were imaged on a 1% agarose pad on the Nikon TiE using Phase, GFP, and mCherry filter sets and settings (see Methods). A) mCherry-PopZ localization in predivisional cells in the wild-type (bipolar) versus the *podJ* deletion *C. crescentus* (monopolar).

Bars, 2 µm. B) Quantitative analysis reveals a substantial reduction of PopZ abundance at the new cell pole of Δ*podJ* predivisional cells. Cell poles (new or old) were distinguished and orientated manually by observation of a stalk. The signal intensity was normalized with the highest value as 100% in each strain. Profile measurements were done using MicrobeJ's intensity profile feature. 50 or more cells were averaged for each condition. Experiment, analysis, and figure provided by Wei Zhao.

mCherry-PopZ displayed bipolar localization in the wild-type background, but when PodJ was absent from cells, mCherry-PopZ accumulated 5-times less at the new cell pole (Figure 5–5A,B). mCherry-PopZ new pole localization was restored when sfGFP-PodJ was expressed from the xylose locus (Figure 5–5A,B). To ensure this localization was due to recruitment by PodJ, we also tested PodJ localization capabilities in the absence of PopZ (Figure 5–6A).

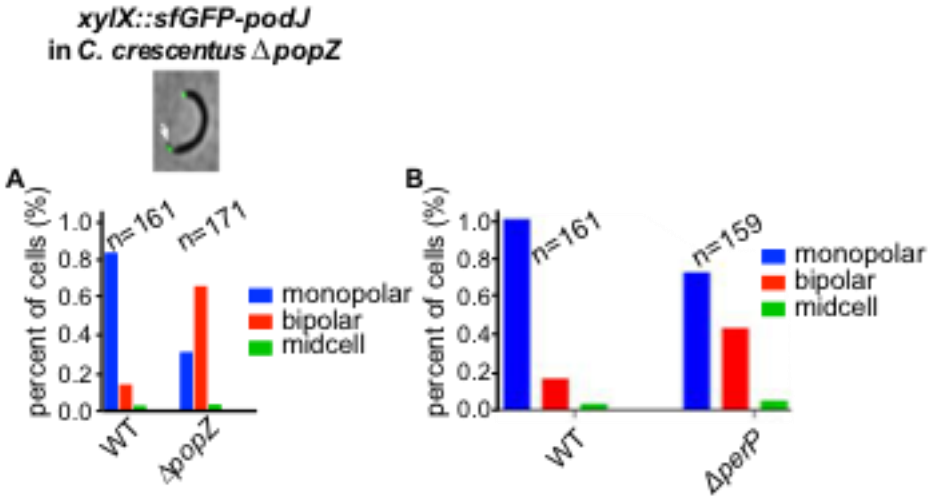

Figure 5–6 PodJ localization in different deletion strains.
Expression of constructs was completed by growing cells overnight at 28ºC in M2G containing antibiotics to OD_{600} of 0.2. A final concentration of 0.03% xylose was used to induce expression for 3 hours. Cells were imaged on a 1% agarose pad on the Nikon T*i*E using Phase and GFP filter sets and settings (see Methods). A) sfGFP-PodJ localization in WT and *popZ* deletion background. B) sfGFP-PodJ localization in wild-type and Δ*perP* strains**.** Experiment, analysis, and figure provided by Wei Zhao and Kim Kowallis.

PodJ was able to localize, though the population became more bipolar, potentially due to misregulation of PerP or MmpA. We observed sfGFP-PodJ in a Δ*perP* background and did see an increase in bipolar sfGFP-PodJ accumulation though not at the same levels observed in Δ*popZ* (Figure 5–6B). There are likely other factors related to deletion of *popZ* that are regulating this process.

To dig deeper into PodJ impact on PopZ localization, we moved to a system where mCherry-PopZ was under control its native promoter. We subsequently deleted *podJ* and complemented with sfGFP-PodJ in this P_{popZ}::mCherry-popZ background. We observed that cells containing PodJ had a ratio of roughly 1:1 mCherry signal at the old and new cell poles and had a higher mCherry signal at the new cell pole than in cells than cells where *podJ* had been deleted (Figure 5–7A). Additionally, Δ*podJ* cells has less overall mCherry signal, indicating that overall PopZ expression was down (Figure 5–7B). The old:new pole ratio of mCherry-PopZ was around 2:1, indicating the low amount of mCherry-PopZ accumulation at the new cell pole (Figure 5–7B).

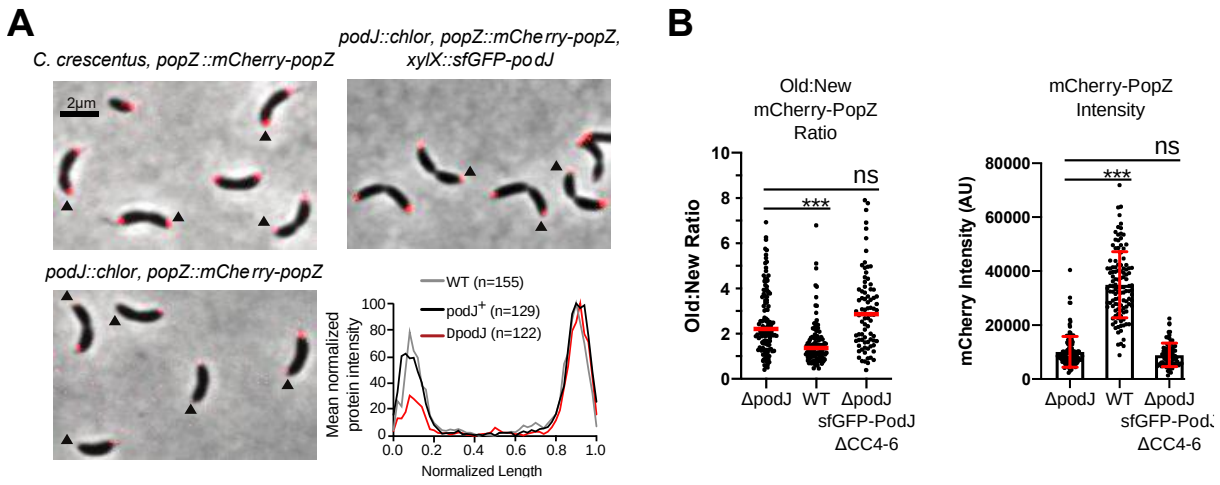

Figure 5–7 PodJ impact on PopZ colocalization expressed from its native promoter.
Expression of constructs was completed by growing cells overnight at 28ºC in peptone yease extract (PYE) containing antibiotics to OD_{600} of 0.2. A final concentration of 0.03% xylose was used to induce expression for 3 hours. Cells were imaged on a 1% agarose pad on the Nikon T*i*E using Phase and mCherry filter sets and settings (see Methods). Black triangles indicate the new cell poles in each image. A) mCherry-PopZ localization where PopZ is expressed from its native promoter in wild-type, Δ*podJ*, and Δ*podJ* complemented with sfGFP-podJ. Fluorescent intensity profiles were normalized for each condition by making the highest intensity equal to 100. Cells were oriented using the stalk. The stalk pole is represented by 1.0 on the x-axis. B) Measurement of mCherry-PopZ ratio at the old and new cell poles and overall intensity of PopZ in wild-type, Δ*podJ* cell, and complementary strain. *** indicates $p <$ 0.0001. Data is of three biological replicates. Red line indicates mean. Red bars indicated mean ± standard deviation. Statistical analysis done using student's t-test. Greater then 100 cells for each condition, represents two biological replicates.

This observation follows what was observed when mCherry-PopZ was under control of an inducible promoter. When sfGFP-PodJ was expressed in the Δ*podJ* background, mCherry-PopZ accumulation at the new cell pole returned to wild-type levels (Figure 5–5). This complementation

was not able to return overall mCherry-PopZ intensity to wild-type levels (data not shown), indicating that transcriptional control of *popZ* was still impacted even with rescuing the new cell pole localization. This is likely due to the deletion of *podJ* impacting downstream factors that control *popZ* transcription.

To further understand the how PodJ recruits PopZ to the new cell pole, we turned to heterologous expression in *E. coli*, which can act as a "test tube" to study orthogonal protein interactions.[134,240] Fluorescently labeled truncations of PodJ and full length PopZ were coexpressed in *E. coli* and colocalization of PodJ and PopZ was observed (Figure 5–8).

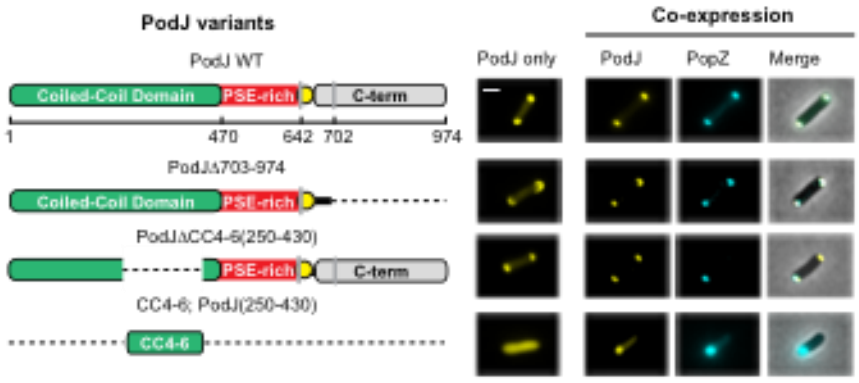

Figure 5–8 PodJ truncation series coupled with heterologous expression in *E. coli* to identify PodJ-PopZ interacting domains.
E. coli BL21 containing plasmids were grown overnight at 37ºC in LB containing antibiotics. Cells were diluted into fresh LB containing antibiotics at a 1:100 dilution. Cells were grown for two hours at 37ºC at which point expression was induced using a final concentration of 100 µM isopropyl β-D-1-thiogalactopyranoside (IPTG). Cells were then grown for two hours at 28ºC and imaged on 1% agarose pads on the Nikon T*i*E using a Phase, YFP, and CFP filter set and settings (See Methods). PodJ only is shown to identify if that truncation of PodJ can self-assemble at the cell poles. Scale bar is 2 µm. Experiment, analysis, and figure provided by Wei Zhao.

PodJ on its own displays a bipolar localization in *E. coli* and can bipolarize PopZ in *E. coli* which is monopolar when expressed alone.[134] Of note from this panel is PodJ-fusion where amino acids in the coiled-coil region 4-6 (CC4-6) have been deleted, referred to hereafter as PodJΔCC4-6. PodJΔCC4-6-fusion forms a bipolar localization population in *E. coli* but can longer localize PopZ in a bipolar form (Figure 5–8). To determine if the CC4-6 region was a PopZ binding site, YFP-CC4-6 fusion was expressed with and without PopZ present. In the absence of PopZ, YFP-

CC4-6 fusion was diffuse throughout the cell (Figure 5–8). Upon coexpression with PopZ, the YFP-CC4-6 variant localized to one cell pole with PopZ (Figure 5–8). Removal of CC4-6 from PodJ was the only way to lose colocalization with PopZ in *E. coli.* To test whether this interaction pattern persisted in *C. crescentus*, we expressed an sfGFP labeled PodJΔCC4-6 in the strain expressing P_{popZ}::mCherry-popZ strain and compared localization at the new cell pole to wild-type and Δ*podJ* cells (Figure 5–7B). sfGFP labeled PodJΔCC4-6 was unable to return mCherry PopZ at the new cell pole to wild-type levels, indicating a domain responsible for scaffolding PopZ had been removed (Figure 5–7B). PodJΔCC4-6 was able to localize at the new cell pole similarly to sfGFP-PodJ, so loss of mCherry-PopZ localization is not due to loss of sfGFP-PodJ localization (Figure 5–9A,B).

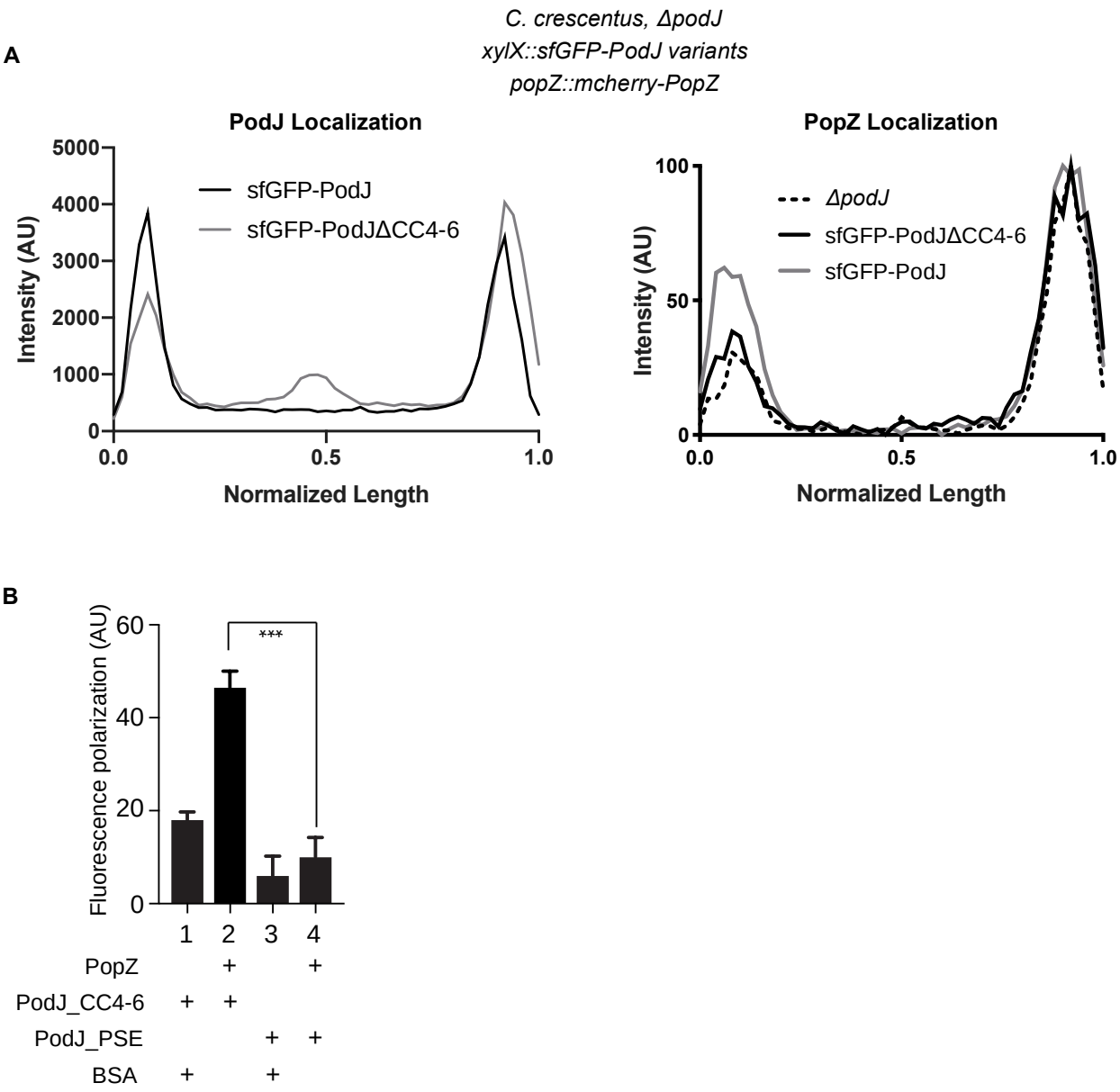

Figure 5–9 PodJCC4-6 is the recruitment domain for PopZ.
Expression of constructs was completed by growing cells overnight at 28ºC PYE containing antibiotics to OD_{600} of 0.2. A final concentration of 0.03% xylose was used to induce expression for 3 hours. Cells were imaged on a 1% agarose pad on the Nikon T*i*E using Phase, GFP, and mCherry filter sets and settings (see Methods). A) Fluorescence intensity profiles of sfGFP labeled PodJ variants in Δ*podJ* cells and fluorescence intensity profile of mCherry-PopZ expressed from its native promoter in Δ*podJ* cells either expressing no PodJ (Δ*podJ*), sfGFP-PodJ, or sfGFP-PodJΔCC4-6. Only full length PodJ increases localization above Δ*podJ* levels. Profile was normalized to the old cell pole intensity. B) FP binding assay of the BODIPY dye-labeled PodJ PSE or PodJΔCC4-6 mixed with 10 µM PopZ, using BSA as a negative control. PopZ binds specifically to the CC4-6 domain of PodJ. Protein purification methods can be found in Methods. FP assay analysis and figure provided by Dylan Tomares.

PodJΔCC4-6 also formed a population at the midcell likely due to the high expression levels from the xylose promoter (Figure 5–9A). We also wanted to determine if this interaction

held up *in vitro,* so we measured purified PodJ binding to PopZ using FP. FP can be used to quantify binding affinity by correlating binding interactions with the amount of polarized light the molecule emits. Light polarization is inversely proportional to the rotational movement of the molecule, so the more it is rotating (tumbling), the less polarized light is emitted. Proteins can be labeled with a fluorophore and FP can be measured in the presence of other proteins. If a fluorescently labeled protein binds, it will tumble less and FP will increase.[272] Bovine serum albumin (BSA) was used a negative control for nonspecific interactions and PodJ PSE domain was also used as a negative control. When BODIPY labeled PodJCC4-6 was mixed with PopZ, FP increased in a statistically significant manner when compared to BSA or PodJ PSE (Figure 5–9C). These results point to PodJ CC4-6 being the domain responsible for recruiting PopZ to the new cell pole. What happens to cells when PodJ is no longer present in cells, or when it cannot recruit PopZ to the new cell pole? We next explored impact on downstream partners of PopZ.

5.2.2 Losing PopZ at the new cell pole impacts chromosome segregation and the divisome

In addition to recruiting CckA[134] to the new cell pole and acting to slow down diffusion of ChpT and CtrA[273], PopZ acts as a sink for ParA monomers[229] and a tether for ParB.[132,133] ParB binds *parS, a* DNA site near the origin of replication, and acts as a tether that pulls the newly replicated chromosome to new cell pole, where it binds to PopZ to anchor the chromosome.[132,133] This anchoring action enables the daughter cells to each inherit a copy of the chromosome. Domains and residues involved in ParB binding PopZ have been elucidated[240], and dynamics of the ParB localizing at the cell poles have been studied in wild-type cells.[174] The effects on ParB copies per cell and localization have been studied in the Δ*zitP* background so we began studying the effects of deleting *podJ* on ParB dynamics.

We began by determining the number of chromosomes in a strain where *podJ* had been deleted. Wild-type and Δ*podJ* cells grown to OD_{600} 0.1 in PYE overnight and rifampicin (20 µg/mL) was then added to stall replication. Cells were then grown for 3 more hours to allow for complete replication of DNA. Cells were fixed and permeabilized in ethanol and DNA was stained with SYTOX Green nucleic acid stain. Fixed cells were then analyzed by flow cytometry. In wild-type cells, two populations appear that correspond to one chromosome (1N) or two chromosomes (2N) (Figure 5–10).

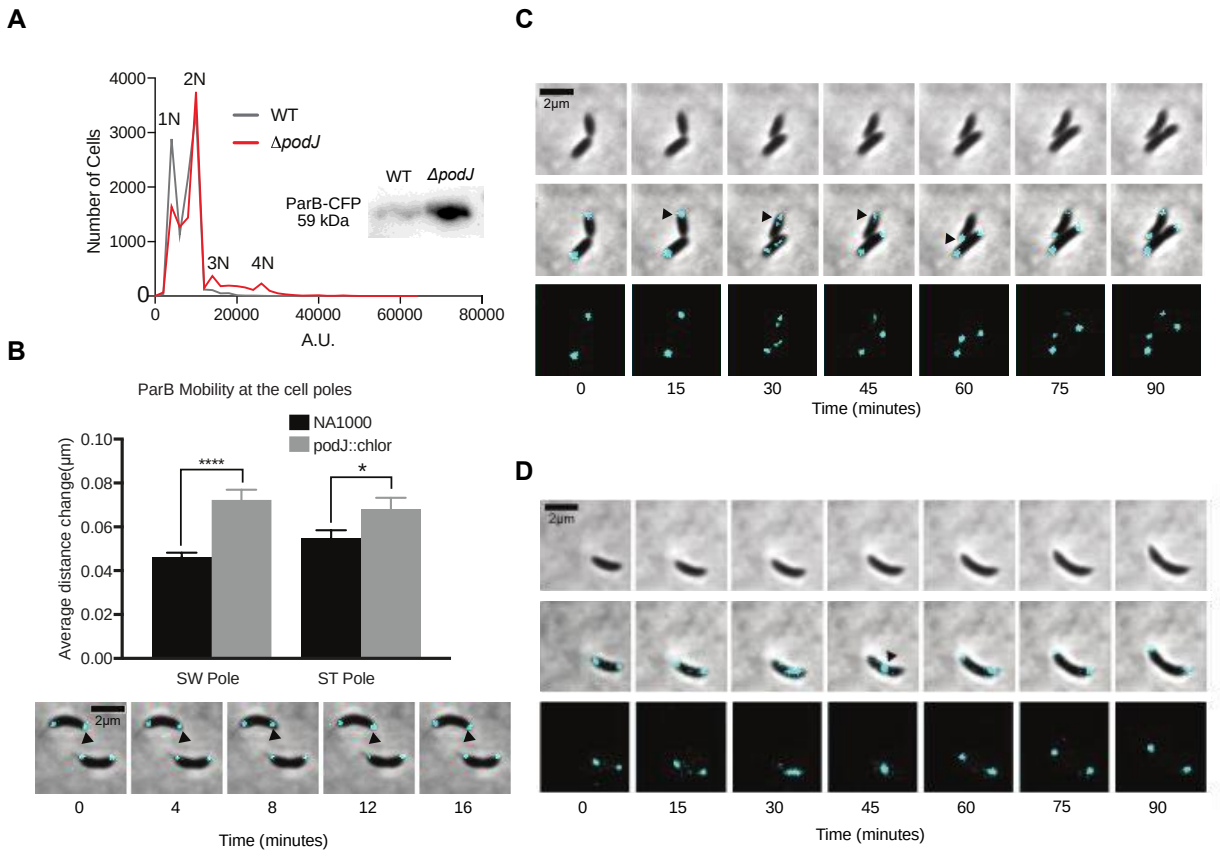

Figure 5–10 Analysis of chromosome and ParB dynamics in a Δ*podJ* mutant.
All cells were grown overnight in PYE containing antibiotics to OD_{600} of 0.2. A) Flow cytometry of *parB::CFP-parB* and Δ*podJ*, *parB::CFP-parB* cells with chromosome staining using Sytox Green (ThermoFisher), see Methods for detailed protocol. Western blot for ParB-CFP in *parB::CFP-parB* and Δ*podJ*,*parB::CFP-parB* inlaid, see Methods for detailed protocol. B) CFP-ParB tracking of new (SW) and old (ST) cell pole CFP-ParB. Black triangle on cell image shows the mobility of CFP-ParB at the new cell pole in the Δ*podJ* background. **** indicates $p < 0.0001$. * indicates $p<0.01$. Bars represent standard deviation. Data is of two biological replicates. Statistical analysis done using student's t-test. MicrobeJ was used to track CFP-ParB foci during fast time-lapse experiments. Predivisional cells that had already segregated a CFP-ParB focus to the new cell pole were at t=0 were analyzed. Maxima were tracked, and

the raw distance changes for each 4-minute difference were averaged for new and old cell pole CFP-ParB foci. Averages for two separate experiments were pooled and plotted. C,D) CFP-ParB phenotypes in the Δ*podJ* background.

In cells where *podJ* was deleted, the number of cells with 1N chromosomes decreases and two new populations appear that correspond to 3N and 4N chromosomes (Figure 5–10A). This means that the *podJ* deletion strain results in over replication of the chromosome during one cell cycle for a subset of cells. This could be the result of loss of ParB mediated tethering to the cell poles by PopZ or it could be the result of PodJ regulatory impact upon CtrA. Notably CtrA is a well-studied inhibitor of replication initiation.[122] To explore this, we observed CFP-ParB dynamics in single cells in wild-type and Δ*podJ* backgrounds. To quantify CFP-ParB dynamics, we measured mobility of translocated CFP-ParB at the new and old cell poles. Past studies by Bowman and co-workers identified that the new cell pole CFP-ParB complex was more dynamic than ParB tethered at the old cell pole complex.[174] To measure stability, we grew cells to mid-log phase and used a continuous time-lapse imaging procedure where the same cells were imaged every 4 minutes (Figure 5–10B). Cells with bipolar CFP-ParB populations were identified and CFP-ParB foci were tracked over four minutes intervals at the μm scale. The distance changes every four minutes for CFP-ParB foci was averaged over 20 minutes total (5 total movements, Figure 5–10B). Interestingly, CFP-ParB foci at both old and new cell poles in Δ*podJ* displayed larger statistically significant displacement changes compared to wild-type cells (Figure 5–10). This mobility can be seen in the cell shown in Figure 5–10B marked with a black triangle. This change was expected for the new cell pole, where less PopZ accumulation results in less binding sites for ParB. The old cell pole mobility could be attributed to the overall decrease in PopZ expression in the Δ*podJ* background. In addition to this increased mobility, we also identified more severe phenotypes in individual cells where CFP-ParB foci translocated from one pole to another after initial localization at a pole (Figure 5–10C) or where CFP-ParB foci would move to middle

of the cell to form one focus, then return to each cell pole (Figure 5–10D). Due to the increased dynamics of CFP-ParB we also checked downstream factors from ParB.

During translocation of the replicating chromosome, other proteins in the divisome begin to be positioned in order to complete cell division.[274,275] Two proteins that begin positioning themselves after one ParB focus translocates are MipZ[230] and FtsZ.[250,274,276] MipZ is a gradient forming P-loop ATPase that helps position FtsZ to the mid-cell.[230] (Figure 5–11A).

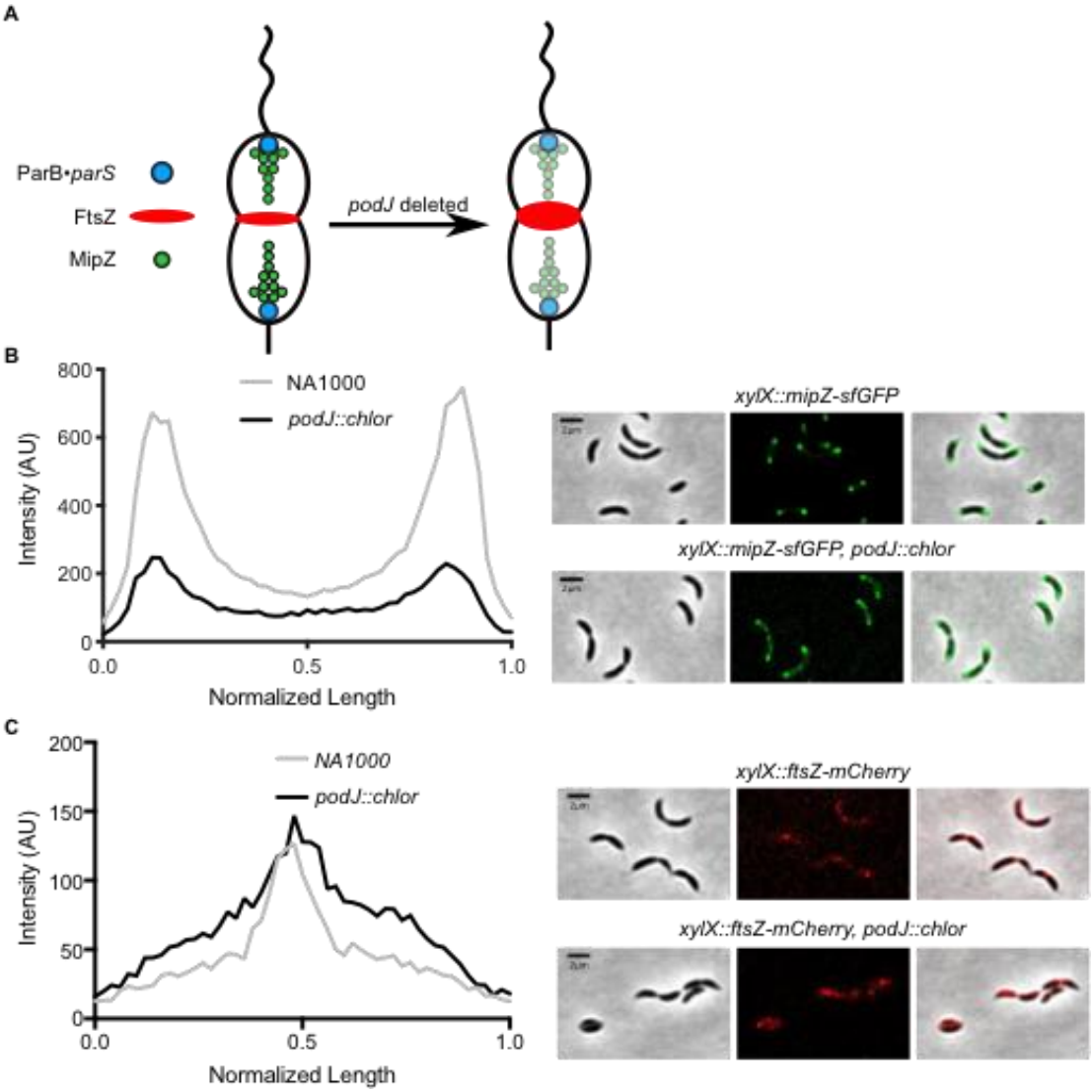

Figure 5–11 Fluorescence intensity profiling of MipZ and FtsZ fusions in wild-type and Δ*podJ*.
Expression of constructs was completed by growing cells overnight at 28ºC in PYE containing antibiotics to OD_{600} of 0.2. A final concentration of 0.003% xylose was used to induce expression for 3 hours. Cells were imaged on a 1% agarose pad on the Nikon T*i*E using Phase-Constrast, GFP, and mCherry filter sets and settings (see Methods). A)

Schematic for ParB•*parS*, FtsZ, and MipZ localization in cells with (left) or without (right) *podJ*. B) MipZ-sfGFP profiling for NA1000 (wild-type) and Δ*podJ* conditions and representative cell images. C) FtsZ-mCherry intensity profile for wild-type and Δ*podJ* and representative cells.

MipZ interacts with ParB•*parS* complex at both cell poles thus creating a high FtsZ depolymerization effect at the cell poles and a low effect at the midcell.[277] FtsZ is the Z-ring protein responsible for constriction at the site of division and has precise timing for constriction related to the start of the cell-cycle (Figure 5–11A).[276] We chose these two factors due to their well-established localization pattern phenotypes and their timing in the division machinery placement.[274] To determine whether the loss of PodJ impacts downstream cell division processes mediated by MipZ and FtsZ we expressed fluorescently labeled copies of each from an inducible xylose promoter and characterized their position in wild-type and Δ*podJ* backgrounds. We used fluorescent intensity profiling to compare positioning of the MipZ gradient and FtsZ ring between the two backgrounds. MipZ-sfGFP was able to form a gradient in wild-type cells consistent with previous work (Figure 5–11B).[230] In Δ*podJ* cells, MipZ-sfGFP formed a similar gradient but at lower intensity levels (Figure 5–11B). Both experiments were done under the same inducer concentrations so intensity differences are likely due to lower binding rates for MipZ to the ParB•*parS* complexes at the new and old cell poles or a potential unknown post-transcriptional regulation. FtsZ-mCherry was expressed in wild-type and Δ*podJ* resulting in the characteristic mid-cell localization in cells that is hallmark for FtsZ.[250] In Δ*podJ* cells, we did observe that FtsZ-mCherry did not form a tight and robust mid-cell ring, indicating that midcell positioning may be hampered (Figure 5–11C). This result follows with the distorted MipZ gradient formation and is likely due to the loss of MipZ binding to the ParB•*parS* complex. Overall these results point towards misregulation of ParB impacting downstream factors due to the loss of overall PopZ expression and localization at the new cell pole.

5.3 Discussion

In summary, we have identified a domain of PodJ responsible for recruitment of PopZ (CC4-6, Figure 5–12) and established an important connection between PopZ localization and ParB.

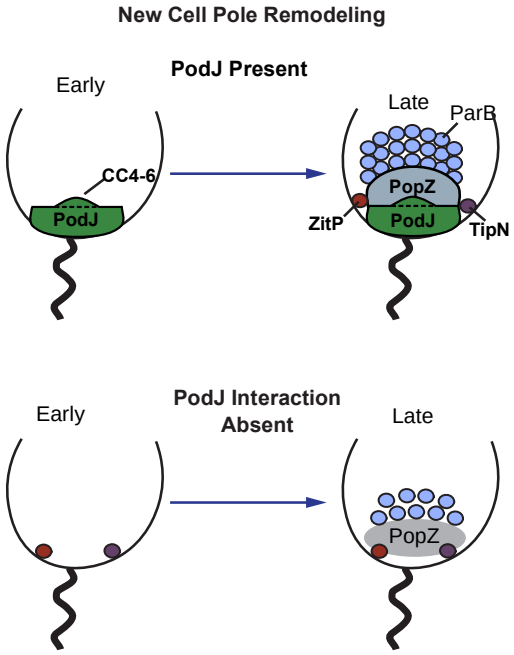

Figure 5–12 PodJ is required for robust PopZ recruitment.
When PodJ is present in cells it can recruit PopZ to the new cell pole through an interaction in the CC4-6 domain with PopZ. As the cell cycle progresses, the recruitment of PopZ allows for ParB stabilization and correct positioning of the chromosome. If PodJ is absent or CC4-6 is removed, the PopZ is recruited less robustly by ZitP and TipN leading to less PopZ recruitment and poor ParB stabilization.

The relationship between ParB and PopZ is well understood, but before these experiments it was unknown whether a factor upstream of PopZ (in this case PodJ) had a direct effect on PopZ ability to recruit client proteins (Summary Figure). In the absence of PodJ or CC4-6, two other PopZ localization factors remain (ZitP and TipN) to localize PopZ, but the new cell pole localization is up to 5 times lower than in wild-type independent of how PopZ is produced (inducible (Figure 5–5) or native promoter (Figure 5–7)) . This loss of localization results in

weaker ParB binding at the new cell pole and ultimately impacts MipZ gradient formation and FtsZ ring positioning (Figure 5–12).

5.4 Future directions

5.4.1 How many factors are required for PopZ localization?

Some important questions remain about the impact of PodJ on additional or subsequent new cell pole factors. We observed a 4-fold decrease in PopZ localization at the new cell pole (Figure 5–7). This indicates that PopZ relies upon redundant mechanisms for new cell pole accumulation due to localization not being completely abolished upon *podJ* deletion. Therefore, a knowledge gap remains in the variety of factors that redundantly contribute to PopZ accumulation. We plan to investigate this redundancy in three ways. First is to use western blots to see if we can quantify the differences in accumulation of PopZ in wild-type cells versus Δ*podJ*. We were able to distinguish between these populations using mCherry fluorescence (Figure 5–7B) so we should be able to identify a decrease in mCherry-popZ levels using a western blot. Once we are able to quantify protein levels in this way we will attempt to make three multi-deletion strains: Δ*zitP*Δ*podJ*, Δ*tipN*Δ*podJ*, and Δ*zitP*Δ*podJ*Δ*tipN* all with mCherry-PopZ expression controlled by the native *popZ* promoter. We will generate these strains using a two-step deletion plasmid.[169] This plasmid works by carrying a selectable and counter-selectable marker, a kanamycin resistance gene and *sacB* in the backbone. *sacB* converts sucrose to levan, when levan accumulates in cells it results in cell death.[278] Flanking an antibiotic resistance gene, such as the gentamycin resistance

gene, with 1000 base pairs up and down stream of the gene of interest on the two-step plasmid generates homologous regions with the chromosome (Figure 5–13A).

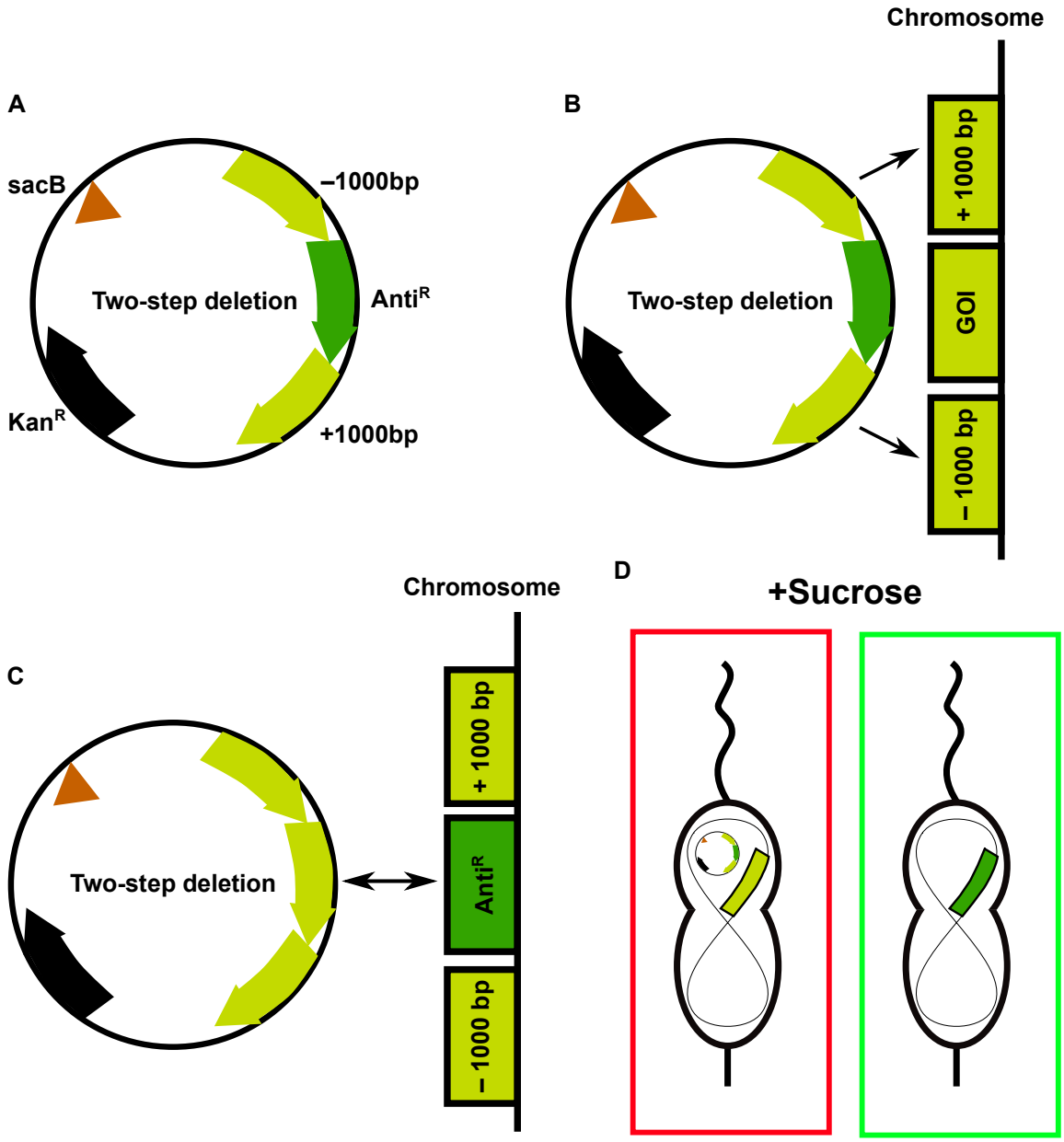

Figure 5–13 Two step deletion plasmid procedure overview.
A) Two-step deletion plasmid design. The plasmid contains a Kan^R marker and *sacB* gene for counter selections. 1000 basepairs up and downstream of the gene of interest flank an antibiotic cassette to be inserted into the genome. B) After the plasmid enters the cell, homology between flanking regions results in double homologous recombination. C) Double homologous recombination results in the gene of interest on the plasmid and the antibiotic resistance marker on the chromosome. D) Counter selection with sucrose results in cells with the plasmid and no recombination dying. Cells with the antibiotic resistance marker on the chromosome and no longer containing the plasmid survive on sucrose.

When the plasmid is electroporated into cells, single and double homologous recombination results in the swapping of the gene of interest with the antibiotic resistance gene (Figure 5–13B,C). By then growing cells under no antibiotic selection, the plasmid, which now contains the gene of interest, will be lost. Plating these cells on agar containing sucrose and the antibiotic matching the resistance marker on the chromosome can remove cells that have only undergone a single homologous recombination event. Cells without the original plasmid that have undergone double homologous recombination will survive, while cells containing the plasmid and only underwent a single homologous crossover event will die due to the *sacB* gene (Figure 5–13D). It is important to do this counterselection due to the rate of single homologous crossover events occurring more often than double homologous crossover events. Cells can then undergo further selection using antibiotics and counter selection on kanamycin. Colony PCR can then be used to determine if colonies contain the antibiotic resistance gene. We have already been able to generate a Δ*zitP*Δ*podJ* P_{popZ}::*mCherry-popZ* strain that remains viable (Figure 5–14A).

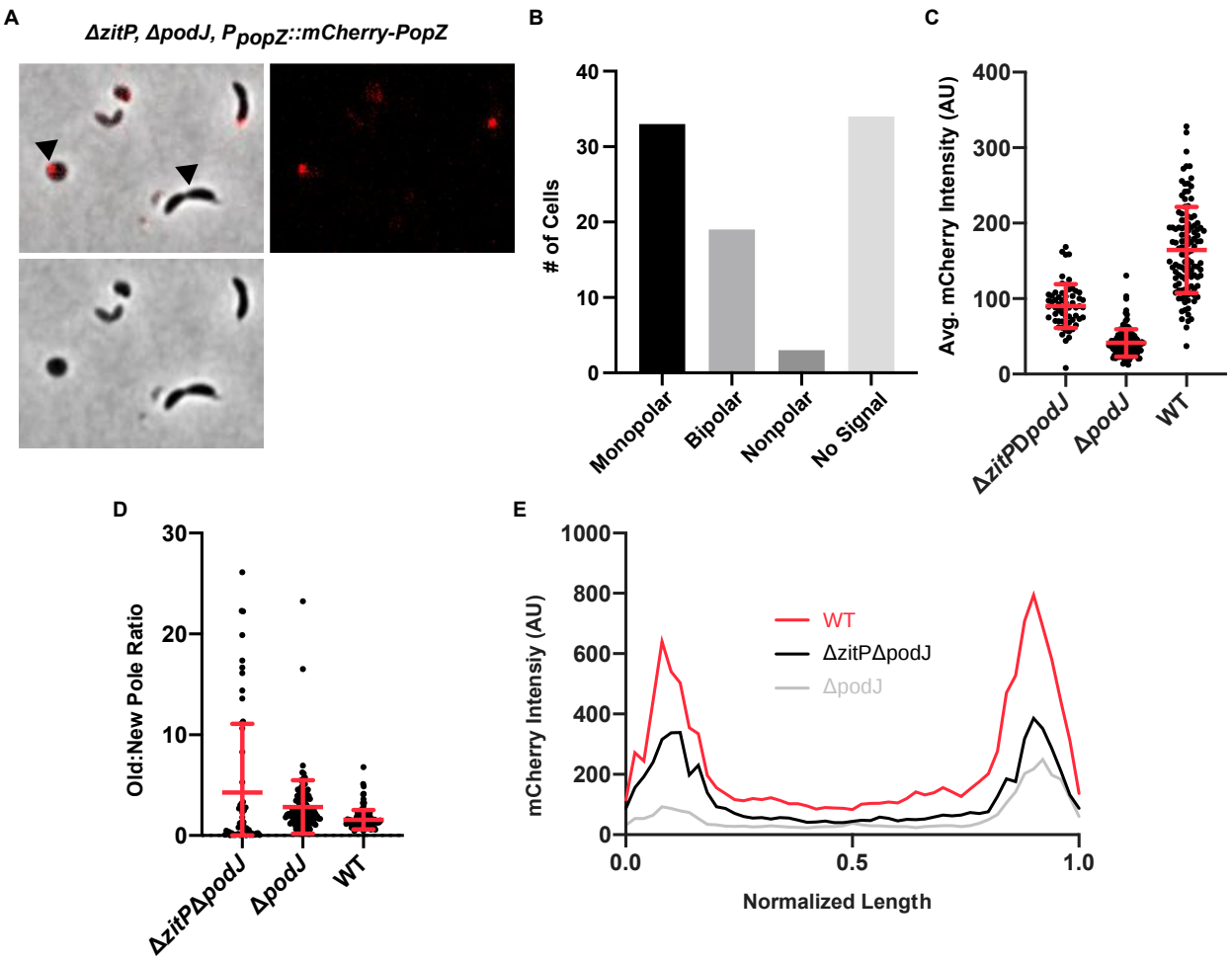

Figure 5–14 Δ*zitP* impacts mCherry-PopZ localization in *podJ* mutant.
Cells were grown overnight in PYE containing antibtiocs at 28ºC to and OD_{600} of 0.2-0.4. Cells were plated on 1% agarose pads and imaged using Phase and mCherry filters and settings (see Methods). A) Cells expressing mCherry-PopZ in cells with *zitP* and *podJ* deleted. Black triangles indicate cells with no mCherry-PopZ or round shape. B) Cell counts for one biological replicate. C) Average mCherry intensity of cells producing mCherry-PopZ from its native promoter. N greater than 80 for each condition. Only cells with mCherry signal were included. D) Old:New pole ratio of mCherry-PopZ. N greater than 80 for each condition. Only cells with mCherry signal were included. E) Average fluorescence intensity profile of cells expressing mCherry-PopZ from its native promoter. Cells were oriented using the stalk, 1.0 represents the stalk cell pole. Average or greater than 80 cells for each condition. Only cells with mCherry signal were included.

Analysis of the dual deletion mutant showed interesting phenotypes, mainly that many cells did not contain any detectable mCherry-PopZ signal using microscopy and the formation of round cells with mCherry-PopZ foci (Figure 5–14A, marked with black triangles). Greater than 1/3rd of cells counted were lacking any mCherry-PopZ signal detectable above background in cells (Figure 5–14B). We decided to analyze the cells that did contain mCherry-PopZ signal to determine their

localization and distribution. Using cells with mCherry fluorescence above background and visible stalks for pole positioning, we measured the average mCherry intensity in cells and observed higher average levels compared to Δ*podJ* only, but lower than wild-type (WT) (Figure 5–14C). We also surveyed old:new pole ratio and found that cells displayed two populations, either zero or above 10 with an average of 4.3 (Figure 5–14D). Cells either had very little old pole PopZ but higher levels at the new pole (population near 0) or a smaller population had very little new pole PopZ but a large amount at the old pole (above 10 population). This finding is in contrast to both wild-type (average of 1.6) and Δ*podJ* (average of 2.8). This increase is due to a greater population of cells containing less PopZ at the new cell pole compared to wild-type and Δ*podJ*. This finding is somewhat masked when averaging the new and old cell poles for fluorescence intensity profiling, where the new and old cell poles look equal for Δ*zitP*Δ*podJ* (Figure 5–14E). Overall this points to the loss of another recruitment factor impacting PopZ localization at the new cell pole. The average cell intensity increasing compared to Δ*podJ* may also indicated transcriptional changes due to deleting a second gene. A western blot will be used to confirm relative protein levels or fusion degradation and if those appear similar, RT-qPCR can be employed to monitor *popZ* mRNA accumulation. A time-lapse experiment of cells can also help to track down why some cells have no PopZ. Likely, some cells are not inheriting PopZ and after dividing do not produce more. What is concerning and exciting is the appearance of round cells (Figure 5–14A). Round cells point toward cell defects related to insertion of new peptidoglycan and peptidoglycan linking with the membrane possibly due to incorrect regulation of MreB.[279,280] If we aim to delete one more gene (*tipN*) to generate a *ΔtipNΔzitP* mutant , these cells may not be viable after another deletion related to new cell pole localization. If this is the case, we will make a complementary strain of PodJ under the xylose promoter so that one new cell pole localization factor will be

expressed at all times. In addition, we will be able to deplete PodJ and observe phenotypes related to all of the new cell pole factors being absent. This experiment will be able to tell us if PopZ is still able to form foci at the new cell pole. If it does, it opens up the possibility for other recruitment factors or a previously unexplained property of PopZ to recognize the new cell pole in the absence of other cell pole factors.

5.4.2 Do ZitP and TipN depend on PodJ for localization?

With a Δ*zitP*Δ*podJ* mutant already made and Δ*tipN*Δ*podJ* possible, we also want to determine if deletion of PodJ impacts the localization of ZitP or TipN. TipN is likely not dependent on PodJ as it is the first protein that localizes to the new cell pole.[281] The possibility remains that after it localizes to the new cell pole, PodJ could stabilize it there. ZitP localization could be dependent on PodJ as it appears after PodJ arrives at the new cell pole. Using the deletion strains, we can express fluorescent protein labeled copies of ZitP^{261} and TipN^{281} in their respective double deletion strains and observe localization. If both are able to localize to the new cell pole we can verify that neither is impacted by the loss PodJ.

5.4.3 Optimizing native *podJ* promoters for live cell imaging

Use of native promoters in molecular biology can be important for maintaining the status quo in cells. As an example, when PodJ is expressed from a xylose promoter instead of its native promoter, PodJ fusion levels end up at least 10-fold higher. This can lead to effects (ectopic poles, Chapter 6) that are not relevant for studying the cell-cycle. One drawback to using native promoters is that if transcriptional levels are low, it can be difficult to produce enough genetically encoded,

fluorescently labeled protein to visualize on standard epifluorescent microscopes. We encountered this problem with PodJ. In our experience so far, using one of the brightest fluorescent proteins to date, mNeonGreen[282], was not bright enough to visualize PodJ localization by epifluorescence microscopy (data not shown). In the past, immunofluorescence was used to visualize PodJ localization.[259] The drawback to immunofluorescence is the requirement to fix cells blocks the ability to track changes through a cell-cycle in live cells. In order to visualize PodJ without the need to fix cells we need to overcome the low amount of total photons produced by genetically encoded PodJ fusions. One way we will explore to overcome this issue is the use of confocal microscopy coupled with super resolution techniques.

Confocal has an advantage over widefield microscopy by limiting out-of-focus light, thereby increasing the resolution of the features in the focal plane. Due to the low fusion expression levels from *podJ* promoters, confocal microscopy will enable us to revisit PodJΔCC4-6 self-assembly and recruitment of PopZ. We will then be able to apply this technique to other forms of PodJ fusions. Additionally, super resolution microscopy will allow us to image PodJ below the diffraction-limit of 200 nm. Single-molecule tracking using YFP labeled PopZ has been able to resolve PopZ dynamics in living cells.[258,283] These techniques could also be applied to PodJ to track dynamics in living cells.

5.5 Methods

Growth Conditions: *E. coli* DH5*α* strains were grown at 37 °C with shaking overnight in LB media supplemented with antibiotics (SI Table 6). *C. crescentus* strains were grown in PYE or

M2G media supplemented with antibiotics (SI Table 6) at 28 °C with shaking overnight or for specified times for imaging.

Transformations: 10-50 ng of DNA was transformed into KCM chemically competent cells and plated on LB/agar supplemented with the appropriate antibiotic.

Electroporation: *C. crescentus* was harvested by centrifuging 4 mL for 5 minutes at 21,100 x g. Supernatant was removed and cells were washed in 100 µL of cold, sterile water and centrifuged for 1 minute at 21,100 x g. This step was repeated 2 more times, followed by suspension of cells in a final volume of 80 µL. Integrating plasmids (12.5 µL) or replication plasmids (3 µL) were then added to the cells and electroporated on the *E. coli* setting of a BioRad GenePulser using 0.1 cm electroporation cuvettes (BioRad). Cells were then resuspended in 1 mL of 2xPYE and shaken at 28 °C for 3 hours, then 100 µL of cells were then plated on PYE/antibiotic plates. The remaining cells were pelleted, resuspended in 100 µL of 2xPYE, and plated on PYE/antibiotic plates. Cells were grown at 28 °C for 3 days and colonies were streaked onto a PYE/antibiotic plate. Colonies that grew after streaking were screened for using colony PCR (DreamTaq Green) using primers for integration at the xylose locus (RecUni-1, RecXyl-2), vanillate locus (RecUni-1, RecVan-2), or for replicating plasmids (Pvan-for, M13-for) according to the manufacturer's protocol with 5 minute extension times.

Two-step *sacB* Counterselection For Deletion Isolation: After electroporating two-step deletion plasmid into desired strain, cells were plated on PYE Kanamycin/desired insert antibiotic and incubated at 28ºC for 2-3 days. Colonies were then streaked on PYE plates containing the same antibiotics. Colonies were then screened for correct insertion. *podJ* deletions were screened using primers PODJ-KO-C-F and PODJ-KO-C-R. *zitP* deletions were screened using primers nSWD121 and nSWD122. A colony with the correct insertion was then grown in PYE with no

antibiotic for 24 hours with shaking at 28ºC in order to lose the original plasmid. 5 µL of cells were then plated on PYE containing 3% sucrose and the desired insert antibiotic and incubated at 28ºC for 2-3 days. 10 µL of cells were then diluted into 1 mL of PYE and were grown for 24 hours at 28ºC with shaking. 5 µL of cells were then plated on PYE containing 3% sucrose and the desired insert antibiotic and incubated at 28ºC for 2-3 days. After colonies formed, colonies were streaked onto PYE containing the desired insert antibiotic. Streaks that grew were then streaked onto PYE/kanamycin plates for counterselection. Streaks that grew on the desired insert antibiotic and did not grow on kanamycin were then screened with the primers listed above. Successful screens indicated an insert of the antibiotic resistance gene.

Imaging Conditions: *C. crescentus* strains for single time point imaging were grown overnight in M2G media supplemented with antibiotics to an OD_{600} 0.1-0.2. If cells required expression from a xylose or vanillate inducible vector, they were then induced with xylose (0.03% w/v) or vanillate (0.05 mM) for 3 hours. 2 µL of cells were deposited on a 1% agarose/M2G pad on a glass slide and covered with a glass coverslip. *E. coli* strains used for single time point imaging were grown overnight in LB media supplemented shaking at 37ºC with antibiotics to saturation. Cultures were then diluted at a 1:100 ratio into fresh LB supplemented with antibiotics. Cultures were grown to an OD of 0.2 (~ 2 hours). Induction of IPTG inducible vectors was completed using a final concentration of 100 µM IPTG.

Time-lapse Imaging: *C. crescentus* strains for single time point imaging were grown overnight in M2G media supplemented with antibiotics to an OD_{600} 0.1-0.2. If cells required expression from a xylose or vanillate inducible vector, they were then induced with xylose (0.03% w/v) for 2 hours. 2 µL of cells were deposited on a 1% agarose/M2G pad on a glass slide and

covered with a glass coverslip. The glass coverslip was then sealed with wax to prevent the pad from drying. Images were taken every 30 minutes.

Microscopy: Images were taken on a Nikon T*i*E inverted setup using an APO Lambda 100X oil objective with Phase Contrast or Differential Interference Contrast (DIC) using Zeiss Immersol 518F Immersion Oil using Nikon Element AR software to control the setup. A halogen lamp was used for the white light source. Spectra X light engine was used for all fluorescence excitation. An Andor Ixon Ultra 897 EMCCD camera was used for all imaging. All filter sets used were purchased from Chroma. CFP/YFP/mCherry (77074157) and GFP (77074160) filter cubes were used with emission filter sets GFP (77074161) and CFP/YFP/mCherry (77074158).

Purification of PodJ, PopZ, and SpmX: Protein expression of all PodJ variants followed the same protocol and is described in detail below for PodJ (1-635). To purify the cytoplasmic portion of PodJ(1-635), Rosetta (DE3) containing plasmid pwz091 was grown in 6 liters LB medium (20 µg/ml chloramphenicol and 100 µg/ml ampicillin) at 37°C. The culture was then induced at an OD_{600} of 0.4–0.6 with 0.5 mM IPTG overnight at 18°C. The cells were harvested, resuspended in the lysis buffer (50 mM Tris-HCl, 700 mM KCl, 20 mM Imidazole, 0.05% dextran sulfate, pH 8.0), in the presence of protease inhibitor cocktail tablets without EDTA (Roche). The cell suspension was lysed with three passes through an EmulsiFlex-C5 cell disruptor (AVESTIN, Inc., Ottawa, Canada), and the supernatant was collected by centrifuging at 13000 *g* for 30 min at 4°C. Also, the insoluble cell debris was resuspended in recovery buffer (50 mM Tris-HCl, 1000 mM KCl, 20 mM Imidazole, 0.05% dextran sulfate, pH 8.0) and its supernatant was collected as well as the previous centrifugation. The combined supernatants were loaded onto a 5 ml HisTrap™ HP column (GE Healthcare) and purified with the ÄKTA™ FPLC System. After washing with 10 volumes of wash buffer (50 mM Tris-HCl, 300 mM KCl, and 25 mM imidazole, pH 8.0), the

protein was collected by elution from the system with elution buffer (50 mM Tris-HCl, 300 mM KCl, and 500 mM imidazole, pH 8.0), and concentrated to a 3 ml volume using Amicon Centrifugal Filter Units, resulting in > 95% purity. All PodJ variants were dialyzed with a buffer containing 50 mM Tris-HCl (pH 8.0), 300 mM KCl, and then aliquoted to a small volume (100 µl) and kept frozen at -80°C until use. His-SpmX (1-365) expression and purification followed the same protocol except using a different lysis buffer (50 mM Tris-HCl, 300 mM KCl, 20 mM Imidazole, pH 8.0) and without a recovery step as in PodJ purification. His-PopZ was expressed and purified the same as described [240].

Fluorescence Polarization Assay: To label PodJ_PSE (471-635) and PodJ_CC4-6 (250-430), we inserted a cysteine codon just after the 6X-His-tag proteins at the N-terminal of each protein. PodJ_PSE (Cys) and PodJ_CC4-6 (Cys) expression and purification followed the same protocol as PodJ mentioned above. These two proteins were labeled at the cysteine using thiol-reactive BODIPY™ FL N-(2-Aminoethyl) Maleimide (Thermo Fisher). The proteins were mixed with 10-fold excess BODIPY™ FL N-(2-Aminoethyl) Maleimide and allowed to react for 2 hours at room temperature, and the unreacted dye was quenched with mercaptoethanol (5% final concentration). The labeled proteins were purified via dialysis to remove unreacted fluorescent dye (5 times, 500 ml buffer, and 30 mins each). Fluorescence polarization binding assays were performed by mixing 100 nM labeled proteins with 0, 0.25, 0.5, 1, 2, 4, 8, 16 µM partner protein (PopZ, SpmX, PleC, or BSA) for 45 minutes to reach binding equilibrium at the room temperature. Fluorescent proteins were excited at 470 nm, and emission polarization was measured at 530 nm in a UV-vis Evol 600 spectrophotometer (Thermo). Fluorescent polarization measurements were performed in triplicates, and three independent trials were averaged with error bars representing the standard deviation.

Intrinsically Disordered Region Analysis: The probability of intrinsically disordered regions over the primary sequence of PodJ was predicted (Figure 2C) by three independent programs, *i.e.*, Metadisorder MD2 [263] SPOT [264], and Cspritz [265]. The average scores of these programs were plotted against the PodJ sequence. Regions with probability > 75% were considered disordered in this study.

Flow Cytometry: Strains analyzed were grown overnight in PYE under antibiotic selection pressure at 28ºC. Cells were diluted to an OD_{600} of 0.1 in PYE/antibiotic and induced with 0.03% xylose for 4 hours, if applicable. Rifampicin (20 µg/mL) was then added and cells were grown for 3 more hours to allow for complete replication of DNA. Cells were then fixed in cold 70% ethanol overnight at 4ºC for up to one week by adding 700 µL of 200 proof ethanol to 300 µL of cell culture. To stain, cells were collected by centrifugation at 6,000g for 2 minutes and resuspended in 1mL of Tris-HCl buffer (20 mM Tris-HCl, pH=7.5, 150 mM NaCl) containing 0.2 µg/mL RNase (RNase A, 10 mg/mL, ThermoFisher) and 1 µM SYTOX Green nucleic acid stain. Cells were incubated at room temperature for 15 minutes then samples were run on a Cytoflex S (Beckman-Coulter) using a 488 nm laser with a FitC filter (525 nm). Cells were selected using FSC-H and SSC-H gained to 10 and 20, respectively. Cells were thresholded in FitC-H at 1000. 10000 events were collected flowing at 10 µL per minute with an abort rate of less than 5%. Raw data was exported to Prism and histograms were generated.

CFP-ParB Tracking Analysis: MicrobeJ[166] was used to track CFP-ParB foci during fast time-lapse experiments. Predivisional cells that had already segregated a CFP-ParB focus to the new cell pole were at were analyzed at time=0 minutes. Fluorescence maxima were tracked, and the raw distance changes for each 4-minute difference were averaged for new and old cell pole

CFP-ParB foci. Averages for two separate experiments were pooled and plotted. A student's t-test was used to determine statistical significance.

Fluorescence Intensity Profile Analysis: Strains expressing sfGFP-PodJ variants and also expressing mCherry-PopZ from the native PopZ promoter were imaged using the above methods. After imaging, predivisional cells expressing sfGFP-PodJ variants were oriented by visualization of the stalk. The average fluorescence intensity profile using normalized cell length was generated using MicrobeJ[166] with the new pole at 0.0 and old pole at 1.0. mCherry-PopZ was made in the same way in the same strains. MipZ and FtsZ analysis were performed in the same way.

Plasmid Construction: The plasmids used in this study can be found in Table 5–1with details on their construction listed below. The lists of oligonucleotides used in this study can be found in Table 5–2. All oligos were ordered from IDT. The strains used can be found in Table 5–3 and methods to generate strains are listed below. Phusion polymerase (ThermoFisher) was used for amplification of PCR products used in Gibson assembly and isolated using gel electrophoresis using a 1% agarose, 1xTAE gel with ethidium bromide added for visualization by UV light. Band sizes were determined using a GeneRuler 1 kb DNA Ladder (ThermoFisher). Bands were excised from the gel and extracted using a GeneJet Gel Extraction Kit (ThermoFisher) following manufacturer's protocols, with the addition of a 100 µL binding buffer wash step following the spin through of DNA/agarose/binding buffer. Water was used for elution. DNA concentrations were determined using a NanoDrop 2000 spectrophotometer (Thermo Scientific). All reactions were done according to the manufacturer's protocols with annealing temperature at 55 °C.

pCZ393 (pXyl-2-sfGFP-podJ): pXGFPN-2-Pxyl-PodJ was used as vector template and amplified using primer CZ10980 and CZ10981, Gibson assembly was used to insert sfGFP

amplified from pSR58.6 using primers CZ10982 and CZ10983. Integration into *C. crescentus* was tested by colony PCR using primers RecXyl-2 and RecUni-1[284].

pWZ0139 (pVCHYN-6-mCherry-popZ): The *mCherry-popZ* gene was PCR amplified from the plasmid WSC1273 (pCDFDuet1-mCherry-PopZ) by using primers WZ0330 and WZ0331. The backbone including the P*van* promoter and the HRSAT linker was PCR amplified from the plasmid pVCHYN-6 by using primers WZ0328 and WZ0329. The two purified PCR products (100 ng backbone and 200 ng *mCherry-popZ* fragment) were employed to perform Gibson assembly to generate the plasmid pVCHYN-6-P*van*-mCherry-PopZ. The selected plasmid with mCherry fused at the N terminal of PopZ was verified by sequencing using primers Pvan-for and M13-for [284]. Integrations into *C. crescentus* were tested by colony PCR using primers RecVan-2 and RecUni-1 [284].

p166: To create an in-frame deletion of *podJ* on the chromosome of *C. crescentus* WSC1141, we constructed a two-step deletion plasmid pNPTS138-PodJup-chlor-PodJdw. We first amplified the upstream (PodJup, 1000 bp) and the downstream (PodJdw, 1000 bp) of *podJ* gene using PCR, as well as the antibiotic resistance gene *cat* using PCR. These three fragments were purified and inserted into the backbone pNPTS138 via Gibson assembly. The selected plasmid was tested by PCR using primers pnpts138-C-F and pnpts138-C-R and then verified by sequencing.

pWZ012, podJ02, podj-delta-250-430, pWZ046: We use pWZ012 here as an example to show how to construct these plasmids here. To generate the plasmid pWZ012 (pCDFDuet1-YFP-PodJ) in WSC1232 strain, we linearized the backbone pCDFDuet1 at *Nde*I by restriction digestion and amplified the two inserts *yfp* and *podJ* gene from plasmid pXYFPC-6 using PCR and from genomic DNA, respectively. In this case, an HRSAT linker codon was inserted at the

junction between YFP and PodJ was designed to be embedded in the forward primer for *podJ* gene (WZ0011). The purified backbone and inserts (100 ng backbone and 200 ng insert fragments) were employed to perform Gibson assembly (One-step isothermal reaction). The selected plasmid was tested by colony PCR using primers T7_for and T7_ter, and confirmed by sequencing. The verified correct plasmid (100 ng) was then transformed into BL21 for imaging experiments or protein expression.

pWZ096-cys (pTEV5-cys-podJ(471-635)): As an example for pTEV5 plasmids. pTEV5 was amplified using WZH348 and WZH349. Insert was amplified using WZH497 and WZH498 and included the cysteine codon sequence in the forward primer. The purified backbone and inserts (100 ng backbone and 200 ng insert fragments) were employed to perform Gibson assembly (One-step isothermal reaction). The selected plasmid was tested by colony PCR using primers T7_for and T7_ter, and confirmed by sequencing. The verified correct plasmid (100 ng) was then transformed into BL21 for imaging experiments or protein expression.

WSC1406: pXCHYC-2_SacI digested vector was used as a backbone for Gibson assembly with insert FtsZ. The constructed plasmid was electroporated into WSC1407 and integration was tested by colony PCR using primers RecXyl-2 and RecUni-1.[284] Gibson primers are below.

WSC1405: pXCFPC-2_Sac1_Nhe1 digested vector was used as a backbone for Gibson assembly with inserts MipZ-HRSAT and sfGFP. The constructed plasmid was electroporated into WSC1407 and integration was tested by colony PCR using primers RecXyl-2 and RecUni-1[284]. Gibson primers are below.

WZ367: pXYFPN-2-P*xyl*-sfGFP-PodJΔ250-430 used the same template plasmid pXYFPN-2-P*xyl*-sfGFP-PodJ but used different overlapping primers. The purified PCR products (100 ng) were transformed directly into DH5α, selecting for kanamycin resistance. Correct

plasmids (1 µg) were then electroporated and integrated into the *xylX* locus of Δ*podJ, P_{popZ}-mCherry-PopZ* strain, generating WSC1403 The integration was confirmed by colony PCR using primers RecXyl-2 and RecUni-1.[284]

5.6 Tables

Table 5–1 Plasmids utilized in this study.

Name	Description	Reference/Addgene #
pWZ0139	pVCHYN-6-mCherry-PopZ	This work
pWZ012	pCDF-YFP-podJ	This work
podJ02	pCDF-YFP-podJ(1-702)	This work
podj-delta250-430	pCDF-YFP-podJ(Δ250-430)	This work
pWZ046	pBAD-CFP-popZ	This work
pWZ096-cys	pTEV5-cys-podJ(471-635)	This work
pWZ098-cys	pTEV5-cys-podJ(250-430)	This work
WZ367	pXYFPN-2-sfGFP-podJ(Δ250-430)	This work
pCZ393	pXyl-2-sfGFP-podJ	This work
pSWD261	pXyl-2-mipZ-sfGFP	This work
pKAK0213	pXyl-2-ftsZ-mCherry	This work
p166	pNPTS138-podJ1000base pairs upstream-chlor resistance gene-1000base pairs downstream	This work
pSWD287	pNPTS138-zitP1000base pairs upstream-spec/strep resistance gene-1000base pairs downstream	This work

Table 5–2 DNA primers utilized in this study.

Name	Sequence (5'-3')
WZ0025	CTTAGTATATTAGTTAAGTATAAGAAGGAGATATAATGGTGAGCAAGGGCGAGGAGC
WZ0010	GGTGGCCGACCGGTGCTTGTACAGCTCGTCCATGCCG
WZ0011	GACGAGCTGTACAAGCACCGGTCGGCCACCATGACGGCGGCTTCGCCATGG

WZ0026	GTGGCCGGCCGATATCCAATTGAGATCTGCTTAGCGCGCGTAGACCGACAGG
WZ0099_(pbad)_forward	GGACGCGGCGCCTAAGAAGCTTGGCTGTTTTGGCGG
WZ0051_(PBAD)_reverse	CGCCCTTGCTCACCATTTAATTCCTCCTGTTAGCCCAAAAA
WZ0052_(YFP-PODJ)_forward	AACAGGAGGAATTAAATGGTGAGCAAGGGCGAGGAGC
WZ0103_(cfp)_(hrsat)_reverse	GACTGATCGGACATGGTGGCCGACCGGTGCTTGTACAGCTCGTCCATGCCG
WZ0104_(popz)_forward	GCACCGGTCGGCCACCATGTCCGATCAGTCTCAAGAACCTACAATGG
WZ0105_(popz)_reverse	CAAAACAGCCAAGCTTCTTAGGCGCCGCGTCCCCGAG
WZ184-podj02-f	GCGCGCCGCCTAAGCAGATCTCAATTGGAT
WZ185-podj02-r	GATCTGCTTAGGCGGCGCGCGGCGCGCCGG
WZ0328_(pvan)_forward	GGACGCGGCGCCTAATCTAGAGCGGCCATTCACTGGCC
WZ0329_(pvan)_reverse	GCCCTTGCTCACCATATGCGTTTCCTCGCATCGTGGTTCG
WZ0330_(mch-popz)_forward	TGCGAGGAAACGCATATGGTGAGCAAGGGCGAGGAGG
WZ0331_(mch-popz)_reverse	AATGGCCGCTCTAGATTAGGCGCCGCGTCCCCGAG
WZH348-PTEV5-PODJ471-635-F	GGCGCTAGCCCGTCGCCGCCGCCCGCGCA
WZH349-PTEV5-PODJ471-635-R	CGCGGATCCTTACAAGCGCGCCTTCGACT
WZH352-PTEV5-PODJ250-430-F	GGCGCTAGCTTGGGCGCCGTCGAGACTGC
WZH353-PTEV5-PODJ250-430-R	CGCGGATCCTTAGCTGGAACGTTCGTGGC
WZ0410_(pnpts138)_forward	GTAGAGGACCGCGTCGTCTAGTCAAGGCCTTAAGTGAGTCG
WZ0411_(pnpts138)_reverse	GCTCGTCCATCATGGTCTTCAATTGCACGGGCCCCAC
WZ0412_(podj-up)_forward	GCCCGTGCAATTGAAGACCATGATGGACGAGCTGAAGTC
WZ0413_(podj-up)_reverse	CCAAAATCCCTTAACGCGAATCGATCTCCCCGCACC

WZ0414_(chlor)_forward	GGGAGATCGATTCGCGTTAAGGGATTTTGGTCATCGAACCCCA
WZ0415_(chlor)_reverse	GAGGTCGCGAGGCGTTTACGCCCCGCCCTGCCACT
WZ0416_(podj-down)_forward	CAGGGCGGGGCGTAAACGCCTCGCGACCTCGCGCT
WZ0417_(podj-down)_reverse	CTTAAGGCCTTGACTAGACGACGCGGTCCTCTACAAGGAGAGA
WZH497-pwz096-CYS-F	TTTTCAGGGCTGTGCTAGCCCGTCGCCGCCGC
WZH498-pwz096-CYS-R	GGCTAGCACAGCCCTGAAAATACAGGTTTTC
WZH499-pwz098-CYS-F	TTCAGGGCTGTGCTAGCTTGGGCGCCGTCGA
WZH500-pwz098-CYS-R	CAAGCTAGCACAGCCCTGAAAATACAGGTTTTC
WZH570-pxyfpn-2-Pxyl-sfGFP-PodJΔ250-430-F	GGATCAGCGCCAGGAACTGGTCGACCGCAT
WZH571-pxyfpn-2-Pxyl-sfGFP-PodJΔ250-430-R	CCAGTTCCTGGCGCTGATCCAGGGCCTGGA
CZ10980_(pXGFPN-2)_forward	GGATGAACTGTACAAACACCGGTCGGCCACCATGACG
CZ10981_(pXGFPN-2)_reverse	CGCCTTTACGCATATGGTCGTCTCCCCAAAACTCGAGC
CZ10982_(sfGFP)_forward	GGGAGACGACCATATGCGTAAAGGCGAAGAGCTGTTCACTG
CZ10983_(sfGFP)_reverse	GGTGGCCGACCGGTGTTTGTACAGTTCATCCATACCATGCGTGATGCC
KAK330_(FtsZ)_forward	GGCGCCTTAATTAATATGCATGGTACCTTAAGATCTATGGCTATTTCTCTTTCCGCGCCGC
KAK331_(FtsZ)_reverse	CGTTCGAATTCTCCGGAGCTCGTCAGTTGGCCAGGCGGCG
SWD796_(start)_(mipZ)_forward	ATATGCATGGTACCTTAAGATCTCGAATGGCCGAAACGCGCGTTATCGTCG
SWD797_(mipZ)_(HRSAT)_reverse	CTTCTCCTTTGCTGGTGGCCGACCGGTGCTGCGCCGCCAGCATCGTC

SWD798_(sfgfp)_forward	CCGGTCGGCCACCAGCAAAGGAGAAGAACTTTTCACTGG
SWD799_(sfgfp)_(stop)_reverse	ACTAGTGGATCCCCCGGGCTGCAGCTTCATTTGTAGAGCTCATCCATGCC
T7_for	GGATCTCGACGCTCTCCCT
T7_ter	GCTAGTTATTGCTCAGCGG
pnpts138-C-F	TGCTTCCGGCTCGTATGTTG
pnpts138-C-R	GTAATACGACTCACTTAAGG
PODJ-KO-C-F	CTTCTAGGCCTGCGACAATC
PODJ-KO-C-R	TGGAGTTTATCCCGAACAGG
Pxyl-for	CCCACATGTTAGCGCTACCAAGTGC
M13-for	GCCAGGGTTTTCCCAGTCACGA
Pvan-for	GACGTCCGTTTGATTACGATCAAGATTGG
RecUni-1	ATGCCGTTTGTGATGGCTTCCATGTCG
RecVan-2	CAGCCTTGGCCACGGTTTCGGTACC
RecXyl-2	TCTTCCGGCAGGAATTCACTCACGCC
nSWD035	CCAAGGTCATCAGCTTCATCC
nSWD036	CGCTGGTGCGTAATCCG

Table 5–3 Strains used in this study.

Name	**Genotype**	**Plasmid**	**Reference**
WSC1119	*E. coli*, DH5*α*	none	Novagen
WSC1411	*C. crescentus*, NA1000	none	Lucy Shapiro
WSC1205	*C. crescentus*, *vanA::mCherry-popZ*	pWZ0139	This study
WSC1230	*C. crescentus*, *xylX::sfGFP-podJ*, *vanA::mcherry-popZ*	none	This study
WSC1232	*E. coli*, DH5*α*	pWZ012	This study
WSC1237	*E. coli*, DH5*α*	podJ02	This study
WSC1269	*E. coli*, DH5*α*	podj-delta250-430	This study
WSC1274	*E. coli*, DH5*α*	pWZ046	This study
WSC1324	*E. coli*, DH5*α*	p166, pnpts138-podjup-cholor-podjdw	This study
WSC1330	*E. coli*, DH5*α*	pWZ096-cys	This study
WSC1331	*E. coli*, DH5*α*	pWZ098-cys	This study

WSC1343	*E. coli*, BL21	pWZ012	This study
WSC1367	*E. coli*, BL21	podJ02	This study
WSC1369	*E. coli*, BL21	pWZ046	This study
WSC1383	*E. coli*, DH5*α*	WZ367	
WSC1396	*C.crescentus*, NA1000	P*popZ*-mCherry-popZ	[132]
WSC1397	*C.crescentus*, *podJ::chlor*	P*popZ*-mCherry-popZ	[132], This study
WSC1398	*C.crescentus*, *podJ::chlor*	P*popZ*-mCherry-popZ, pCZ393	[132], This study
WSC1399	*E. coli*, DH5*α*	pCZ393	This study
WSC1400	*C.crescentus*, *podJ::chlor*, *parB::CFP-parB*	none	[132], This study
WSC1403	*C.crescentus*, *podJ::chlor*, *parB::CFP-parB*	WZ367	This study
WSC1405	*C.crescentus*, *podJ::chlor*	pSWD261	This study
WSC1406	*C.crescentus*, *podJ::chlor*	pKAK0213	This study
SWD642	*E. coli*, DH5*α*	pSWD261	This study
SWD667	*C. crescentus*, NA1000	pSWD261	This study
SWD668	*C. crescentus*, NA1000	pKAK0213	This study
SWD694	*E. coli*, DH5*α*	pSWD287	This study
SWD697	*C.crescentus*, *podJ::chlor*, *zitP::spec/strep*	P*popZ*-mCherry-popZ	This study
KAK440	*E. coli*, DH5*α*	pKAK0213	This study

6.0 PodJ self-assembly and its impact on localization and ectopic pole formation

6.1 Introduction to localization and self-assembly

Protein localization plays an important role in coordinating essential processes in all domains of life. Cell signaling, protein sequestration, and replication are all regulated in some part by proteins localizing to different regions in a cell. Nature has developed numerous mechanisms to localize proteins to the cellular regions. In bacteria, protein localization can occur through recognition of positive or negative membrane curvature (e.g., SpoVM and DivIVA)[285], nucleoid occlusion[133], a diffusion and capture mechanism[133], polar factor recognition, or even combinations of these mechanisms in order to assemble large complexes at cell poles (Figure 6–1).[132,286,287]

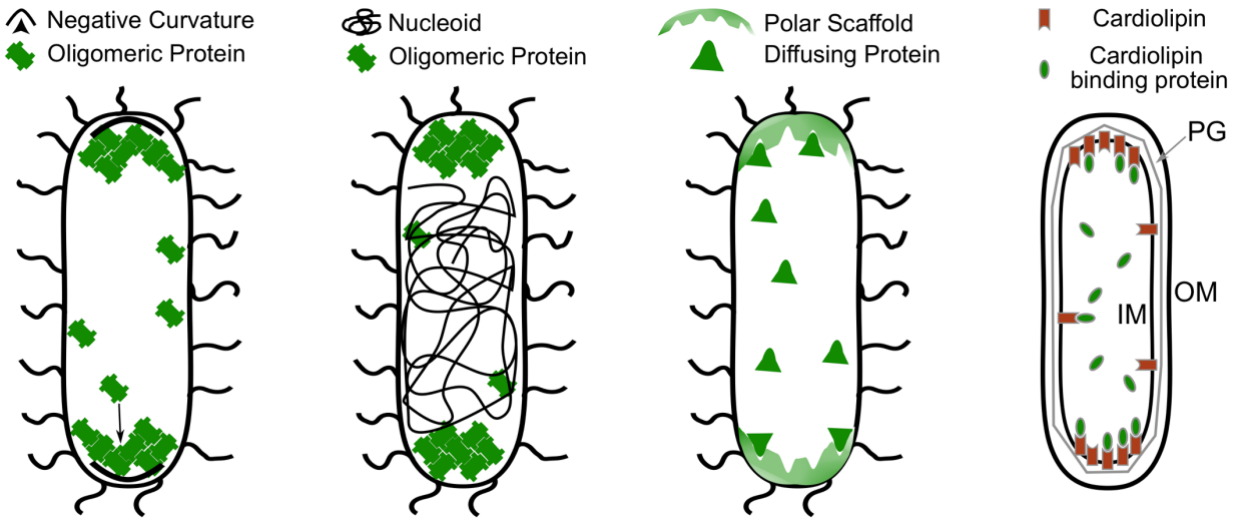

Figure 6–1 Methods for protein localization in bacteria.
Bacteria utilize a number of ways to localize proteins to the cell poles. Negative curvature can drive accumulation at the cell poles over the lateral membrane due to the space restrictions. Nucleoid occlusion can drive large oligomers to the cell poles in order to lower the energy of having a large complex in the nucleoid. Scaffolds can recruit diffusing proteins to the cell poles to generate areas of high concentration. Some bacteria utilize different lipid composition at the cell poles, such as increased cardiolipin. Proteins can recognize this lipid and accumulate at the cell poles. Adapted from Laloux, *et al. J. Cell. Sci.* **2014** *127*(1), 11-19.

Protein scaffolds often form large oligomers in order to generate a sufficient number of binding sites for client proteins.[132] Another result of this oligomerization can be nucleoid occlusion.[286] PopZ, the polar organelle protein that recruits members of the CtrA signaling pathway, becomes a large oligomer that is energetically unfavorable to remain in the nucleoid region, so it is pushed to a cell pole where it becomes nucleoid occluded.[174] Oligomerization can also lead to a negative curvature sensing model.[286] When scaffolding proteins begin to seed large oligomers, space constraints lead to the cooperative assembly in the negative curvature space of the cell pole. Another mechanism for localization is affinity for features at the cell envelope, especially at the cell poles.[286] ProP in *E. coli* preferentially recognizes cardiolipin, a lipid found at higher concentrations at the cell poles, and self-assembles at the cell poles in order to increase the cellular concentration of organic osmolytes upon sensing increasing osmolarity.[288] Finally, scaffolding proteins can be recruited by other scaffolding proteins.[286] The chromosome segregation machinery helps to recruit ParA1, the chromosome binding protein in *Vibrio cholerae* to the cell pole in order to segregate the chromosome.[289] Any of these listed mechanisms could be used by scaffolding proteins, and it is often hard to predict exactly how a protein may assemble at a certain region of the cell.

Bacteria display a variety of cell shapes that contain different types of curvature: Spherical cocci[290], rod[291], spirochaetes[292], and more, as well as derivations within these groups (Figure 6–2).[293,294]

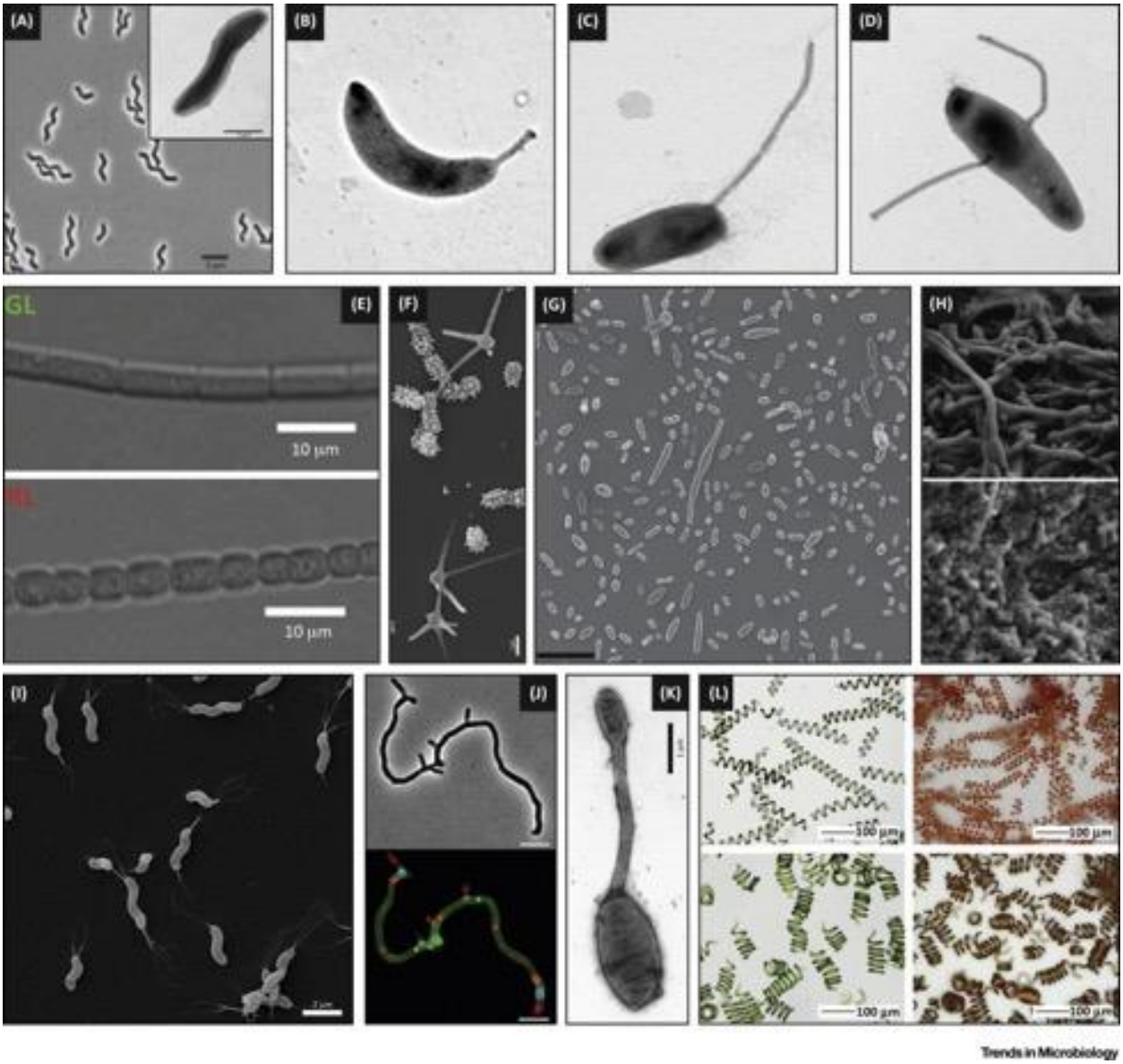

Figure 6–2 Diverse bacterial morphologies produce distinct curvature.
A) Uncharacterized spiral-shaped methanotroph. Phase-contrast with inset electron micrograph. B) *C. crescentus*. Single polar prostheca. C) *Asticcacaulis excentricus*. Single subpolar prostheca. D) *Asticcacaulis biprosthecum*. Two bilateral prosthecae. E) *Fremyella diplosiphon*. Complimentary chromatic adaptation (CCA)-mediated pleomorphism. Cells grown in green light (GL, top) are elongated and rectangular. Cells grown in red light (RL, bottom) are short and rounded. (F) *Prosthecomicrobium hirschii*. Electron micrograph showing short- and long-prosthecate morphotypes. (G) *Dinoroseobacter shibae*. Scanning electron micrograph showing the inherent morphological heterogeneity of wild-type *Dinoroseobacter shibae*. Scale bar = 5 µm. (H) *Lactococcus lactis*. Scanning electron micrograph showing different regions of the same *L. lactis* biofilm. The upper region of the biofilm contains elongated rods (top), while the lower region contains ovoid cells (bottom). (I) *Helicobacter pylori*. Scanning electron microscope images of wild-type *Helicobacter pylori*. (J) *Streptomyces venezuelae*. Virtual time-lapse of polarly growing *Streptomyces venezuelae* labeled with a long pulse (cell body) of green fluorescent D-amino acid (FDAA), followed by sequential short pulses of orange, blue, and red FDAAs (apical tips). Top = phase, bottom = fluorescence, scale bar = 5 µm. (Image courtesy of Yen-Pang Hsu, Indiana University.) (K) *Hyphomonas adhaerens* (related to *Hypomonas neptunium*). The mother cell (bottom), the prostheca (middle), and the developing daughter bud (top) are visible. (L) *Spirulina* (*Arthrospira platensis*). *Spirulina* biotemplated microcoils. The helical pitch of the cyanobacteria

can be modified by tuning the culture conditions (left panels). Copper microcoils are produced through an electroless plating technique using *Spirulina* as the template (right panels). Figure and caption used with permission from Caccamo, *et al. Trends Microbiol.* **2018** *26*(3), 191-208.

Different shapes arise from the rigid structure of peptidoglycan and the cell wall remodeling that occurs during a cell's life cycle; often, this is related to the environment the bacteria have evolved to live in.[295] The alphaproteobacterium *Caulobacter crescentus* is a crescent-shaped bacterium whose shape arises from a rod shape that is curved by a membrane associated filamentous protein, CreS.[296,297] Due to this extra curvature, *C. crescentus* cells have more areas of varied curvature within a cell than a typical rod shaped bacterium like *E. coli* (Figure 6–3).

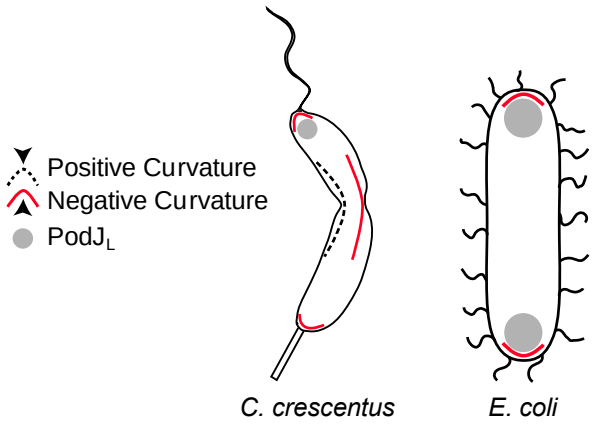

Figure 6–3 *C. crescentus* curved shape introduces new areas of curvature compared to rod-shaped bacteria. Compared to rod shaped bacteria like *E. coli*, *C. crescentus* has two more regions of curvature brought about by the filamentous protein CreS. This distortion in shape results in an additional negative and positive curvature space in cells. $PodJ_L$ in *C. crescentus* preferentially forms foci at the new cell pole, a negative curvature space. In *E. coli*, $PodJ_L$ will form foci at both cell poles.

This curved shape has been shown to promote a fitness advantage over uncurved cells lacking CreS.[298] Additionally, the pathogenic bacteria *Vibrio cholerae* utilizes CrvA to promote motility and advantage in colonization and pathogenesis.[299]

The scaffolding protein PodJ can be post-translationally modified into a short and long form during the cell-cycle. After $PodJ_S$ (PodJ Short) at the old cell pole is cleared from the cell, new $PodJ_L$ (PodJ Long) is synthesized and localizes to the new cell pole where it can scaffold other

proteins important for the cell-cycle[259,269] (e.g., PopZ[134,174], PleC[135,259]) and coordinate flagellar and pili biogenesis (Figure 6–4).[257]

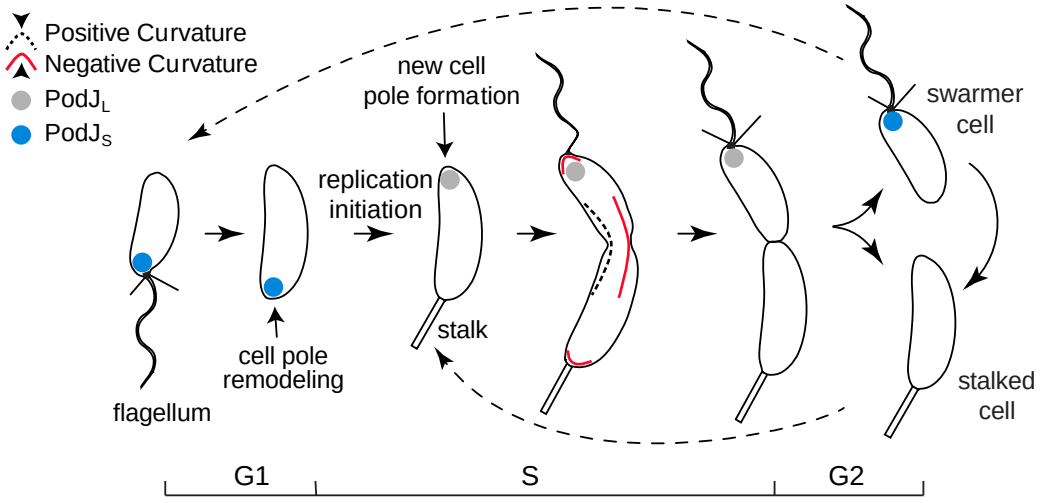

Figure 6–4 PodJ$_L$ assembles at the new cell pole instead of other curvature spaces.
During early S phase, newly synthesized PodJ$_L$ localizes to the new cell pole. This is one of four curvature spaces in cells as shown in the predivisional cell. Red lines indicate negative curvature space and black dotted lines indicated positive curvature space. As the cell divides, PodJ$_L$ is proteolyzed to PodJ$_S$ by PerP, then MmpA releases PodJS from the membrane resulting in clearing from the cell through degradation.

Because of *C. crescentus* curved shape, it contains three regions of negative cell curvature (both cell poles and the outer crescent region) and one area of positive curvature (inner crescent region) (Figure 6–4). PodJ$_L$ preferentially binds the negative curvature region of *C. crescentus* new cell pole and will localize to both negative curvature regions when expressed heterologously in *E. coli* (Figure 6–3). This difference in polarity is likely due to one of the known modes of protein localization in bacteria. We suspect it is due to curvature sensing in cells. Additionally, curvature at the cell poles could be different such that PodJ recognizes the new pole. In order to begin to understand how PodJ can sense curvature, we will explore PodJ oligomerization. We studied PodJ scaffolding abilities in Chapter 5. Scaffolding proteins often oligomerize in order to generate sufficient client sites. This oligomerization may also aid in curvature recognition and polar assembly in cells. By studying the mechanisms leading to PodJ polar recognition, we can connect PodJ self-assembly to both client recruitment and new pole recognition.

6.2 Introduction to ectopic pole formation

Gram-negative bacteria have a layer of peptidoglycan surrounding by the inner and outer cell membranes that is covalently linked to the outer membrane by the lipoprotein Lpp.[300] This peptidoglycan layer, or murein, is a crystal lattice structure of glycan strands that are cross-linked by short peptides.[300] The glycan strands are composed of two different polysaccharides: N-acetylglucosamine (GlcNAc) and N-acetylmuramic acid (MurNAc). D-lactoyl group of each MurNAc strand is substituted by a peptide stem typically composed of L-Ala, D-Glu, *meso*-A_2pm or L-Lys, D-Ala, and D-Ala.[300] The order can change but typically the strand consists of five of these amino with L-Ala coming first, *meso*-A_2pm or L-Lys in the third position, and D-Ala last (Figure 6–5).[300]

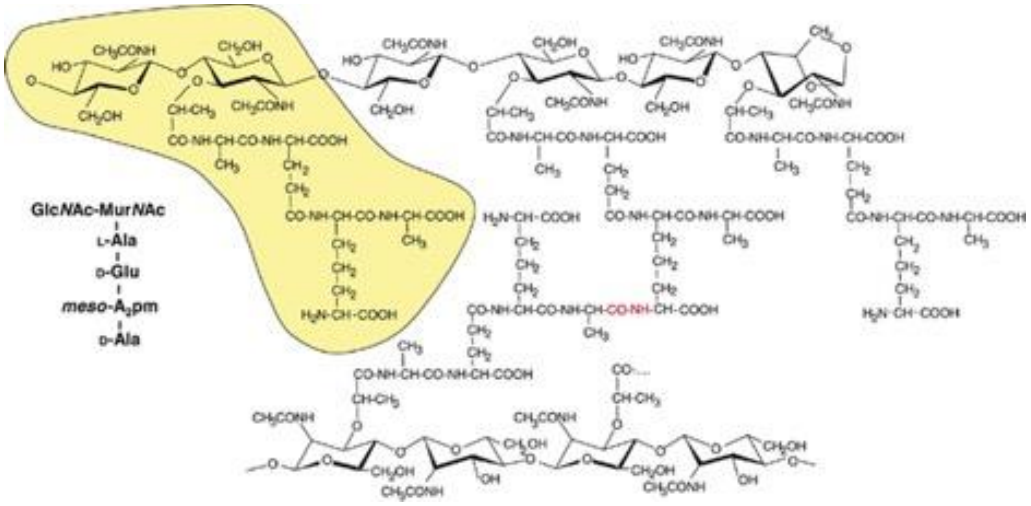

Figure 6–5 Peptidoglycan structure in *E. coli*.
The glycan strands consist of alternating, β-1→4-linked Glc*N*Ac and Mur*N*Ac residues, and are terminated by a 1,6-anhydroMur*N*Ac residue. The yellowish labelled part represents the basic disaccharide tetrapeptide subunit (monomer), which is also written with the conventional amino acid and hexosamine abbreviations on the left-hand side. The middle part shows a cross-linked peptide, with the amide group connecting both peptide stems drawn in red. Figure and caption used with permission from Vollmer *et al. FEMS Microbiol. Rev.* **2008** *32*(2), 149-167.

The fifth position D-Ala is also lost in the formation of the peptide cross-link. These features can all differ between different species of bacteria, and can be used as an early identifier

for different species of bacteria before the advent of mass spectroscopy.[301,302] Though the composition differs, the biophysical properties of peptidoglycan remain similar throughout bacteria. One of the most important roles of peptidoglycan is producing cell shape.[294] Bacterial cell shapes can vary widely and often relate to their environmental niche.[294] In some instances, bacterial cell shape can take a non-canonical turn when the expression of certain proteins that interact with peptidoglycan is perturbed. Penicillin-binding proteins (PBPs), which have often been exploited for the development of antibiotics that target the peptidoglycan machinery[303], can bind peptidoglycan with high affinity. This affinity for peptidoglycan has also been adopted by other endogenous enzymes, such as lysozyme, in order to disrupt peptidoglycan in bacteria, resulting in cell death.[304] In addition to these processes, bacteria have also evolved protein localization schemes using peptidoglycan-binding domains that often lack enzymatic activity. One example of this is the sporulation repeat (SPOR) domain, a class of PBPs that have evolved to target proteins, often peptidoglycan enzymes themselves, to sites of cell division in order to enrich the breakdown and buildup of peptidoglycan.[305,306] When localization of these enzymes is mis-regulated, one phenotype that arises is the ectopic pole. Ectopic poles are a phenomenon in bacteria that result in branching, kinks, or bends in the cell (Figure 6–6).[307]

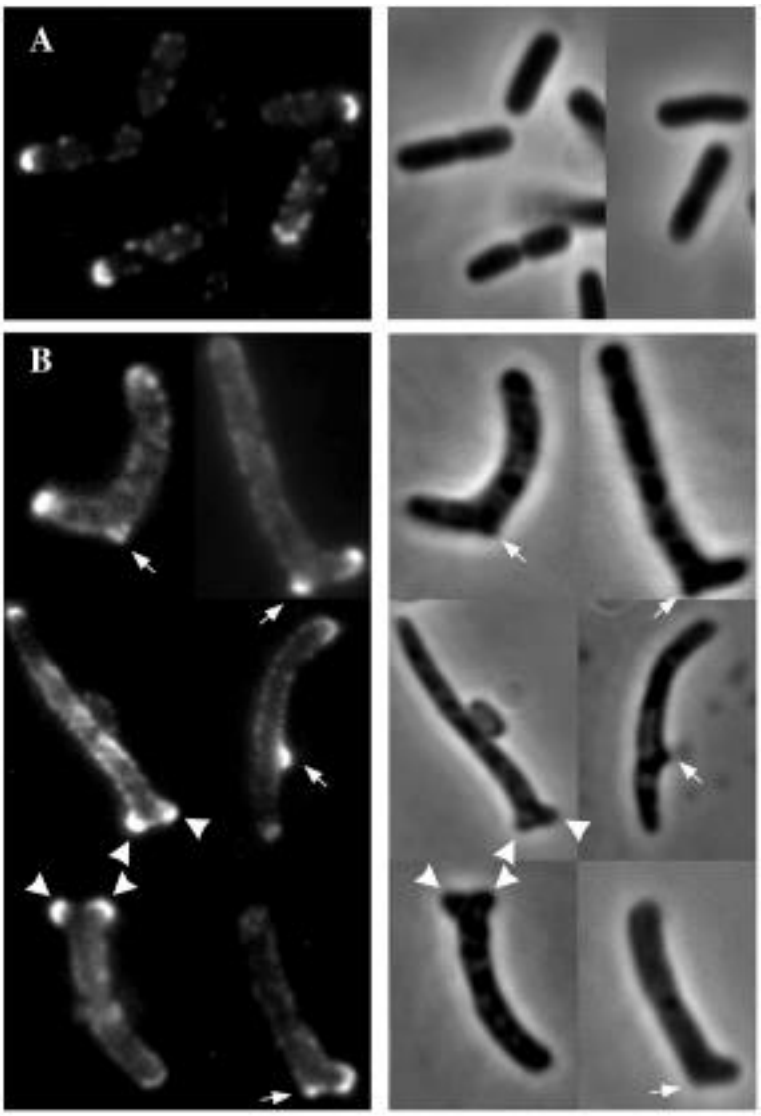

Figure 6–6 Stable outer membrane regions display strong fluorescent signal in *E. coli*.
Immunofluorescence was used to stain a polar protein in *E. coli*. A) In wild-type, the fluorescence only appears at the two cell poles. B) In a PBP mutant, ectopic poles form and contain the polar protein. White arrows mark ectopic poles. Figure used with permission from Nilsen *et al. Mol. Micro.* **2004** *52*(4), 1045-1054.

Ectopic poles have been characterized in model organisms like *E. coli* and *C. crescentus* and are often the result of overexpression of proteins that localize to the cell poles or growth regions. Overexpression results in formation of protein complexes in new regions of the cells, resulting in a new growth region forming. In order for an ectopic pole to form, certain biochemical processes need to occur. Peptidoglycan strands (glycan and peptide) must be broken by specific

hydrolases, followed by insertion of new glycan strands that can then be crosslinked to form a stable complex (Figure 6–7).[308]

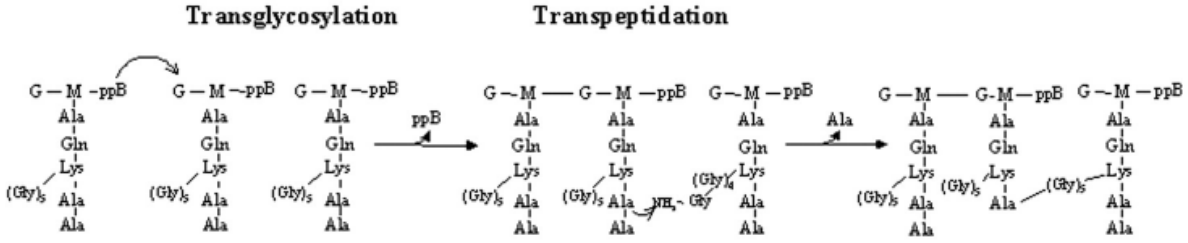

Figure 6–7 Transglycosylation and transpeptidation schematics.
New peptidoglycan is inserted by first linking glycan strands by a transgycosylase. A transpeptidase can then cross-link amino acids in the peptide chain. This can occur through linked or unlinked glycan strands. Figure used with permission from Scheffers, *et al. Microbiol. Mol. Biol. Rev.* **2005** *69*(4), 585-607.

Bacteria normally use these steps in order to grow in three dimensions, but these processes go awry when occurring away from typical areas of growth. These poles can be detrimental to cell viability due to increased energy consumption required to generate excess poles as well as new shapes that can be less than optimal for motility or cell division.[309] *C. crescentus* has two proteins that have been shown to form ectopic poles under overexpression conditions.[256,281] SpmX[256] and TipN[281] are important proteins for establishing the old (SpmX) and new (TipN) cell poles in *C. crescentus*. At normal expression levels, these proteins localize to the cell poles and recruit cell pole factors. But when overexpressed, SpmX and TipN complexes can begin to form away from the cell poles, resulting in ectopic poles.[256,281] The mechanism for why these proteins form ectopic poles is not well understood. It remains uncharacterized what enzymes are involved in this process, or why these specific proteins enable ectopic pole formation. In addition to these proteins, PodJ is also able to form ectopic poles. The ability of PodJ to cause ectopic pole formation is also not well understood and here we reconcile the ability of PodJ to form ectopic poles with its self-assembling capabilities.

6.3 Results

6.3.1 PodJ self-assembles into a large oligomer that form biomolecular condensates *in vitro*

To begin to dissect why PodJ is able to form complexes at the cell pole, we wanted to look at its oligomerization capabilities. Oligomerization is important for assembly of scaffolding proteins at the cell poles (Figure 6–1). The only mechanism for localization at the pole that does not depend on oligomerization is the diffusion/capture method (Figure 6–1). In order to test PodJ self-assembly, we purified a form of PodJ, PodJ_N (PodJ(1-635)), which removes the periplasmic and transmembrane regions (residues 636-974) of PodJ in order to increase solubility of the protein (Figure 6–8A).

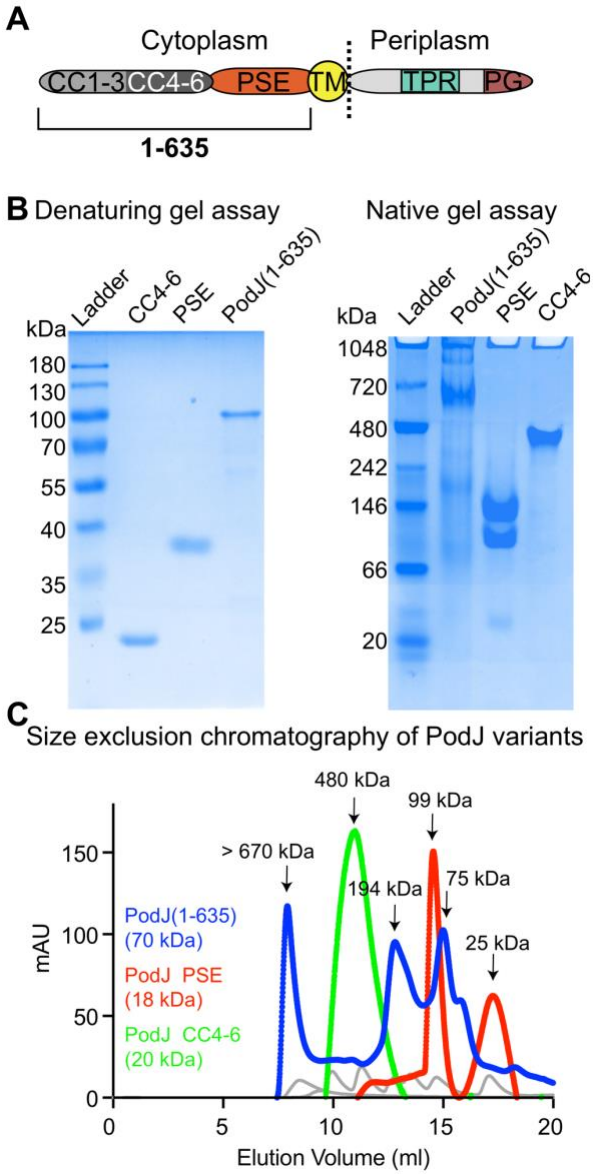

Figure 6–8 N-terminal domains of PodJ produce self assembly.
For protein expression and purification conditions, see Methods. A) PodJ domain architecture. PodJ(1-635) corresponds to the first 635 residues of PodJ and does not include the transmembrane tether or periplasmic domains. PodJCC4-6 constitues residues 250-430 and PodJPSE constitutes 431-625. B) Denaturing (see Methods) and native PAGE gel (see Methods) electrophoresis of PodJ(1-635), PodJPSE, and PodJCC4-6. kDa labels correspond to ladder. Protein was separated on native PAGE gel (8% separation gel) at 80 V for at least 4 hours at 4 ºC, using a Native protein ladder (range from 66 to 669 kDa, Thermo Fisher). C) Analytical size exclusion chromatography of PodJ(1-635), PodJPSE, and PodJCC4-6. Gray line indicates molecular weight standards. A gel filtration standard (Sigma) containing thyroglobulin (bovine, 669 kDa), carbonic anhydrase (bovine, 29 kDa), blue dextran (2,000 kDa), apoferritin (horse, 443 kDa), β-Amylase (sweet potato, 200 kDa), alcohol dehydrogenase (yeast, 150 kDa), and albumin (bovine, 66 kDa) were used to generate a molecular weight standard plot using a Superdex 200 10/300 GL column (GE Healthcare). A 3.2 mg/ml sample of His-PodJ(1-635) was loaded onto the column and eluted after 7.9 ml, 12.8 ml, and 15.0 ml of buffer, corresponding to a molecular weight of 1,851 kDa, 194 kDa, and 70.7 kDa (theoretical monomer = 73.0 kDa). One representative result of triplicates was shown. Expression, purification, and experiments performed and provided by Wei Zhao.

By purifying only the cytoplasmic region of PodJ, we were able to assay it for oligomer formation in two ways: native PAGE gel electrophoresis, and analytical size exclusion chromatography (SEC). In addition to PodJ(1-635), we also purified PodJ PSE domain (PodJPSE) and PodJ CC4-6 domain (Figure 6–8B). Under denaturing conditions, each variant displays a single band corresponding to its predicted molecular weight, with the exception of PodJPSE, which is 18 kDa. The proline rich nature of the PSE region results in secondary structures that are not denatured by SDS, causing decreased electrophoretic mobility (Figure 6–8B). Under native conditions, each construct was able to form large oligomers (Figure 6–8B). PodJ(1-635) has multiple bands appearing at molecular weights of 66-1048 kDa, PodJPSE forms two bands between 66-146 kDa, and PodJCC4-6 produces one band near 480 kDa (Figure 6–8B). Therefore, the cytoplasmic region of PodJ assembles as multiple, large oligomeric complexes and PodJCC4-6's single band at approximately 480 kDa corresponds to a large multimeric complex that is mediated by coiled-coil interactions. Further characterization of PodJCC4-6 needs to be completed in order to investigate the assembly mechanism of this domain.[310] PodJPSE is composed primarily of proline, serine, and glutamate. This construct, which is predicted to be disordered based on disorder protein calculations, also displayed large oligomers. To further characterize the sizes of these oligomers, we used analytical SEC. Using a standard of varied molecular weights, we were able to confirm that PodJ(1-635) forms high molecular weight oligomers (>670 kDa; 670 kDa is the largest size standard run) along with other smaller oligomers corresponding to 194 kDa and 75 kDa, likely representing a dimer and monomer, respectively (Figure 6–8C). PodJCC4-6 ran as one oligomer at 480 kDa, corresponding to a large oligomeric complex that was also observed by native gel (Figure 6–8C). PodJPSE displayed peaks at 99 kDa and 25 kDa, likely representing a tetramer and monomer, respectively (Figure 6–8C). Together, these experiments indicate that the tested

cytoplasmic domains of PodJ self-assemble as a large oligomeric complex *in vitro*. This result shows that PodJ has multiple regions contributing to oligomerization. This multivalent property is a hallmark of proteins capable of phase condensate formation.

Recently, our lab discovered that bacterial proteins are able to form phase condensates *in vitro* and *in vivo*.[311,312] Our lab found that RNaseE is able to form condensates dependent upon RNA, salt, and polyethylene glycol (PEG). In order to explore whether PodJ could also form condensates, we used purified sfGFP-PodJ(1-635), sfGFP-PodJΔCC1-3 (amino acid residues 250-635), and sfGFP, using similar salt and PEG concentrations to RNaseE conditions.[311] Using 20 µM protein, 50 mM Tris-Cl pH 8.0, and 300 mM NaCl, PEG(8000) concentrations were varied from 0% to 5% (Figure 6–9).

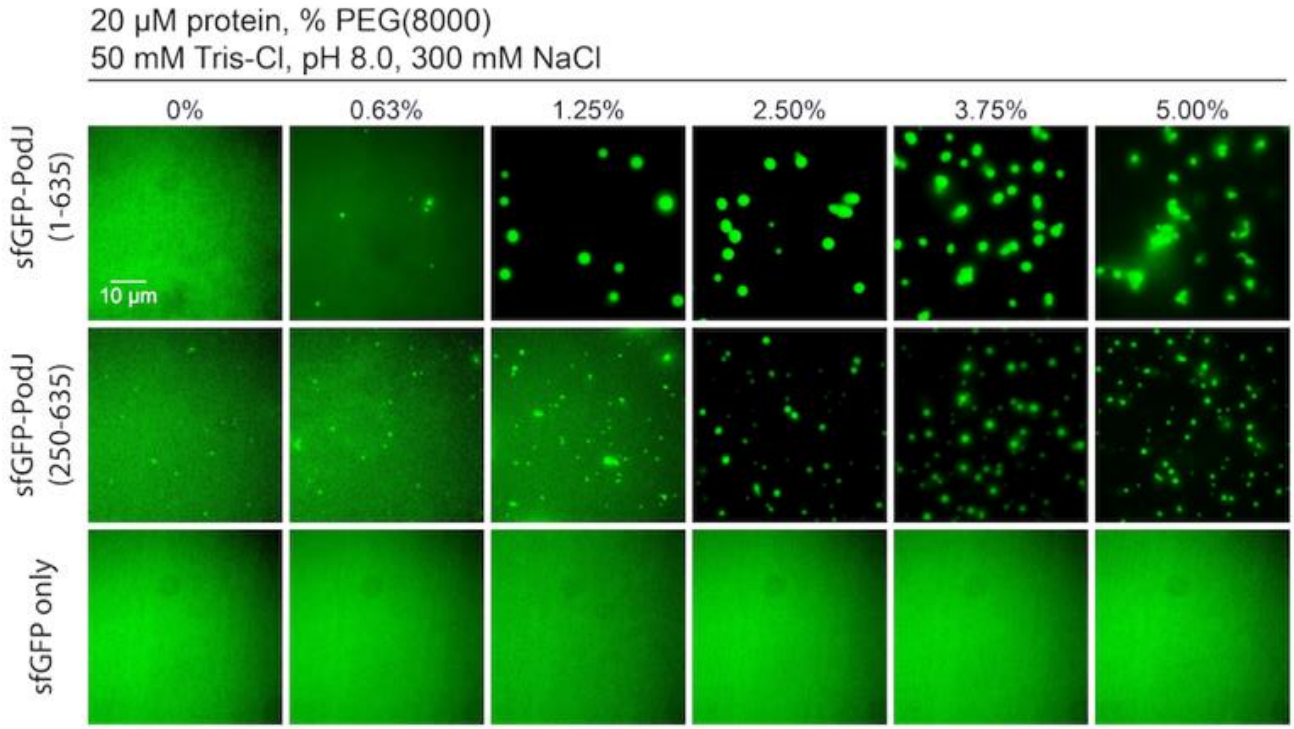

Figure 6–9 PodJ 1-635 and PodJ 250-635 (PodJΔCC1-3) form condensates with addition of PEG(8000). Purified sfGFP fusions to PodJ(1-635) and PodJΔCC1-3 were mixed with a fixed Tris buffer and salt condition. Concentrations of PEG(8000) were varied. sfGFP only was used a negative control for condensate formation. After mixing, the solutions were then sealed onto a glass slide to be imaged. See Methods for imaging and purification conditions. Scale bar denotes 5 µm. Purification and droplet assays were performed by Kim Kowallis, Dylan Tomares, and Chao Zhang. Figure provided by Dylan Tomares and Chao Zhang.

sfGFP-PodJ(1-635), sfGFP-PodJΔCC1-3 both formed condensates (Figure 6–9). sfGFP-PodJ(1-635) formed condensates at 1% PEG(8000) and above while sfGFP-PodJΔCC1-3 displayed low intensity condensates at 0% PEG(8000). sfGFP-PodJΔCC1-3 condensates were also smaller than sfGFP-PodJ(1-635) condensates. The sfGFP negative control did not form condensates under any PEG(8000) concentrations tested indicating sfGFP is unlikely to be the driver of condensate formation (Figure 6–9). This result provides further evidence that PodJ assembly is a multivalent process. This *in vitro* assembly is also independent of cell curvature, since experiments were carried out on glass slides.

6.3.2 PodJ and PopZ assembly *in vivo* is independent of curvature

To verify that PodJ assembles *in vivo*, we expressed YFP-PodJ in *E. coli*, which provides a more biologically relevant set of conditions than *in vitro* experiments. *E. coli* cells contain negative and positive curvature (Figure 6–3). In order to determine if PodJ focus formation in cells is dependent on negative polar curvature at the cell poles, which is a prominent way that scaffolding proteins can localize in cells, we generated spherical *E. coli* cells containing no negative polar curvature. MreB is an actin homologue that forms part of the bacterial cytoskeleton.[280] A22 inhibits MreB polymerization and causes rod-shaped *E. coli* cells to form spheres.[313] By treating cells with A22 then expressing fluorescent-protein-labeled PodJ, we can monitored foci formation in a curvature independent environment. We expressed both YFP-PodJ and CFP-PopZ in spherical cells, and both were able for form foci (Figure 6–10).

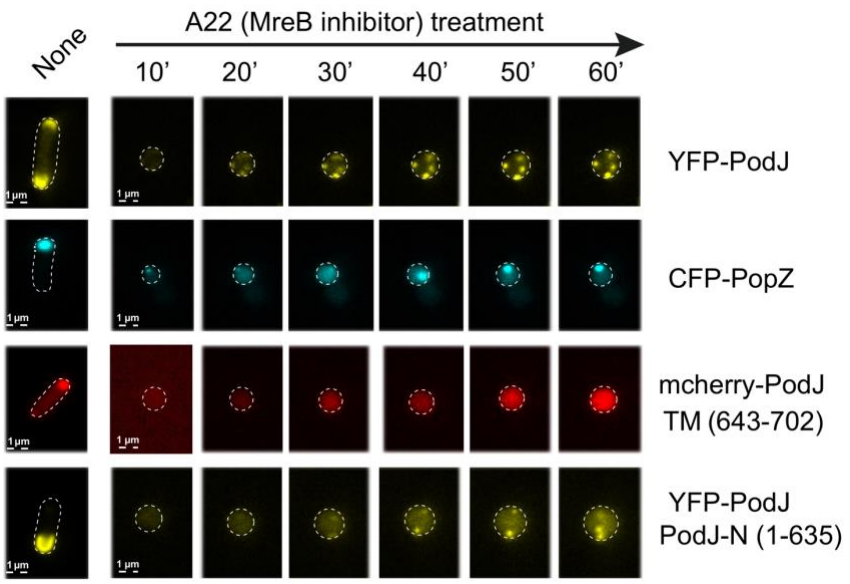

Figure 6–10 Generation of spheroplasts does not inhibit PodJ and PopZ foci formation in *E. coli.*
E. coli cells containing plasmids were grown overnight in LB containing antibiotics at 37ºC. Cells were diluted 1:100 into fresh LB containing antibiotics, then grown for 3 hours at 37ºC. MreB inhibitor A22 (50 μM) was added to induce spheroidal cells. After 5-hours with A-22 inhibitor, cells were imaged on 1% agarose pads containing 100 μM IPTG or 0.5mM arabinose for protein expression, 50 μM A22, and antibiotics. Cells were imaged every ten minutes using corresponding filters sets (see Methods). PodJ forms multiple foci in spherical cells. PopZ forms a single focus in spherical cells. PodJ's transmembrane tether does not form foci upon loss of negative curvature. PodJ_N (1-635) is able to form foci without negative curvature.

YFP-PodJ formed multiple foci, while CFP-PopZ formed a single focus (Figure 6–10). This result indicates that both proteins have intrinsic assembly capabilities that do not require varied curvature. This result is consistent with our observations of condensate formation *in vitro*. We also tested the ability of the PodJ transmembrane tether to assemble independent of curvature. When transmembrane tether of PodJ is expressed in rod-shaped *E. coli*, it forms a polar focus (Figure 6–10). When it is expressed in spherical cells, however, it remains diffuse (Figure 6–10). When we express YFP-PodJ(1-635) in spherical cells, it is still able to form foci (Figure 6–10). Both of these results point toward PodJ cytoplasmic domains being the drivers for foci formation, which is consistent with our condensate assays. These results also show that since the transmembrane tether required regions of curvature to form a focus, it may play a secondary role in anchoring cells at regions of negative curvature. To further explore what cytosolic domains are

required for foci formation in *E. coli*, we used a domain deletion approach and assessed foci formation.

6.3.3 PodJ accumulation at the cell poles in *E. coli* is dependent upon the CC1-3 domain

To study the impact of these domains in a cellular context, we turned to expression in *E. coli* and *C. crescentus*. Expression in *E. coli* can act as a "test tube" for studying protein assembly and interactions; this approach has been extensively used to study *C. crescentus* proteins.[134,314] We tested whether there was a correlation between oligomerization *in vitro* and foci formation *in vivo*. To do this, we generated a series of PodJ truncations and single domain expressions in *E. coli* BL21 (Figure 6–11A).

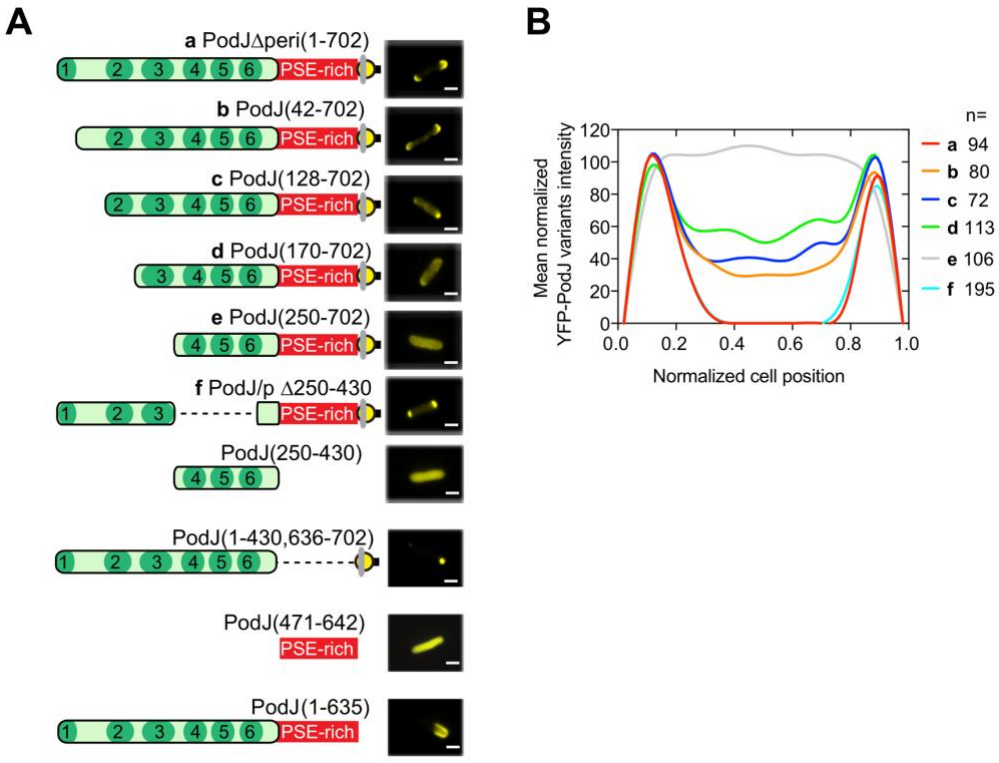

Figure 6–11 PodJ truncations in *E. coli* impact cell pole localization.
E. coli BL21 containing plasmid were grown overnight at 37ºC in LB containing antibiotics. Cells were diluted into fresh LB containing antibiotics at a 1:100 ratio. Cells were grown for two hours at 37ºC, at which point expression was induced using a final concentration of 100 µM IPTG. Cells were then grown for two hours at 28ºC and imaged

on 1% agarose pads on the Nikon T*i*E using a Phase-Contrast and YFP filter set and settings (see Methods). A) Expression of PodJ constructs, all without periplasmic domains (703-974). Green circles indicate position of individual coiled coils 1-6. PSE region is in red. Transmembrane tether denoted by yellow circle. Scale bar indicates 2 μm. B) Fluorescence intensity profiles of cell images from A). Letters correspond to constructs in A). Intensity of YFP was normalized to the PodJ_N. Cell length was normalized to 1.0. Data and figure provided by Wei Zhao.

In this domain deletion library, we deleted each of the following domains to evaluate their contributions to cell pole accumulation: CC1-3, CC4-6, PSE, the transmembrane tether, and the periplasmic domains. PodJ could reliably accumulate at the cell pole in constructs lacking the periplasmic domain (Figure 6–11A), therefore, to match the *in vitro* experiment, we used constructs with no periplasmic domain. We observed that PodJ could accumulate at the cell poles lacking the PodJCC4-6 or PodJPSE domains. However, we observed that removal of PodJCC1-3 eliminated PodJ accumulation at the cell poles. Therefore, we generated a series of truncations within the PodJCC1-3 region (a-e) by removing small regions of PodJCC1-3. By measuring fluorescence intensity along the profile of the cell, foci formation at the cell poles decreased as each piece of PodJCC1-3 was deleted indicating PodJCC1-3 is required for foci formation in cells (Figure 6–11B). Therefore, these constructs indicate that PodJCC1-3 contributes to the ability of PodJ to accumulate at the cell poles in *E. coli.*

We also test individual domains for foci formation. We expressed YFP-PodJCC4-6, YFP-PodJPSE and YFP-PodJCC1-3 alone. Both CC4-6 and the PSE domain displayed no foci formation in cells (Figure 6–11A). This observation is interesting because it does not directly correlate oligomerization with foci formation in *E. coli*. PodJCC4-6 and PodJPSE are both able to form oligomers *in vitro,* but that may be driven by high concentrations and optimal buffering conditions In contrast, we observed that YFP-PodJCC1-3 self-assembled as monopolar foci in *E. coli* (Figure 6–12A,B).

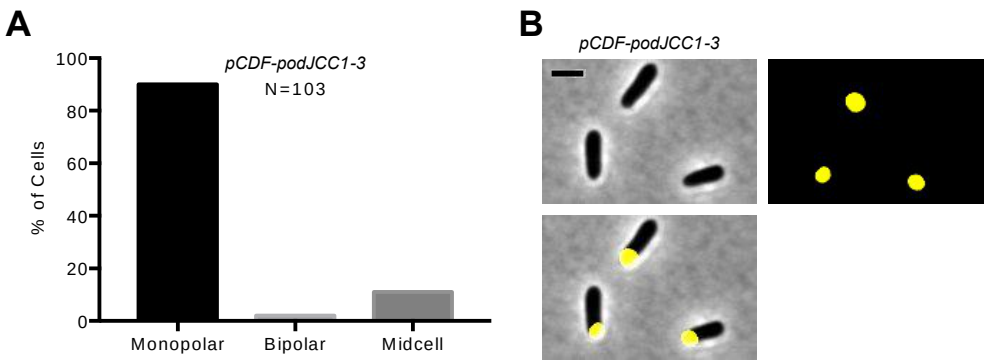

Figure 6–12 Expression of YFP fused to CC1-3 in *E. coli*.
E. coli BL21 containing plasmid were grown overnight at 37ºC in LB containing antibiotics. Cells were diluted into fresh LB containing antibiotics at a 1:100 ratio. Cells were grown for two hours at 37ºC at which point expression was induced using a final concentration of 100 µM IPTG. Cells were then grown for two hours at 28ºC and imaged on 1% agarose pads on the Nikon T*i*E using a Phase-Contrast and YFP filter set and settings (see Methods). A) Cell counts of YFP-CC1-3 expression in *E. coli*. No cell displayed diffuse YFP signal. B) Cell images of *E. coli* expressing YFP-CC1-3.

This result established that PodJCC1-3 is the minimal oligomerization domain of PodJ in *E. coli* and is critical to initiate oligomerization of PodJ(1-702), which contains CC1-3, CC4-6, PSE, and a transmembrane tether.

6.3.4 PodJ accumulation at the cell poles in *C. crescentus* requires CC1-3 and the transmembrane tether

To test PodJ oligomerization in its native environment, we turned back to expression in *C. crescentus*. We expressed an sfGFP-PodJCC1-3 fusion under the control of the xylose promoter in cells lacking endogenous PodJ (Δ*podJ)*. This fusion was mostly diffuse (61%) and formation of foci was "patchy" and not typically found at either cell pole (Figure 6–13A,B).

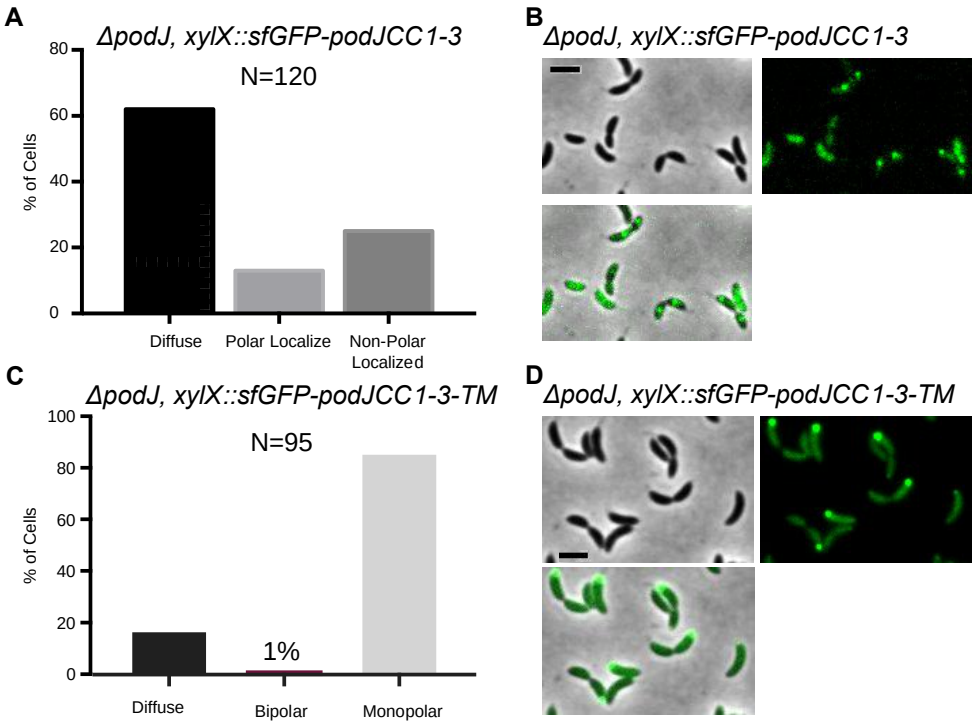

Figure 6–13 PodJ transmembrane tether impacts cell pole accumulation of CC1-3.
Expression of constructs was completed in Δ*podJ* strains by growing cells overnight at 28ºC in M2G containing antibiotics to OD_{600} of 0.2. A final concentration of 0.03% xylose was used to induce expression for 3 hours. Cells were imaged on a 1% agarose pad on the Nikon T*i*E using Phase-Contrast and GFP filter sets and settings (see Methods). A) Counts of sfGFP-CC1-3 expressed under the xylose promoter in *C. crescentus*. Polar localize represents both monopolar and bipolar PodJ foci in cells. Non-polar localized represents foci away from the cell poles. B) Representative cells of graph A. C) Counts of sfGFP-CC1-3-TM expressed under the xylose promoter shows primarily monopolar localization at the stalk pole. Monopolar cells contain a focus at either pole. D) Representative cells of graph C.

To evaluate the contribution of the transmembrane tether, we reattached the PodJ transmembrane tether to sfGFP-PodJCC1-3 and observed foci formation at either both cell poles (39%), one pole (60%), or diffuse (1%) (Figure 6–13C,D). This result implicates that the transmembrane tether in addition to PodJCC1-3 are needed for cell pole accumulation of PodJ in *C. crescentus*. In contrast, the transmembrane tether was not required for PodJ cell pole accumulation in *E. coli*. We next examined the localization pattern when PodJCC1-3 was deleted. With the transmembrane tether, the sfGFP-PodJΔCC1-3-TM made foci at both cells poles with a higher intensity focus at the old cell pole (Figure 6–14A,B).

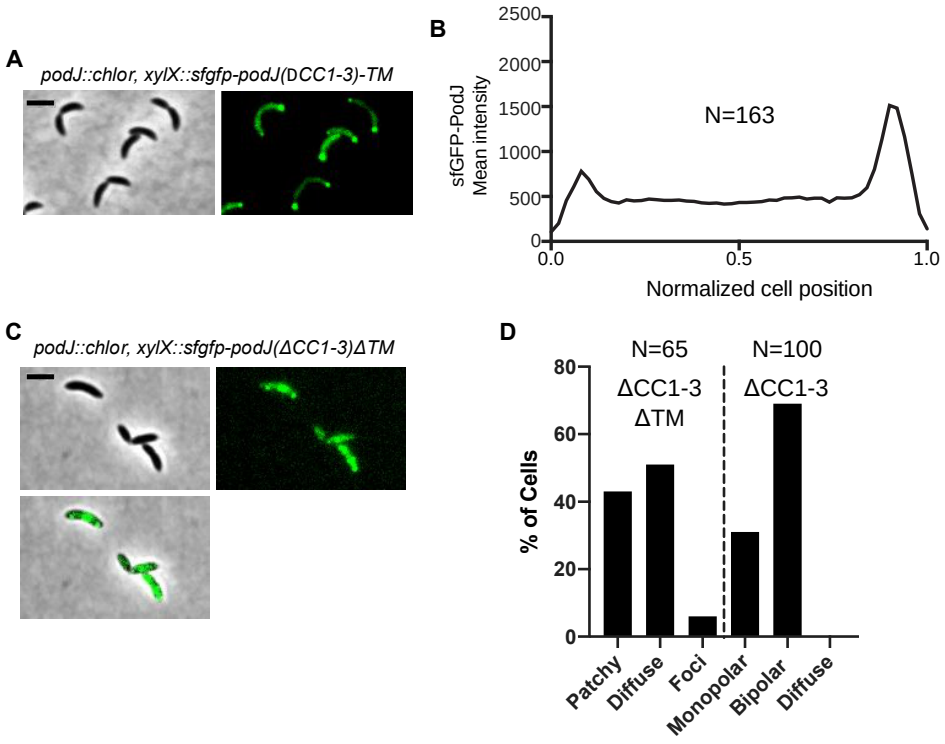

Figure 6–14 PodJ transmembrane tether rescues PodJ cell pole localization in absence of CC1-3.
Expression of constructs was completed by growing cells overnight at 28ºC in M2G containing antibiotics to OD_{600} of 0.2. A final concentration of 0.03% xylose was used to induce expression for 3 hours. Cells were imaged on a 1% agarose pad on the Nikon T*i*E using Phase-Contrast and GFP filter sets and settings (see Methods). A) Cells expressing sfGFP-PodJΔCC1-3-TM from the xylose locus and in a *podJ* deletion background are able to localize to the cell poles. B) sfGFP-PodJΔCC1-3-TM predominantly forms at the old cell pole (position 1.0 in fluorescence intensity profile). C) Cells expressing sfGFP-PodJΔCC1-3ΔTM from the xylose locus and in a *podJ* deletion background do not form foci frequently at the cell poles. D) Cell counts for sfGFP-PodJΔCC1-3ΔTM and sfGFP-PodJΔCC1-3. Patchy was used to describe non-diffuse fluorescence in cells that were not foci at the cell poles.

This observation was surprising, since similar constructs in *E. coli* remaining diffuse. When we removed the transmembrane tether, intensity at the cell poles decreased (foci 4%), and was replaced by a patchy (43%) or diffuse (53%) populations in cells, similar to what we observed when we expressed CC1-3 with no transmembrane tether (Figure 6–14C,D). These results together indicate that the transmembrane tether has a large impact on the ability of PodJ to accumulate at the cell pole in *C. crescentus*. Moreover, the experiments indicate that sfGFP-CC1-3-TM can accumulate at the cell poles in the absence of endogenous PodJ.

To further examine the impact of PodJ domains on polar assembly, we subsequently deleted the CC4-6 region and the PSE region of PodJ to determine if foci formation at the cell

poles was impacted. The periplasmic domain was also included for comparison to full-length PodJ. Both PodJΔCC4-6 and PodJΔPSE retained cell pole localization (Figure 6–15).

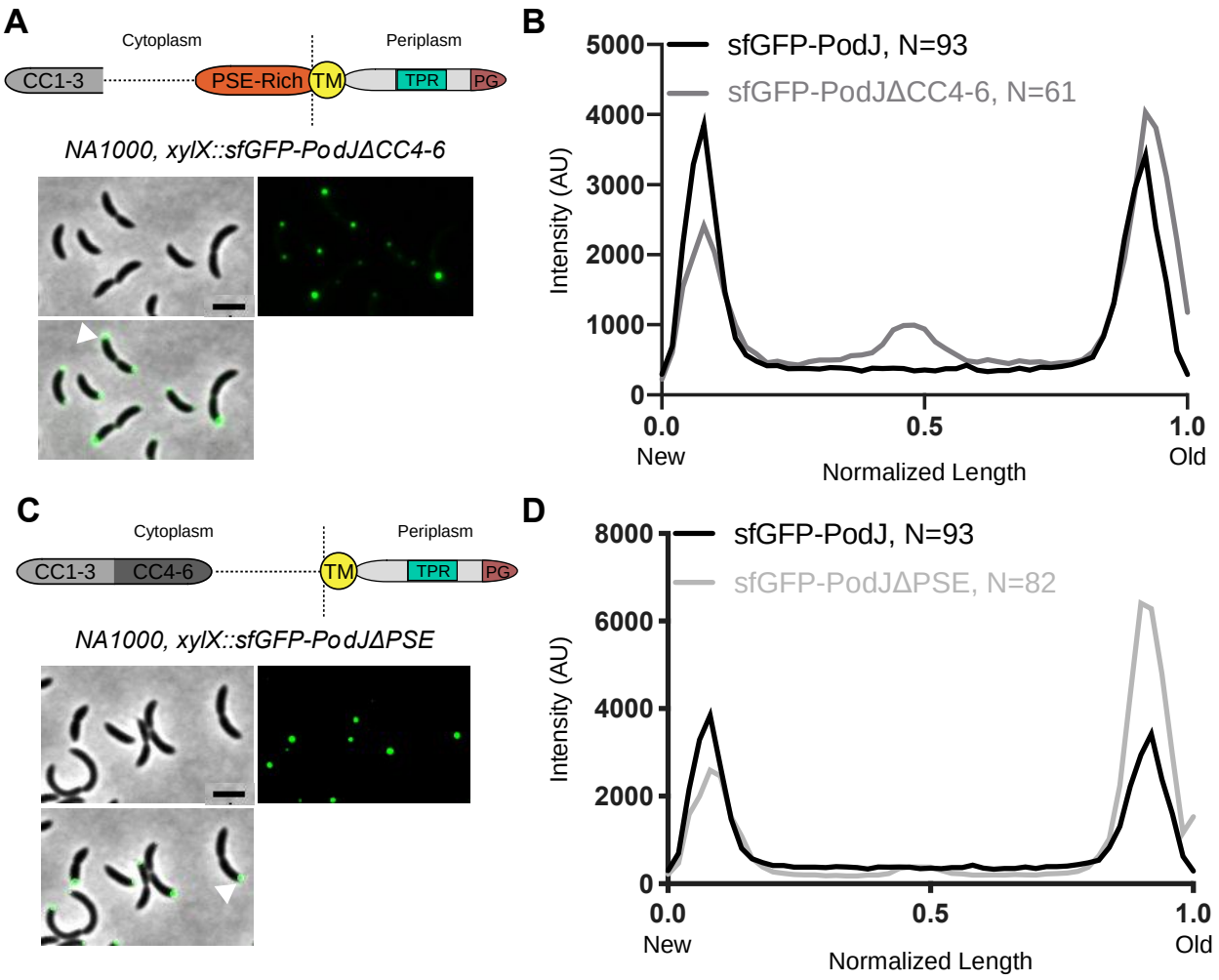

Figure 6–15 PodJ truncations retain foci formation in *C. crescentus*.
Expression of constructs was completed by growing cells overnight at 28ºC in M2G containing antibiotics to OD_{600} of 0.2. A final concentration of 0.03% xylose was used to induce expression for 3 hours. Cells were imaged on a 1% agarose pad on the Nikon T*i*E using Phase-Contrast and GFP filter sets and settings (see Methods). A) Cells expressing ΔCC4-6 from the xylose locus. B) Fluorescence intensity profile of ΔCC4-6 and full-length PodJ. 0.0 is the new cell pole, and 1.0 is the old cell pole. C) Cells expressing ΔPSE from the xylose locus. D) Fluorescence intensity profile of ΔPSE and full-length PodJ. 0.0 is the new cell pole, and 1.0 is the old cell pole.

However, we observed a reduction in ratio of new:old cell pole localization compared to wild type (Figure 6–15). This result supports the hypothesis that PodJCC1-3 and transmembrane tether play a role in polar localization while PodJPSE and PodJCC4-6 are related to recruitment (Chapter 5).

6.3.5 Overexpression of PodJ in *C. crescentus* results in foci with preference for negative curvature

Upon overexpression of PodJ, we observed that PodJ accumulates at both poles and preferentially on the side of the cell containing negative curvature. (Figure 6–16A,C).

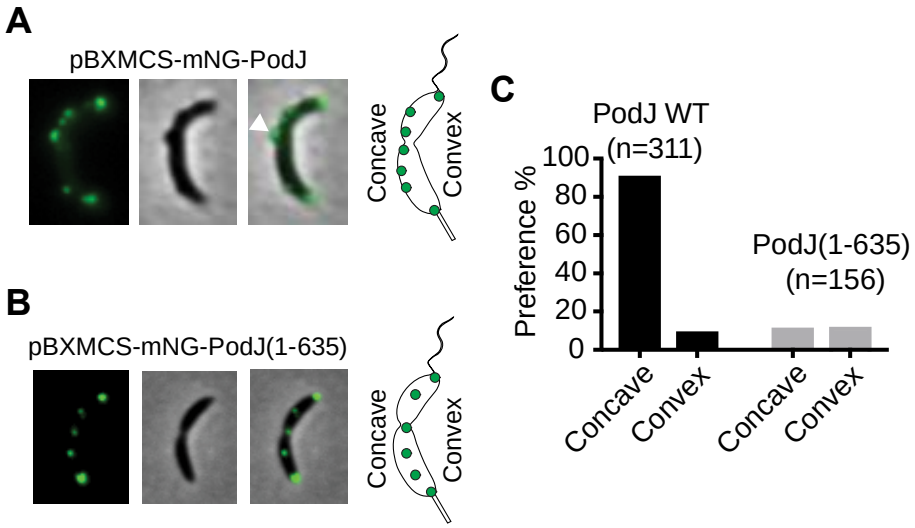

Figure 6–16 PodJ recognizes negative curvature using its periplasmic domain.
Expression was completed by growing cells overnight in M2G to an OD_{600} of 0.2. Protein expression was induced by a final concentration of 0.3% xylose. Cells were imaged on a 1% agarose pad on the Nikon T*i*E using Phase-Contrast and GFP filter sets and settings (see Methods). A) Cells expressing mNeonGreen (mNG)-PodJ from a high copy, xylose inducible vector. Cartoon depiction represents a typical cell overexpressing mNG-PodJ. B) Cells expressing mNG-PodJ(1-635) from a high copy, xylose inducible vector. Cartoon depiction represents a typical cell overexpressing mNG-PodJ(1-635). C) Graph displaying percent of cells with higher number of foci on concave vs convex surface of the cell for both mNG-PodJ (PodJ WT) and mNG-PodJ(1-635). Cells with no concave or convex foci are not listed, but represent the percent not shown. Cell images and data analysis provided by Wei Zhao.

This preference for the concave side of cells could be disrupted by removing the transmembrane tether through the periplasmic domains (PodJ(1-635)) (Figure 6–16B,C). These results suggest that PodJ may have weak affinity for negative curvature (concave side of cell). Moreover, this weak affinity is dependent upon the cytoplasmic domains and its association with the membrane. To our surprise, we also observed the position of these PodJ foci corelated with the formation of ectopic cell poles or smaller bumps along the concave side of the cell. Therefore,

concave curvature preference and the formation of ectopic poles requires the periplasmic domains of PodJ.

Ectopic poles have also been reported for the scaffolding proteins SpmX and TipN.[256,281] In order to determine if PodJ can form ectopic poles independent of these proteins, we overexpressed mNeonGreen-PodJ (mNG-PodJ) in *spmX* and *tipN* deletion backgrounds (Figure 6–17).

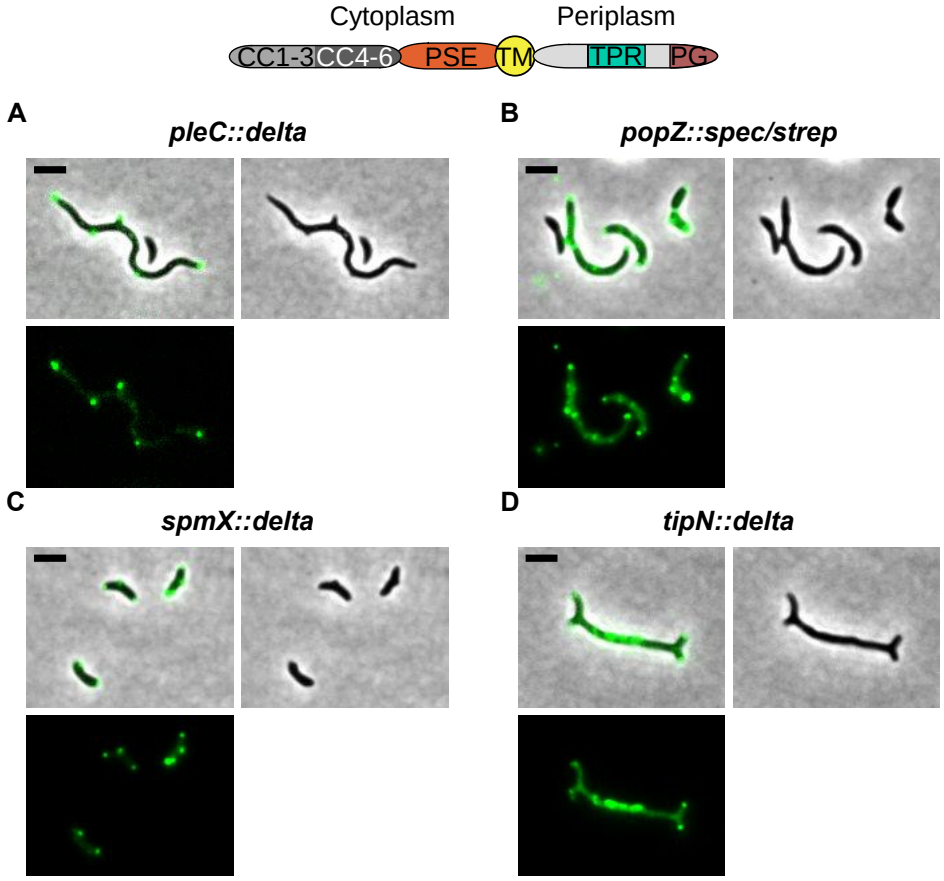

Figure 6–17 PodJ overexpression in scaffold and cell pole factor deletion backgrounds.
Imaging conditions for all cells was done by growing overnight in PYE to OD_{600} 0.1-0.2. Expression was induced for 5 hours using a final concentration of 0.3% xylose. Cells were imaged on a 1% agarose pad on the Nikon T*i*E using Phase-Contrast and GFP filter sets and settings (see Methods). All expressed full length mNG-PodJ from a high copy, xylose inducible vector. A) *pleC::delta* cells expressing mNG-PodJ. B) *popZ::spec/strep* cells expressing mNG-PodJ. C) *spmX::delta* cells expressing mNG-PodJ. D) *tipN::delta* cells expressing mNG-PodJ.

We observed the formation of small and large ectopic poles in both of these backgrounds, indicating PodJ was responsible for ectopic pole formation. Additionally, we checked whether two

factors recruited by PodJ, PopZ and PleC, could also be responsible. We overexpressed mNG-PodJ in *pleC* and *popZ* deletion backgrounds and observed ectopic poles for both (Figure 6–17). These results indicate that PodJ, or a not yet described factor recruited by PodJ, is responsible for ectopic poles when PodJ is overexpressed in cells.

We followed up on this ectopic pole phenotype be evaluating a set of PodJ domain deletions for their capability to initiate ectopic poles. Each domain deletion was tagged N-terminally with sfGFP and expressed from a high copy plasmid. We observed that expression of full-length PodJ resulted in a large number of foci per cell, and 72% of cells displayed ectopic phenotypes. In some cases, cells displayed greater than 5 foci per cell (Figure 6–18A, E-F).

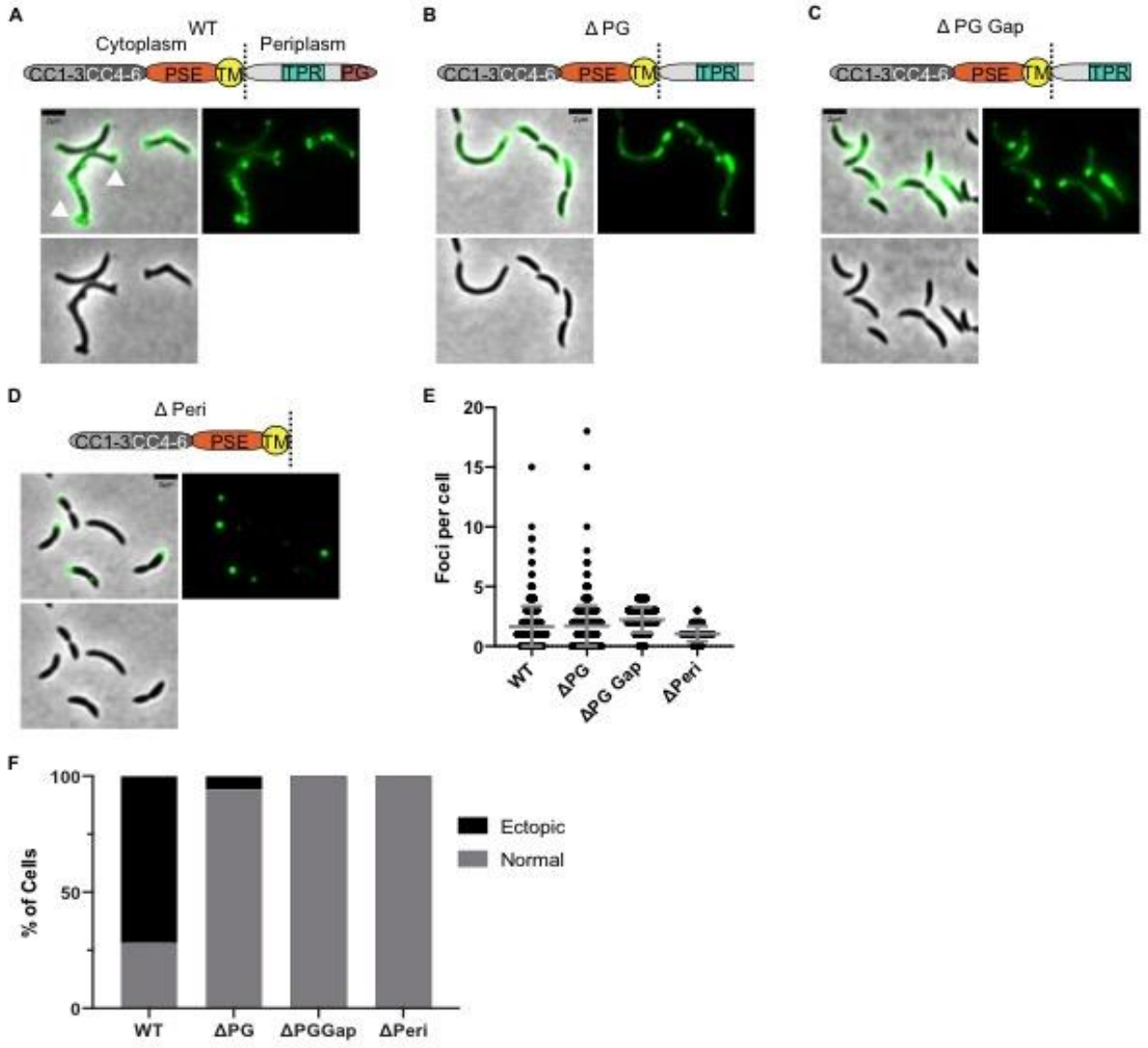

Figure 6–18 PodJ PG domain is required for the formation of ectopic poles.
All cells shown are NA1000. All cells were grown overnight in PYE to OD_{600} 0.1-0.2. Expression was induced for 5 hours using a final concentration of 0.3% xylose. Cells were imaged on a 1% agarose pad on the Nikon T*i*E using Phase-Contrast and GFP filter sets and settings (see Methods). A) Cells expressing full-length sfGFP-PodJ from a high copy expression vector. White triangles mark ectopic poles. B) Cells expressing sfGFP-PodJΔPG from a high copy expression vector. C) Cells expressing sfGFP-PodJΔPGgap from a high copy expression vector. D) Cells expressing sfGFP-PodJΔPeri from a high copy expression vector. E) Analysis of foci per cell completed using the particle analysis feature of MicrobeJ. Threshold for foci was set per condition based on fluorescence intensity of particles. Gray line indicates average, gray bars indicate standard deviation. N>50 cells for all conditions. F) Percent of cells in each condition with at least one ectopic pole corresponding to a nonpolar focus. Cells were manually counted. N>100 for each condition.

Upon deletion of the peptidoglycan binding (PG) domain, foci per cell remained at similar levels to full length sfGFP-PodJ expression (Figure 6–18B, E). Moreover, deletion of the PG

domain resulted in a reduction of ectopic pole formation from 72% to approximately 3% (Figure 6–18F). This result indicates that PodJ foci formation does not require the PG domain, however the PG domain is necessary for ectopic pole formation.

We next asked whether PodJ cytoplasmic domains could impact ectopic pole formation by analyzing overexpression of PodJ variants lacking CC1-3, CC4-6, PSE, or the TM domain. We expressed each in the same manner as the full-length variant that was able to induce ectopic pole formation. PodJΔCC1-3 was still able to form foci (Figure 6–19A,E) and induced ectopic pole formation (25% of cells) (Figure 6–19A,E-F).

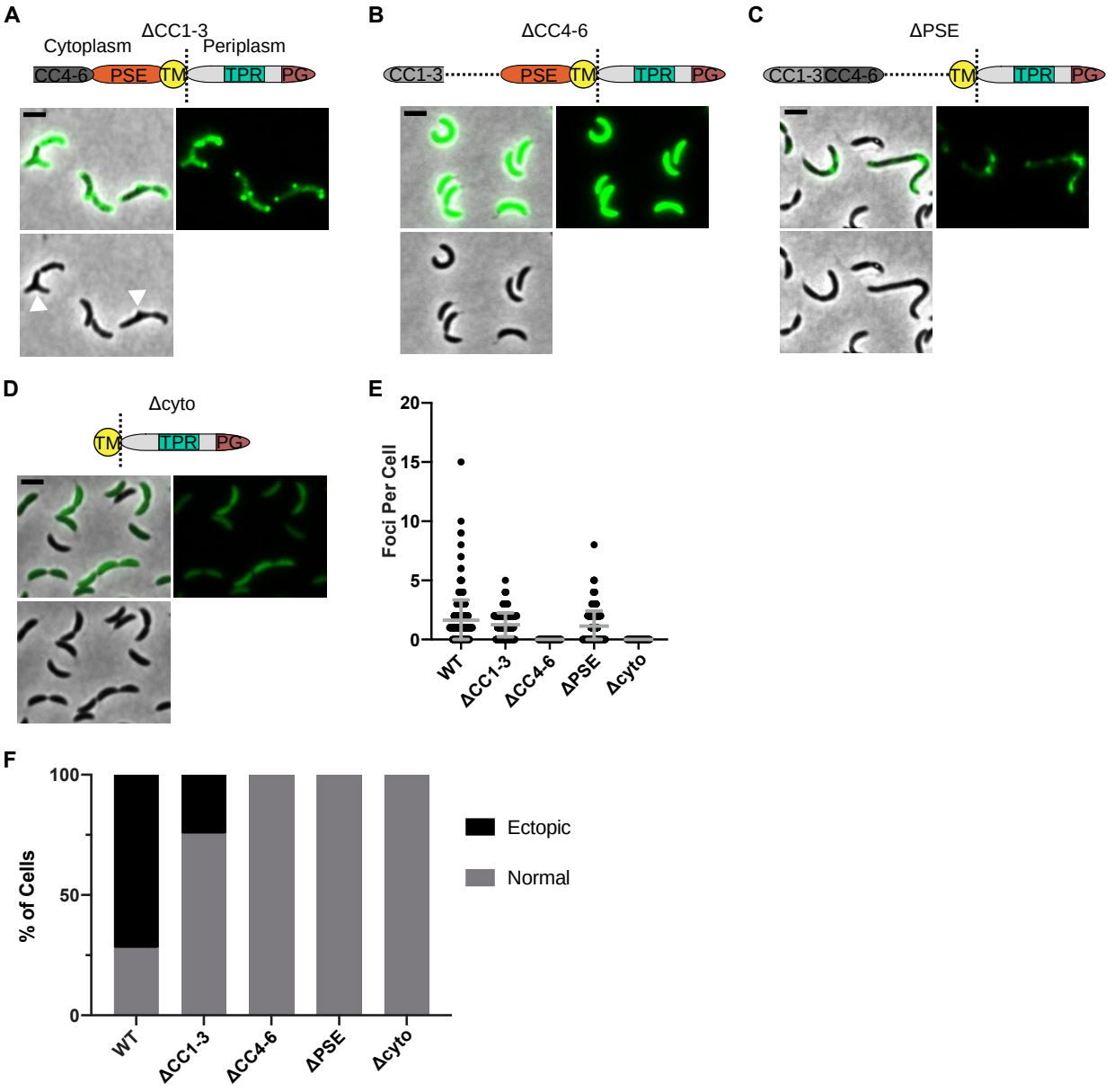

Figure 6–19 Deletion of PodJ cytosolic domains decreases ectopic pole formation upon PodJ overexpression. All cells shown are NA1000. All cells were grown overnight in PYE to OD_{600} 0.1-0.2. Expression was induced for 5 hours using a final concentration of 0.3% xylose. Cells were imaged on a 1% agarose pad on the Nikon T*i*E using Phase-Contrast and GFP filter sets and settings (see Methods). A) Cells expressing full-length sfGFP-ΔCC1-3 from a high copy expression vector. B) Cells expressing sfGFP-ΔCC4-6 from a high copy expression vector. C) Cells expressing sfGFP-ΔPSE from a high copy expression vector. D) Cells expressing sfGFP-Δcyto from a high copy expression vector. E) Analysis of foci per cell completed using the particle analysis feature of MicrobeJ. Threshold for foci was set per condition based on fluorescence intensity of particles. For cells with large patches of fluorescent signal, patches were counted as one focus. Gray line indicates average, gray bars indicate standard deviation. N>100 cells for all conditions. F) Percent of cells in each condition with at least ectopic pole corresponding to a nonpolar focus. Cells were manually counted. N>100 for each condition.

We observed that PodJΔCC4-6 and PodJΔcyto (Figure 6–19B,D) displayed a diffuse localization pattern. PodJΔCC4-6 (Figure 6–19B) displayed a diffuse population, which runs counter to our observations when the same construct was expressed at lower levels and will be followed up with western blot analysis to ensure that the PodJ variant remains tethered to GFP.

6.3.6 Testing specificity of the PG domain of PodJ

pfam01471, PG_binding_domain_1, is a family of peptidoglycan (PG)-binding proteins often found in lytic enzymes.[315] One of the most well-studied proteins in this family is the endolysin KZ144 of ΦKZ, a *P. aeruginosa* phage.[316] Sequence analysis of PodJ found that the PodJ PG domain lacks the repeat structure (D G (Pho)$_2$ G (K,N) (G,N) T) found in the pfam01471 superfamily of PG-binding domains and KZ144 (Figure 6–20A).[317]

A

Consensus repeat D G (Pho)$_2$ G (K,N) (G,N) T

KZ144 17-QTLLNLCGYDKGKP**DGIFGNNT**FNQVVKFQKDNCLDS**DGIVGKNT**WAELFSKYS-71

PodJ$_{CC}$ 921-QRVLSQLGYYQGPR**DGVSSPAL**RMAIAAYQRDQGLPP**TGSVDAET**LNRLSVYAR-974

PodJ$_{AT}$ 1231-QAILNKNGFDAGQP**DGKLGKNT**VTAIKDFQKSVGQTP**DGRITNEL**VTALLARNK-1274

B

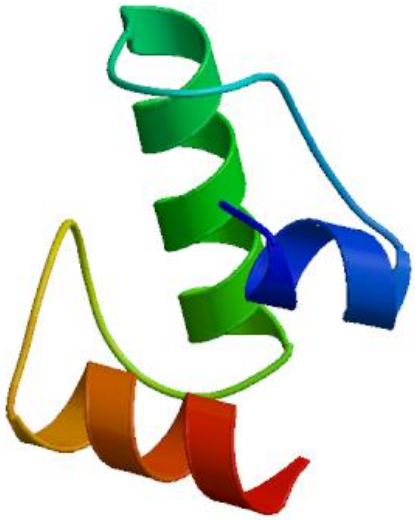

Figure 6–20 Sequence alignment of PG-binding domains and consensus sequence.
A) Consensus repeat of KZ144 and KZ144, PodJCC, and PodJAT sequence alignments. Alignments were performed using NCBI Protein BLAST.[318] Bold letters indicate consensus repeat, red letters in PodJCC and PodJAT represent divergences from the consensus sequence. Underlines indicate α-helices predicted by Jpred 4.[319] B) Model of PodJCC PG binding domain modeled using PDB 4C2H crystal structure as a template by Swiss Model ExPasy.[320,321]

This could indicate that PodJ utilizes a different PG-binding domain that has not been annotated. A close relative of *C. crescentus* is the plant pathogen *A. tumefaciens*.[96] *A. tumefaciens* contains an ortholog of PodJ with a similar domain arrangement, hereby referred to as PodJ$_{AT}$. PodJ$_{AT}$ shares more sequence similarity with KZ144 and contains almost one full consensus repeat (Figure 6–20A). All three PG binding domains consist of three α-helices (Figure 6–20B). Past studies have shown that the PodJ$_{AT}$ deletion strain resulted in ectopic poles in *A. tumefaciens*, which is the reverse of *C. crescentus*.[322] Therefore, we compared PodJ$_{AT}$ and PodJ in *C. crescentus*,

hereby referred to as PodJ$_{CC}$ domain structures. PodJ$_{AT}$ also contains a coiled-coil region followed by an intrinsically disordered region (IDR) (Figure 6–21A).

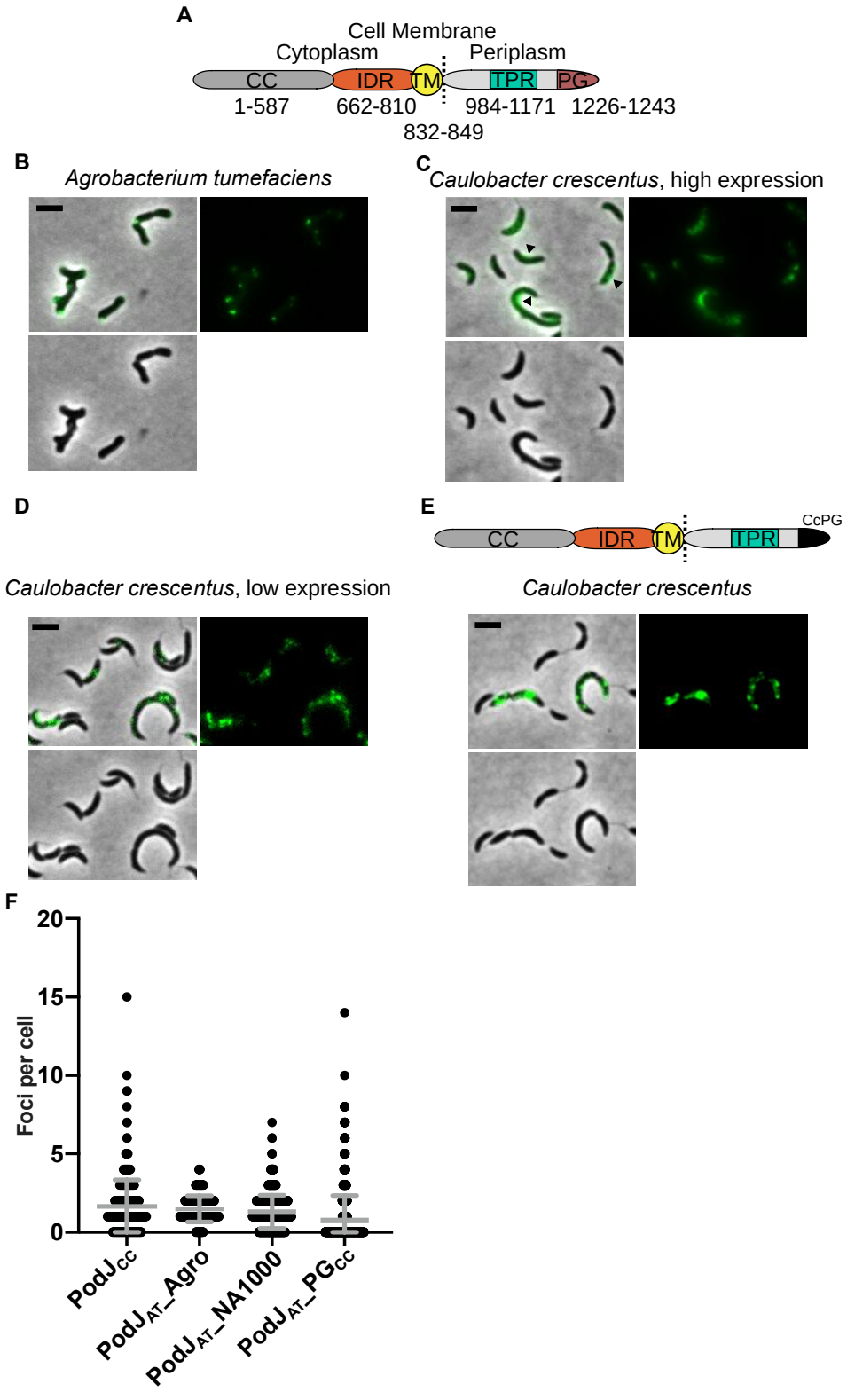

Figure 6–21 PodJ$_{CC}$ PG domain is not enough to induce ectopic pole formation.
Cell type indicated above image. All cells were grown overnight in PYE to OD_{600} 0.1-0.2. Expression was induced for 5 hours using a final concentration of 0.3% xylose for high expression, 0% xylose for low expression. Cells were

imaged on a 1% agarose pad on the Nikon T*i*E using Phase-Contrast and GFP filter sets and settings (see Methods). A) Domain annotation of $PodJ_{AT}$. $PodJ_{AT}$ shares a similar domain arrangement to $PodJ_{CC}$ where a coiled-coil domain is followed by a disordered region, transmembrane tether, TPR repeat domain, and PG domain. B) *A. tumefaciens* cells expressing $PodJ_{AT}$ from a high copy, xylose inducible vector. C) *C. crescentus* cells expressing PodJAT high copy, xylose inducible vector at high expression levels. D) *C. crescentus* cells expressing $PodJ_{AT}$ from a high copy, xylose inducible vector at low expression levels. E) Cartoon schematic representing the hybrid $PodJ_{AT}$-PG_{CC} construction. *C. crescentus* cells expressing $PodJ_{AT}$ high copy, xylose inducible vector at high expression levels. F) Analysis of foci per cell completed using the particle analysis feature of MicrobeJ. Threshold for foci was set per condition based on fluorescence intensity of particles. For cells with large patches of fluorescent signal, patches were counted as one focus. Gray line indicates average, gray bars indicate standard deviation. N>100 cells for all conditions.

$PodJ_{AT}$ IDR is also composed of proline, serine, and glutamic acid, but also contains higher amounts of arginine, aspartic acid, and leucine. It is followed by a transmembrane tether and the same periplasmic domain architecture (Figure 6–21A). When $PodJ_{AT}$ is expressed at high levels in *A. tumefaciens*, we observed ectopic pole formation (Figure 6–21B). Since we observed ectopic pole formation in *A. tumefaciens*, we asked whether $PodJ_{AT}$ overexpression could also induce ectopic poles in *C. crescentus*. At high expression levels, we observed foci and large patches of fluorescence along the side of cells (Figure 6–21C, black arrows). We did observe more foci at low expression levels (Figure 6–21D), but neither condition was able to generate ectopic poles in >1% of cells (data now shown). This could indicate the $PodJ_{CC}$ PG domain is required for ectopic poles to form, as *A. tumefaciens* and *C. crescentus* contain different peptidoglycan structures. *A. tumefaciens* contains a greater than 50% L,D 3-3-crosslinks between mDap residues in the peptide stems compared to *E. coli*, which only contains 10% of these links (Figure 6–22A,B).[323,324] *C. crescentus*, in contrast, contains primarily D,D 4-3-crosslinks between mDap and mAla (Figure 6–22C).[325]

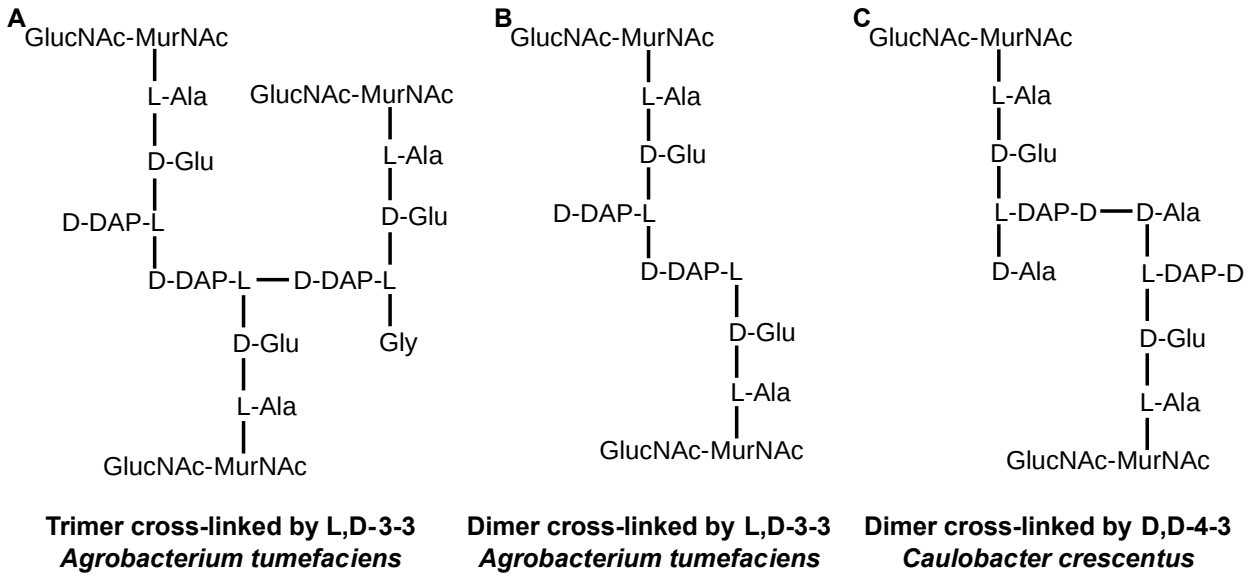

Figure 6–22 Peptidoglycan architecture in two alphaproteobacterium.
A) Trimer cross-linked by DAP-DAP, L,D-3-3. The nomenclature reads that D-DAP-L makes cross links in between the L and D peptide bonds. Found commonly in *A. tumefaciens*. B) Dimer cross-linked by L,D-3-3 peptide bonds found commonly in *A. tumefaciens*. C) Dimer cross-linked by D,D-4-3 between L-DAP-D and D-Ala. Found in *C. crescentus*.

To test if PG domain specificity differences led to the loss of ectopic pole formation upon $PodJ_{AT}$ overexpression, we generated a construct where the $PodJ_{AT}$ PG domain was swapped with the PodJCC PG domain (Figure 6–21E). Overexpression of this hybrid PodJ was not able to induce ectopic poles but was able to form a similar number of foci to $PodJ_{CC}$ in cells (Figure 6–21F). This result is similar to the PodJΔPSE result, where foci and patches formed, but no ectopic poles formed even with the PG domain intact. If only a PG binding interaction and oligomerization were required for ectopic pole formation, the hybrid construct would likely have formed ectopic poles. This further strengthens our hypothesis that the PG domain alone is not responsible for formation of ectopic poles.

6.4 Discussion

6.4.1 PodJ localization mechanism

PodJ oligomerization is tied to its ability to make foci and recognize curvature in cells. We have identified that PodJ contains three domains that assist in self-assembly *in vitro.* This multivalency for oligomerization results in the formation of biomolecular condensates. The ability to self-assemble does not depend on the curvature around it, as evidenced by condensate formation and foci formation in *E. coli* spheroplasts. In *E. coli*, PodJCC1-3 is the minimal polar self-assembling domains, while in *C. crescentus*, the transmembrane tether plus PodJCC1-3 is required for polar formation, due to the loss of multivalency. Due to PodJ multivalency, PodJΔCC1-3 still forms polar foci. PodJΔCC1-3ΔTM is unable to form polar foci showing how important the transmembrane tether is in negative curvature recognition. This is consistent with our observation in spheroplasts where loss of polar curvature resulted in diffuse localization of the transmembrane tether only. Full-length PodJ predominantly recognizes negative curvature in *C. crescentus* when overexpressed. Taken together, these results point to a two-step process where PodJ must first self-assemble into a large oligomer. Once large enough, its transmembrane tethers interact with negative curvature at the cell pole and fix PodJ in place, where it can then act as a scaffold for downstream factors (Figure 6–23).

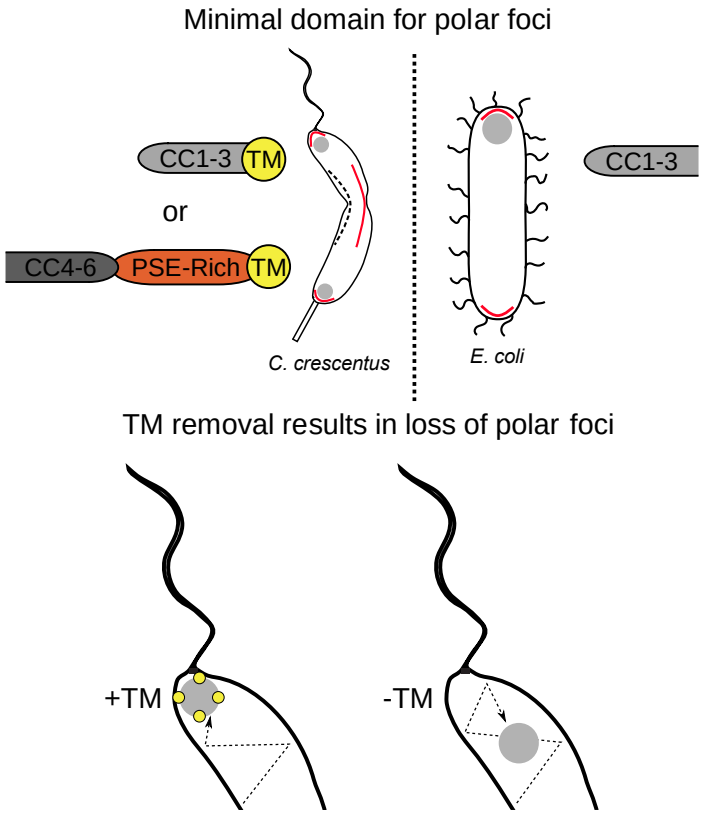

Figure 6–23 CC1-3 and transmembrane tether make up minimal polar forming units.
In *C. crescentus*, the TM is required for polar recruitment of PodJ CC1-3 or ΔCC1-3. Without the TM, CC1-3 or ΔCC1-3 will only form patchy fluorescence away from the cell poles. In *E. coli*, on the CC1-3 domain is required to form polar foci. If PodJ contains a self-assembly domain and its transmembrane tether, it will form an oligomer that forms a focus at the pole. If the transmembrane tether is removed, the oligomer will not anchor in place at the pole.

Loss of any multivalency results in the transmembrane tether playing a large role in assembly. The fact that the transmembrane tether is not required for polar formation in *E.* coli also points to the higher amount curvature in *C. crescentus* competing for PodJ. Due to *E. coli* only having curvature at the cell poles, it forms large oligomers and polar foci. In contrast, *C. crescentus* contains two additional regions of curvature which can compete with the cell poles for PodJ when it lacks its transmembrane tether. When PodJ has filled the space at the cell poles, it can then assemble with preference for the negative curvature wall of the cell. What remains unknown is why PodJ, under its native promoter, recognizes the new cell pole exclusively. It could be that the combination of multivalency and transmembrane tether is enough to localize at the new cell pole.

But this only explains the polar foci formation, not foci formation at the new cell pole only. A factor that recruits PodJ to the new cell pole or blocks PodJ at the old cell pole could exist. Future experiments will need to be developed to answer why PodJ assembles at the new cell pole.

6.4.2 Ectopic pole formation

Cell shape is often tied to cellular environment due to certain shapes generating advantages. While ectopic poles in most bacteria would typically be due a system going awry, some bacteria, like *Streptomyces coelicolor*, take advantage of this atypical phenomenon to generate structures like aerial hyphae.[326] Aerial hyphae give the soil bacterium an advantage in sporulation.[327] While *C. crescentus* is unlikely to sporulate from ectopic poles, we can use PodJ ectopic pole formation as way to learn about the biophysical characteristics of PodJ. Critically, we observed that some PodJ constructs can form foci and ectopic poles and others cannot, independent of other proteins known to cause ectopic poles (Figure 6–24).

PodJ Variant	Foci (+/–)	Ectopic Poles (+/–)
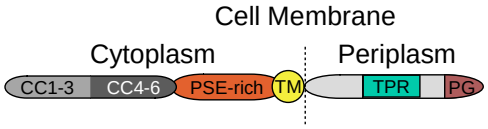	+	+
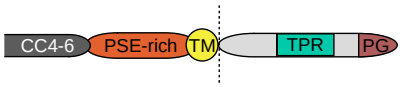	+/–	+/–
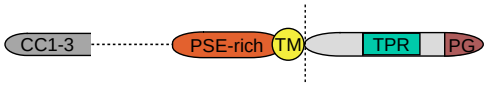	–	–
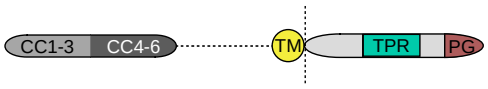	+/–	–
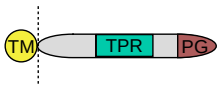	–	–
	+	–
	+/–	–
	+/–	–

Figure 6–24 Summary table of PodJ overexpression phenotypes in *C. crescentus*.
PodJ variants indicate the version of PodJ overexpressed in cells. Foci indicates whether cells displayed foci numbers similar to full length PodJ overexpression (+), less than full length but greater than 2 foci (+/–), or no foci (–). No cells contained a single focus. Ectopic poles displays whether cells formed ectopic poles at similar levels to full length PodJ (+), less than full length PodJ (+/–), or no ectopic poles (–).

We observed that the PG domain was required for robust ectopic pole formations. Removal of cytosolic self-assembly domains resulted in either lowered ectopic pole formation and foci formation or diffuse signal. PodJ$_{CC}$ PG domain does share homology with other PG-binding

domains but lacks consensus repeats. When $PodJ_{AT}$ is overexpressed in *C. crescentus*, ectopic poles do not form even when $PodJ_{CC}$ PG domain was swapped in.

Based on these observations, we can begin to construct a model of how PodJ is able to form ectopic poles in cells. Two requirements for robust PodJ mediated ectopic pole formation are the presence of the PG domain and the cytoplasmic domains that mediate self-assembly (Figure 6–25).

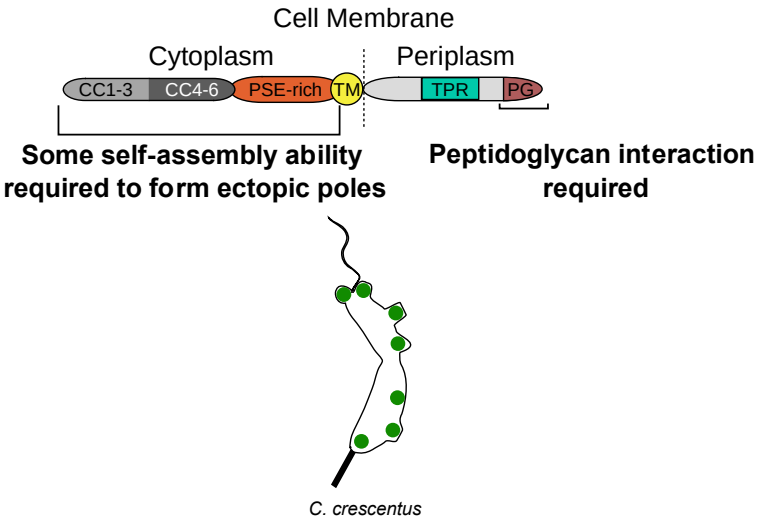

Figure 6–25 PodJ requires both cytosolic and PG domains for ectopic pole formation.
In order to form ectopic poles, PodJ requires both cytosolic and periplasmic factors to act in cooperation. In the cytoplasm, PodJ self-assembly domains must retain some ability to oligomerize in order to form robust (>50% of cells contain ectopic poles) ectopic poles. In the periplasm, the interaction with peptidoglycan must be maintained for robust ectopic pole formation.

These observations lend to two possible models for ectopic pole formation. One model is that the PodJ PG domain could act to reshape the peptidoglycan layer by binding to the PG. Alternatively, PodJ may recruit other PG modifying enzymes to the site of interaction (Figure 6–26A,B).

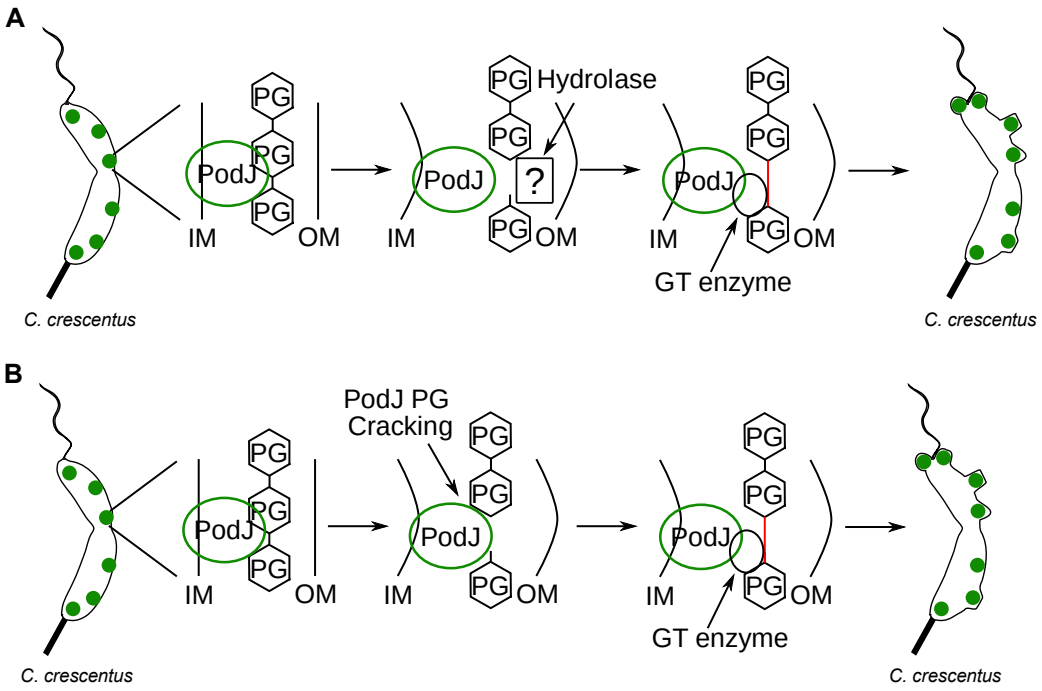

Figure 6–26 Models of PodJ ectopic pole formation.
A) PodJ recruitment model. PodJ self-assembles and at high concentrations interacts with the side-wall peptidoglycan. A hydrolase is then recruited either by another PodJ domain, or by the PG-peptidoglycan interaction. After the hydrolase cleaves the peptidoglycan, a glycosyl transferase (GT) helps insert new peptidoglycan. B) PodJ cracking model. An alternative to recruitment of a hydrolase is that PodJ PG domain can break peptidoglycan strands. As multiple PodJ PG domains bind peptidoglycan, the force of PodJ large oligomer pushes against the peptidoglycan, eventually breaking it. GT enzymes then insert new peptidoglycan at the break site. This new space allows for release of tension caused by the oligomer.

In the first model, (Figure 6–26A), when PodJ is able to form large oligomers either at the cell pole or along the sidewall of cells, its PG-binding domain binds to peptidoglycan. A peptidoglycan hydrolase is then recruited to this site where it can cleave peptidoglycan bonds. The natural cellular repair machinery is then able to fill in the gaps with new peptidoglycan units, with glycosyltransferases (GT enzyme) linking the new glycan strands (Figure 6–26A). This recruitment could be either direct (binds PG domain) or cooperative (binds peptidoglycan already bound by the PG domain) (Figure 6–26A). Another domain, such as the TPR domain could also be the recruitment factor since TPR domains have been shown to recruit protein complexes.[328] This model would explain why deletion of the PG domain results in a loss of ectopic pole formation.

The other model relies solely on PodJ. Because the PodJ PG domain is predicted to be peptidoglycan binding, if PodJ oligomerizes and enough PG domains are bound to peptidoglycan, the bonds could be broken through the mechanical force of PodJ pushing against the peptidoglycan layer (Figure 6–26B). *In vitro* studies have confirmed that protein crowding at membranes by peripheral proteins can induce curvature.[329] This effect was shown using HisEGFP, a protein with no intrinsic curvature inducing or sensing abilities as well as no higher order oligomeric capabilities.[329] It is unlikely that PodJ PG domain can act as a hydrolase as it lacks any common catalytic motifs. After cracking the peptidoglycan, GT enzymes can incorporate new peptidoglycan and relieve the stress induced by PodJ. This model can explain why when the PG domain is intact but self-assembly is impacted, the ectopic pole formation is depressed but not abolished. Future experiments will be designed to try to resolve these models.

6.5 Future directions

6.5.1 Development of methods to test PodJ curvature sensing model

One major mystery related to PodJ is that newly synthesized PodJ (at endogenous levels) recognizes the new cell pole over the old cell pole.[259,269] Without PodJ localization at the new cell pole exclusively, the histidine kinase PleC would be improperly localized, resulting in misregulation of the cell-cycle.[135] PodJ is able to assemble at the cell poles, and form ectopic poles, independent of other known scaffolding proteins and cell pole proteins.

It is unlikely that PodJ solely recognizes a polar feature, since each domain can be deleted and cell pole localization persists. Furthermore, localization occurs in *E. coli*, which should lack

polar features found in *C. crescentus*. This leaves two likely models: nucleoid occlusion or curvature recognition. Narrowing it down even further, nucleoid occlusion is unlikely to produce a system in which PodJ can differentiate between the new and old cell poles. This leaves us with a model for curvature recognition. To determine whether or not PodJ can recognize curvature in cells, we have turned to a technique that forces cells to grow into different shapes. Microchannels in agarose can be generated using a solid support for making patterns. PDMS (polydimethylsiloxane) with raised microchannels was generated using established protocols.[330] V and W shapes at different angles were able to be constructed. To generate microchannels in agar using this PDMS as a template, a 3% agarose solution containing antibiotics for plasmid selection, 25 µg/mL cephalexin in order to filament cells, and IPTG to induce protein expression was poured over the PDMS and allowed to solidify. Five minutes before adding cells to the agarose pad, 25 µg/mL of cephalexin was added to promote cell filamentation. We used this system to express fluorescently labeled PodJ and PopZ in *E. coli* in order to determine the extent to which PodJ can recognize curvature. We used PopZ as a control due its established nucleoid occlusion model for localization. We expressed YFP-PodJ(1-702) and mCherry-PodJ from an IPTG-inducible vector in *E. coli* and imaged cells either untreated or treated with cephalexin. Cells untreated with cephalexin displayed the bipolar localization (Figure 6–27A,B).

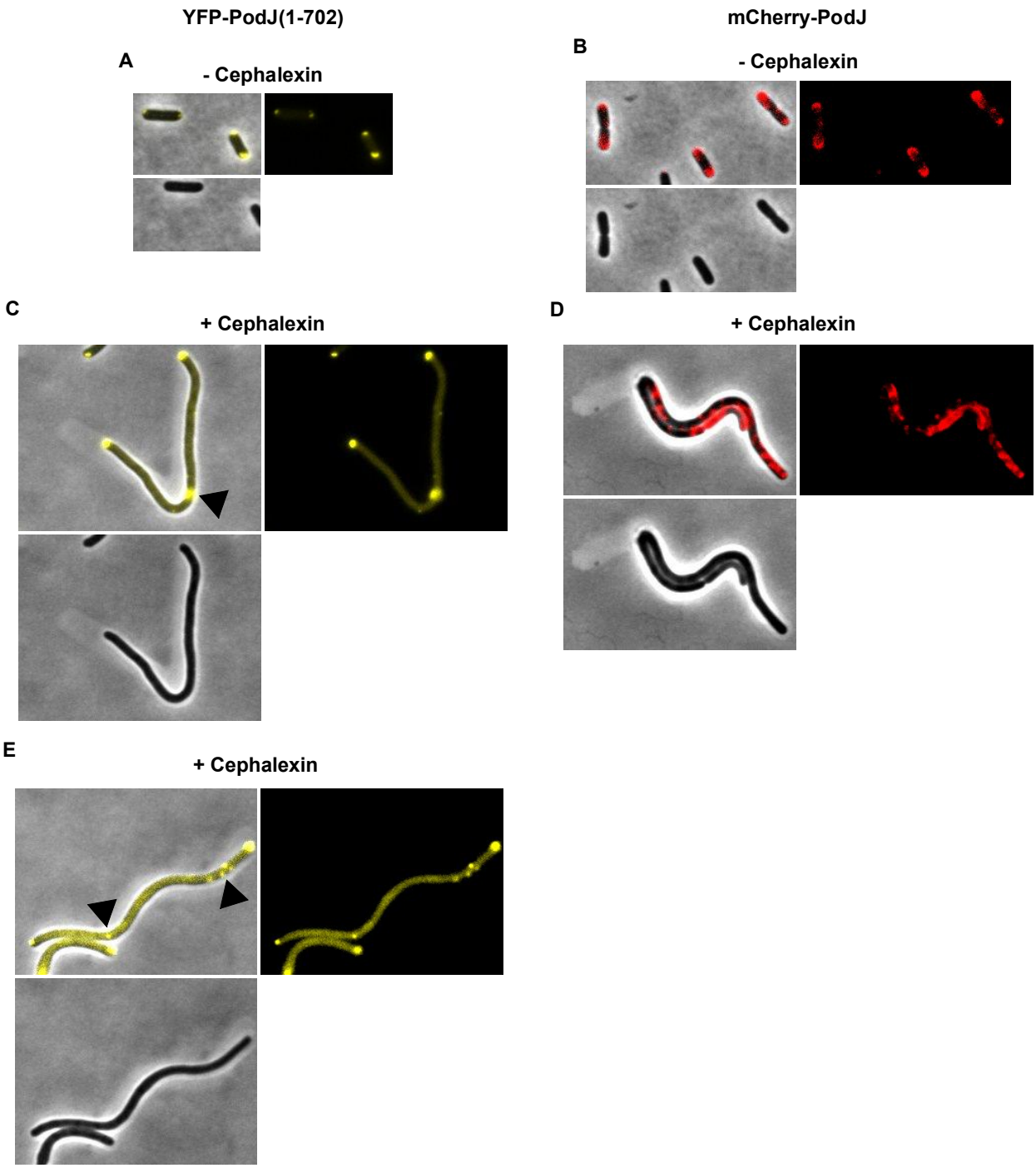

Figure 6–27 Using agarose microchannels to generate regions of curvature in cells.
E. coli BL21 containing plasmid were grown overnight at 37ºC in LB containing antibiotics. Cells were diluted into fresh LB containing antibiotics at a 1:100 ratio. Cells were grown for one hour at 37ºC, at which point expression was induced using a final concentration of 100 µM IPTG. Cells were then grown for two hours at 37ºC and a final concentration of 25 µg/mL cephalexin was added to induce filamentation. Cells were shaken for five minutes at 37ºC after addition and were added to prepared agarose microchannels (see Methods). Slides were sealed with wax and placed at 37ºC for 1 hour. Imaging was done on the Nikon T*i*E using a Phase-Contrast, YFP, and mCherry filter sets and settings (See Methods). A) Cells expressing YFP-PodJ(1-702) from a pCDF IPTG-inducible vector without cephalexin. B) Cells expressing mCherry-PodJ from a pCDF IPTG inducible vector without cephalexin. C) Cells

expressing YFP-PodJ(1-702) from a pCDF IPTG-inducible vector with cephalexin and plated on V-shaped microchannels. Black triangles indicate foci formation at regions of induced curvature. D) Cells expressing mCherry-PodJ from a pCDF IPTG-inducible vector with cephalexin and plated on W-shaped microchannels. E) Cells expressing YFP-PodJ(1-702) from a pCDF IPTG-inducible vector with cephalexin and plated on W-shaped microchannels. Black triangles indicate foci formation at regions of induced curvature.

Cells treated with cephalexin and grown in agarose microchannels did grow to match the shapes in which they rested (Figure 6–27C-E). YFP-PodJ(1-702) formed foci at the poles for both V and W shapes, but also exhibited foci at or near curves (Figure 6–27C,E, black triangles). mCherry-PopZ also formed polar foci but also appeared throughout cells (Figure 6–27D). At this point, we have not been able to grow cells in sufficient numbers in microchannels. Further optimization of generating PDMS stamps needs to be completed to improve the number of wells filled by cells. In addition, a different control from PodJ may be required due to mCherry-PodJ foci formation occurring along all sides. Potential new controls would include a native *E. coli* protein that recognizes a feature at the cell poles or PopZ from *C. crescentus*. This result for PodJ is promising and points toward this being a viable method for screening curvature sensing proteins in *C. crescentus*. We hope to expand this platform to other self-assembling proteins in *C. crescentus* including SpmX, TipN, and PodJ$_{AT}$.

For curvature sensing in *C. crescentus,* methods for detection of foci on negative and positive curvature in cells needs to be developed. Using the bacterial analysis software plugin MicrobeJ,[166] an analysis macro can be developed in order to detect foci in positive and negative curvature regions. PodJ overexpression experiments can then be analyzed for whether or not PodJ variants recognize certain curvatures in cells. This will allow us to identify domains that may be responsible for curvature recognition.

6.5.2 Determining PodJ$_{CC}$ and PodJ$_{AT}$ peptidoglycan affinity or activity

To ensure that PodJ$_{CC}$ is not able to hydrolyze peptidoglycan and if it has affinity for peptidoglycan, we will use a peptidoglycan association assay. It has previously been shown that by attaching a fluorescent protein, like sfGFP, to a PG domain and recombinantly expressing and purifying from *E. coli*, a functional PG domain could be obtained.[316] Briers, *et al.* were able to generate sacculi, intact peptidoglycan without lipids or intracellular components, in order to test association.[316] For most bacteria, boiling in 2% SDS can be used to remove cell components other than peptidoglycan. Purified sfGFP-PG can then be mixed with free peptidoglycan and association can be determined by epifluorescence microscopy.[316] We plan to follow this experimental setup using sfGFP-PG$_{CC}$ and sfGFP-PG$_{AT}$. We will be able to study the association of each with its native peptidoglycan and whether it can associate with each other's peptidoglycan. In addition, if breakdown of peptidoglycan occurs, this would also be a marker of hydrolase activity. We would use sfGFP as a negative control for association and peptidoglycan breakdown.

6.5.3 Determination of hydrolase responsible for ectopic pole formation

C. crescentus has at least 8 annotated transglycosylases in its genome. Rather than doing a stepwise deletion of each and overexpressing PodJ, we have taken a narrower approach. One lytic transglycosylase, PleA, is known to be recruited to the cell pole by PodJ.[331] PleA shares similarity to the *E. coli* soluble lytic transglycosylase and lytic transglycoslyases found on conjugative plasmids of bacteriophage.[332] These enzymes cleave the β-1,4-glycosidic bond between N-acetyl-muramic acid and N-acetyl-glucosamine using a conserved, catalytically active glutamate that is present in PleA (E36).[333] PleA is involved in placement of the pili and flagellum in *C. crescentus*,

where its enzymatic activity is required for the placement of the pore protein CpaC.[259] Without PleA, cells cannot open peptidoglycan for placement of these features. PleA cannot be recruited to the site of pili and flagellum placement without PodJ.[259] Because PleA is recruited by PodJ, it would make sense for it to be the enzyme responsible for the first step in forming ectopic poles. To determine if this is the case, we will use a classical approach of deleting *pleA* using a two-step deletion method commonly employed in *C. crescentus*.[169] *pleA* deletions carry a negative swarm phenotype[331] that can be used to determine successful deletions, along with confirmation of deletion by PCR. After deletion, we will generate two complementary strains where PleA is tagged individually with the fluorescent protein mCherry on both termini. PleA has not been successfully fused with a fluorescent protein label, and localization has not been visualized using immunofluorescence for PleA.[331] In addition to individually labeling both termini, mCherry will be used due to its ability to properly mature in the periplasm.[334] mCherry shows better folding propensity than fluorescent proteins derived from GFP, though some periplasmic fluorescent proteins have been developed.[335] Tagged strains will be expressed from integrated, vanillate-inducible vectors and repletion of swarm ability will be determined. Strains that are able to swarm again will then be visualized by epifluorescent microscopy for mCherry fluorescence. Successful fluorescent fusions will then be subjected to ectopic pole forming conditions and colocalization with ectopic poles will be determined. Western blotting will be used to confirm that all labeled proteins are stable under these conditions. If we are not able to produce a fluorescent fusion of PleA or observe colocalization between PleA and PodJ at ectopic poles, we will turn to more broad approach to determine the lytic transglycosylase involved.

When tracking down protein-protein interaction targets in biology, proximity labeling schemes have been a highly successful tool for interactome mapping. Biotin[336], carbene[337], and

biotin-radical combination systems (APEX)[338] have all been successfully used to map interactomes in bacteria and eukaryotes. In particular, proximity labeling schemes using biotin have been developed over time to increase the speed of labeling, decrease the proximity of the labeling, and decrease the size of the labeling protein.[339] The original BioID system used BirA, a biotin ligase native to *E. coli*, in order to biotinylate nearby proteins.[336,340] By attaching BirA to proteins of interest, protein-protein interactions can be identified by using streptavidin to pull-down biotinylated proteins. Analysis using mass-spectroscopy could then identify the proteins that had been pulled-down.[336,339] BirA has drawbacks including slow labelling times, wide proximity of labeling, and size of the protein.[336] To overcome these issues, TurboID and miniTurboID were developed.[339] Both were using yeast surface display combined with FACS. Error prone PCR to mutagenize BirA was used. TurboID (15 mutations) and miniTurboID (13 mutations, deletion of N-terminal domain) both have faster kinetics for labeling (10 minutes compared to 18-24 hours for BirA).[339] miniTurboID is smaller in size and less likely to biotinylate using endogenous biotin (less background).[339] Using these new version of BioID, we have begun to use PodJ and PopZ as test cases for this technology in *C. crescentus*. We chose PodJ and PopZ as test cases because we are trying to answer what PodJ might be interacting with in the periplasm and PopZ as a control for establishing the extent of this technology due to its known interacting partners.[134] We started by designing sfGFP-TurboID fusions to both in order to be able to determine if localization was impacted by attaching TurboID to the N-terminus of each protein. Each protein has proven amenable to N-terminal fluorescent protein fusions. We expressed tagged copies of each protein from high-copy, xylose-inducible vectors in order to produce easily identifiable phenotypes. We observed that the PodJ fusion did not localize, though sfGFP fluorescence was detected (Figure 6–28A).

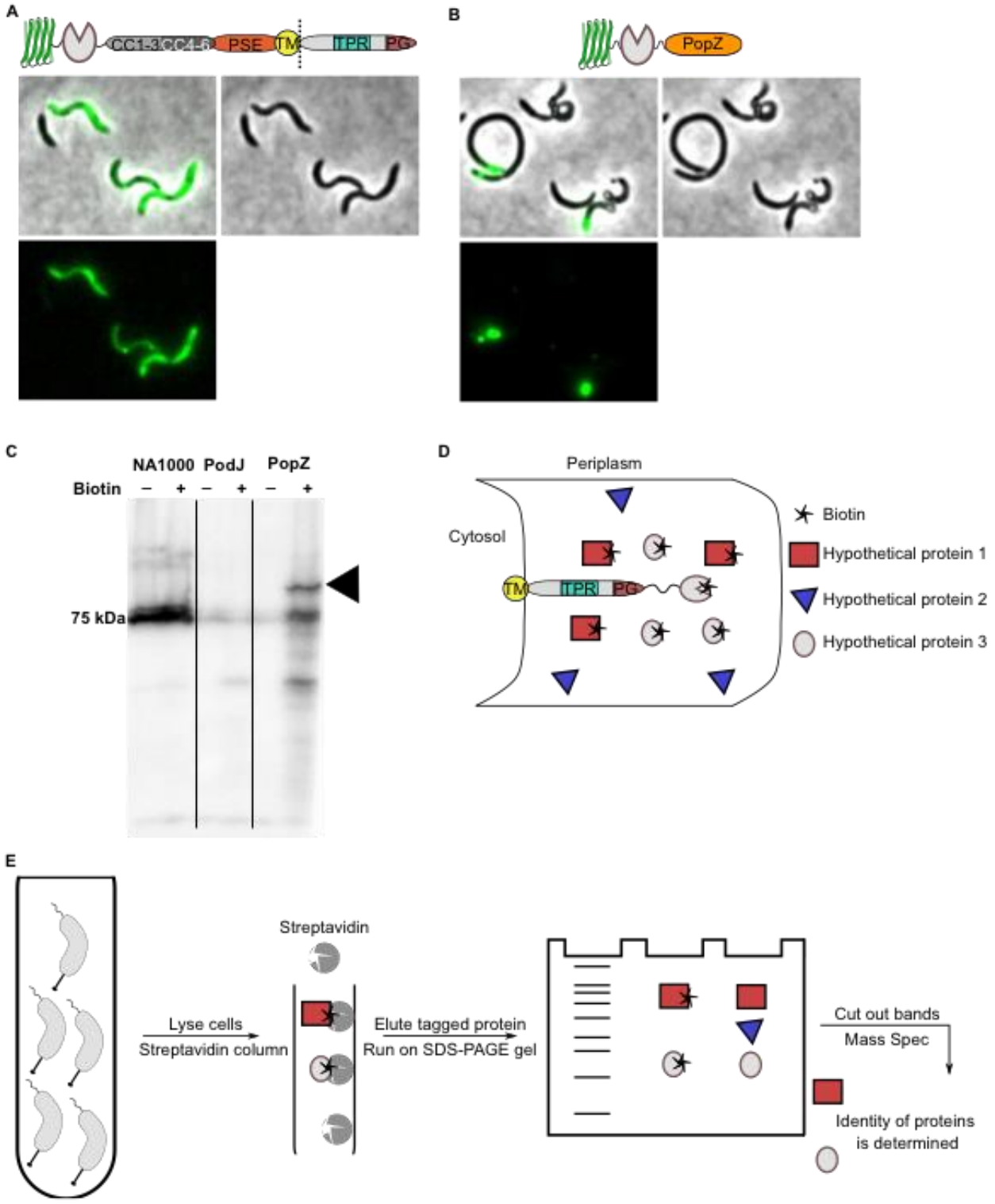

Figure 6–28 TurboID biotinylation using self-assembling proteins.
All cells were grown overnight in PYE to OD_{600} 0.1-0.2. Expression was induced for 5 hours using a final concentration of 0.3% xylose. Cells were imaged on a 1% agarose pad on the Nikon T*i*E using Phase-Contrast and GFP filter sets and settings (see Methods). A) Cells expressing sfGFP-TurboID-PodJ from a high copy, xylose inducible vector. B) Cells expressing sfGFP-TurboID-PopZ from a high copy, xylose inducible vector. C) Western

blot using HRP labeled streptavidin to detect biotinylated proteins. See Methods for experimental setup. NA1000 cells with no plasmid were used a negative control for background biotinylation by native biotin ligase in *C. crescentus*. Black triangle indicates presence of band not seen in negative control. D) Cartoon schematic for future biotinylation of periplasmic proteins. E) Cartoon flow chart showing process to go from biotinylation *in vivo* to identification of biotinylated targets.

The PopZ fusion did localize and displayed the classic "plug" phenotype for PopZ overexpression (Figure 6–28B). After confirming the fluorescence of both, we split cultures and added either 0 µM biotin or 50 µM biotin. Cells were then grown overnight and harvested the next day. NA1000 was used as a control for background biotinylation. We probed for biotinylated proteins by following a standard western blotting protocol. Instead of using antibodies, we exposed blots to HRP labeled streptavidin (ProteinTech). NA1000 produced similar band profiles for plus and minus biotin conditions (Figure 6–28C). The large band at 75 kDa is likely due to biotinylation by the native BirA gene CCNA_02014 which contains both conserved sequences related to biotinylation.[341] The 75 kDa band could be the target of this BirA, CCNA_01960, the biotin carbonyl carrier protein, which is the traditional target of BirA in *E. coli*, though further analysis to determine the exact identity will be required.[341] PodJ shows no biotinylation, likely due to lack of localization in cells. PopZ does show the appearance of a new band (marked by the black triangle, Figure 6–28C) indicating we are likely seeing biotinylation due to TurboID. In addition to localization, this represents a good first step towards using this technology in *C. crescentus*. Future work will involve generating more TurboID fusions of PodJ by removing sfGFP and instead including a 6xHis tag or 3xFLAG tag in order to complete immunofluorescence studies of TurboID-PodJ constructs since sfGFP labeling appears to have a negative effect. TurboID will also be moved to the C-terminal end of PodJ in order to generate fusions that can label periplasmic factors related to PodJ. Biotinylation in the periplasm has been reported, though at lower labeling rates.[342] Once localization is confirmed, conditions will be optimized for biotin labeling. This will be followed by the workflow in Figure 6–28E, where cells will be lysed, and lysate will be passed

through a streptavidin column to pull-down biotinylated proteins. Elutions will be run on gels, stained using Coomassie Blue or blotted with streptavidin-HRP, and bands that appear in both will be excised and sent for mass spectroscopic (MS) analysis (in-gel digestion followed by LC-MS/MS). We will collaborate with the BioMS Center at the University of Pittsburgh for mass spectroscopy and help troubleshooting optimizing conditions. By working on PopZ and PodJ in tandem, if the PodJ periplasmic work fails, we can still show what targets PopZ biotinylates, potentially discovering new PopZ microdomain occupants.[273]

6.5.4 *C. crescentus* unnatural amino acid incorporation

Unnatural amino acid (UAA) incorporation has proven to be a powerful tool for studying biological systems.[343] UAA mutagenesis was developed by Schultz and others in order to expand the functionality of amino acids to unlock new chemistries.[344] By using an orthogonal transfer ribonucleic acid (tRNA) synthetase/tRNA pair and a gene of interest containing a stop codon for UAA placement, UAAs can be incorporated in a protein of interest (Figure 6–29).

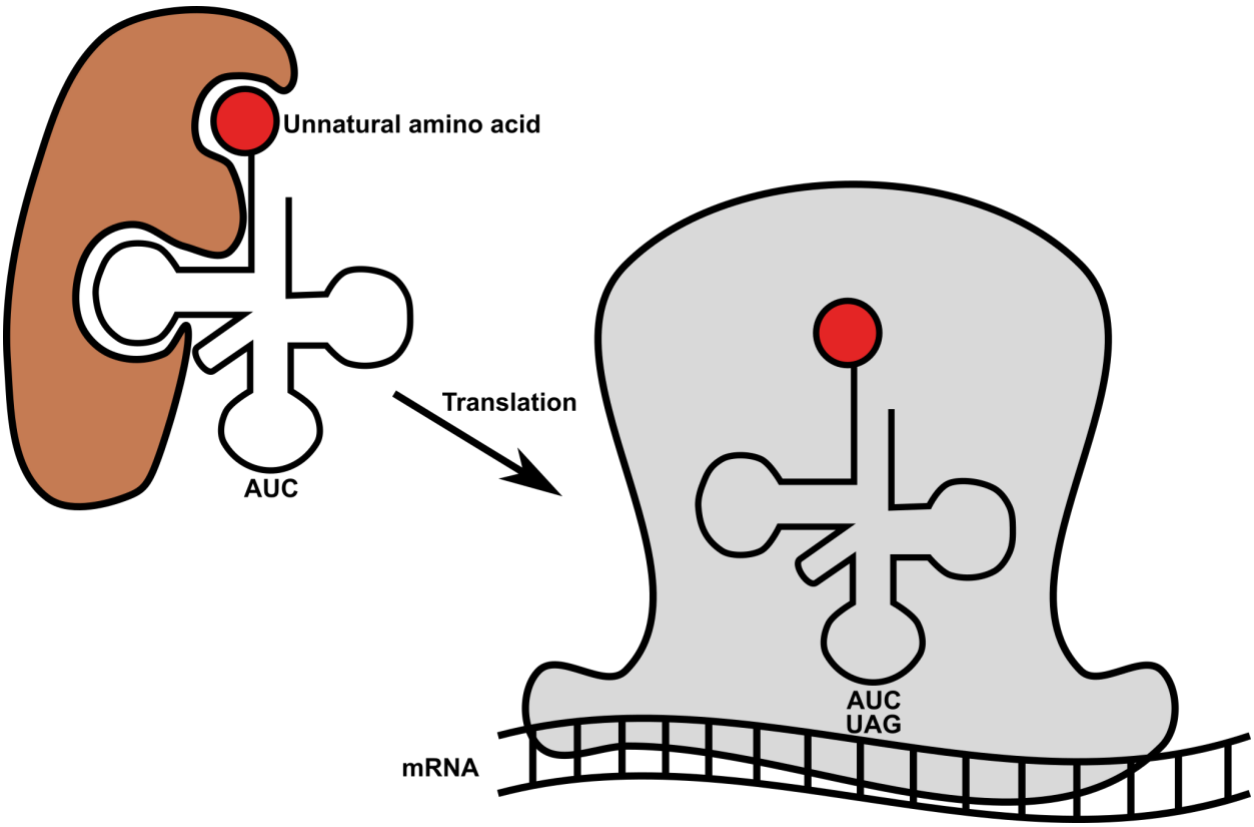

Figure 6–29 Unnatural amino acid incorporation.
A tRNA harboring a stop codon recognition site of AUC is charged with a UAA by a paired synthetase (brown) that recognizes both the UAA and tRNA. After charging, the tRNA recognizes the UAG codon on a translating mRNA strand and it's UAA is incorporated into the polypeptide chain by the ribosome (gray).

Optochemical control and biorthogonal handles have proven to be of great use when studying biological questions.[345,346] Current UAA systems are used in *E. coli*[343], human cell lines[347], and *Caenorhabditis elegans*,[348] to name a few. UAA incorporation has also been done in *C. crescentus*.[349] Ko, *et al.* were able to show that read-through of stop codons in *C. crescentus* was possible. This identified two important features in this system: the *E. coli* HisRS/$tRNA^{His}_{CUA}$ pair suppressed amber codons in *C. crescentus* and was orthogonal.[349] The authors outlined a future for UAA in *C. crescentus* including recombinant protein production and secretion using RsaA pathways[350] and for studying cell-cycle questions using optochemical and labeling tools. What remained to be developed was a more robust system for stop codon read-through. The authors were only able to restore 4% of fluorescence for $mCherry_{22TAG}$ compared to wild-type

mCherry expressed under the same xylose promoter.[349] Due to the immense possibilities for genetic code expansion in *C. crescentus*, we wanted to continue develop a system for robust stop codon read-through. We decided on using the pBK system from *E. coli* as inspiration.[343] The pBK system utilizes expression of the gene of interest under the arabinose promoter (P_{ara}) and an evolved pyrrolysyl-tRNA (pylT) synthetase/tRNA pair to incorporate allyloxycarbonyl lysine (AllocK) (Figure 6–30A).[351]

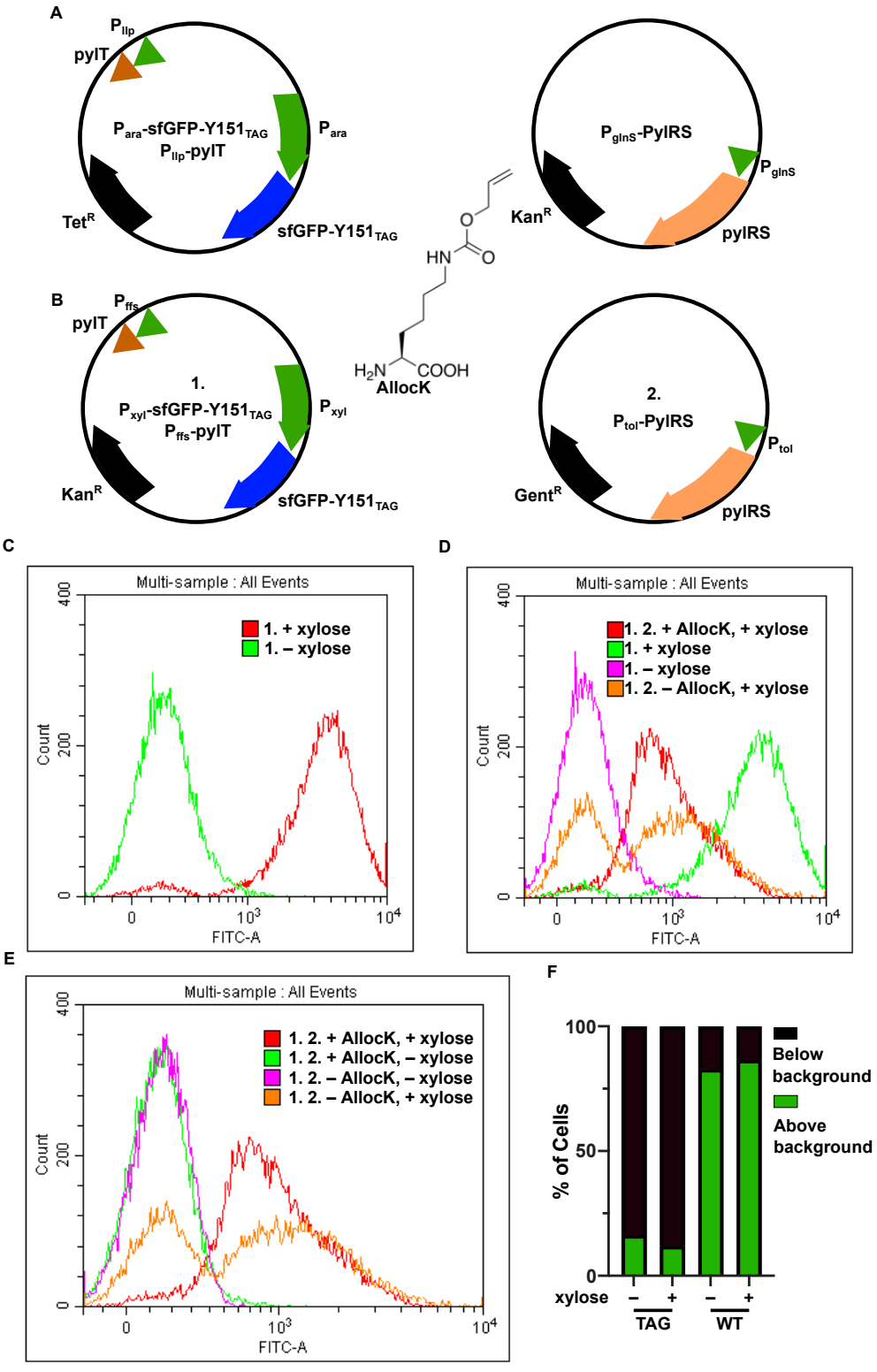

Figure 6–30 Plasmid system and flow cytometry data of UAA incorporation into sfGFP-Y151$_{TAG}$.
A) pBK plasmid system used to incorporate AllocK (inlaid). B) Two plasmid system for UAA incorporation in *C. crescentus* to incorporate AllocK. C) Flow cytometry distributions for plasmid 1 only with or without xylose. Cells were grown overnight in M2G containing antibiotics at 28ºC to OD_{600} 0.1-0.2. Expression was induced for 3 hours

using a final concentration of 0.3% xylose. See Methods for flow cytometry details. D) Flow cytometry distributions for plasmid 1 or plasmid 1 and 2, with and without xylose, and with and without AllocK. For trials ± AllocK, cells were grown overnight in M2G at 28ºC to OD_{600} 0.1-0.2. AllocK lysine was added at a final concentration of 0.5 mM. Cells were grown at 28ºC for 30 minutes. After 30 minutes, a final concentration of 0.3% xylose was added and cells were grown overnight at 20ºC. See Methods for flow cytometry details. E) Two plasmid system flow cytometry distributions for ± AllocK, ± xylose. See Methods for flow cytometry details. F) Percent of cells with or without green fluorescence above background for sfGFP-Y151TAG or sfGFP, ± xylose. Cells were grown overnight in PYE containing antibiotics at 28ºC. Cells were diluted into PYE containing antibiotics to an OD_{600} 0.1-0.2. Expression was induced for 3 hours using a final concentration of 0.3% xylose. Cells were manually counted for green fluorescence above background.

The system consists of two plasmids. The first plasmid contains the sfGFP-$Y151_{TAG}$ gene of interest under the P_{ara} promoter. The pylT tRNA with the CUA stop codon recognition site is included on this plasmid under the P_{llp} promoter, a constitutive promoter in *E. coli* for expression of murein lipoprotein.[352] The synthetase is contained on a second plasmid under the constitutive *glnS* promoter.[353] By using a two plasmid system, one can ensure there are high levels of tRNA and synthetase before addition of UAA. Once the UAA is added, charging of the tRNA by the synthetase occurs. After sufficient time, the gene of interest can be expressed resulting in UAA incorporation. We mimicked this system by creating two plasmids in a similar manner. We used the high copy, replicating plasmid pBXMCS-2 in order to house the sfGFP-$Y151_{TAG}$ under control of xylose (Figure 6–30B).[169] In a non-coding region of the plasmid, we inserted the pylT sequence under control of the *ffs C. crescentus* promoter.[349] This plasmid is referred to as plasmid 1. We then utilized a second high-copy plasmid with the *tol* promoter controlling expression of PylRS. *tol* is a strong constitutive promoter in *C. crescentus*.[354] This plasmid is referred to as plasmid 2. This system also incorporates AllocK. To start testing this system, we used flow cytometry to monitor the expression levels of sfGFP-$Y151_{TAG}$ from plasmid 1 alone. Cells were grown overnight in HiGG media (see Methods), a minimal media used for *C. crescentus* growth, to OD_{600} of 0.2. sfGFP expression was induced using 0.3% xylose for 2 hours. 100 µL of cells were pelleted and resuspended in 1 mL of phosphate buffered solution (PBS). Samples were run using the 510/20 filter set on the Beckman Coulter Cytoflex S to monitor sfGFP levels at 15,000 counts per sample.

We observed that the with the addition of xylose, background expression of sfGFP-Y151$_{TAG}$ was observed (Figure 6–30C). This result was striking because it indicates that *C. crescentus* is able to naturally read-through the UAG stop codon. To determine if the addition of the synthetase or AllocK could produce any background suppression, we repeated the experiment with the two-plasmid system (Figure 6–30D). For these experiments, AllocK was added to a final concentration of 0.5 mM and cells were returned to the incubator for 30 minutes. sfGFP-Y151$_{TAG}$ expression was induced overnight at 20ºC using 0.3% xylose. This experiment produced an interesting result where the two-plasmid system generated two populations. Without AllocK, but with xylose, we observed a distribution indicative of two populations: no expression, and expression in roughly equal amounts (Figure 6–30D, orange line). With the addition of AllocK, the population corresponding to no sfGFP signal decreased, and the population with sfGFP increased (Figure 6–30D, red). This increased population was no able to reach the same intensity as the one plasmid system plus xylose (Figure 6–30D, green). This may indicate that the efficiency of incorporation is lower overall when the synthetase is present. We also tested conditions with AllocK and no xylose using the two-plasmid system and observed no background incorporation (Figure 6–30E, green). Additionally, no AllocK and no xylose produced low intensity (Figure 6–30E, purple). Taken together, these results represent two pathways for why sfGFP-Y151$_{TAG}$ expression levels are not zero in the absence of AllocK. The most likely reason is that *C. crescentus* is able to read-through this stop codon (UAG). In *E. coli*, UAG is the least used stop codon. In *C. crescentus*, frequency per thousand usage is UGA (1.5), UAG (1.0), and UAA (0.6). UAG is recognized by release factor 1 (RF1) which also recognizes UAA.[355] Stop codon translation can occur through either misrecognition of an aminoacylated tRNA or through *trans*-translation, where the factor *ssrA* which encodes for transfer-messenger RNA (tmRNA) which enables a stalled ribosome to

"jump" over to the tmRNA. The tmRNA contains a reading frame that the ribosome can read through and terminate, therefore freeing it up to continue translation.[356] Release of nonstop ribosomes is essential in *C. crescentus*.[356] With an influx of stop codon containing sfGFP, cells need to use misrecognition or *trans*-translation in order to remain viable. Misrecognition is more likely than *trans*-translation because we are observing high sfGFP fluorescence by flow cytometry. Wobble base pairing between tRNA and mRNA could occur for the UAG site and result in incorporation of a natural amino acid at the UAG site.[357] The other, less likely option for why we are seeing expression is aminoacylation of the orthogonal tRNA by a native *C. crescentus* synthetase. This would mean that the pylT from Archaea is able to be recognized and charged by a supposedly orthogonal synthetase. It has been reported in *E. coli* that multiple tRNAs are mischarged by native synthetases.[358] To test these two models, we will first express the sfGFP-Y151$_{TAG}$ mutant in the absence of pylT and look for generation of fluorescence. If we observe fluorescence above background, this will indicate tRNA mismatch. We will then isolate sfGFP-Y151$_{TAG}$ from *C. crescentus* on a gel and determine mass using in-gel digestion followed by mass spectrometry. If the mass matches or differs from the expected mass, it would further confirm incorporation of an amino acid at the UAG site. In addition, the amino acid identity could be determined. Lack of fluorescence would indicate that pylT is required. We could then isolate sfGFP-Y151$_{TAG}$ expressed with pylT and isolate by gel followed by in-gel digestion and mass spectrometry. This would be able identify which amino acid is being incorporated and answer which synthetase is charging pylT. Either way, optimization of the system will be required. One way to optimize is to change the stop codon recognition from UAG to UAA, the least used stop codon in *C. crescentus*. Using the least used stop codon could decrease background readthrough. In addition, expression levels of the pylT and sfGFP-Y151$_{TAG}$ could be modulated down by using

a lower copy plasmid. We will also optimize growth conditions, including media. Once this optimization is done, we can return to AllocK incorporation and repeat it, followed by isolation and in-gel digestion of sfGFP-Y151$_{TAG}$ and mass spectrometry to confirm incorporation. These steps will then enable us to incorporate other UAAs that the PylRS is known to incorporate, which include azide and alkyne click groups for labeling. Of interest for studying protein-protein interactions of PodJ, we would aim to incorporate an aliphatic diazirine for protein photocrosslinking. This would enable us to site-selectively label PodJ and crosslink with neighboring proteins, potentially identifying the hydrolase it may associate with.[359] We will also optimize growth conditions, including media. We observed that when growing cells in rich media rather than minimal media, the number of cells containing only plasmid 1 with green fluorescence was about 60% lower than expression of wild-type sfGFP (Figure 6–30F). Cells with TAG mutant that were green displayed a similar maximum intensity to wild type (data not shown). This indicates that only some cells in a population are reading through. After performing a western blot to confirm differences in protein levels, we could isolate these cells by fluorescence-activated cell sorting to isolate cells with high fluorescence. We could follow that with sequencing to determine if these cells harbor mutations that make them more likely to translate a stop codon.[360] This would help with future UAA optimization by identifying elements that could hinder UAA incorporation in the *C. crescentus* background.

6.6 Methods

Growth Conditions: *E. coli* DH5*α* strains were grown at 37 °C with shaking overnight in LB media supplemented with antibiotics (SI Table 6). *C. crescentus* strains were grown in PYE or

M2G media supplemented with antibiotics (SI Table 6) at 28 °C with shaking overnight or for specified times for imaging.

Transformations: 10-50 ng of DNA was transformed into KCM chemically competent cells and plated on LB/agar supplemented with the appropriate antibiotic. Cells were incubated overnight at 37ºC.

Electroporation: *C. crescentus* cells were harvested by centrifuging 4 mL for 5 minutes at 21,100 x g. Supernatant was removed and cells were washed in 100 µL of cold, sterile water and centrifuged for 1 minute at 21,100 x g. This step was repeated 2 more times, followed by suspension of cells in a final volume of 80 µL. Integrating plasmids (12.5 µL) or replication plasmids (3 µL) were then added to the cells and electroporated on the *E. coli* setting of a BioRad GenePulser using 0.1 cm electroporation cuvettes (BioRad). Cells were then resuspended in 1 mL of 2xPYE and shaken at 28 °C for 3 hours, then 100 µL of cells were then plated on PYE/antibiotic plates. The remaining cells were pelleted, resuspended in 100 µL of 2xPYE, and plated on PYE/antibiotic plates. Cells were grown at 28 °C for 3 days and colonies were streaked onto a PYE/antibiotic plate. Colonies that grew after streaking were screened for using colony PCR (DreamTaq Green) using primers for integration at the xylose locus (RecUni-1, RecXyl-2), vanillate locus (RecUni-1, RecVan-2), or for replicating plasmids (Pvan-for, M13-for) according to the manufacturer's protocol with 5 minute extension times.

Generation of Spheroblasts: *E. coli* cells containing plasmids were grown overnight at 37ºC in LB containing antibiotics. Cells were diluted 1:100 in fresh LB containing antibiotics and grown for 3 hours at 37ºC. MreB inhibitor A22 (Fisher, 50 µM final concentration) was added to induce spheroidal cells. After 5-hours with A-22 inhibitor, cells were imaged on 1% agarose pads containing 100 µM IPTG for protein expression, 50 µM A22, and antibiotics.

***In Vivo* Biotinylation and Blotting:** Cells were grown overnight in PYE containing antibiotics with shaking at 28ºC to OD_{600} of 0.1-0.2. Expression was induced for 5 hours using a final concentration of 0.3% xylose. Cultures were split and either 50 µM or no biotin was then added and cells were grown overnight at 28ºC with shaking. The next day, cells were pelleted and lysed with 4x Sample Buffer and heating at 75ºC for 10 minutes. Samples were loaded onto a 10% resolving SDS-PAGE gel with a 4% stacking gel. Loading volumes were normalized using OD_{600}. The ladder used was ThermoFisher Page Ruler Pre-Stained Ladder. Gels were run at 150V for 1 hour. Transfer was done using ThermoFisher Mini Blot Module with a PVDF transfer membrane for 2 hours at 20 V and 4 °C. After transferring blots were washed with TBST 3 times for 5 minutes each. Streptavidin conjugated to HRP (ProteinTech) was used at 1:1000 concentration in TBST to recognize biotinylated bands. Blots were exposed to chemiluminescent substrate (SuperSignal West Pico PLUS Chemiluminescent Substrate) and imaged using the Chemi Hi Resolution setting on a BioRad ChemiDoc with auto exposure for intense bands.

Imaging Conditions: *C. crescentus* strains for single time point imaging were grown overnight in M2G media supplemented with antibiotics to an OD_{600} 0.1-0.2. If cells required expression from a xylose or vanillate inducible vector, they were then induced with xylose (0.03% w/v) or vanillate (0.05 mM) for 3 hours. If cells were grown to induce ectopic pole formation, 0.3% xylose final concentration was used and cells were grown for 5 + hours. 2 µL of cells were deposited on a 1% agarose/M2G pad on a glass slide and covered with a glass coverslip. *E. coli* strains used for single time point imaging were grown overnight in LB media supplemented shaking at 37ºC with antibiotics to saturation. Cultures were then diluted at a 1:100 ratio into fresh LB supplemented with antibiotics. Cultures were grown to an OD of 0.2 (~ 2 hours). Induction of IPTG inducible vectors was completed using a final concentration of 100 µM IPTG.

Microscopy: Images were taken on a Nikon T*i*E inverted setup using an APO Lambda 100X oil objective with Phase Contrast or Differential Interference Contrast (DIC) using Zeiss Immersol 518F Immersion Oil using Nikon Element AR software to control the setup. A halogen lamp was used for the white light source. Spectra X light engine was used for all fluorescence excitation. An Andor Ixon Ultra 897 EMCCD camera was used for all imaging. All filter sets used were purchased from Chroma. CFP/YFP/mCherry (77074157) and GFP (77074160) filter cubes were used with emission filter sets GFP (77074161) and CFP/YFP/mCherry (77074158).

Foci Per Cell Analysis: Image analysis was completed in MicrobeJ[166] using the Maxima feature as a point. Each condition was thresholded for maxima above background. Patches were counted as one focus.

Fluorescence Intensity Profile Analysis: For *C. crescentus*, sfGFP-PodJ variants expressing mCherry-PopZ from the native *popZ* promoter were imaged using the above methods. After imaging, predivisional cells expressing sfGFP-PodJ variants were oriented by visualization of the stalk. The average fluorescence intensity profile using normalized cell length was generated using MicrobeJ[166] with the new pole at 0.0 and old pole at 1.0. *E. coli* analysis was done in the same manner expect cells were not oriented.

Curvature Platform Generation: Method taken directly from Renner *et al.*[330] We designed patterns of microchannels and microchambers in CleWin (Delta Mask, The Netherlands) and incorporated them into a chrome mask. Using photolithography, we transferred the pattern from the mask into a 2.7-µm thick layer of Shipley photoresist 1827 that was cast on a silicon wafer; the resulting pattern was embossed into the photoresist. We silanized the resulting photoresist master for 8 h using a vapor of (tridecafluoro-1,1,2,2-tetrahydrooctyl)trichlorosilane (Gelest, Inc., Morrisville, PA). Using soft lithography[361], we transferred the pattern into the

silicone elastomer, polydimethylsiloxane (PDMS) (Sylgard 184, Dow Corning) using a ratio of 10:1 (base to curing agent), and cured the polymer overnight at 60°C. The resulting PDMS layer contained patterns of microchannels or microchambers in bas-relief and was used as a stamp to emboss a layer of agarose or agar.[362] We poured a hot solution of 3% agarose or agar containing IPTG and antibiotics (as needed) on PDMS stamps oriented with the features facing up, and cooled them to 25°C to gel the agarose. We cut out the layer of agarose embossed with microchannels or microchambers using a razor blade, added a suspension of bacteria (3–5 μL) to the top surface of the agarose, and trapped cells in the microstructures by placing a glass cover slip in contact with the gel. Using this procedure, we created a pattern of microchannels consisting of six repetitive structures that had a channel length of ~30 μm, a height of 2.7 μm, a width of 1.6 or 2.5 μm, and a central angle of 30°, 45°, 60°, 90°, 120°, or 180°. Bacteria growing in these channels became 'bent' at the mid-cell and adopted a new region of cell wall curvature corresponding to 1, 0.54, 0.47, 0.29, 0.145 or 0 μm^{-1}, respectively.

Curvature Platform Cell Conditions: *E. coli* BL21 containing plasmids were grown overnight at 37ºC in LB containing antibiotics. Cells were diluted into fresh LB containing antibiotics at a 1:100 ratio. Cells were grown for one hour at 37ºC at which point expression was induced using a final concentration of 100 μM IPTG. Cells were then grown for two hours at 37ºC and a final concentration of 25 μg/mL cephalexin was added to induce filamentation. Cells were shaken for five minutes at 37ºC after addition and were added to prepared agarose microchannels containing 100 μM IPTG and 25 μg/mL cephalexin. 5 μL of cells were added to the agarose microchannels and dried under flame for 60 seconds. After a glass coverslip was fixed in place and sealed with wax, the slide was placed in the 37ºC incubator for 1 hour. Cells were then imaged using standard imaging conditions.

Unnatural Amino Acid (UAA) Incorporation: Cells were grown overnight in either M2G or PYE to an OD_{600} of 0.1-0.2. For trials without UAA, a final concentration of 0.3% xylose was used for expression. Cells with UAA were grown with AllocK (0.5 mM final concentration) for 30 minutes at 28ºC with shaking. Expression with 0.3% xylose was then completed overnight with shaking at 20ºC. Cells were then pelleted and resuspended in 1 mL PBS. Cells were then serially diluted into PBS until the abort rate was below 5%. A Cytoflex S (Beckman-Coulter) using a 488 nm laser with a FitC filter (525 nm) was used. Cells were selected using FSC-H and SSC-H gained to 10 and 20, respectively. 10000 events were collected flowing at 10 µL per minute with an abort rate of less than 5%.

Purification of PodJ: Protein expression of all PodJ variants followed the same protocol and is described in detail below for PodJ (1-635) for size exclusion chromatography, native gel electrophoresis, and droplet formation assay. To purify the cytoplasmic portion of PodJ(1-635), Rosetta (DE3) containing plasmid pwz091 was grown in 6 liters LB medium (20 µg/ml chloramphenicol and 100 µg/ml ampicillin) at 37°C. The culture was then induced at an OD_{600} of 0.4–0.6 with 0.5 mM IPTG overnight at 18°C. The cells were harvested, resuspended in the lysis buffer (50 mM Tris-HCl, 700 mM KCl, 20 mM Imidazole, 0.05% dextran sulfate, pH 8.0), in the presence of protease inhibitor cocktail tablets without EDTA (Roche). The cell suspension was lysed with three passes through an EmulsiFlex-C5 cell disruptor (AVESTIN, Inc., Ottawa, Canada), and the supernatant was collected by centrifuging at 13000 *g* for 30 min at 4°C. Also, the insoluble cell debris was resuspended by the recovery buffer (50 mM Tris-HCl, 1000 mM KCl, 20 mM Imidazole, 0.05% dextran sulfate, pH 8.0) and its supernatant was collected as well as the previous centrifugation. The combined supernatants were loaded onto a 5 ml HisTrap™ HP column (GE Healthcare) and purified with the ÄKTA™ FPLC System. After washing with 10

volumes of wash buffer (50 mM Tris-HCl, 300 mM KCl, and 25 mM imidazole, pH 8.0), the protein was collected by elution from the system with elution buffer (50 mM Tris-HCl, 300 mM KCl, and 500 mM imidazole, pH 8.0), and concentrated to a 3 ml volume using Amicon Centrifugal Filter Units, resulting in > 95% purity. All PodJ variants were dialyzed with a buffer containing 50 mM Tris-HCl (pH 8.0), 300 mM KCl, and then aliquoted to a small volume (100 µl) and kept frozen at -80°C until use.

Size-Exclusion Chromatography and Native Gel Assay: A gel filtration standard (Sigma) containing thyroglobulin (bovine, 669 kDa), carbonic anhydrase (bovine, 29 kDa), blue dextran (2,000 kDa), apoferritin (horse, 443 kDa), β-Amylase (sweet potato, 200 kDa), alcohol dehydrogenase (yeast, 150 kDa), and albumin (bovine, 66 kDa) were used to generate a molecular weight standard plot using a Superdex 200 10/300 GL column (GE Healthcare). A 3.2 mg/ml sample of His-PodJ(1-635) was loaded onto the column and peaks eluted after 7.9 ml, 12.8 ml, and 15.0 ml of buffer, corresponding to a molecular weight of 1,851 kDa, 194 kDa, and 70.7 kDa (theoretical monomer = 73.0 kDa). One representative result of triplicates was shown. His-PodJ(1-635) was also analyzed by running a native gel. Protein was separated by gel electrophoresis (8% resolving gel) at 80 V for at least 4 hours at 4^{o}C, using a native protein ladder (range from 66 to 669 kDa, Thermo Fisher). The same protocols were used for PodJCC4-6 and PodJPSE

Droplet Formation Assays: PodJ-sfGFP(1-635), PodJ-sfGFP(250-635), and sfGFP protein aliquots were thawed on ice along with solutions of PEG(8000), NaCl, Tris-Cl pH 8.0 ,and DNase/RNase-free water. All non-protein solutions were passaged through a 0.2 mm cellulose acetate syringe filter (VWR) and were stored in polypropylene 1.7 mL or 2.0 mL tubes (VWR). Working solutions of PodJ-sfGFP, Tris-Cl, and NaCl were combined, diluted with sterile-filtered DNase/RNase-free water to various concentrations, and allowed to incubate on ice for no more

than 15 minutes prior to imaging. Microscope slides were fitted with a SureSeal Spacer (EMS) before being filled with 10 µL of protein solution and sealed with a glass coverslip. All images were taken with an Eclipse Ti-E inverted microscope (Nikon) in both phase-contrast and fluorescent channels using a Plan Apo 100x/1.45 oil objective.

Sequence Alignment and Model Generation: NCBI Protein BLAST[318] was used to align the PG binding domains of KZ144[316], $PodJ_{CC}$, and $PodJ_{AT}$. SWISS-MODEL Expasy[320] was used to generate a model of the $PodJ_{CC}$ PG-binding domain with PDB:4C2H serving as the template.

Construction of Plasmids: Plasmids utilized in this study are in Table 6–1. Plasmid assembly procedures are located in Table 6–2. The lists of oligonucleotides used in this study can be found in Table 6–3. All oligos were ordered from IDT. The strains used can be found in Table 6–4 and methods to generate strains were listed above. Phusion polymerase (ThermoFisher) was used for amplification of PCR products used in Gibson assembly and isolated using gel electrophoresis using a 1% agarose, 1xTAE gel with ethidium bromide added for visualization by UV light. Band sizes were determined using a GeneRuler 1 kb DNA Ladder (ThermoFisher). Bands were excised from the gel and extracted using a GeneJet Gel Extraction Kit (ThermoFisher) following manufacturer's protocols, with the addition of a 100 µL binding buffer wash step following the spin through of DNA/agarose/binding buffer. Water was used for elution. DNA concentrations were determined using a NanoDrop 2000 spectrophotometer (Thermo Scientific). All reactions were done according to the manufacturer's protocols with annealing temperature at 55 °C for 30s, unless otherwise noted. KOD Hot Start Polymerase (Millipore) was used for Quikchange PCR according the manufacturer's protocols and 10 minute extension times. DpnI (Thermofisher) was used to degrade template after reaction was finished. 5 µg of vector was digested at a time using the manufacturer's protocol and isolated the same way as PCR products

(above). If a single restriction enzyme was used, FastAP (ThermoFisher) was used to decrease occurrence of reannealing.

Plasmids: Below is an example of generation of plasmid using the Gibson assembly method and the corresponding table. This can be used as a guide to understand the remainder of plasmids constructed using the Gibson assembly method. Plasmids for Gibson assembly method were designed using J5.[167] All Gibson reaction buffers were made using Phusion polymerase (ThermoFisher), Taq ligase (NEB), and T5 exonuclease (NEB).[168] The plasmid pSWD225 encodes a xylose-inducible copy of sfGFP-PodJCC1-3 linked by a GGSGS linker. The vector pXCFPC-2 was linearized by double digestion with the restriction endonucleases NheI and SacI. PCR products with overhangs for Gibson assembly were generated following the schematic below at a 100 ng scale Gibson reaction scale. Two inserts were generated by PCR that include sfGFP amplified using SWD700 and SWD701 from pSR58.6.[363] Codons 1-249 of *podJ* were amplified by PCR using plasmid pSWD183 (full length PodJ) as a template with primers SWD702 and SWD703, The linearized pXCFPC-2 and both inserts were combined at 100 ng reaction scale and incubated at 50°C for 60 min in a reaction mixture containing T5 exonuclease, Phusion DNA polymerase, and Taq ligase (NEB). 5 µL of the reaction mixture was transformed into KCM competent DH5α *E. coli* cells and plated on LB/agar supplemented with the appropriate antibiotic. Colonies were screened using primers Pxyl-for Thanbichler, *et al.* [169] and M13-for[169] using DreamTaq PCR with a 5 minute extension time. After electroporating in *C. crescentus* cells, colonies were screened using RecXyl-2 and RecUni-1 primers.[169]

6.7 Tables

Table 6–1 Plasmids utilized in this study by appearance in the text.

Name	Description	Reference
pWZ98	pTEV5-CC4-6(250-430)	This study
pWZ96	pTEV5-PSE(471-635)	This study
pWZ91-6	pTEV5PodJ(1-635)	This study
pCZ10388	pTEV5-sfGFP-HRSAT-podJ(1-635)	This study
CZ703	pTEV5-sfGFP-podJDCC1-3 (250-6350	This study
pCZ221	pTEV5-sfGFP	This study
pWZ012	pCDF-YFP-podJ	Chapter 5
pWZ046	pBAD-CFP-PopZ	This study
podJ30	pCDF-mCherry-podJTM(657-702)	This study
podJ23	pCDF-YFP-podJ(1-635)	This study
podJ02	pCDF-YFP-podJ(1-702)	This study
pWZ0202	pCDF-YFP-podJ(42-702)	This study
podJ19	pCDF-YFP-podJ(128-702)	This study
podJ20	pCDF-YFP-podJ(170-702)	This study
podJ21	pCDF-YFP-podJ(250-702)	This study
podJ-delta-250-430	pCDF-YFP-podJ(D250-430)	This study
pWZ94	pCDF-YFP-podJ(250-430)	This study
podJ17	pCDF-YFP-podJ(1-470,643-702)	This study
podJ08	pCDF-mCherry-podJ(471-642)	This study
pWZ013	pCDF-mCherry-PodJ	This study
pSWD226	pACYC-YFP-podJCC1-3(1-249)	This study
pSWD225	pXyl-2-sfGFP-podJCC1-3(1-249)	This study
pSWD277	pXyl-2-sfGFP-podJCC1-3-TM(1-249, 643-702)	This study
pSWD268	pXyl-2-sfGFP-podJΔCC1-3-TM(250-969)	This study
pSWD259	pXyl-2-sfGFP-podJΔCC1-3 (250-670)	This study
WZ367	pXyl-2-sfGFP-podJΔCC4-6(1-249,431-969)	This study
WZ366	pXyl-2-sfGFP-podJΔPSE(1-470,636-969)	This study
pBX-mNG-podJ	pBXMCS-2-mNeonGreen-PodJ	This study
pSWD235	pBXMCS-2-sfGFP-podJΔPG(1-920)	This study
pSWD234	pBXMCS-2-sfGFP-podJΔPGgap(1-865)	This study
pSWD233	pBXMCS-2-sfGFP-podJΔperi(1-670)	This study
pSWD271	pBXMCS-2-sfGFP-podJΔCC1-3(250-969)	This study
pSWD270	pBXMCS-2-sfGFP-podJΔCC4-6(1-250,430-969)	This study

pSWD269	pBXMCS-2-sfGFP-podJΔPSE(1-429,643-969)	This study
pSWD236	pBXMCS-2-sfGFP-podJΔcyto(646-969)	This study
pSWD293	pBXMCS-2-sfGFP-TurboID-podJ	This study
pSWD296	pBXMCS-2-sfGFP-TurboID-popZ	This study
pSWD217	pBXMCS-2-sfGFP-ffs-pylT	This study
pSWD217tag	pBXMCS-2-sfGFP151tag-ffs-pylT	This study
pSWD218	pBVMCS-4-ptol-pylRS	This study

Table 6–2 Assembly of plasmids for this study by name, then number order.

Plasmid	**Insert Description**	**Forward Primer**	**Reverse Primer**	**Template**	**Screening primers**
pCZ10388	pTEV5	CZ10944	CZ10964	pTEV5	nSWD81, nSWD82
	msfGFP	CZ10965	CZ10966	msfGFP	
	podJ (1-635)	CZ10948	CZ10949	*podJ*	
CZ703	Quikchange	CZ-msfGFP-dCC1-3-F	CZ-msfGFP-dCC1-3-R	pCZ10388	nSWD81, nSWD82
pCZ221	pTEV5	CZ10514	CZ10515	pTEV5	nSWD81, nSWD82
	msfGFP	CZ10516	CZ10517	msfGFP	
pWZ91-6	pTEV5			pTEV5	nSWD81, nSWD82
	PodJ(1-635)	WZH346	WZH347	*podJ*	
pWZ98	pTEV5			pTEV5	nSWD81, nSWD82
	PodJCC4-6(250-430)	WZH352	WZH353	*podJ*	
pWZ96	pTEV5			pTEV5	nSWD81, nSWD82
	PodJPSE(471-635)	WZH348	WZH349	*podJ*	
pWZ012	EYFP	WZ0025	WZ0010	pXYFPC-6	T7_for, T7_ter
	PodJ	WZ0011	WZ0026	*podJ*	
	pCDFDuet-1	NdeI			
podJ23	Quikchange	WZ304	WZ305	pWZ012	T7_for, T7_ter
podJ02	Quikchange	WZ184	WZ185	pWZ012	T7_for, T7_ter
pWZ0202	Quikchange	WZH684	WZH685	pWZ012	T7_for, T7_ter
podJ19	Quikchange	WZ296	WZ297	pWZ012	T7_for, T7_ter
podJ20	Quikchange	WZ298	WZ299	pWZ012	T7_for, T7_ter
podJ21	Quikchange	WZ300	WZ301	pWZ012	T7_for, T7_ter

podJ-delta-250-430	Quikchange	podJ-detalCC-F	podJ-detalCC3-R	pWZ012	T7_for, T7_ter
pWZ94	Quikchange	WZ0228	WZ0229	pWZ012	T7_for, T7_ter
podJ17	Quikchange	WZ338	WZ339	pWZ012	T7_for, T7_ter
pWZ013	mCherry	WZ0027	WZWZ0010	pXCHYC-6	T7_for, T7_ter
	PodJ	WZ0011	WZ0026	*podJ*	
	pCDFDuet-1	NdeI			
podJ08	pCDFDuet-1	WZ0135	WZ0136	pWZ013	T7_for, T7_ter
	PodJ(471-642)	WZ0137	WZ0138	*podJ*	
podJ30	Quikchange	WZH454	WZH455	pWZ013	T7_for, T7_ter
pWZ046	pBAD	WZ0099	WZ0051	pBAD	
	ECFP	WZ0052	WZ0103	ECFP	
	PopZ	WZ0104	WZ0105	popZ	
WZ366	Quikchange	WZH568	WZH569	pXYFPN-2-Pxyl-sfGFP-PodJ	WZ144-podJ-1520-F, WZ145-podJ-2522-R
WZ367	Quikchange	WZH570	WZH571	pXYFPN-2-Pxyl-sfGFP-PodJ	WZ144-podJ-1520-F, WZ145-podJ-2522-R
pBX-mNG-podJ	pBXMCS-2	WZ0277	WZ0278	pBXMCS-2	Pxylf-for, M13-for
	mNG-PodJ	WZ0279	WZ0280	pXYFPN-2-PpodJ-nNG-PodJ	
pSWD217/pSWD217tag	pBXMCS-2 region 1	SWD668	SWD669	pBXMCS-2	Pxyl-for, M13-for
	sfGFP/sfGFP151tag	SWD670	SWD671	ptyl-sfGFP/ptyl-sfGFP151tag	
	pBXMCS-2 region 2	SWD672	SWD673	pBXMCS-2	
	pylT_rrnc_terminator/SOE	SWD674	SWD675	pBAD_Myo4TAG_py	
	ffs_promoter/SOE	SWD676	SWD677	ffs_promoter, NA1000	
pSWD218	pBVMCS-4-ptol	SWD678	SWD679	pSWD195	nSWD109, nSWD110
	pylRS	SWD680	SWD681	EV1	

pSWD225	sfGFP	SWD700	SWD701	sfGFP, pSR58.6[363]	Pxyl-for, M13-for
	PodJCC1-3	SWD702	SWD703	podJ (pSWD183)	
	pXCFPC-2_SacI_NheI				
pSWD226	pACYC-EYFP-hrsat	SWD704	SWD705	pWZ054	
	PodJCC1-3	SWD589	SWD706	podJ (pSWD183)	
pSWD233	pBXMCS-2	SWD715	SWD716	pBXMCS-2	Pxyl-for, M13-for
	sfGFP	SWD717	SWD701	sfGFP, pSR58.6	
	PodJ(1-670)	SWD702	SWD718	podJ (pSWD183)	
pSWD234	pBXMCS-2	SWD719	SWD716	pBXMCS-2	Pxyl-for, M13-for
	sfGFP	SWD717	SWD701	sfGFP, pSR58.6	
	PodJ(1-865)	SWD702	SWD720	podJ (pSWD183)	
pSWD235	pBXMCS-2	SWD721	SWD716	pBXMCS-2	Pxyl-for, M13-for
	sfGFP	SWD717	SWD701	sfGFP, pSR58.6	
	PodJ(1-920)	SWD702	SWD722	podJ (pSWD183)	
pSWD236	pBXMCS-2	SWD723	SWD724	pBXMCS-2	Pxyl-for, M13-for
	sfGFP	SWD717	SWD725	sfGFP, pSR58.6	
	PodJ(646-969)	SWD726	SWD727	podJ (pSWD183)	
pSWD259	sfGFP	SWD700	SWD790	sfGFP, pSR58.6	Pxyl-for, M13-for
	PodJ(250-635)	SWD791	SWD792	podJ (pSWD183)	
	pXCFPC-2_SacI_NheI				
pSWD268	sfGFP	SWD700	SWD790	sfGFP, pSR58.6	Pxyl-for, M13-for
	PodJ(ΔCC1-3)	SWD807	SWD590	podJ (pSWD183)	
	pXCFPC-2_SacI_NheI				
pSWD269	pBXMCS-2	SWD808	SWD809	pBXMCS-2	Pxyl-for, M13-for
	sfGFP-PodJΔ471-635	SWD753	SWD727	WZ367	

pSWD270	pBXMCS-2	SWD808	SWD809	pBXMCS-2	Pxyl-for, M13-for
	sfGFP-PodJΔ250-470	SWD753	SWD727	WZ366	
pSWD271	pBXMCS-2	SWD808	SWD809	pBXMCS-2	Pxyl-for, M13-for
	sfGFP-PodJ250-969	SWD753	SWD727	pSWD268	
pSWD277	sfGFP	SWD700	SWD701	sfGFP, pSR58.6	Pxyl-for, M13-for
	PodJ(1-250)	SWD702	SWD819	podJ (pSWD183)	
	PodJ(643-702_	SWD820	SWD821	podJ (pSWD183)	
pSWD293	pBXMCS-2-sfGFP	SWD870	SWD871	pSWD233	Pxyl-for, M13-for
	TurboID	SWD872	SWD873	TurboID-His6_pET21a[339]	
	PodJ	SWD589	SWD874	podJ (pSWD183)	
pSWD296	pBXMCS-2-sfGFP	SWD883	SWD884	pSWD233	Pxyl-for, M13-for
	TurboID	SWD885	SWD886	TurboID-His6_pET21a	
	PopZ	SWD585	SWD887	popZ	

Table 6–3 DNA primers utilized in this study by name, then number order.

Name	**Sequence (5'-3')**
CZ10944_(pTEV5-bb)_forward	CGAAGGCGCGCTTGTAAGCTAGCCATATGGCCATGGA
CZ10964_(pTEV5-bb)_(S)_reverse	GGTGAACAGTTCTTCACCTTTAGACATGCCCTGAAAATACAGGTTTTCACTAGTTGGG
CZ10965_(msfGFP)_forward	TCAGGGCATGTCTAAAGGTGAAGAACTGTTCACCGGTGTTGT
CZ10966_(msfGFP)_(HRSAT)_reverse	CGAAGCCGCCGTCATGGTGGCCGACCGGTGTTTGTAGAGTTCATCCATGCCGTGCGT
CZ10948_(PodJ-1-635)_forward	CCGGTCGGCCACCATGACGGCGGCTTCGCCA
CZ10949_(PodJ-1-635)_reverse	TATGGCTAGCTTACAAGCGCGCCTTCGACTTCTTGGT

CZ-msfGFP-dCC-1-3-F	ACAAACACCGGTCGGCCACCTTGGGCGCCGTCGAGACTGCCAATC
CZ-msfGFP-dCC-1-3-R	GGTGGCCGACCGGTGTTTGTAGAGTTCATCCATGCCGTGCGT
CZ10514_(pTEV5)_forward	GGATGAACTGTACAAATGATGAGCTAGCCATATGGCCATGGAATTCTC
CZ10515_(pTEV5)_reverse	CGCCTTTACGCATGCCCTGAAAATACAGGTTTTCACTAGTTGGGA
CZ10516_(sfgfp)_forward	GTATTTTCAGGGCATGCGTAAAGGCGAAGAGCTGTTCACTGG
CZ10517_(sfgfp)_reverse	CCATATGGCTAGCTCATCATTTGTACAGTTCATCCATACCATGCGTG
WZH346-PTEV5-PODJ1-635-F	GGCGCTAGCATGACGGCGGCTTCGCCATG
WZH347-PTEV5-PODJ1-635-R	GCGGATCCTTACAAGCGCGCCTTCGACTTC
WZH348-PTEV5-PODJ471-635-F	GGCGCTAGCCCGTCGCCGCCGCCCGCGCA
WZH349-PTEV5-PODJ471-635-R	CGCGGATCCTTACAAGCGCGCCTTCGACT
WZH352-PTEV5-PODJ250-430-F	GGCGCTAGCTTGGGCGCCGTCGAGACTGC
WZH353-PTEV5-PODJ250-430-R	CGCGGATCCTTAGCTGGAACGTTCGTGGC
WZ0025	CTTAGTATATTAGTTAAGTATAAGAAGGAGATATAATGGTGAGCAAGGGCGAGGAGC
WZ0010	GGTGGCCGACCGGTGCTTGTACAGCTCGTCCATGCCG
WZ0011	GACGAGCTGTACAAGCACCGGTCGGCCACCATGACGGCGGCTTCGCCATGG
WZ0026	GTGGCCGGCCGATATCCAATTGAGATCTGCTTAGCGCGCGTAGACCGACAGG
T7_for	GGATCTCGACGCTCTCCCT
T7_ter	GCTAGTTATTGCTCAGCGG
WZ304-podj023-f	GGCGCGCTTGTAAGCAGATCTCAATTGGAT
WZ305-podj023-r	GATCTGCTTACAAGCGCGCCTTCGACTTCT
WZ184-podj02-f	GCGCGCCGCCTAAGCAGATCTCAATTGGAT
WZ185-podj02-r	GATCTGCTTAGGCGGCGCGCGGCGCGCCGG
WZH684-podj42-702-f	GTCGGCCACCGGCGATGGTCAGACCGCTGA

WZH685-podj42-702-r	GACCATCGCCGGTGGCCGACCGGTGCTTGT
WZ296-podj19-f	GTCGGCCACCGAGCAGATCGCCGTCGCCGC
WZ297-podj19-r	CGATCTGCTCGGTGGCCGACCGGTGCTTGT
WZ298-podj20-f	GTCGGCCACCTTGCGCGCGCTTGAAGGCGC
WZ299-podj20-r	GCGCGCGCAAGGTGGCCGACCGGTGCTTGT
WZ300-podj021-f	GTCGGCCACCTTGGGCGCCGTCGAGACTGC
WZ301-podj021-r	CGGCGCCCAAGGTGGCCGACCGGTGCTTGT
podj-detalCC3-F	GGATCAGCGCCAGGAACTGGTCGACCGCAT
podj-detalCC3-R	CCAGTTCCTGGCGCTGATCCAGGGCCTGGA
WZ0228_(podj250-430)_forward	CACCGGTCGGCCACCTTGGGCGCCGTCGAGACTGC
WZ0229_(podj250-430)_reverse	CCAATTGAGATCTGCTTAGCTGGAACGTTCGTGGCGTTGG
WZ338-podj17-f	AGCTGCGCCGCTCGTTGTCTTCGCCGCCGC
WZ339-podj17-r	AGACAACGAGCGGCGCAGCTTCCAGCTTCC
WZ0027_(pxchyc-6)_forward	CTTAGTATATTAGTTAAGTATAAGAAGGAGATATAATGGTGAGCAAGGGCGAGGAGG
WZ0010_(PCDF-YFP)_reverse	GGTGGCCGACCGGTGCTTGTACAGCTCGTCCATGCCG
WZ0011_(HRSAT)_(PODJ)_forward	GACGAGCTGTACAAGCACCGGTCGGCCACCATGACGGCGGCTTCGCCATGG
WZ0026_(PodJ)_reverse	GTGGCCGGCCGATATCCAATTGAGATCTGCTTAGCGCGCGTAGACCGACAGG
WZ0135_(pcdf-mcherry)_forward	ACCGTGACGACGGCCTAAGCAGATCTCAATTGGATATCGGCCGGC
WZ0136_(pcdf-mcherry)_reverse	CGGCGACGGGGTGGCCGACCGGTGCTTGTA
WZ0137_(podj08)_forward	TACAAGCACCGGTCGGCCACCCCGTCGCCGCCGCCCGCGCAGG
WZ0138_(podj08)_reverse	AATTGAGATCTGCTTAGGCCGTCGTCACGGTCGCGC
WZH454-podj30-f	GTCGGCCACCGGCGGCCTGCTGCTGCTGAA
WZH455-podj30-r	GCAGGCCGCCGGTGGCCGACCGGTGCTTGT
WZ0099_(pbad)_forward	GGACGCGGCGCCTAAGAAGCTTGGCTGTTTTGGCGG
WZ0051_(PBAD)_reverse	CGCCCTTGCTCACCATTTAATTCCTCCTGTTAGCCCAAAAA

WZ0052_(YFP-PODJ)_forward	AACAGGAGGAATTAAATGGTGAGCAAGGGCGAGGAGC
WZ0103_(cfp)_(hrsat)_reverse	GACTGATCGGACATGGTGGCCGACCGGTGCTTGTACAGCTCGTCCATGCCG
WZ0104_(popz)_forward	GCACCGGTCGGCCACCATGTCCGATCAGTCTCAAGAACCTACAATGG
WZ0105_(popz)_reverse	CAAAACAGCCAAGCTTCTTAGGCGCCGCGTCCCCGAG
WZH568-pxyfpn-2-Pxyl-sfGFP-PodJΔ471-635-F	AGCTGCGCCGGGCGCGACCGTGACGACGGC
WZH569-pxyfpn-2-Pxyl-sfGFP-PodJΔ471-635-R	CGGTCGCGCCCGGCGCAGCTTCCAGCTTCC
WZH570-pxyfpn-2-Pxyl-sfGFP-PodJΔ250-430-F	GGATCAGCGCCAGGAACTGGTCGACCGCAT
WZH571-pxyfpn-2-Pxyl-sfGFP-PodJΔ250-430-R	CCAGTTCCTGGCGCTGATCCAGGGCCTGGA
WZ144-podj-1520-F	TCAGCACGTCTGAGGATGAG
WZ145-podj-2522-R	TCGTAGAGCTGAGCCAGGTT
WZ0277_(PBXMCS2)_forward	GTCTACGCGCGCTAAAAAACGGGCCCCCCCTCGAGG
WZ0278_(PBXMCS2)_reverse	CCCTTGCTCACCATATGGTCGTCTCCCCAAAACTCGAGC
WZ0279_(mneongreen-podj)_forward	GTTTTGGGGAGACGACCATATGGTGAGCAAGGGCGAGGAGG
WZ0280_(mneongreen-podj)_reverse	GGGGGGGCCCGTTTTTTAGCGCGCGTAGACCGACAGG
SWD589_(podJ_stop)_forward	CCGGTCGGCCACCACGGCGGCTTCGCCATGG
SWD668_(pBXMCS_SPA_2)_forward	GCATGCCTCTTTCCCGCTGTGGCCGATCTAGGG

SWD669_(pBXMCS_SPA_2)_reverse	CGCCTTTGCTCATATGGTCGTCTCCCCAAAACTCGAGC
SWD670_(sfgfp)_forward	GGGAGACGACCATATGAGCAAAGGCGAAGAACTGTTTACCGG
SWD671_(sfgfp)_reverse	CGCTTACAATTTTTATTTATACAGTTCATCCATGCCATGTGTAATGCC
SWD672_(rep_and_untranslated_region)_forward	TGGATGAACTGTATAAATAAAAATTGTAAGCGTTAATATTTTGTTAAAATTCGCG
SWD673_(rep_and_untranslated_region)_reverse	GCTAAGGATTTTTTTTACCGCAAACGTGGTCTGGTCG
SWD674_(pylT_rrnc_terminator)_forward	CCAGACCACGTTTGCGGTAAAAAAAATCCTTAGCTTTCGCTAAGATCTGC
SWD675_(pylT_rrnc_terminator)_reverse	CGCGATATAGGCCTCGGGAACCTGATCATGTAGATCGAATGGACT
SWD676_(ffs_promoter)_forward	TGATCAGGTTCCCGAGGCCTATATCGCGACTCATCGCG
SWD677_(ffs_promoter)_reverse	GATCGGCCACAGCGGGAAAGAGGCATGCGCCACTCTGTAGC
SWD678_(pSWD195)_forward	GGCATTAGCACGAACCTGTAAGTTAATATTTTGTTAAAATTCGCGTTAAATTTTTG
SWD679_(pSWD195)_reverse	GTTTTTTATCCATTCGGGATAGGCTCCGTTGG
SWD680_(pylRS)_forward	CGGAGCCTATCCCGAATGGATAAAAAACCGCTGGATGTGCT
SWD681_(pylRS)_reverse	GCGAATTTTAACAAAATATTAACTTACAGGTTCGTGCTAATGCCGT
SWD700_(start)_(sfgfp)_forward	ATATGCATGGTACCTTAAGATCTCGAATGAGCAAAGGAGAAGAACTTTTCACTGG
SWD701_(sfgfp)_(ggsgs)_reverse	GCGAAGCCGCCGTGCTACCACTGCCACCTTTGTAGAGCTCATCCATGCC
SWD702_(podJCC1-3)_forward	TGGCAGTGGTAGCACGGCGGCTTCGCCATGG
SWD703_(podJCC1-3)_(stop)_reverse	ACTAGTGGATCCCCCGGGCTGCAGCTCTAGCCCAAGCGCTGATCCAGGG

SWD704_(pACYC-yfp-hrsat)_forward	GGATCAGCGCTTGGGCTAAGCAGATCTCAATTGGATATCGGCCGGC
SWD705_(pACYC-yfp-hrsat)_reverse	GCGAAGCCGCCGTGGTGGCCGACCGGTGCTTG
SWD706_(podJCC1-3)_reverse	CCAATTGAGATCTGCTTAGCCCAAGCGCTGATCCAGGG
SWD715_(pBXMCS-SPA-2_Nde1)_forward	GCAACAACTCGCCCTAGAGAGCTCCAATTCGCCCTATAGTGAGTCG
SWD716_(pBXMCS-SPA-2_Nde1)_reverse	AGTTCTTCTCCTTTGCTCATATGGTCGTCTCCCCAAAACTCGAGC
SWD717_(sfgfp)_forward	GGGGAGACGACCATATGAGCAAAGGAGAAGAACTTTTCACTGG
SWD718_(podJ1-670)_(stop)_reverse	CGAATTGGAGCTCTCTAGGGCGAGTTGTTGCCGTCGT
SWD719_(pBXMCS-SPA-2_Nde1)_forward	CGCGCTGGGGATTAGAGAGCTCCAATTCGCCCTATAGTGAGTCG
SWD720_(podJ1-865)_(stop)_reverse	CGAATTGGAGCTCTCTAATCCCCAGCGCGGCCGGC
SWD721_(pBXMCS-SPA-2_Nde1)_forward	CCTTGGCGTTGCGTAGAGAGCTCCAATTCGCCCTATAGTGAGTCG
SWD722_(podJ1-920)_(stop)_reverse	GAATTGGAGCTCTCTACGCAACGCCAAGGTTGGCGT
SWD723_(pBXMCS-SPA-2_Nde1)_forward	TCTACGCGCGCTAAAGAGCTCCAATTCGCCCTATAGTGAGTCG
SWD724_(pBXMCS-SPA-2_Nde1)_reverse	CTCCTTTGCTCATATGGTCGTCTCCCCAAAACTCGAGC
SWD725_(sfgfp)_(ggsgs)_reverse	GCGGCGCTACCACTGCCACCTTTGTAGAGCTCATCCATGCC

SWD726_(podJ646-969)_forward	TACAAAGGTGGCAGTGGTAGCGCCGCCGCCGGCGCGCTC
SWD727_(podJ646-969)_reverse	CGAATTGGAGCTCTTTAGCGCGCGTAGACCGACAGG
SWD753_(podJ)_forward	GGTGGCAGTGGTAGCACGGCGGCTTCGCCATGG
SWD790_(sfgfp)_(HRSAT)_reverse	GCCCAAGGTGGCCGACCGGTGTTTGTAGAGCTCATCCATGCC
SWD791_(podJ_251_670)_forward	TACAAACACCGGTCGGCCACCTTGGGCGCCGTCGAGACTG
SWD792_(podJ_251_670)_(stop)_reverse	ACTAGTGGATCCCCCGGGCTGCAGCTTCAGCCCAAGCGCGCCTTCGAC
SWD807_(podJ_DCC1-3_withperi)_forward	AGCTCTACAAACACCGGTCGGCCACCTTGGGCGCCGTCGAGACTG
SWD808_(pBX_sfgfp_ggsgs)_forward	GTCTACGCGCGCTAAAGAGCTCCAATTCGCCCTATAGTGAGTCG
SWD809_(pBX_sfgfp_ggsgs)_reverse	GAAGCCGCCGTGCTACCACTGCCACCTTTGTAGAGC
SWD819_(podJCC1-3)_reverse	AGACAACGAGGCCCAAGCGCTGATCCAGGGCCTGG
SWD820_(podJ_643-702_TM)_forward	GGATCAGCGCTTGGGCCTCGTTGTCTTCGCCGCCGCC
SWD821_(podJ_643-702_TM)_(stop)_reverse	ACTAGTGGATCCCCCGGGCTGCAGCTCTAGGCGGCGCGCGGCGCGCC
SWD870_(pBX_sfgfp_ggsgs)_forward	GGTCTACGCGCGCTGAAGAGCTCCAATTCGCCCTATAGTGAGTCG
SWD871_(pBX_sfgfp_ggsgs)_reverse	GCACAGTATTGTCTTTCATGCTACCACTGCCACCTTTGTAGAGC
SWD872_(start)_(TurboID)_forward	GGTGGCAGTGGTAGCATGAAAGACAATACTGTGCCTCTGAAGCTG

SWD873_(TurboID)_(HRSAT)_reverse	GCGAAGCCGCCGTGGTGGCCGACCGGTGCTTTTCGGCAGACCGCAGACTG
SWD874_(podJ)_(stop)_reverse	GAATTGGAGCTCTTCAGCGCGCGTAGACCGACAGGCG
SWD883_(pBX_sfgfp_ggsgs)_forward	GACGCGGCGCCTAAAGAGCTCCAATTCGCCCTATAGTGAGTCG
SWD884_(pBX_sfgfp_ggsgs)_reverse	GGCACAGTATTGTCTTTGCTACCACTGCCACCTTTGTAGAGC
SWD885_(TurboID)_forward	GGTGGCAGTGGTAGCAAAGACAATACTGTGCCTCTGAAGCTG
SWD886_(TurboID)_(HRSAT)_reverse	GAGACTGATCGGAGGTGGCCGACCGGTGCTTTTCGGCAGACCGCAGACTG
SWD887_(popZ)_reverse	GAATTGGAGCTCTTTAGGCGCCGCGTCCCCG
nSWD109	GCGCCGCTTCATGCCATACG
nSWD110	AGGCGTAGCACCAGGCGTTT
Pxyl-for	CCCACATGTTAGCGCTACCAAGTGC
M13-for	GCCAGGGTTTTCCCAGTCACGA
RecUni-1	ATGCCGTTTGTGATGGCTTCCATGTCG
RecXyl-2	TCTTCCGGCAGGAATTCACTCACGCC

Table 6–4 Strains used in this study by name, then number order.

Name	**Genotype**	**Plasmid**	**Reference**
CZ604	*E. coli*, BL21	pCZ10388	This study
CZ703	*E. coli*, Rosetta	250-635	This study
WSC1040	*A. tumefaciens C58*	none	
WSC1119	*E. coli*, DH5α	none	Novagen
WSC1223	*C. crescentus*	pBX-mNG-podJ	This study
WSC1224	*C. crescentus, pleC::delta*	pBX-mNG-podJ	This study, [267]
WSC1225	*C. crescentus, spmX::delta*	pBX-mNG-podJ	This study, [364]
WSC1226	*C. crescentus, popZ::delta*	pBX-mNG-podJ	This study, [132]

WSC1232	*E. coli*, DH5α	pWZ012	This study
WSC1243	*E. coli*, DH5α	podJ08	This study
WSC1252	*E. coli*, DH5α	podJ17	This study
WSC1254	*E. coli*, DH5α	podJ19	This study
WSC1255	*E. coli*, DH5α	podJ20	This study
WSC1256	*E. coli*, DH5α	podJ21	This study
WSC1258	*E. coli*, DH5α	podJ23	This study
WSC1259	*E. coli*, DH5α	pWZ94	This study
WSC1262	*E. coli*, DH5α	pWZ0202	This study
WSC1265	*E. coli*, DH5α	podJ30	This study
WSC1269	*E. coli*, DH5α	podJ-delta-250-430	This study
WSC1274	*E. coli*, DH5α	pWZ046	This study
WSC1327	*E. coli*, DH5α	pWZ91-6	This study
WSC1328	*E. coli*, DH5α	pWZ96	This study
WSC1329	*E. coli*, DH5α	pWZ98	This study
WSC1343	*E. coli*, BL21	pWZ012	This study
WSC1344	*E. coli*, BL21	podJ17	This study
WSC1369	*E. coli*, BL21	pWZ046	This study
WSC1383	*E. coli*, DH5α	WZ366	This study
WSC1384	*E. coli*, DH5α	WZ367	Chapter 5
WSC1402	*C. crescentus*, P_{popZ}-*mCherry-popZ*	WZ366	This study
WSC1403	*C. crescentus*, P_{popZ}-*mCherry-popZ*	WZ367	Chapter 5
WSC1411	*C. crescentus*, NA1000	none	Lucy Shapiro
WSC1597	*E. coli*, DH5α	pBX-mNG-podJ	This study
SWD540	*E. coli*, DH5α	pSWD217	This study
SWD541	*E. coli*, DH5α	pSWD217tag	This study
SWD545	*C. crescentus*, *tipN::delta*	pBX-mNG-podJ	This study, [365]
SWD561	*E. coli*, DH5α	pSWD218	This study
SWD564	*C. crescentus*	pSWD217	This study
SWD565	*C. crescentus*	pSWD217tag	This study
SWD568	*E. coli*, DH5α	pSWD226	This study
SWD569	*E. coli*, DH5α	pSWD235	This study
SWD576	*C. crescentus*	pSWD235	This study

SWD577	*C. crescentus*	pSWD218	This study
SWD579	*C. crescentus*	pSWD217tag, pSWD218	This study
SWD580	*E. coli*, DH5α	pSWD233	This study
SWD581	*E. coli*, DH5α	pSWD236	This study
SWD583	*E. coli*, BL21	pSWD226	This study
SWD598	*C. crescentus*	pSWD233	This study
SWD599	*C. crescentus*	pSWD236	This study
SWD622	*E. coli*, DH5α	pSWD234	This study
SWD633	*C. crescentus*	pSWD234	This study
SWD639	*E. coli*, DH5α	pSWD225	This study
SWD640	*E. coli*, DH5α	pSWD259	This study
SWD648	*C. crescentus, podJ::chlor*	pSWD225	This study
SWD649	*C. crescentus, podJ::chlor*	pSWD259	This study
SWD657	*A. tumefaciens*	pBX-mNG-podJ	This study
SWD661	*E. coli*, DH5α	pSWD268	This study
SWD662	*E. coli*, DH5α	pSWD270	This study
SWD671	*C. crescentus, podJ::chlor*	pSWD268	This study
SWD672	*C. crescentus,* P_{popZ}*-mCherry-popZ*	pSWD270	This study
SWD680	*E. coli*, DH5α	pSWD269	This study
SWD681	*E. coli*, DH5α	pSWD271	This study
SWD683	*C. crescentus,* P_{popZ}*-mCherry-popZ*	pSWD271	This study
SWD684	*C. crescentus,* P_{popZ}*-mCherry-popZ*	pSWD269	This study
SWD690	*E. coli*, DH5α	pSWD277	This study
SWD696	*C. crescentus, podJ::chlor*	pSWD277	This study
SWD707	*E. coli*, DH5α	pSWD293	This study
SWD707	*C. crescentus, podJ::chlor*	pSWD293	This study
SWD708	*E. coli*, DH5α	pSWD296	This study
SWD708	*C. crescentus*	pSWD296	This study

SWD765	*E. coli*, Rosetta	pCZ221	This study

Bibliography

1 Gao, R. & Stock, A. M. Biological insights from structures of two-component proteins. *Annual review of microbiology* **63**, 133-154, doi:10.1146/annurev.micro.091208.073214 (2009).

2 Zschiedrich, C. P., Keidel, V. & Szurmant, H. Molecular Mechanisms of Two-Component Signal Transduction. *Journal of molecular biology* **428**, 3752-3775, doi:10.1016/j.jmb.2016.08.003 (2016).

3 Galperin, M. Y. Structural classification of bacterial response regulators: diversity of output domains and domain combinations. *J Bacteriol* **188**, 4169-4182, doi:10.1128/JB.01887-05 (2006).

4 Eguchi, Y. *et al.* Angucycline antibiotic waldiomycin recognizes common structural motif conserved in bacterial histidine kinases. *The Journal of antibiotics* **70**, 251-258, doi:10.1038/ja.2016.151 (2017).

5 Ashenberg, O., Rozen-Gagnon, K., Laub, M. T. & Keating, A. E. Determinants of homodimerization specificity in histidine kinases. *Journal of molecular biology* **413**, 222-235, doi:10.1016/j.jmb.2011.08.011 (2011).

6 Casino, P., Rubio, V. & Marina, A. Structural insight into partner specificity and phosphoryl transfer in two-component signal transduction. *Cell* **139**, 325-336, doi:10.1016/j.cell.2009.08.032 (2009).

7 Pettersen, E. F. *et al.* UCSF Chimera--a visualization system for exploratory research and analysis. *Journal of computational chemistry* **25**, 1605-1612, doi:10.1002/jcc.20084 (2004).

8 Jacobs, C., Ausmees, N., Cordwell, S. J., Shapiro, L. & Laub, M. T. Functions of the CckA histidine kinase in Caulobacter cell cycle control. *Molecular microbiology* **47**, 1279-1290 (2003).

9 Lin, Y. H. *et al.* Role of the VirA histidine autokinase of Agrobacterium tumefaciens in the initial steps of pathogenesis. *Frontiers in plant science* **5**, 195, doi:10.3389/fpls.2014.00195 (2014).

10 Cai, S. J. & Inouye, M. EnvZ-OmpR interaction and osmoregulation in Escherichia coli. *The Journal of biological chemistry* **277**, 24155-24161, doi:10.1074/jbc.M110715200 (2002).

11 Wang, B., Zhao, A., Novick, R. P. & Muir, T. W. Activation and inhibition of the receptor histidine kinase AgrC occurs through opposite helical transduction motions. *Mol Cell* **53**, 929-940, doi:10.1016/j.molcel.2014.02.029 (2014).

12 Gooderham, W. J. & Hancock, R. E. Regulation of virulence and antibiotic resistance by two-component regulatory systems in Pseudomonas aeruginosa. *FEMS microbiology reviews* **33**, 279-294, doi:10.1111/j.1574-6976.2008.00135.x (2009).

13 Matamouros, S., Hager, K. R. & Miller, S. I. HAMP Domain Rotation and Tilting Movements Associated with Signal Transduction in the PhoQ Sensor Kinase. *MBio* **6**, e00616-00615, doi:10.1128/mBio.00616-15 (2015).

14 Schultz, J. E., Kanchan, K. & Ziegler, M. Intraprotein signal transduction by HAMP domains: a balancing act. *Int J Med Microbiol* **305**, 243-251, doi:10.1016/j.ijmm.2014.12.007 (2015).

15 Diensthuber, R. P., Bommer, M., Gleichmann, T. & Moglich, A. Full-length structure of a sensor histidine kinase pinpoints coaxial coiled coils as signal transducers and modulators. *Structure* **21**, 1127-1136, doi:10.1016/j.str.2013.04.024 (2013).

16 Lesne, E. *et al.* Coiled-Coil Antagonism Regulates Activity of Venus Flytrap-Domain-Containing Sensor Kinases of the BvgS Family. *mBio* **9**, doi:ARTN e02052-17 10.1128/mBio.02052-17 (2018).

17 Marina, A., Waldburger, C. D. & Hendrickson, W. A. Structure of the entire cytoplasmic portion of a sensor histidine-kinase protein. *The EMBO journal* **24**, 4247-4259, doi:10.1038/sj.emboj.7600886 (2005).

18 Albanesi, D. *et al.* Structural plasticity and catalysis regulation of a thermosensor histidine kinase. *Proceedings of the National Academy of Sciences of the United States of America* **106**, 16185-16190, doi:10.1073/pnas.0906699106 (2009).

19 Ferris, H. U., Zeth, K., Hulko, M., Dunin-Horkawicz, S. & Lupas, A. N. Axial helix rotation as a mechanism for signal regulation inferred from the crystallographic analysis of the E. coli serine chemoreceptor. *J Struct Biol* **186**, 349-356, doi:10.1016/j.jsb.2014.03.015 (2014).

20 Wang, C. *et al.* Mechanistic insights revealed by the crystal structure of a histidine kinase with signal transducer and sensor domains. *PLoS biology* **11**, e1001493, doi:10.1371/journal.pbio.1001493 (2013).

21 Mechaly, A. E., Sassoon, N., Betton, J. M. & Alzari, P. M. Segmental helical motions and dynamical asymmetry modulate histidine kinase autophosphorylation. *PLoS biology* **12**, e1001776, doi:10.1371/journal.pbio.1001776 (2014).

22 Szurmant, H., Bu, L., Brooks, C. L., 3rd & Hoch, J. A. An essential sensor histidine kinase controlled by transmembrane helix interactions with its auxiliary proteins. *Proc Natl Acad Sci U S A* **105**, 5891-5896, doi:10.1073/pnas.0800247105 (2008).

23 Goldberg, S. D., Clinthorne, G. D., Goulian, M. & DeGrado, W. F. Transmembrane polar interactions are required for signaling in the Escherichia coli sensor kinase PhoQ. *Proc Natl Acad Sci U S A* **107**, 8141-8146, doi:10.1073/pnas.1003166107 (2010).

24 Krikos, A., Conley, M. P., Boyd, A., Berg, H. C. & Simon, M. I. Chimeric chemosensory transducers of Escherichia coli. *Proceedings of the National Academy of Sciences of the United States of America* **82**, 1326-1330 (1985).

25 Utsumi, R. *et al.* Activation of Bacterial Porin Gene-Expression by a Chimeric Signal Transducer in Response to Aspartate. *Science* **245**, 1246-1249, doi:Doi 10.1126/Science.2476847 (1989).

26 Jin, T. & Inouye, M. Mutational Analysis of the Cytoplasmic Linker Region of Taz1-1, a Tar-Envz Chimeric Receptor in Escherichia-Coli. *Journal of molecular biology* **244**, 477-481, doi:Doi 10.1006/Jmbi.1994.1746 (1994).

27 Zhu, Y. & Inouye, M. Analysis of the role of the EnvZ linker region in signal transduction using a chimeric Tar/EnvZ receptor protein, Tez1. *Journal of Biological Chemistry* **278**, 22812-22819, doi:10.1074/jbc.M300916200 (2003).

28 Moglich, A., Ayers, R. A. & Moffat, K. Structure and signaling mechanism of Per-ARNT-Sim domains. *Structure* **17**, 1282-1294, doi:10.1016/j.str.2009.08.011 (2009).

29 Harper, S. M., Christie, J. M. & Gardner, K. H. Disruption of the LOV-Jalpha helix interaction activates phototropin kinase activity. *Biochemistry* **43**, 16184-16192, doi:10.1021/bi048092i (2004).

30 Moglich, A., Ayers, R. A. & Moffat, K. Design and signaling mechanism of light-regulated histidine kinases. *Journal of molecular biology* **385**, 1433-1444, doi:10.1016/j.jmb.2008.12.017 (2009).

31 Crosson, S., Rajagopal, S. & Moffat, K. The LOV domain family: photoresponsive signaling modules coupled to diverse output domains. *Biochemistry* **42**, 2-10, doi:10.1021/bi026978l (2003).

32 Bury, A. & Hellingwerf, K. J. Design, characterization and in vivo functioning of a light-dependent histidine protein kinase in the yeast Saccharomyces cerevisiae. *AMB Express* **8**, 53, doi:10.1186/s13568-018-0582-7 (2018).

33 Iniesta, A. A., Hillson, N. J. & Shapiro, L. Cell pole-specific activation of a critical bacterial cell cycle kinase. *Proceedings of the National Academy of Sciences of the United States of America* **107**, 7012-7017, doi:10.1073/pnas.1001767107 (2010).

34 Shivaji, S. & Prakash, J. S. How do bacteria sense and respond to low temperature? *Archives of microbiology* **192**, 85-95, doi:10.1007/s00203-009-0539-y (2010).

35 Draheim, R. R., Bormans, A. F., Lai, R. Z. & Manson, M. D. Tuning a bacterial chemoreceptor with protein-membrane interactions. *Biochemistry* **45**, 14655-14664, doi:10.1021/bi061259i (2006).

36 Norholm, M. H., von Heijne, G. & Draheim, R. R. Forcing the issue: aromatic tuning facilitates stimulus-independent modulation of a two-component signaling circuit. *ACS synthetic biology* **4**, 474-481, doi:10.1021/sb500261t (2015).

37 Lehning, C. E., Heidelberger, J. B., Reinhard, J., Norholm, M. H. H. & Draheim, R. R. A Modular High-Throughput In Vivo Screening Platform Based on Chimeric Bacterial Receptors. *ACS synthetic biology* **6**, 1315-1326, doi:10.1021/acssynbio.6b00288 (2017).

38 de Planque, M. R. *et al.* The effects of hydrophobic mismatch between phosphatidylcholine bilayers and transmembrane alpha-helical peptides depend on the nature of interfacially exposed aromatic and charged residues. *Biochemistry* **41**, 8396-8404 (2002).

39 de Planque, M. R. *et al.* Sensitivity of single membrane-spanning alpha-helical peptides to hydrophobic mismatch with a lipid bilayer: effects on backbone structure, orientation, and extent of membrane incorporation. *Biochemistry* **40**, 5000-5010 (2001).

40 Crosson, S., McGrath, P. T., Stephens, C., McAdams, H. H. & Shapiro, L. Conserved modular design of an oxygen sensory/signaling network with species-specific output. *Proceedings of the National Academy of Sciences of the United States of America* **102**, 8018-8023, doi:10.1073/pnas.0503022102 (2005).

41 Lopez, D., Fischbach, M. A., Chu, F., Losick, R. & Kolter, R. Structurally diverse natural products that cause potassium leakage trigger multicellularity in Bacillus subtilis. *Proceedings of the National Academy of Sciences of the United States of America* **106**, 280-285, doi:10.1073/pnas.0810940106 (2009).

42 Ganesh, I., Ravikumar, S., Lee, S. H., Park, S. J. & Hong, S. H. Engineered fumarate sensing Escherichia coli based on novel chimeric two-component system. *Journal of biotechnology* **168**, 560-566, doi:10.1016/j.jbiotec.2013.09.003 (2013).

43 Ganesh, I., Ravikumar, S., Yoo, I. K. & Hong, S. H. Construction of malate-sensing Escherichia coli by introduction of a novel chimeric two-component system. *Bioprocess and biosystems engineering* **38**, 797-804, doi:10.1007/s00449-014-1321-3 (2015).

44 Ravikumar, S., David, Y., Park, S. J. & Choi, J. I. A Chimeric Two-Component Regulatory System-Based Escherichia coli Biosensor Engineered to Detect Glutamate. *Applied biochemistry and biotechnology*, doi:10.1007/s12010-018-2746-y (2018).

45 Selvamani, V., Ganesh, I., Maruthamuthu, M. K., Eom, G. T. & Hong, S. H. Engineering chimeric two-component system into Escherichia coli from Paracoccus denitrificans to sense methanol. *Biotechnol Bioproc E* **22**, 225-230, doi:10.1007/s12257-016-0484-y (2017).

46 Tabor, J. J., Levskaya, A. & Voigt, C. A. Multichromatic control of gene expression in Escherichia coli. *J Mol Biol* **405**, 315-324, doi:10.1016/j.jmb.2010.10.038 (2011).

47 Daeffler, K. N. *et al.* Engineering bacterial thiosulfate and tetrathionate sensors for detecting gut inflammation. *Mol Syst Biol* **13**, 923, doi:10.15252/msb.20167416 (2017).

48 Schrader, J. *et al.* Methanol-based industrial biotechnology: current status and future perspectives of methylotrophic bacteria. *Trends in biotechnology* **27**, 107-115, doi:10.1016/j.tibtech.2008.10.009 (2009).

49 Ziolkowska, J. R. Prospective technologies, feedstocks and market innovations for ethanol and biodiesel production in the US. *Biotechnology reports* **4**, 94-98, doi:10.1016/j.btre.2014.09.001 (2014).

50 Ang, J., Harris, E., Hussey, B. J., Kil, R. & McMillen, D. R. Tuning response curves for synthetic biology. *ACS Synth Biol* **2**, 547-567, doi:10.1021/sb4000564 (2013).

51 Batchelor, E. & Goulian, M. Robustness and the cycle of phosphorylation and dephosphorylation in a two-component regulatory system. *Proc Natl Acad Sci U S A* **100**, 691-696, doi:10.1073/pnas.0234782100 (2003).

52 Landry, B. P., Palanki, R., Dyulgyarov, N., Hartsough, L. A. & Tabor, J. J. Phosphatase activity tunes two-component system sensor detection threshold. *Nat Commun* **9**, 1433, doi:10.1038/s41467-018-03929-y (2018).

53 Huynh, T. N., Noriega, C. E. & Stewart, V. Conserved mechanism for sensor phosphatase control of two-component signaling revealed in the nitrate sensor NarX. *Proceedings of the National Academy of Sciences of the United States of America* **107**, 21140-21145, doi:10.1073/pnas.1013081107 (2010).

54 Huynh, T. N., Noriega, C. E. & Stewart, V. Missense substitutions reflecting regulatory control of transmitter phosphatase activity in two-component signalling. *Mol Microbiol* **88**, 459-472, doi:10.1111/mmi.12195 (2013).

55 Zhu, Y. & Inouye, M. The role of the G2 box, a conserved motif in the histidine kinase superfamily, in modulating the function of EnvZ. *Mol Microbiol* **45**, 653-663 (2002).

56 Sutton, M. A. *et al. The European Nitrogen Assessment : Sources, Effects and Policy Perspectives*. (Cambridge University Press, 2011).

57 Smanski, M. J. *et al.* Functional optimization of gene clusters by combinatorial design and assembly. *Nature biotechnology* **32**, 1241-1249, doi:10.1038/nbt.3063 (2014).

58 Casino, P., Rubio, V. & Marina, A. The mechanism of signal transduction by two-component systems. *Curr Opin Struct Biol* **20**, 763-771, doi:10.1016/j.sbi.2010.09.010 (2010).

59 Ferris, H. U. *et al.* Mechanism of regulation of receptor histidine kinases. *Structure* **20**, 56-66, doi:10.1016/j.str.2011.11.014 (2012).

60 Zitzewitz, J. A., Ibarra-Molero, B., Fishel, D. R., Terry, K. L. & Matthews, C. R. Preformed secondary structure drives the association reaction of GCN4-p1, a model coiled-coil system. *J Mol Biol* **296**, 1105-1116, doi:10.1006/jmbi.2000.3507 (2000).

61 Hidaka, Y., Park, H. & Inouye, M. Demonstration of dimer formation of the cytoplasmic domain of a transmembrane osmosensor protein, EnvZ, of Escherichia coli using Ni-histidine tag affinity chromatography. *FEBS Lett* **400**, 238-242 (1997).

62 Cochran, A. G. & Kim, P. S. Imitation of Escherichia coli aspartate receptor signaling in engineered dimers of the cytoplasmic domain. *Science* **271**, 1113-1116 (1996).

63 Wang, Y., Gao, R. & Lynn, D. G. Ratcheting up vir gene expression in Agrobacterium tumefaciens: coiled coils in histidine kinase signal transduction. *Chembiochem* **3**, 311-317 (2002).

64 Gao, R. & Lynn, D. G. Integration of rotation and piston motions in coiled-coil signal transduction. *J Bacteriol* **189**, 6048-6056, doi:10.1128/JB.00459-07 (2007).

65 Wang, B. *et al.* Functional Plasticity of the AgrC Receptor Histidine Kinase Required for Staphylococcal Virulence. *Cell Chem Biol* **24**, 76-86, doi:10.1016/j.chembiol.2016.12.008 (2017).

66 Winans, S. C. Two-way chemical signaling in Agrobacterium-plant interactions. *Microbiol Rev* **56**, 12-31 (1992).

67 Doty, S. L., Yu, M. C., Lundin, J. I., Heath, J. D. & Nester, E. W. Mutational analysis of the input domain of the VirA protein of Agrobacterium tumefaciens. *J Bacteriol* **178**, 961-970 (1996).

68 Zimmermann, L. *et al.* A Completely Reimplemented MPI Bioinformatics Toolkit with a New HHpred Server at its Core. *J Mol Biol*, doi:10.1016/j.jmb.2017.12.007 (2017).

69 McLean, B. G., Greene, E. A. & Zambryski, P. C. Mutants of Agrobacterium VirA that activate vir gene expression in the absence of the inducer acetosyringone. *J Biol Chem* **269**, 2645-2651 (1994).

70 Reyes, D. *et al.* Coordinated regulation by AgrA, SarA, and SarR to control agr expression in Staphylococcus aureus. *J Bacteriol* **193**, 6020-6031, doi:10.1128/JB.05436-11 (2011).

71 Childers, W. S. *et al.* Cell fate regulation governed by a repurposed bacterial histidine kinase. *PLoS biology* **12**, e1001979, doi:10.1371/journal.pbio.1001979 (2014).

72 Ozaki, S. *et al.* Activation and polar sequestration of PopA, a c-di-GMP effector protein involved in Caulobacter crescentus cell cycle control. *Mol Microbiol* **94**, 580-594, doi:10.1111/mmi.12777 (2014).

73 Gao, R. & Lynn, D. G. Environmental pH sensing: resolving the VirA/VirG two-component system inputs for Agrobacterium pathogenesis. *Journal of bacteriology* **187**, 2182-2189, doi:10.1128/JB.187.6.2182-2189.2005 (2005).

74 Moglich, A., Ayers, R. A. & Moffat, K. Addition at the Molecular Level: Signal Integration in Designed Per-ARNT-Sim Receptor Proteins. *Journal of molecular biology* **400**, 477-486, doi:10.1016/j.jmb.2010.05.019 (2010).

75 Eswaramoorthy, P. *et al.* Expression level of a chimeric kinase governs entry into sporulation in Bacillus subtilis. *Journal of bacteriology* **193**, 6113-6122, doi:10.1128/JB.05920-11 (2011).

76 Mann, T. H. & Shapiro, L. Integration of cell cycle signals by multi-PAS domain kinases. *Proceedings of the National Academy of Sciences of the United States of America* **115**, E7166-E7173, doi:10.1073/pnas.1808543115 (2018).

77 Eswaramoorthy, P., Guo, T. & Fujita, M. In vivo domain-based functional analysis of the major sporulation sensor kinase, KinA, in Bacillus subtilis. *Journal of bacteriology* **191**, 5358-5368, doi:10.1128/JB.00503-09 (2009).

78 Eswaramoorthy, P. *et al.* Expression Level of a Chimeric Kinase Governs Entry into Sporulation in Bacillus subtilis. *Journal of bacteriology* **193**, 6113-6122, doi:10.1128/JB.05920-11 (2011).

79 Rowland, M. A. & Deeds, E. J. Crosstalk and the evolution of specificity in two-component signaling. *Proceedings of the National Academy of Sciences of the United States of America* **111**, 5550-5555, doi:10.1073/pnas.1317178111 (2014).

80 Chambonnier, G. *et al.* The Hybrid Histidine Kinase LadS Forms a Multicomponent Signal Transduction System with the GacS/GacA Two-Component System in Pseudomonas aeruginosa. *PLoS genetics* **12**, e1006032, doi:10.1371/journal.pgen.1006032 (2016).

81 Goodman, A. L. *et al.* Direct interaction between sensor kinase proteins mediates acute and chronic disease phenotypes in a bacterial pathogen. *Genes & development* **23**, 249-259, doi:10.1101/gad.1739009 (2009).

82 Capra, E. J. & Laub, M. T. Evolution of two-component signal transduction systems. *Annual review of microbiology* **66**, 325-347, doi:10.1146/annurev-micro-092611-150039 (2012).

83 Skerker, J. M. *et al.* Rewiring the specificity of two-component signal transduction systems. *Cell* **133**, 1043-1054, doi:10.1016/j.cell.2008.04.040 (2008).

84 Atchley, W. R., Wollenberg, K. R., Fitch, W. M., Terhalle, W. & Dress, A. W. Correlations among amino acid sites in bHLH protein domains: an information theoretic analysis. *Molecular biology and evolution* **17**, 164-178, doi:10.1093/oxfordjournals.molbev.a026229 (2000).

85 Fodor, A. A. & Aldrich, R. W. Influence of conservation on calculations of amino acid covariance in multiple sequence alignments. *Proteins* **56**, 211-221, doi:10.1002/prot.20098 (2004).

86 Varughese, K. I., Tsigelny, I. & Zhao, H. The crystal structure of beryllofluoride Spo0F in complex with the phosphotransferase Spo0B represents a phosphotransfer pretransition state. *Journal of bacteriology* **188**, 4970-4977, doi:10.1128/JB.00160-06 (2006).

87 Podgornaia, A. I., Casino, P., Marina, A. & Laub, M. T. Structural basis of a rationally rewired protein-protein interface critical to bacterial signaling. *Structure* **21**, 1636-1647, doi:10.1016/j.str.2013.07.005 (2013).

88 Whitaker, W. R., Davis, S. A., Arkin, A. P. & Dueber, J. E. Engineering robust control of two-component system phosphotransfer using modular scaffolds. *Proceedings of the National Academy of Sciences of the United States of America* **109**, 18090-18095, doi:10.1073/pnas.1209230109 (2012).

89 Bhattacharyya, R. P., Reményi, A., Yeh, B. J. & Lim, W. A. Domains, Motifs, and Scaffolds: The Role of Modular Interactions in the Evolution and Wiring of Cell Signaling Circuits. *Annual Review of Biochemistry* **75**, 655-680, doi:10.1146/annurev.biochem.75.103004.142710 (2006).

90 Jin, T. & Inouye, M. Ligand binding to the receptor domain regulates the ratio of kinase to phosphatase activities of the signaling domain of the hybrid Escherichia coli transmembrane receptor, Taz1. *J Mol Biol* **232**, 484-492, doi:10.1006/jmbi.1993.1404 (1993).

91 Skerker, J. M., Prasol, M. S., Perchuk, B. S., Biondi, E. G. & Laub, M. T. Two-component signal transduction pathways regulating growth and cell cycle progression in a bacterium: a system-level analysis. *PLoS biology* **3**, e334, doi:10.1371/journal.pbio.0030334 (2005).

92 Townsend, G. E., Raghavan, V., Zwir, I. & Groisman, E. A. Intramolecular arrangement of sensor and regulator overcomes relaxed specificity in hybrid two-component systems. *Proceedings of the National Academy of Sciences* **110**, E161-E169, doi:10.1073/pnas.1212102110 (2013).

93 Capra, E. J. *et al.* Spatial tethering of kinases to their substrates relaxes evolutionary constraints on specificity. *Mol Microbiol* **86**, 1393-1403, doi:10.1111/mmi.12064 (2012).

94 Tsokos, C. G., Perchuk, B. S. & Laub, M. T. A dynamic complex of signaling proteins uses polar localization to regulate cell-fate asymmetry in Caulobacter crescentus. *Developmental cell* **20**, 329-341, doi:10.1016/j.devcel.2011.01.007 (2011).

95 Poindexter, J. S. Biological Properties and Classification of the Caulobacter Group. *Bacteriological reviews* **28**, 231-295 (1964).

96 Charles, T. C. & Nester, E. W. A chromosomally encoded two-component sensory transduction system is required for virulence of Agrobacterium tumefaciens. *Journal of bacteriology* **175**, 6614-6625 (1993).

97 Wilson, R. & Dowling, R. B. Lung infections. 3. Pseudomonas aeruginosa and other related species. *Thorax* **53**, 213-219 (1998).

98 Bassler, B. L., Wright, M. & Silverman, M. R. Multiple signalling systems controlling expression of luminescence in Vibrio harveyi: sequence and function of genes encoding a second sensory pathway. *Molecular microbiology* **13**, 273-286 (1994).

99 Aguilar, P. S., Hernandez-Arriaga, A. M., Cybulski, L. E., Erazo, A. C. & de Mendoza, D. Molecular basis of thermosensing: a two-component signal transduction thermometer in Bacillus subtilis. *The EMBO journal* **20**, 1681-1691, doi:10.1093/emboj/20.7.1681 (2001).

100 Hess, J. F., Bourret, R. B. & Simon, M. I. Histidine phosphorylation and phosphoryl group transfer in bacterial chemotaxis. *Nature* **336**, 139-143, doi:10.1038/336139a0 (1988).

101 Mahoney, T. F. & Silhavy, T. J. The Cpx stress response confers resistance to some, but not all, bactericidal antibiotics. *Journal of bacteriology* **195**, 1869-1874, doi:10.1128/JB.02197-12 (2013).

102 Kocan, M. *et al.* Two-component systems of Corynebacterium glutamicum: deletion analysis and involvement of the PhoS-PhoR system in the phosphate starvation response. *Journal of bacteriology* **188**, 724-732, doi:10.1128/JB.188.2.724-732.2006 (2006).

103 Flemming, H. C. *et al.* Biofilms: an emergent form of bacterial life. *Nature reviews. Microbiology* **14**, 563-575, doi:10.1038/nrmicro.2016.94 (2016).

104 Cotter, P. A. & Stibitz, S. c-di-GMP-mediated regulation of virulence and biofilm formation. *Current opinion in microbiology* **10**, 17-23, doi:10.1016/j.mib.2006.12.006 (2007).

105 Falke, J. J., Bass, R. B., Butler, S. L., Chervitz, S. A. & Danielson, M. A. The two-component signaling pathway of bacterial chemotaxis: a molecular view of signal transduction by receptors, kinases, and adaptation enzymes. *Annual review of cell and developmental biology* **13**, 457-512, doi:10.1146/annurev.cellbio.13.1.457 (1997).

106 Pruss, B. M. Involvement of Two-Component Signaling on Bacterial Motility and Biofilm Development. *Journal of bacteriology* **199**, doi:10.1128/JB.00259-17 (2017).

107 Jacobs, C., Domian, I. J., Maddock, J. R. & Shapiro, L. Cell cycle-dependent polar localization of an essential bacterial histidine kinase that controls DNA replication and cell division. *Cell* **97**, 111-120 (1999).

108 Casino, P., Miguel-Romero, L. & Marina, A. Visualizing autophosphorylation in histidine kinases. *Nature communications* **5**, 3258, doi:10.1038/ncomms4258 (2014).

109 Laub, M. T. & Goulian, M. Specificity in two-component signal transduction pathways. *Annual review of genetics* **41**, 121-145, doi:10.1146/annurev.genet.41.042007.170548 (2007).

110 Nasa, I. & Kettenbach, A. N. Coordination of Protein Kinase and Phosphoprotein Phosphatase Activities in Mitosis. *Front Cell Dev Biol* **6**, 30, doi:10.3389/fcell.2018.00030 (2018).

111 Angelastro, P. S., Sliusarenko, O. & Jacobs-Wagner, C. Polar localization of the CckA histidine kinase and cell cycle periodicity of the essential master regulator CtrA in Caulobacter crescentus. *Journal of bacteriology* **192**, 539-552, doi:10.1128/JB.00985-09 (2010).

112 Laub, M. T., Chen, S. L., Shapiro, L. & McAdams, H. H. Genes directly controlled by CtrA, a master regulator of the Caulobacter cell cycle. *Proceedings of the National Academy of Sciences of the United States of America* **99**, 4632-4637, doi:10.1073/pnas.062065699 (2002).

113 Mann, T. H., Seth Childers, W., Blair, J. A., Eckart, M. R. & Shapiro, L. A cell cycle kinase with tandem sensory PAS domains integrates cell fate cues. *Nature communications* **7**, 11454, doi:10.1038/ncomms11454 (2016).

114 Blair, J. A. *et al.* Branched signal wiring of an essential bacterial cell-cycle phosphotransfer protein. *Structure* **21**, 1590-1601, doi:10.1016/j.str.2013.06.024 (2013).

115 Hsing, W. & Silhavy, T. J. Function of conserved histidine-243 in phosphatase activity of EnvZ, the sensor for porin osmoregulation in Escherichia coli. *Journal of bacteriology* **179**, 3729-3735 (1997).

116 Dubey, B. N. *et al.* Cyclic di-GMP mediates a histidine kinase/phosphatase switch by noncovalent domain cross-linking. *Science advances* **2**, e1600823, doi:10.1126/sciadv.1600823 (2016).

117 Christen, M. *et al.* Asymmetrical distribution of the second messenger c-di-GMP upon bacterial cell division. *Science* **328**, 1295-1297, doi:10.1126/science.1188658 (2010).

118 Abel, S. *et al.* Bi-modal distribution of the second messenger c-di-GMP controls cell fate and asymmetry during the caulobacter cell cycle. *PLoS genetics* **9**, e1003744, doi:10.1371/journal.pgen.1003744 (2013).

119 Biondi, E. G. *et al.* Regulation of the bacterial cell cycle by an integrated genetic circuit. *Nature* **444**, 899-904, doi:10.1038/nature05321 (2006).

120 Chen, Y. E. *et al.* Spatial gradient of protein phosphorylation underlies replicative asymmetry in a bacterium. *Proceedings of the National Academy of Sciences of the United States of America* **108**, 1052-1057, doi:10.1073/pnas.1015397108 (2011).

121 Quon, K. C., Marczynski, G. T. & Shapiro, L. Cell cycle control by an essential bacterial two-component signal transduction protein. *Cell* **84**, 83-93 (1996).

122 Quon, K. C., Yang, B., Domian, I. J., Shapiro, L. & Marczynski, G. T. Negative control of bacterial DNA replication by a cell cycle regulatory protein that binds at the chromosome origin. *Proceedings of the National Academy of Sciences of the United States of America* **95**, 120-125 (1998).

123 Siam, R. & Marczynski, G. T. Cell cycle regulator phosphorylation stimulates two distinct modes of binding at a chromosome replication origin. *The EMBO journal* **19**, 1138-1147, doi:10.1093/emboj/19.5.1138 (2000).

124 Kowallis, K. A. *et al.* Synthetic Control of Signal Flow Within a Bacterial Multi-Kinase Network. *ACS synthetic biology* **9**, 1705-1713, doi:10.1021/acssynbio.0c00043 (2020).

125 Gao, R. & Stock, A. M. Quantitative Analysis of Intracellular Response Regulator Phosphatase Activity of Histidine Kinases. *Methods in enzymology* **607**, 301-319, doi:10.1016/bs.mie.2018.04.004 (2018).

126 Bhate, M. P., Molnar, K. S., Goulian, M. & DeGrado, W. F. Signal transduction in histidine kinases: insights from new structures. *Structure* **23**, 981-994, doi:10.1016/j.str.2015.04.002 (2015).

127 Gadella, T. W. J. *FRET and FLIM techniques*. (Elsevier, 2009).

128 Iniesta, A. A., Hillson, N. J. & Shapiro, L. Cell pole-specific activation of a critical bacterial cell cycle kinase. *Proceedings of the National Academy of Sciences of the United States of America* **107**, 7012-7017, doi:10.1073/pnas.1001767107 (2010).

129 Angelastro, P. S., Sliusarenko, O. & Jacobs-Wagner, C. Polar Localization of the CckA Histidine Kinase and Cell Cycle Periodicity of the Essential Master Regulator CtrA in Caulobacter crescentus. *Journal of bacteriology* **192**, 539-552, doi:10.1128/jb.00985-09 (2010).

130 Chen, Y. E., Tsokos, C. G., Biondi, E. G., Perchuk, B. S. & Laub, M. T. Dynamics of Two Phosphorelays Controlling Cell Cycle Progression in Caulobacter crescentus. *Journal of bacteriology* **191**, 7417-7429, doi:10.1128/jb.00992-09 (2009).

131 Bowman, G. R. *et al.* Caulobacter PopZ forms a polar subdomain dictating sequential changes in pole composition and function. *Molecular Microbiology* **76**, 173-189, doi:10.1111/j.1365-2958.2010.07088.x (2010).

132 Bowman, G. R. *et al.* A polymeric protein anchors the chromosomal origin/ParB complex at a bacterial cell pole. *Cell* **134**, 945-955, doi:10.1016/j.cell.2008.07.015 (2008).

133 Ebersbach, G., Briegel, A., Jensen, G. J. & Jacobs-Wagner, C. A self-associating protein critical for chromosome attachment, division, and polar organization in caulobacter. *Cell* **134**, 956-968, doi:10.1016/j.cell.2008.07.016 (2008).

134 Holmes, J. A. *et al.* Caulobacter PopZ forms an intrinsically disordered hub in organizing bacterial cell poles. *Proceedings of the National Academy of Sciences of the United States of America* **113**, 12490-12495, doi:10.1073/pnas.1602380113 (2016).

135 Wheeler, R. T. & Shapiro, L. Differential localization of two histidine kinases controlling bacterial cell differentiation. *Molecular cell* **4**, 683-694 (1999).

136 Aldridge, P., Paul, R., Goymer, P., Rainey, P. & Jenal, U. Role of the GGDEF regulator PleD in polar development of Caulobacter crescentus. *Molecular microbiology* **47**, 1695-1708 (2003).

137 Curtis, P. D. & Brun, Y. V. Getting in the loop: regulation of development in Caulobacter crescentus. *Microbiology and molecular biology reviews : MMBR* **74**, 13-41, doi:10.1128/MMBR.00040-09 (2010).

138 Lakowicz, J. R. & SpringerLink (Online service). (Springer Science+Business Media, LLC,, Boston, MA, 2006).

139 Sarkar, P. *et al.* Deciphering CaMKII Multimerization Using Fluorescence Correlation Spectroscopy and Homo-FRET Analysis. *Biophysical journal* **112**, 1270-1281, doi:10.1016/j.bpj.2017.02.005 (2017).

140 Watanabe, S. [Fluorescent indicators for Ca2+ based on green fluorescent proteins and calmodulin]. *Tanpakushitsu kakusan koso. Protein, nucleic acid, enzyme* **52**, 1770-1771 (2007).

141 Bajar, B. T., Wang, E. S., Zhang, S., Lin, M. Z. & Chu, J. A Guide to Fluorescent Protein FRET Pairs. *Sensors* **16**, doi:10.3390/s16091488 (2016).

142 Bajar, B. T. *et al.* Improving brightness and photostability of green and red fluorescent proteins for live cell imaging and FRET reporting. *Scientific reports* **6**, 20889, doi:10.1038/srep20889 (2016).

143 Kredel, S. *et al.* Optimized and far-red-emitting variants of fluorescent protein eqFP611. *Chemistry & biology* **15**, 224-233, doi:10.1016/j.chembiol.2008.02.008 (2008).

144 Ohashi, T., Galiacy, S. D., Briscoe, G. & Erickson, H. P. An experimental study of GFP-based FRET, with application to intrinsically unstructured proteins. *Protein science : a publication of the Protein Society* **16**, 1429-1438, doi:10.1110/ps.072845607 (2007).

145 Leahy, D. J., Aukhil, I. & Erickson, H. P. 2.0 A crystal structure of a four-domain segment of human fibronectin encompassing the RGD loop and synergy region. *Cell* **84**, 155-164 (1996).

146 Harnos, J. *et al.* Dishevelled-3 conformation dynamics analyzed by FRET-based biosensors reveals a key role of casein kinase 1. *Nature communications* **10**, 1804, doi:10.1038/s41467-019-09651-7 (2019).

147 Tsokos, C. G. & Laub, M. T. Polarity and cell fate asymmetry in Caulobacter crescentus. *Current opinion in microbiology* **15**, 744-750, doi:10.1016/j.mib.2012.10.011 (2012).

148 Lori, C. *et al.* Cyclic di-GMP acts as a cell cycle oscillator to drive chromosome replication. *Nature* **523**, 236-239, doi:10.1038/nature14473 (2015).

149 Schrader, J. M. & Shapiro, L. Synchronization of Caulobacter crescentus for investigation of the bacterial cell cycle. *J Vis Exp*, doi:10.3791/52633 (2015).

150 Jacobs, C., Ausmees, N., Cordwell, S. J., Shapiro, L. & Laub, M. T. Functions of the CckA histidine kinase in Caulobacter cell cycle control. *Molecular Microbiology* **47**, 1279-1290 (2003).

151 Moore, J. O. & Hendrickson, W. A. An asymmetry-to-symmetry switch in signal transmission by the histidine kinase receptor for TMAO. *Structure* **20**, 729-741, doi:10.1016/j.str.2012.02.021 (2012).

152 Nadler, D. C., Morgan, S. A., Flamholz, A., Kortright, K. E. & Savage, D. F. Rapid construction of metabolite biosensors using domain-insertion profiling. *Nature communications* **7**, 12266, doi:10.1038/ncomms12266 (2016).

153 Miller, S. I., Kukral, A. M. & Mekalanos, J. J. A two-component regulatory system (phoP phoQ) controls Salmonella typhimurium virulence. *Proceedings of the National Academy of Sciences of the United States of America* **86**, 5054-5058 (1989).

154 Francis, V. I., Stevenson, E. C. & Porter, S. L. Two-component systems required for virulence in Pseudomonas aeruginosa. *FEMS Microbiol Lett* **364**, doi:10.1093/femsle/fnx104 (2017).

155 Duvall, S. W. & Childers, W. S. Design of a Histidine Kinase FRET Sensor to Detect Complex Signal Integration within Living Bacteria. *ACS Sens*, doi:10.1021/acssensors.0c00008 (2020).

156 Yuan, J., Jin, F., Glatter, T. & Sourjik, V. Osmosensing by the bacterial PhoQ/PhoP two-component system. *Proceedings of the National Academy of Sciences* **114**, E10792, doi:10.1073/pnas.1717272114 (2017).

157 Ames, P., Zhou, Q. & Parkinson, J. S. Mutational Analysis of the Connector Segment in the HAMP Domain of Tsr, the Escherichia coli Serine Chemoreceptor. *Journal of bacteriology* **190**, 6676, doi:10.1128/JB.00750-08 (2008).

158 Castelli, M. E., Cauerhff, A., Amongero, M., Soncini, F. C. & Vescovi, E. G. The H box-harboring domain is key to the function of the Salmonella enterica PhoQ Mg2+-sensor in the recognition of its partner PhoP. *The Journal of biological chemistry* **278**, 23579-23585, doi:10.1074/jbc.M303042200 (2003).

159 Bader, M. W. *et al.* Recognition of Antimicrobial Peptides by a Bacterial Sensor Kinase. *Cell* **122**, 461-472, doi:https://doi.org/10.1016/j.cell.2005.05.030 (2005).

160 Cho, U. S. *et al.* Metal Bridges between the PhoQ Sensor Domain and the Membrane Regulate Transmembrane Signaling. *Journal of molecular biology* **356**, 1193-1206, doi:https://doi.org/10.1016/j.jmb.2005.12.032 (2006).

161 Prost, L. R. *et al.* Activation of the Bacterial Sensor Kinase PhoQ by Acidic pH. *Molecular cell* **26**, 165-174, doi:10.1016/j.molcel.2007.03.008 (2007).

162 Goldberg, S. D., Clinthorne, G. D., Goulian, M. & DeGrado, W. F. Transmembrane polar interactions are required for signaling in the Escherichia coli sensor kinase PhoQ. *Proceedings of the National Academy of Sciences* **107**, 8141-8146, doi:10.1073/pnas.1003166107 (2010).

163 Duvall, S. W. & Childers, W. S. Design of a Histidine Kinase FRET Sensor to Detect Complex Signal Integration within Living Bacteria. *ACS Sens* **5**, 1589-1596, doi:10.1021/acssensors.0c00008 (2020).

164 Ely, B. & Johnson, R. C. Generalized Transduction in CAULOBACTER CRESCENTUS. *Genetics* **87**, 391-399 (1977).

165 Schindelin, J. *et al.* Fiji: an open-source platform for biological-image analysis. *Nature methods* **9**, 676-682, doi:10.1038/nmeth.2019 (2012).

166 Ducret, A., Quardokus, E. M. & Brun, Y. V. MicrobeJ, a tool for high throughput bacterial cell detection and quantitative analysis. *Nature microbiology* **1**, 16077, doi:10.1038/nmicrobiol.2016.77 (2016).

167 Hillson, N. J., Rosengarten, R. D. & Keasling, J. D. j5 DNA assembly design automation software. *ACS synthetic biology* **1**, 14-21, doi:10.1021/sb2000116 (2012).

168 Gibson, D. G. *et al.* Enzymatic assembly of DNA molecules up to several hundred kilobases. *Nature methods* **6**, 343-345, doi:10.1038/nmeth.1318 (2009).

169 Thanbichler, M., Iniesta, A. A. & Shapiro, L. A comprehensive set of plasmids for vanillate- and xylose-inducible gene expression in Caulobacter crescentus. *Nucleic Acids Research* **35**, e137, doi:10.1093/nar/gkm818 (2007).

170 Papon, N. & Stock, A. M. Two-component systems. *Current biology : CB* **29**, R724-R725, doi:10.1016/j.cub.2019.06.010 (2019).

171 West, A. H. & Stock, A. M. Histidine kinases and response regulator proteins in two-component signaling systems. *Trends in biochemical sciences* **26**, 369-376, doi:10.1016/s0968-0004(01)01852-7 (2001).

172 Ho, Y. S., Burden, L. M. & Hurley, J. H. Structure of the GAF domain, a ubiquitous signaling motif and a new class of cyclic GMP receptor. *The EMBO journal* **19**, 5288-5299, doi:10.1093/emboj/19.20.5288 (2000).

173 Iniesta, A. A., Hillson, N. J. & Shapiro, L. Polar remodeling and histidine kinase activation, which is essential for Caulobacter cell cycle progression, are dependent on DNA replication initiation. *Journal of bacteriology* **192**, 3893-3902, doi:10.1128/JB.00468-10 (2010).

174 Bowman, G. R. *et al.* Caulobacter PopZ forms a polar subdomain dictating sequential changes in pole composition and function. *Molecular microbiology* **76**, 173-189, doi:10.1111/j.1365-2958.2010.07088.x (2010).

175 Sommer, J. M. & Newton, A. Pseudoreversion analysis indicates a direct role of cell division genes in polar morphogenesis and differentiation in Caulobacter crescentus. *Genetics* **129**, 623-630 (1991).

176 Vo, C. D. *et al.* Repurposing Hsp90 inhibitors as antibiotics targeting histidine kinases. *Bioorganic & medicinal chemistry letters* **27**, 5235-5244, doi:10.1016/j.bmcl.2017.10.036 (2017).

177 Kiianitsa, K., Solinger, J. A. & Heyer, W. D. NADH-coupled microplate photometric assay for kinetic studies of ATP-hydrolyzing enzymes with low and high specific activities. *Analytical biochemistry* **321**, 266-271, doi:10.1016/s0003-2697(03)00461-5 (2003).

178 Schneider, C. A., Rasband, W. S. & Eliceiri, K. W. NIH Image to ImageJ: 25 years of image analysis. *Nat Methods* **9**, 671-675 (2012).

179 Holmes, J. A. *et al.* Caulobacter PopZ forms an intrinsically disordered hub in organizing bacterial cell poles. *Proceedings of the National Academy of Sciences*, doi:10.1073/pnas.1602380113 (2016).

180 Rocco, C. J., Dennison, K. L., Klenchin, V. A., Rayment, I. & Escalante-Semerena, J. C. Construction and use of new cloning vectors for the rapid isolation of recombinant proteins from Escherichia coli. *Plasmid* **59**, 231-237, doi:10.1016/j.plasmid.2008.01.001 (2008).

181 Thanbichler, M., Iniesta, A. A. & Shapiro, L. A comprehensive set of plasmids for vanillate- and xylose-inducible gene expression in Caulobacter crescentus. *Nucleic Acids Res* **35**, e137, doi:10.1093/nar/gkm818 (2007).

182 Zhao, W. *et al.* A circuit of protein-protein regulatory interactions enables polarity establishment in a bacterium. *bioRxiv*, 503250, doi:10.1101/503250 (2018).

183 Ventola, C. L. The antibiotic resistance crisis: part 1: causes and threats. *P & T : a peer-reviewed journal for formulary management* **40**, 277-283 (2015).

184 Ventola, C. L. The antibiotic resistance crisis: part 2: management strategies and new agents. *P & T : a peer-reviewed journal for formulary management* **40**, 344-352 (2015).

185 Perez-Perez, M., Jorge, P., Perez Rodriguez, G., Pereira, M. O. & Lourenco, A. Quorum sensing inhibition in Pseudomonas aeruginosa biofilms: new insights through network mining. *Biofouling* **33**, 128-142, doi:10.1080/08927014.2016.1272104 (2017).

186 Papenfort, K. *et al.* A Vibrio cholerae autoinducer-receptor pair that controls biofilm formation. *Nature chemical biology* **13**, 551-557, doi:10.1038/nchembio.2336 (2017).

187 Chen, X. *et al.* Structural identification of a bacterial quorum-sensing signal containing boron. *Nature* **415**, 545-549, doi:10.1038/415545a (2002).

188 Dutta, R. & Inouye, M. GHKL, an emergent ATPase/kinase superfamily. *Trends in biochemical sciences* **25**, 24-28 (2000).

189 Maloney, A. & Workman, P. HSP90 as a new therapeutic target for cancer therapy: the story unfolds. *Expert opinion on biological therapy* **2**, 3-24, doi:10.1517/14712598.2.1.3 (2002).

190 Khan, T. *et al.* DNA gyrase inhibitors: Progress and synthesis of potent compounds as antibacterial agents. *Biomed Pharmacother* **103**, 923-938, doi:10.1016/j.biopha.2018.04.021 (2018).

191 Guarne, A. The functions of MutL in mismatch repair: the power of multitasking. *Prog Mol Biol Transl Sci* **110**, 41-70, doi:10.1016/B978-0-12-387665-2.00003-1 (2012).

192 Wilke, K. E., Fihn, C. A. & Carlson, E. E. Screening serine/threonine and tyrosine kinase inhibitors for histidine kinase inhibition. *Bioorganic & medicinal chemistry* **26**, 5322-5326, doi:10.1016/j.bmc.2018.04.047 (2018).

193 Schaller, G. E., Shiu, S. H. & Armitage, J. P. Two-component systems and their co-option for eukaryotic signal transduction. *Current biology : CB* **21**, R320-330, doi:10.1016/j.cub.2011.02.045 (2011).

194 Hanks, S. K. & Hunter, T. Protein kinases 6. The eukaryotic protein kinase superfamily: kinase (catalytic) domain structure and classification. *FASEB journal : official publication of the Federation of American Societies for Experimental Biology* **9**, 576-596 (1995).

195 Kathiravan, M. K., Khilare, M. M., Nikoomanesh, K., Chothe, A. S. & Jain, K. S. Topoisomerase as target for antibacterial and anticancer drug discovery. *J Enzyme Inhib Med Chem* **28**, 419-435, doi:10.3109/14756366.2012.658785 (2013).

196 Guarnieri, M. T., Zhang, L., Shen, J. & Zhao, R. The Hsp90 inhibitor radicicol interacts with the ATP-binding pocket of bacterial sensor kinase PhoQ. *Journal of molecular biology* **379**, 82-93, doi:papers3://publication/doi/10.1016/j.jmb.2008.03.036 (2008).

197 Boibessot, T. *et al.* The Rational Design, Synthesis, and Antimicrobial Properties of Thiophene Derivatives That Inhibit Bacterial Histidine Kinases. *Journal of medicinal chemistry* **59**, 8830-8847, doi:10.1021/acs.jmedchem.6b00580 (2016).

198 Goswami, M., Wilke, K. E. & Carlson, E. E. Rational Design of Selective Adenine-Based Scaffolds for Inactivation of Bacterial Histidine Kinases. *Journal of medicinal chemistry* **60**, 8170-8182, doi:10.1021/acs.jmedchem.7b01066 (2017).

199 Wilke, K. E., Francis, S. & Carlson, E. E. Inactivation of multiple bacterial histidine kinases by targeting the ATP-binding domain. *ACS chemical biology* **10**, 328-335, doi:10.1021/cb5008019 (2015).

200 Mehdi, S. J. *et al.* Protein Kinases and Parkinson's Disease. *International journal of molecular sciences* **17**, doi:10.3390/ijms17091585 (2016).

201 Ryder, J., Su, Y. & Ni, B. Akt/GSK3beta serine/threonine kinases: evidence for a signalling pathway mediated by familial Alzheimer's disease mutations. *Cell Signal* **16**, 187-200, doi:10.1016/j.cellsig.2003.07.004 (2004).

202 Stewart, R. C., VanBruggen, R., Ellefson, D. D. & Wolfe, A. J. TNP-ATP and TNP-ADP as probes of the nucleotide binding site of CheA, the histidine protein kinase in the chemotaxis signal transduction pathway of Escherichia coli. *Biochemistry* **37**, 12269-12279, doi:10.1021/bi980970n (1998).

203 Niesen, F. H., Berglund, H. & Vedadi, M. The use of differential scanning fluorimetry to detect ligand interactions that promote protein stability. *Nature protocols* **2**, 2212-2221, doi:10.1038/nprot.2007.321 (2007).

204 Steinberg, T. H., Jones, L. J., Haugland, R. P. & Singer, V. L. SYPRO orange and SYPRO red protein gel stains: one-step fluorescent staining of denaturing gels for detection of nanogram levels of protein. *Analytical biochemistry* **239**, 223-237, doi:10.1006/abio.1996.0319 (1996).

205 Pantoliano, M. W. *et al.* High-density miniaturized thermal shift assays as a general strategy for drug discovery. *Journal of biomolecular screening : the official journal of the Society for Biomolecular Screening* **6**, 429-440, doi:10.1089/108705701753364922 (2001).

206 Lo, M. C. *et al.* Evaluation of fluorescence-based thermal shift assays for hit identification in drug discovery. *Analytical biochemistry* **332**, 153-159, doi:10.1016/j.ab.2004.04.031 (2004).

207 Mohedano, M. L. *et al.* Evidence that the essential response regulator YycF in Streptococcus pneumoniae modulates expression of fatty acid biosynthesis genes and alters membrane composition. *Journal of bacteriology* **187**, 2357-2367, doi:10.1128/JB.187.7.2357-2367.2005 (2005).

208 Lopez-Redondo, M. L. *et al.* Environmental control of phosphorylation pathways in a branched two-component system. *Molecular microbiology* **78**, 475-489, doi:10.1111/j.1365-2958.2010.07348.x (2010).

209 Velikova, N. *et al.* Putative histidine kinase inhibitors with antibacterial effect against multi-drug resistant clinical isolates identified by in vitro and in silico screens. *Scientific reports* **6**, 26085, doi:10.1038/srep26085 (2016).

210 Cozzini, P. *et al.* Target flexibility: an emerging consideration in drug discovery and design. *Journal of medicinal chemistry* **51**, 6237-6255, doi:10.1021/jm800562d (2008).

211 Bilwes, A. M., Quezada, C. M., Croal, L. R., Crane, B. R. & Simon, M. I. Nucleotide binding by the histidine kinase CheA. *Nat Struct Biol* **8**, 353-360, doi:10.1038/86243 (2001).

212 Bick, M. J. *et al.* How to switch off a histidine kinase: crystal structure of Geobacillus stearothermophilus KinB with the inhibitor Sda. *Journal of molecular biology* **386**, 163-177, doi:10.1016/j.jmb.2008.12.006 (2009).

213 Rogers, D. & Hahn, M. Extended-connectivity fingerprints. *J Chem Inf Model* **50**, 742-754, doi:10.1021/ci100050t (2010).

214 Brough, P. A. *et al.* 4,5-diarylisoxazole Hsp90 chaperone inhibitors: potential therapeutic agents for the treatment of cancer. *Journal of medicinal chemistry* **51**, 196-218, doi:10.1021/jm701018h (2008).

215 Cheung, K.-M. J. *et al.* The identification, synthesis, protein crystal structure and in vitro biochemical evaluation of a new 3,4-diarylpyrazole class of Hsp90 inhibitors. *Bioorganic & medicinal chemistry letters* **15**, 3338-3343, doi:papers3://publication/doi/10.1016/j.bmcl.2005.05.046 (2005).

216 Kasibhatla, S. R. *et al.* Rationally designed high-affinity 2-amino-6-halopurine heat shock protein 90 inhibitors that exhibit potent antitumor activity. *Journal of medicinal chemistry* **50**, 2767-2778, doi:10.1021/jm050752 (2007).

217 Bao, R. *et al.* CUDC-305, a novel synthetic HSP90 inhibitor with unique pharmacologic properties for cancer therapy. *Clinical cancer research : an official journal of the American Association for Cancer Research* **15**, 4046-4057, doi:10.1158/1078-0432.CCR-09-0152 (2009).

218 Groisman, E. A. The pleiotropic two-component regulatory system PhoP-PhoQ. *Journal of bacteriology* **183**, 1835-1842, doi:10.1128/JB.183.6.1835-1842.2001 (2001).

219 Roe, S. M. *et al.* Structural basis for inhibition of the Hsp90 molecular chaperone by the antitumor antibiotics radicicol and geldanamycin. *Journal of medicinal chemistry* **42**, 260-266, doi:10.1021/jm980403y (1999).

220 Guarnieri, M. T., Blagg, B. S. & Zhao, R. A high-throughput TNP-ATP displacement assay for screening inhibitors of ATP-binding in bacterial histidine kinases. *Assay Drug Dev Technol* **9**, 174-183, doi:10.1089/adt.2010.0289 (2011).

221 Broglie, K. E. & Takahashi, M. Fluorescence studies of threonine-promoted conformational transitions in aspartokinase I using the substrate analogue 2'(3')-O-(2,4,6-trinitrophenyl)adenosine 5'-triphosphate. *The Journal of biological chemistry* **258**, 12940-12946 (1983).

222 Vo, C. D. *et al. Repurposing Hsp90 inhibitors as antibiotics targeting histidine kinases* (2017, under review).

223 Wu, J., Ohta, N. & Newton, A. An essential, multicomponent signal transduction pathway required for cell cycle regulation in Caulobacter. *Proceedings of the National Academy of Sciences of the United States of America* **95**, 1443-1448 (1998).

224 Dymock, B. W. *et al.* Novel, potent small-molecule inhibitors of the molecular chaperone Hsp90 discovered through structure-based design. *Journal of medicinal chemistry* **48**, 4212-4215, doi:10.1021/jm050355z (2005).

225 Cheung, K. M. *et al.* The identification, synthesis, protein crystal structure and in vitro biochemical evaluation of a new 3,4-diarylpyrazole class of Hsp90 inhibitors. *Bioorganic & medicinal chemistry letters* **15**, 3338-3343, doi:10.1016/j.bmcl.2005.05.046 (2005).

226 Clark, D. Factors affecting the entry of antibiotics into Escherichia coli. *Microbios* **41**, 107-115 (1984).

227 Poindexter, J. S. The role of calcium in stalk development and in phosphate acquisition in Caulobacter crescentus. *Archives of microbiology* **138**, 140-152 (1984).

228 Alangaden, G. J. *et al.* Mechanism of resistance to amikacin and kanamycin in Mycobacterium tuberculosis. *Antimicrob Agents Chemother* **42**, 1295-1297, doi:10.1128/AAC.42.5.1295 (1998).

229 Ptacin, J. L. *et al.* A spindle-like apparatus guides bacterial chromosome segregation. *Nature cell biology* **12**, 791-798, doi:10.1038/ncb2083 (2010).

230 Thanbichler, M. & Shapiro, L. MipZ, a spatial regulator coordinating chromosome segregation with cell division in Caulobacter. *Cell* **126**, 147-162, doi:10.1016/j.cell.2006.05.038 (2006).

231 Kinoshita, E., Kinoshita-Kikuta, E. & Koike, T. Separation and detection of large phosphoproteins using Phos-tag SDS-PAGE. *Nature protocols* **4**, 1513-1521, doi:10.1038/nprot.2009.154 (2009).

232 Ryan, K. R., Judd, E. M. & Shapiro, L. The CtrA response regulator essential for Caulobacter crescentus cell-cycle progression requires a bipartite degradation signal for temporally controlled proteolysis. *Journal of molecular biology* **324**, 443-455 (2002).

233 Iniesta, A. A. & Shapiro, L. A bacterial control circuit integrates polar localization and proteolysis of key regulatory proteins with a phospho-signaling cascade. *Proceedings of the National Academy of Sciences of the United States of America* **105**, 16602-16607, doi:10.1073/pnas.0808807105 (2008).

234 Toro, E., Hong, S. H., McAdams, H. H. & Shapiro, L. Caulobacter requires a dedicated mechanism to initiate chromosome segregation. *Proceedings of the National Academy of*

Sciences of the United States of America **105**, 15435-15440, doi:10.1073/pnas.0807448105 (2008).

235 Mohl, D. A., Easter, J., Jr. & Gober, J. W. The chromosome partitioning protein, ParB, is required for cytokinesis in Caulobacter crescentus. *Molecular microbiology* **42**, 741-755 (2001).

236 Soh, Y. M. *et al.* Self-organization of parS centromeres by the ParB CTP hydrolase. *Science* **366**, 1129-1133, doi:10.1126/science.aay3965 (2019).

237 Osorio-Valeriano, M. *et al.* ParB-type DNA Segregation Proteins Are CTP-Dependent Molecular Switches. *Cell* **179**, 1512-1524 e1515, doi:10.1016/j.cell.2019.11.015 (2019).

238 Jalal, A. S., Tran, N. T. & Le, T. B. ParB spreading on DNA requires cytidine triphosphate in vitro. *Elife* **9**, doi:10.7554/eLife.53515 (2020).

239 Pogliano, J. The bacterial cytoskeleton. *Curr Opin Cell Biol* **20**, 19-27, doi:10.1016/j.ceb.2007.12.006 (2008).

240 Ptacin, J. L. *et al.* Bacterial scaffold directs pole-specific centromere segregation. *Proceedings of the National Academy of Sciences of the United States of America* **111**, E2046-2055, doi:10.1073/pnas.1405188111 (2014).

241 Wang, S. C. & Shapiro, L. The topoisomerase IV ParC subunit colocalizes with the Caulobacter replisome and is required for polar localization of replication origins. *Proceedings of the National Academy of Sciences of the United States of America* **101**, 9251-9256, doi:10.1073/pnas.0402567101 (2004).

242 Peng, H. & Marians, K. J. Escherichia coli topoisomerase IV. Purification, characterization, subunit structure, and subunit interactions. *The Journal of biological chemistry* **268**, 24481-24490 (1993).

243 Koteva, K. *et al.* A vancomycin photoprobe identifies the histidine kinase VanSsc as a vancomycin receptor. *Nature chemical biology* **6**, 327-329, doi:10.1038/nchembio.350 (2010).

244 Rodriguez, N. & Goossen, L. J. Decarboxylative coupling reactions: a modern strategy for C-C-bond formation. *Chemical Society reviews* **40**, 5030-5048, doi:10.1039/c1cs15093f (2011).

245 Murale, D. P., Hong, S. C., Haque, M. M. & Lee, J. S. Photo-affinity labeling (PAL) in chemical proteomics: a handy tool to investigate protein-protein interactions (PPIs). *Proteome Sci* **15**, 14, doi:10.1186/s12953-017-0123-3 (2016).

246 Zhang, S. C., Wernig, M., Duncan, I. D., Brustle, O. & Thomson, J. A. In vitro differentiation of transplantable neural precursors from human embryonic stem cells. *Nature biotechnology* **19**, 1129-1133, doi:10.1038/nbt1201-1129 (2001).

247 Faux, M. C. & Scott, J. D. Molecular glue: kinase anchoring and scaffold proteins. *Cell* **85**, 9-12, doi:10.1016/s0092-8674(00)81075-2 (1996).

248 Good, M. C., Zalatan, J. G. & Lim, W. A. Scaffold proteins: hubs for controlling the flow of cellular information. *Science* **332**, 680-686, doi:10.1126/science.1198701 (2011).

249 Garbett, D. & Bretscher, A. The surprising dynamics of scaffolding proteins. *Molecular biology of the cell* **25**, 2315-2319, doi:10.1091/mbc.E14-04-0878 (2014).

250 Xiao, J. & Goley, E. D. Redefining the roles of the FtsZ-ring in bacterial cytokinesis. *Current opinion in microbiology* **34**, 90-96, doi:10.1016/j.mib.2016.08.008 (2016).

251 Young, E. J. *et al.* Engineering the Bacterial Microcompartment Domain for Molecular Scaffolding Applications. *Frontiers in microbiology* **8**, 1441, doi:10.3389/fmicb.2017.01441 (2017).

252 Kysela, D. T., Brown, P. J., Huang, K. C. & Brun, Y. V. Biological consequences and advantages of asymmetric bacterial growth. *Annual review of microbiology* **67**, 417-435, doi:10.1146/annurev-micro-092412-155622 (2013).

253 Matroule, J. Y., Lam, H., Burnette, D. T. & Jacobs-Wagner, C. Cytokinesis monitoring during development; rapid pole-to-pole shuttling of a signaling protein by localized kinase and phosphatase in Caulobacter. *Cell* **118**, 579-590, doi:10.1016/j.cell.2004.08.019 (2004).

254 Lasker, K., Mann, T. H. & Shapiro, L. An intracellular compass spatially coordinates cell cycle modules in Caulobacter crescentus. *Current opinion in microbiology* **33**, 131-139, doi:10.1016/j.mib.2016.06.007 (2016).

255 Jacobs, C., Hung, D. & Shapiro, L. Dynamic localization of a cytoplasmic signal transduction response regulator controls morphogenesis during the Caulobacter cell cycle. *Proceedings of the National Academy of Sciences of the United States of America* **98**, 4095-4100, doi:10.1073/pnas.051609998 (2001).

256 Perez, A. M. *et al.* A Localized Complex of Two Protein Oligomers Controls the Orientation of Cell Polarity. *mBio* **8**, doi:10.1128/mBio.02238-16 (2017).

257 Curtis, P. D. *et al.* The scaffolding and signalling functions of a localization factor impact polar development. *Molecular microbiology* **84**, 712-735, doi:10.1111/j.1365-2958.2012.08055.x (2012).

258 Dahlberg, P. D. *et al.* Cryogenic single-molecule fluorescence annotations for electron tomography reveal in situ organization of key proteins in Caulobacter. *Proceedings of the National Academy of Sciences of the United States of America* **117**, 13937-13944, doi:10.1073/pnas.2001849117 (2020).

259 Viollier, P. H., Sternheim, N. & Shapiro, L. Identification of a localization factor for the polar positioning of bacterial structural and regulatory proteins. *Proceedings of the*

National Academy of Sciences of the United States of America **99**, 13831-13836, doi:10.1073/pnas.182411999 (2002).

260 Schofield, W. B., Lim, H. C. & Jacobs-Wagner, C. Cell cycle coordination and regulation of bacterial chromosome segregation dynamics by polarly localized proteins. *The EMBO journal* **29**, 3068-3081, doi:10.1038/emboj.2010.207 (2010).

261 Berge, M. *et al.* Modularity and determinants of a (bi-)polarization control system from free-living and obligate intracellular bacteria. *Elife* **5**, doi:10.7554/eLife.20640 (2016).

262 Lawler, M. L., Larson, D. E., Hinz, A. J., Klein, D. & Brun, Y. V. Dissection of functional domains of the polar localization factor PodJ in Caulobacter crescentus. *Molecular microbiology* **59**, 301-316, doi:10.1111/j.1365-2958.2005.04935.x (2006).

263 Kozlowski, L. P. & Bujnicki, J. M. MetaDisorder: a meta-server for the prediction of intrinsic disorder in proteins. *BMC bioinformatics* **13**, 111, doi:10.1186/1471-2105-13-111 (2012).

264 Hanson, J., Yang, Y., Paliwal, K. & Zhou, Y. Improving protein disorder prediction by deep bidirectional long short-term memory recurrent neural networks. *Bioinformatics* **33**, 685-692, doi:10.1093/bioinformatics/btw678 (2017).

265 Walsh, I. *et al.* CSpritz: accurate prediction of protein disorder segments with annotation for homology, secondary structure and linear motifs. *Nucleic Acids Res* **39**, W190-196, doi:10.1093/nar/gkr411 (2011).

266 Skerker, J. M. & Shapiro, L. Identification and cell cycle control of a novel pilus system in Caulobacter crescentus. *The EMBO journal* **19**, 3223-3234, doi:10.1093/emboj/19.13.3223 (2000).

267 Viollier, P. H., Sternheim, N. & Shapiro, L. A dynamically localized histidine kinase controls the asymmetric distribution of polar pili proteins. *The EMBO journal* **21**, 4420-4428, doi:10.1093/emboj/cdf454 (2002).

268 Del Medico, L., Cerletti, D., Schachle, P., Christen, M. & Christen, B. The type IV pilin PilA couples surface attachment and cell-cycle initiation in Caulobacter crescentus. *Proceedings of the National Academy of Sciences of the United States of America* **117**, 9546-9553, doi:10.1073/pnas.1920143117 (2020).

269 Hinz, A. J., Larson, D. E., Smith, C. S. & Brun, Y. V. The Caulobacter crescentus polar organelle development protein PodJ is differentially localized and is required for polar targeting of the PleC development regulator. *Molecular microbiology* **47**, 929-941, doi:10.1046/j.1365-2958.2003.03349.x (2003).

270 Schrader, J. M. *et al.* Dynamic translation regulation in Caulobacter cell cycle control. *Proceedings of the National Academy of Sciences of the United States of America* **113**, E6859-E6867, doi:10.1073/pnas.1614795113 (2016).

271 Balleza, E., Kim, J. M. & Cluzel, P. Systematic characterization of maturation time of fluorescent proteins in living cells. *Nature methods* **15**, 47-51, doi:10.1038/nmeth.4509 (2018).

272 Du, Y. Fluorescence polarization assay to quantify protein-protein interactions in an HTS format. *Methods in molecular biology (Clifton, N.J.)* **1278**, 529-544, doi:10.1007/978-1-4939-2425-7_35 (2015).

273 Lasker, K. *et al.* Selective sequestration of signalling proteins in a membraneless organelle reinforces the spatial regulation of asymmetry in Caulobacter crescentus. *Nature microbiology* **5**, 418-429, doi:10.1038/s41564-019-0647-7 (2020).

274 Goley, E. D. *et al.* Assembly of the Caulobacter cell division machine. *Molecular microbiology* **80**, 1680-1698, doi:10.1111/j.1365-2958.2011.07677.x (2011).

275 Goley, E. D. Tiny cells meet big questions: a closer look at bacterial cell biology. *Molecular biology of the cell* **24**, 1099-1102, doi:10.1091/mbc.E12-11-0788 (2013).

276 Quardokus, E. M., Din, N. & Brun, Y. V. Cell cycle and positional constraints on FtsZ localization and the initiation of cell division in Caulobacter crescentus. *Molecular microbiology* **39**, 949-959 (2001).

277 Corrales-Guerrero, L. *et al.* Molecular architecture of the DNA-binding sites of the P-loop ATPases MipZ and ParA from Caulobacter crescentus. *Nucleic Acids Res* **48**, 4769-4779, doi:10.1093/nar/gkaa192 (2020).

278 Li, X. T., Thomason, L. C., Sawitzke, J. A., Costantino, N. & Court, D. L. Positive and negative selection using the tetA-sacB cassette: recombineering and P1 transduction in Escherichia coli. *Nucleic Acids Res* **41**, e204, doi:10.1093/nar/gkt1075 (2013).

279 Sun, Y., Sun, T. L. & Huang, H. W. Physical properties of Escherichia coli spheroplast membranes. *Biophysical journal* **107**, 2082-2090, doi:10.1016/j.bpj.2014.09.034 (2014).

280 Figge, R. M., Divakaruni, A. V. & Gober, J. W. MreB, the cell shape-determining bacterial actin homologue, co-ordinates cell wall morphogenesis in Caulobacter crescentus. *Molecular microbiology* **51**, 1321-1332, doi:10.1111/j.1365-2958.2003.03936.x (2004).

281 Lam, H., Schofield, W. B. & Jacobs-Wagner, C. A landmark protein essential for establishing and perpetuating the polarity of a bacterial cell. *Cell* **124**, 1011-1023, doi:10.1016/j.cell.2005.12.040 (2006).

282 Shaner, N. C. *et al.* A bright monomeric green fluorescent protein derived from Branchiostoma lanceolatum. *Nature methods* **10**, 407-409, doi:10.1038/nmeth.2413 (2013).

283 Biteen, J. S. & Moerner, W. E. Single-molecule and superresolution imaging in live bacteria cells. *Cold Spring Harbor perspectives in biology* **2**, a000448, doi:10.1101/cshperspect.a000448 (2010).

284 Thanbichler, M., Iniesta, A. A. & Shapiro, L. A comprehensive set of plasmids for vanillate- and xylose-inducible gene expression in Caulobacter crescentus. *Nucleic Acids Research* **35**, doi:e137 10.1093/nar/gkm818 (2007).

285 Updegrove, T. B. & Ramamurthi, K. S. Geometric protein localization cues in bacterial cells. *Current opinion in microbiology* **36**, 7-13, doi:10.1016/j.mib.2016.12.001 (2017).

286 Laloux, G. & Jacobs-Wagner, C. How do bacteria localize proteins to the cell pole? *Journal of cell science* **127**, 11-19, doi:10.1242/jcs.138628 (2014).

287 Huang, K. C. & Ramamurthi, K. S. Macromolecules that prefer their membranes curvy. *Molecular microbiology* **76**, 822-832, doi:10.1111/j.1365-2958.2010.07168.x (2010).

288 Romantsov, T., Battle, A. R., Hendel, J. L., Martinac, B. & Wood, J. M. Protein localization in Escherichia coli cells: comparison of the cytoplasmic membrane proteins ProP, LacY, ProW, AqpZ, MscS, and MscL. *Journal of bacteriology* **192**, 912-924, doi:10.1128/JB.00967-09 (2010).

289 Yamaichi, Y. *et al.* A multidomain hub anchors the chromosome segregation and chemotactic machinery to the bacterial pole. *Genes & development* **26**, 2348-2360, doi:10.1101/gad.199869.112 (2012).

290 Zapun, A., Vernet, T. & Pinho, M. G. The different shapes of cocci. *FEMS microbiology reviews* **32**, 345-360, doi:10.1111/j.1574-6976.2007.00098.x (2008).

291 Chang, F. & Huang, K. C. How and why cells grow as rods. *BMC biology* **12**, 54, doi:10.1186/s12915-014-0054-8 (2014).

292 Wolgemuth, C. W. Flagellar motility of the pathogenic spirochetes. *Semin Cell Dev Biol* **46**, 104-112, doi:10.1016/j.semcdb.2015.10.015 (2015).

293 Cabeen, M. T. & Jacobs-Wagner, C. Bacterial cell shape. *Nature reviews. Microbiology* **3**, 601-610, doi:10.1038/nrmicro1205 (2005).

294 Caccamo, P. D. & Brun, Y. V. The Molecular Basis of Noncanonical Bacterial Morphology. *Trends in microbiology* **26**, 191-208, doi:10.1016/j.tim.2017.09.012 (2018).

295 Yang, D. C., Blair, K. M. & Salama, N. R. Staying in Shape: the Impact of Cell Shape on Bacterial Survival in Diverse Environments. *Microbiology and molecular biology reviews : MMBR* **80**, 187-203, doi:10.1128/MMBR.00031-15 (2016).

296 Ausmees, N., Kuhn, J. R. & Jacobs-Wagner, C. The bacterial cytoskeleton: an intermediate filament-like function in cell shape. *Cell* **115**, 705-713, doi:10.1016/s0092-8674(03)00935-8 (2003).

297 Cabeen, M. T. *et al.* Bacterial cell curvature through mechanical control of cell growth. *The EMBO journal* **28**, 1208-1219, doi:10.1038/emboj.2009.61 (2009).

298 Persat, A., Stone, H. A. & Gitai, Z. The curved shape of Caulobacter crescentus enhances surface colonization in flow. *Nature communications* **5**, 3824, doi:10.1038/ncomms4824 (2014).

299 Bartlett, T. M. *et al.* A Periplasmic Polymer Curves Vibrio cholerae and Promotes Pathogenesis. *Cell* **168**, 172-185 e115, doi:10.1016/j.cell.2016.12.019 (2017).

300 Vollmer, W., Blanot, D. & de Pedro, M. A. Peptidoglycan structure and architecture. *FEMS microbiology reviews* **32**, 149-167, doi:10.1111/j.1574-6976.2007.00094.x (2008).

301 Schleifer, K. H. & Kandler, O. Peptidoglycan types of bacterial cell walls and their taxonomic implications. *Bacteriological reviews* **36**, 407-477 (1972).

302 Sauer, S. & Kliem, M. Mass spectrometry tools for the classification and identification of bacteria. *Nature reviews. Microbiology* **8**, 74-82, doi:10.1038/nrmicro2243 (2010).

303 Pandey, N. & Cascella, M. in *StatPearls* (2020).

304 Sharon, N. The chemical structure of lysozyme substrates and their cleavage by the enzyme. *Proc R Soc Lond B Biol Sci* **167**, 402-415, doi:10.1098/rspb.1967.0037 (1967).

305 Yahashiri, A., Jorgenson, M. A. & Weiss, D. S. The SPOR Domain, a Widely Conserved Peptidoglycan Binding Domain That Targets Proteins to the Site of Cell Division. *Journal of bacteriology* **199**, doi:10.1128/JB.00118-17 (2017).

306 Duncan, T. R., Yahashiri, A., Arends, S. J., Popham, D. L. & Weiss, D. S. Identification of SPOR domain amino acids important for septal localization, peptidoglycan binding, and a disulfide bond in the cell division protein FtsN. *Journal of bacteriology* **195**, 5308-5315, doi:10.1128/JB.00911-13 (2013).

307 Nilsen, T., Ghosh, A. S., Goldberg, M. B. & Young, K. D. Branching sites and morphological abnormalities behave as ectopic poles in shape-defective Escherichia coli. *Molecular microbiology* **52**, 1045-1054, doi:10.1111/j.1365-2958.2004.04050.x (2004).

308 Scheffers, D. J. & Pinho, M. G. Bacterial cell wall synthesis: new insights from localization studies. *Microbiology and molecular biology reviews : MMBR* **69**, 585-607, doi:10.1128/MMBR.69.4.585-607.2005 (2005).

309 Margolin, W. Sculpting the bacterial cell. *Current biology : CB* **19**, R812-822, doi:10.1016/j.cub.2009.06.033 (2009).

310 Park, W. M. Coiled-Coils: the Molecular Zippers that Self-Assemble Protein Nanostructures. *International journal of molecular sciences* **21**, doi:10.3390/ijms21103584 (2020).

311 Al-Husini, N., Tomares, D. T., Childers, W. S. & Schrader, J. α-proteobacterial RNA degradosomes assemble liquid-liquid phase separated RNP bodies. *Molecular cell* (2018).

312 Al-Husini, N. *et al.* BR-Bodies Provide Selectively Permeable Condensates that Stimulate mRNA Decay and Prevent Release of Decay Intermediates. *Molecular cell*, doi:10.1016/j.molcel.2020.04.001 (2020).

313 Bean, G. J. *et al.* A22 disrupts the bacterial actin cytoskeleton by directly binding and inducing a low-affinity state in MreB. *Biochemistry* **48**, 4852-4857, doi:10.1021/bi900014d (2009).

314 Kiekebusch, D., Michie, K. A., Essen, L. O., Lowe, J. & Thanbichler, M. Localized dimerization and nucleoid binding drive gradient formation by the bacterial cell division inhibitor MipZ. *Molecular cell* **46**, 245-259, doi:10.1016/j.molcel.2012.03.004 (2012).

315 Ghuysen, J. M., Lamotte-Brasseur, J., Joris, B. & Shockman, G. D. Binding site-shaped repeated sequences of bacterial wall peptidoglycan hydrolases. *FEBS Lett* **342**, 23-28, doi:10.1016/0014-5793(94)80577-6 (1994).

316 Briers, Y. *et al.* Muralytic activity and modular structure of the endolysins of Pseudomonas aeruginosa bacteriophages phiKZ and EL. *Molecular microbiology* **65**, 1334-1344, doi:10.1111/j.1365-2958.2007.05870.x (2007).

317 Chen, Y., Simmonds, R. S. & Timkovich, R. Proposed docking interface between peptidoglycan and the target recognition domain of zoocin A. *Biochem Biophys Res Commun* **441**, 297-300, doi:10.1016/j.bbrc.2013.09.087 (2013).

318 Gish, W. & States, D. J. Identification of protein coding regions by database similarity search. *Nat Genet* **3**, 266-272, doi:10.1038/ng0393-266 (1993).

319 Drozdetskiy, A., Cole, C., Procter, J. & Barton, G. J. JPred4: a protein secondary structure prediction server. *Nucleic Acids Res* **43**, W389-394, doi:10.1093/nar/gkv332 (2015).

320 Waterhouse, A. *et al.* SWISS-MODEL: homology modelling of protein structures and complexes. *Nucleic Acids Res* **46**, W296-W303, doi:10.1093/nar/gky427 (2018).

321 Mastny, M. *et al.* CtpB assembles a gated protease tunnel regulating cell-cell signaling during spore formation in Bacillus subtilis. *Cell* **155**, 647-658, doi:10.1016/j.cell.2013.09.050 (2013).

322 Anderson-Furgeson, J. C., Zupan, J. R., Grangeon, R. & Zambryski, P. C. Loss of PodJ in Agrobacterium tumefaciens Leads to Ectopic Polar Growth, Branching, and Reduced Cell Division. *Journal of bacteriology* **198**, 1883-1891, doi:10.1128/jb.00198-16 (2016).

323 Brown, P. J. *et al.* Polar growth in the Alphaproteobacterial order Rhizobiales. *Proceedings of the National Academy of Sciences of the United States of America* **109**, 1697-1701, doi:10.1073/pnas.1114476109 (2012).

324 Cameron, T. A., Anderson-Furgeson, J., Zupan, J. R., Zik, J. J. & Zambryski, P. C. Peptidoglycan synthesis machinery in Agrobacterium tumefaciens during unipolar growth and cell division. *mBio* **5**, e01219-01214, doi:10.1128/mBio.01219-14 (2014).

325 Stankeviciute, G. *et al.* Differential modes of crosslinking establish spatially distinct regions of peptidoglycan in Caulobacter crescentus. *Molecular microbiology* **111**, 995-1008, doi:10.1111/mmi.14199 (2019).

326 McCormick, J. R., Su, E. P., Driks, A. & Losick, R. Growth and viability of Streptomyces coelicolor mutant for the cell division gene ftsZ. *Molecular microbiology* **14**, 243-254, doi:10.1111/j.1365-2958.1994.tb01285.x (1994).

327 Chater, K. F. Genetics of differentiation in Streptomyces. *Annual review of microbiology* **47**, 685-713, doi:10.1146/annurev.mi.47.100193.003345 (1993).

328 Zeytuni, N. & Zarivach, R. Structural and functional discussion of the tetra-trico-peptide repeat, a protein interaction module. *Structure* **20**, 397-405, doi:10.1016/j.str.2012.01.006 (2012).

329 Chen, Z., Atefi, E. & Baumgart, T. Membrane Shape Instability Induced by Protein Crowding. *Biophysical journal* **111**, 1823-1826, doi:10.1016/j.bpj.2016.09.039 (2016).

330 Renner, L. D., Eswaramoorthy, P., Ramamurthi, K. S. & Weibel, D. B. Studying biomolecule localization by engineering bacterial cell wall curvature. *PloS one* **8**, e84143, doi:10.1371/journal.pone.0084143 (2013).

331 Viollier, P. H. & Shapiro, L. A lytic transglycosylase homologue, PleA, is required for the assembly of pili and the flagellum at the Caulobacter crescentus cell pole. *Molecular microbiology* **49**, 331-345, doi:10.1046/j.1365-2958.2003.03576.x (2003).

332 Koonin, E. V. & Rudd, K. E. A conserved domain in putative bacterial and bacteriophage transglycosylases. *Trends in biochemical sciences* **19**, 106-107, doi:10.1016/0968-0004(94)90201-1 (1994).

333 Engel, H., Kazemier, B. & Keck, W. Murein-metabolizing enzymes from Escherichia coli: sequence analysis and controlled overexpression of the slt gene, which encodes the soluble lytic transglycosylase. *Journal of bacteriology* **173**, 6773-6782, doi:10.1128/jb.173.21.6773-6782.1991 (1991).

334 Pena, M. M. *et al.* mCherry fusions enable the subcellular localization of periplasmic and cytoplasmic proteins in Xanthomonas sp. *PloS one* **15**, e0236185, doi:10.1371/journal.pone.0236185 (2020).

335 Meiresonne, N. Y. *et al.* Superfolder mTurquoise2(ox) optimized for the bacterial periplasm allows high efficiency in vivo FRET of cell division antibiotic targets. *Molecular microbiology* **111**, 1025-1038, doi:10.1111/mmi.14206 (2019).

336 Choi-Rhee, E., Schulman, H. & Cronan, J. E. Promiscuous protein biotinylation by Escherichia coli biotin protein ligase. *Protein science : a publication of the Protein Society* **13**, 3043-3050, doi:10.1110/ps.04911804 (2004).

337 Geri, J. B. *et al.* Microenvironment mapping via Dexter energy transfer on immune cells. *Science* **367**, 1091-1097, doi:10.1126/science.aay4106 (2020).

338 Rees, J. S., Li, X. W., Perrett, S., Lilley, K. S. & Jackson, A. P. Selective Proteomic Proximity Labeling Assay Using Tyramide (SPPLAT): A Quantitative Method for the Proteomic Analysis of Localized Membrane-Bound Protein Clusters. *Curr Protoc Protein Sci* **80**, 19 27 11-19 27 18, doi:10.1002/0471140864.ps1927s80 (2015).

339 Branon, T. C. *et al.* Efficient proximity labeling in living cells and organisms with TurboID. *Nature biotechnology* **36**, 880-887, doi:10.1038/nbt.4201 (2018).

340 Roux, K. J., Kim, D. I., Burke, B. & May, D. G. BioID: A Screen for Protein-Protein Interactions. *Curr Protoc Protein Sci* **91**, 19 23 11-19 23 15, doi:10.1002/cpps.51 (2018).

341 Chapman-Smith, A. & Cronan, J. E., Jr. Molecular biology of biotin attachment to proteins. *J Nutr* **129**, 477S-484S, doi:10.1093/jn/129.2.477S (1999).

342 Jander, G., Cronan, J. E., Jr. & Beckwith, J. Biotinylation in vivo as a sensitive indicator of protein secretion and membrane protein insertion. *Journal of bacteriology* **178**, 3049-3058, doi:10.1128/jb.178.11.3049-3058.1996 (1996).

343 Ryu, Y. & Schultz, P. G. Efficient incorporation of unnatural amino acids into proteins in Escherichia coli. *Nature methods* **3**, 263-265, doi:10.1038/nmeth864 (2006).

344 Chin, J. W. Expanding and reprogramming the genetic code of cells and animals. *Annual review of biochemistry* **83**, 379-408, doi:10.1146/annurev-biochem-060713-035737 (2014).

345 Courtney, T. & Deiters, A. Recent advances in the optical control of protein function through genetic code expansion. *Curr Opin Chem Biol* **46**, 99-107, doi:10.1016/j.cbpa.2018.07.011 (2018).

346 Kim, C. H., Axup, J. Y. & Schultz, P. G. Protein conjugation with genetically encoded unnatural amino acids. *Curr Opin Chem Biol* **17**, 412-419, doi:10.1016/j.cbpa.2013.04.017 (2013).

347 Liu, W., Brock, A., Chen, S., Chen, S. & Schultz, P. G. Genetic incorporation of unnatural amino acids into proteins in mammalian cells. *Nature methods* **4**, 239-244, doi:10.1038/nmeth1016 (2007).

348 Parrish, A. R. *et al.* Expanding the genetic code of Caenorhabditis elegans using bacterial aminoacyl-tRNA synthetase/tRNA pairs. *ACS chemical biology* **7**, 1292-1302, doi:10.1021/cb200542j (2012).

349 Ko, J. H., Llopis, P. M., Heinritz, J., Jacobs-Wagner, C. & Soll, D. Suppression of amber codons in Caulobacter crescentus by the orthogonal Escherichia coli histidyl-tRNA synthetase/tRNAHis pair. *PloS one* **8**, e83630, doi:10.1371/journal.pone.0083630 (2013).

350 Duncan, G. *et al.* Evaluation of a new system for developing particulate enzymes based on the surface (S)-layer protein (RsaA) of Caulobacter crescentus: fusion with the beta-1,4-glycanase (Cex) from the cellulolytic bacterium Cellulomonas fimi yields a robust, catalytically active product. *Applied biochemistry and biotechnology* **127**, 95-110, doi:10.1385/abab:127:2:095 (2005).

351 Uprety, R. *et al.* Genetic encoding of caged cysteine and caged homocysteine in bacterial and mammalian cells. *Chembiochem* **15**, 1793-1799, doi:10.1002/cbic.201400073 (2014).

352 Wang, L., Brock, A., Herberich, B. & Schultz, P. G. Expanding the genetic code of Escherichia coli. *Science* **292**, 498-500, doi:10.1126/science.1060077 (2001).

353 Chatterjee, A., Sun, S. B., Furman, J. L., Xiao, H. & Schultz, P. G. A versatile platform for single- and multiple-unnatural amino acid mutagenesis in Escherichia coli. *Biochemistry* **52**, 1828-1837, doi:10.1021/bi4000244 (2013).

354 Zhou, B. *et al.* The global regulatory architecture of transcription during the Caulobacter cell cycle. *PLoS genetics* **11**, e1004831, doi:10.1371/journal.pgen.1004831 (2015).

355 Mora, L. *et al.* The essential role of the invariant GGQ motif in the function and stability in vivo of bacterial release factors RF1 and RF2. *Molecular microbiology* **47**, 267-275, doi:10.1046/j.1365-2958.2003.03301.x (2003).

356 Feaga, H. A., Viollier, P. H. & Keiler, K. C. Release of Nonstop Ribosomes Is Essential. *mBio* **5**, e01916-01914, doi:10.1128/mBio.01916-14 (2014).

357 Armengod, M. E. *et al.* Modification of the wobble uridine in bacterial and mitochondrial tRNAs reading NNA/NNG triplets of 2-codon boxes. *RNA Biology* **11**, 1495-1507, doi:10.4161/15476286.2014.992269 (2014).

358 Ruan, B. *et al.* Quality control despite mistranslation caused by an ambiguous genetic code. *Proceedings of the National Academy of Sciences* **105**, 16502-16507, doi:10.1073/pnas.0809179105 (2008).

359 Chou, C., Uprety, R., Davis, L., Chin, J. W. & Deiters, A. Genetically encoding an aliphatic diazirine for protein photocrosslinking. *Chemical Science* **2**, 480-483, doi:10.1039/C0SC00373E (2011).

360 Daugherty, P. S., Iverson, B. L. & Georgiou, G. Flow cytometric screening of cell-based libraries. *Journal of Immunological Methods* **243**, 211-227, doi:https://doi.org/10.1016/S0022-1759(00)00236-2 (2000).

361 Xia, Y. & Whitesides, G. M. Soft Lithography. *Angewandte Chemie* **37**, 550-575, doi:10.1002/(SICI)1521-3773(19980316)37:5<550::AID-ANIE550>3.0.CO;2-G (1998).

362 Takeuchi, S., DiLuzio, W. R., Weibel, D. B. & Whitesides, G. M. Controlling the shape of filamentous cells of Escherichia coli. *Nano Lett* **5**, 1819-1823, doi:10.1021/nl0507360 (2005).

363 Schmidl, S. R., Sheth, R. U., Wu, A. & Tabor, J. J. Refactoring and optimization of light-switchable Escherichia coli two-component systems. *ACS synthetic biology* **3**, 820-831, doi:10.1021/sb500273n (2014).

364 Radhakrishnan, S. K., Thanbichler, M. & Viollier, P. H. The dynamic interplay between a cell fate determinant and a lysozyme homolog drives the asymmetric division cycle of Caulobacter crescentus. *Genes & development* **22**, 212-225, doi:10.1101/gad.1601808 (2008).

365 Huitema, E., Pritchard, S., Matteson, D., Radhakrishnan, S. K. & Viollier, P. H. Bacterial birth scar proteins mark future flagellum assembly site. *Cell* **124**, 1025-1037, doi:10.1016/j.cell.2006.01.019 (2006).